Stretching, bursting, splashing and bouncing: Electrohydrodynamics of microfluidic drops

by
Rohit Pillai
Multiphysics Fluid Dynamics Group
Department of Chemical and Biomolecular Engineering
University of Melbourne

A thesis submitted in fulfilment of the requirements of the degree of Doctor of Philosophy

September 2017

To Kasturi, whose joy (relief?) at every milestone of this work exceeded even mine.

I stand at the seashore, alone, and start to think.
There are the rushing waves,
mountains of molecules, each stupidly minding its own business,
trillions apart yet forming white surf in unison.

Ages on ages before any eyes could see,
year after year thunderously pounding the shore as now.
For whom, for what? On a dead planet, with no life to entertain.

Never at rest, tortured by energy,
wasted prodigiously by the sun, poured into space.
A mite makes the sea roar.

Deep in the sea, all molecules repeat the patterns of one another,
till complex new ones are formed.
They make others like themselves and a new dance starts.

Growing in size and complexity,
living things, masses of atoms, DNA, protein,
dancing a pattern ever more intricate.

Out of the cradle onto the dry land, here it is standing,
atoms with consciousness, matter with curiosity.
Stands at the sea, wonders at wondering,
I, a universe of atoms,
an atom in the universe.

-Richard Feynman

Contents

Abstract

The technologies used to drive the miniaturisation of computers have had subsequent impact in other fields, and are now being used by researchers to shrink chemical/biological laboratories onto a single silicon-chip. Droplet-based 'lab-on-a-chip' (LoC) devices use a microscale drop in lieu of a test-tube, converting the traditional steps involved in chemical-analysis to precise manipulations of the drop in a micron-sized channel. Typical drop manipulations in LoC devices include drop formation, fission, and fusion, which are commonly achieved by an applied electric field. While LoC devices can potentially revolutionise the chemical and life sciences, their development hinges on a fundamental understanding of electrically induced fluid-flow, or electrohydrodynamics, at the microscale.

Using microfluidic drop manipulation in LoC devices as motivation, this thesis presents and analyses the results of a numerical investigation undertaken using a recently-developed, multiphase electrokinetic fluid-flow model. A large number of simulations were conducted for single-drop, drop-interface, and drop-drop systems, encompassing a wide range of physical, material, and electrical parameters. Despite their apparent simplicity, systems involving one or two electrified drops display rich and complex, but poorly understood, electrohydrodynamic phenomena. The objectives of the investigation were to: (i) identify the physical mechanisms responsible for the observed phenomena, (ii) develop qualitative phase-maps using the relevant parameters, and (iii) use this understanding in conjunction with scaling theory to quantitatively predict key output parameters, such as the size and charge of satellite drops formed during drop breakup, for example.

The results from this work will inform the design, material selection, and operating conditions of electrohydrodynamic lab-on-a-chip devices. In addition, the insights developed into the physics of breakup/coalescence of microscale drops will be applicable to a wide range of related soft-matter systems.

Declaration

The work presented in this document builds on a wide body of literature. I hereby certify that:

- The thesis comprises only my original work towards the PhD. Whenever applicable, due acknowledgement has been made in the text to all other material used. Any direct quotes are included inside double quotation marks.
- All other text has been written by me (with advice from my supervisors Malcolm Davidson, Joseph Berry, and Dalton Harvie), and all figures have been generated by me using data generated from simulations that I have run.
- This thesis is fewer than 100,000 words in length, exclusive of tables, figures, and bibliography.

Rohit Pillai

Acknowledgements

First, I sincerely thank all of my supervisors for ensuring that they were able to meet every week to discuss my research, without fail, over the last four years. The regular feedback that I received on my work was crucial to any progress that I was able to make. I also learned immensely from all our discussions, even those in which I was merely an observer. It has been an absolute pleasure and a privilege to interact with each of you. In addition to research, your comments and suggestions on my writing and presentations has (hopefully!) made me a better scientific communicator as well.

I thank my primary supervisor, A/Prof. Malcolm Davidson, for being generous with his time whenever I knocked on his door, and always being eager to discuss any aspect of my research. You encouraged me to pursue my independent research ideas, while also deftly nudging me back onto more productive paths whenever I went astray. I tried to absorb as much as I could from your wide-ranging experience in computational fluid dynamics, and am much the better for it. I remain indebted to all your contributions for making this thesis possible. As I leaf through it, I can, unsurprisingly, see your influence on every page.

I thank my co-supervisor, Dr. Joseph Berry, for always helping me with any issues I faced with coding, running simulations, and interpreting results. I cannot overstate the importance of your unending patience with my questions, both in person and on email/gtalk, both during work hours and on evenings/weekends. I remain grateful for all your assistance with issues as varied as writing scripts to automate tasks, to drafting presentatons in Beamer. I also appreciate your constant encouragement on all aspects of my work, delivered with your characteristic indefatigable cheerfulness that I try to emulate.

I thank my co-supervisor, A/Prof. Dalton Harvie, for his fierce skepticism that taught me to critique my own work more closely, and thus become a better researcher. I valued your insightful ideas and thoughts during our meetings, whose importance I usually only fully grasped a few days/months after, and which would nevertheless inevitably become

key to the problem I was studying at the time. I also appreciate the financial support during the thesis writing period, which allowed me to make this thesis better.

I have been lucky to been surrounded by the brilliant and supportive fellow members of the Multiphysics Fluid Dynamics Group, who have gone on to become close friends. Lachlan and Christian were extremely helpful in getting me set up initially, answering questions like "How do you do 'X' in bash again?" multiple times without the slightest hint of irritation. Over the years, they were an invaluable resource that I could bank on whenever needed, for assistance with everything from debugging code to simplifying concepts I did not understand. Wei-Lun was always available to discuss electrokinetics, and provided useful advice at every stage of my PhD. The other fellow graduate students, postdocs, and academics that have been part of this journey are too numerous to include here, but I do appreciate your contributions. I also acknowledge the support provided by the University of Melbourne in the form of a PhD stipend and a travel grant, and the Particulate Fluids Processing Centre in the form of a (separate) travel grant.

Finally, I'd like to thank my parents for their unconditional love and support; if it were not for the sacrifices they made to ensure I could pursue an education overseas, I would not be here. I am indebted to my partner and fiancée, Kasturi, whose love and companionship has been the bedrock of my life for eleven years now, each better than the one before. Being at university with her has been one of the most joyful experiences of my life, and everything during my PhD, as before it, has been immeasurably improved by her presence.

Rohit Pillai
December 2016

Published/presented work

Journal publications

1. **R. Pillai**, J.D. Berry, D.J.E. Harvie and M.R. Davidson. Electrophoretically mediated partial coalescence of a charged microdrop, *Chemical Engineering Science*, 169, 273-283, 2017.
2. **R. Pillai**, J.D. Berry, D.J.E. Harvie and M.R. Davidson. Electrokinetics of isolated electrified drops, *Soft Matter*, 12, 3310, 2016.
3. M.R. Davidson, J.D. Berry, **R. Pillai** and D.J.E. Harvie. Numerical simulation of two-fluid flow of electrolyte solution with charged deforming interfaces, *Applied Mathematical Modelling*, 40(3), 1989-2011, 2016.
4. **R. Pillai**, J.D. Berry, D.J.E. Harvie and M.R. Davidson. Electrohydrodynamic deformation and interaction of microscale drop pairs, *International Journal of Computational Methods and Experimental Measurements*, 4(1), pp. 33-41, 2016.
5. **R. Pillai**, J.D. Berry, D.J.E. Harvie and M.R. Davidson. Electrolytic drops in an electric field: A numerical study of drop deformation and breakup, *Physical Review E*, 93(1), pp. 013007, 2015.

Journal publications in preparation

6. **R. Pillai**, J.D. Berry, D.J.E. Harvie and M.R. Davidson. Rebound and fission of a charged microdrop with a planar interface.
7. **R. Pillai**, J.D. Berry, D.J.E. Harvie and M.R. Davidson. Electrical suppression of partial coalescence of dielectric drops.
8. **R. Pillai**, J.D. Berry, D.J.E. Harvie and M.R. Davidson. Electrohydrodynamics and morphologies of microdrop coalescence.
9. **R. Pillai**, J.D. Berry, D.J.E. Harvie and M.R. Davidson. Merge to bounce: Transition from coalescence to non-coalescence for oppositely-charged microdrops (near submission).

Peer-reviewed conference papers

10. **R. Pillai**, J.D. Berry, D.J.E. Harvie and M.R. Davidson. Electrophoretic Effects on Satellite Droplet Formation During Electrocoalescence of Microdrops, in *CSIRO 11th International Conference on CFD in the Minerals and Process Industries*, 7-9 December 2015, Melbourne, Australia.
    This paper was a runner-up for the **Best student paper** award, and the accompanying presentation won the **Best student presentation** award.
11. **R. Pillai**, J.D. Berry, D.J.E. Harvie and M.R. Davidson. Effect of Interfacial Tension and Electric Field on Charge Separation Dynamics Inside Stable and Unstable Microdrops, in *19th Australasian Fluid Mechanics Conference*, 8-11 December 2014, Melbourne, Australia.

Other conference presentations

12. J.D. Berry, **R. Pillai**, D.J.E. Harvie and M.R. Davidson. Modelling instabilities in electrokinetic multiphase flows, in *Computational Techniques and Applications Conference*, 27-30 November, 2016, Melbourne, Australia.
13. **R. Pillai**, J.D. Berry, D.J.E. Harvie and M.R. Davidson. An Electrokinetic Study of Binary Drop Electrocoalescence, in *8th International Conference on Computational and Experimental Methods in Multiphase and Complex Flow*, 20-22 April 2015, Valencia, Spain.
14. J.D. Berry, **R. Pillai**, D.J.E. Harvie and M.R. Davidson. Electrokinetic Instabilities in Multiphase Microfluidic Flows, in *7th Biennial Australian Colloid and Interface Symposium*, 1-5 February 2015, Hobart, Australia.

List of Symbols

Acronyms

μTAS	Miniaturized Total Analysis Systems	3
AC	Alternating Current	190
AMR	Adaptive Mesh Refinement	192
ATP	Adenosine Triphosphate	11
ATPS	Aqueous Two Phase Systems	191
BEM	Boundary Element Method	35
BF	Body Force	68
BIM	Boundary Integral Method	86
C-NC	Coalescence to Non-coalescence	178
CCEP	Contact Charge Electrophoresis	145
CDS	Complete Divergence of Stress Tensor	68
CFD	Computational Fluid Dynamics	21
CLSVoF	Combined Level Set Volume of Fluid	61
CSF	Continuum Surface Formulation	51
DC	Direct Current	15
DNA	Deoxyribonucleic Acid	11
ECD	Electrophoresis of a Charged Drop	145
EDL	Electric Double Layer	41
FCT	Flux Corrected Transport	57
FEM	Finite Element Method	36
FGVT	Fine Grid Volume Tracking	60
FVM	Finite Volume Method	37

Roman variables

List of Figures

List of Tables

1 Introduction

> *Why cannot we write the entire 24 volumes of the Encyclopedia Brittanica on the head of a pin?*
>
> Richard Feynman

Electrohydrodynamics is the science of electrically induced fluid flow, involving the coupling of electromagnetism and hydrodynamics. The origins of electrohydrodynamics can be traced back more than five hundred years, when William Gilbert[1] brought a statically-charged piece of amber[2] close to a *drop* of water and discovered that the drop assumed a conical shape in response (Gilbert, 1600). Our understanding of electrohydrodynamics has, expectedly, advanced significantly since Gilbert's time; today, we know that in addition to their ability to *deform* liquid drops, electrohydrodynamic forces can *breakup* and *coalesce* drops as well. These electrical manipulations of drops have applications to natural processes, such as the dynamics of raindrops in thunderstorms (Rayleigh, 1882), and to industrial processes such as solvent extraction (Eow & Ghadiri, 2002). In the last few decades, electrohydrodynamics of liquid drops has also found application in *microfluidic* flows, with applications across physics, chemistry, biology, and medicine (Li, 2004; Chang & Yeo, 2010). The relative importance of the governing forces changes as the microscale is approached, and the electrically-induced motion of mobile charge, or electrokinetics, becomes important. However, our understanding of the fundamentals of electrokinetic microfluidic flow involving drops is still developing. This work attempts to fill in some of the knowledge gaps, by numerically simulating simplified scenarios of relevance to microfluidic devices using an electrokinetic model. It is expected that the results in this thesis will aid the design, operation, and development of microscale electrohydrodynamic devices.

[1] William Gilbert was a polymath; in addition to authoring the earliest published work on electricity and magnetism, he also briefly served as Queen Elizabeth's personal physician.

[2] Amber is *electrum* in Latin, which, due to its significance to Gilbert's experiments, serves as the etymological root of the modern day word *electricity*.

This chapter first introduces the topic of microfluidics, tracing its early history through to the current application to small-scale devices (§ 1.1). Despite their vast potential, these devices haven't become as commonplace as was expected two decades ago. The challenges preventing the widespread commercialisation of such devices are outlined (§ 1.2). The diverse array of potential applications are reviewed (§ 1.3), and the drop manipulations necessary for their development are listed (§ 1.4). Electrohydrodynamics is introduced and the relevant electrohydrodynamic phenomena are defined (§ 1.5). The deficiencies in the literature on this topic are highlighted (§ 1.6) and a succinct thesis statement is provided (§ 1.7). The chapter concludes with an outline of the remainder of the dissertation (§ 1.8).

1.1 A brief history of microfluidics

Microfluidics, as a field of study, emerged in the early 1950's as a response to the problem of accurately dispensing tiny amounts of liquids (down to the order of picolitres) as a continuous stream of drops for ink-jet printing (Le, 1998). The continuous-inkjet printer that resulted was probably the first microscale electrohydrodynamic device; it used a hydrodynamic instability to break up a liquid ink filament into drops, and an electric field to control the trajectories of the drops as they impacted the paper (Sweet, 1965). Around the same time, a revolution was under way in microelectronics, starting with the invention of integrated circuits (IC) (Norman & Haas, 1960). This breakthrough, made possible by the discovery that semiconductor devices can capably replace vacuum tubes, fundamentally altered our lives and our science. This large scale integration of miniature transistors resulted in a mass-produced building block approach to circuit design, and consequent exponential development.[3] This led to rapid adoption and commercialisation, which in turn spurred further miniaturization, creating a positive feedback-loop. A consequence of this *microelectronic* revolution is that, for example, smartphones today have multiple orders of magnitude more computing power than the entire Apollo space program of 1969.[4]

Early in the 1970's, the expectation was that the recent microelectronic revolution would translate to a consequent *microfluidic* revolution, especially in analytical chemistry

[3] Gordon Moore, in a clairvoyant article, predicted this exponential growth would continue for the next 10 years (till 1975), a prediction that would come to be known as *Moore's law*. Moore's law has largely held up till today, more than 50 years since publication of the original article (Moore, 1965).

[4] The Apollo Guidance Computer had 64 kb of RAM and operated at 0.043 MHz (Saran, 2009). In comparison, an iPhone 7 has 2 GB of RAM and operates at 2.3 GHz (Wikipedia, 2016).

(Whitesides, 2006). The reasons for these expectations were two-fold; first, microfabrication techniques such as wet-chemical etching and photolithography - developed to structure silicon for microelectronic circuits - could be readily used to create microchannels and reservoirs. Second, the inefficiencies in macroscopic circuits (large arrays of vacuum-tubes) were analogous to those in chemical analysis (large-scale, specialized and expensive instrumentation). The common denominator of miniaturization was expected to result in microfluidics-based systems displacing the latter, as IC had the former. Terry *et al.* (1979) were the first to use IC fabrication techniques to construct a microfluidic gas chromatograph, by etching a microchannel, valve and detector onto a 5 cm diameter silicon wafer. This microfabricated system could fit in a 1.5 m long capillary column and separate compounds in a matter of seconds, while still being three orders of magnitude smaller than its conventional counterpart; it did, however, depend on an external flow controller to supply the carrier gas, and a data processing unit to analyse the results. Shoji *et al.* (1988) similarly miniaturized some parts of a blood pH monitoring system on a 2×2 cm^2 silicon cell. Their prototype included three valves and a pH sensor, and required a sample volume of only 10 μL.

Following the pioneering accomplishments of Terry *et al.* (1979) and Shoji *et al.* (1988), Manz *et al.* (1990) envisaged the creation of automated, portable devices for chemical analysis, which integrated multiple processing steps (for e.g. sampling, pre-treatment, chemical reactions, analytical separations, sample detection, and data analysis) onto a single silicon-wafer sized chip. They coined the term 'miniaturized total analysis systems', or 'μTAS', to describe such (hypothetical) devices. μTAS, in theory, offered several advantages over conventional approaches in chemical-sensing - associated with scaling laws - namely a decrease in analysis times, higher efficiency in utilization of samples and reagents, lower operational costs, and a smaller device footprint (Manz *et al.*, 1992). μTAS development hinged, however, on developments in microfluidics; precise microfluidic manipulation was required for the metering/valving/mixing of samples/reagents necessary for μTAS functioning. The earliest review of microfluidics describes this close association of microfluidics and μTAS research, by stating that while "the history of microfluidics is short; the number of fluidic components is limited and the number of microfluidic systems is even smaller", microfluidics had recently become a "hot research topic" due to the demand for "complex microfluid handling systems for chemical analyses" (Gravesen *et al.*, 1993).

1.1.1 μTAS to LoC

μTAS was conceived as a means to usefully bridge the research programs of the microfabrication and analytical chemistry communities. Initially, μTAS research was motivated by component-level development with an eventual goal to integrate the components into functional devices, analogous to how component-level logic gates led to development of computer processors. Consequently, components such as micro-electronics and sensors (Verpoorte & De Rooij, 2003), micropumps (Laser & Santiago, 2004), micromixers (Nguyen & Wu, 2005) and microvalves (Oh & Ahn, 2006) developed into mature technologies. However, the integration of these technologies into useful, widely-accessible μTAS devices did not materialise. See the two-part review on early μTAS research for more details (Reyes *et al.*, 2002; Auroux *et al.*, 2002).

In addition to integration difficulties, μTAS development soon faced technological hurdles as it became clear that photolithography on silicon (or silica-based ceramics such as glass) - while being an excellent solution for microelectronics applications - was less appropriate for most μTAS.[5] Photolithography was relatively expensive, and provided little control over the surface properties of the microchannel which were instrumental to determining the nature of the flow within them (Stone *et al.*, 2004). Consequently, while early - 1990's and before - μTAS primarily employed (mechanically hard) silicon or glass structured by conventional microfabrication techniques, later - post 2000 - μTAS tended to employ (mechanically soft) elastomers using novel fabrication techniques specifically developed for these substrates. These microfabrication techniques, developed to precisely microstructure soft matter (microcontact printing, replica molding and microtransfer molding among others), were collectively referred to as 'soft lithography' (Xia & Whitesides, 1998). Soft lithography techniques did not require expensive clean-room facilities, and had higher resolution of up to < 100 nm, compared to ~ 250 nm for photolithography, giving greater control of surface topography. The most common polymeric substrate used for soft lithography was polydimethylsiloxane (PDMS) (Mcdonald *et al.*, 2000), which is an affordable, unreactive, optically-transparent and moldable polymer; consequently, the resulting device prototypes were "low in capital cost, easy to learn, straightforward to apply, and accessible to a wide range of users" (Whitesides *et al.*, 2001).

[5] Note that silicon, due to its toughness and durability, is still viable for chemistry applications involving contact with high temperatures or strong solvents. Similarly, glass continues to be useful for its surface characteristics that make it suitable for capillary electrophoresis, for example (Whitesides, 2006).

Depending on choice of polymer substrate, chemical treatments and micromachining processes, the mechanical (elasticity, porosity, permeability) and chemical (wettability, pH, surface charge) properties of the surfaces of the microchannel could now be customized. These advantages, along with the low cost and quick prototyping, accelerated the opening of new avenues of μTAS design, broadening the research focus to the life sciences (Beebe *et al.*, 2002); a large number of prototypes were developed for applications as diverse as cellomics (Andersson & van den Berg, 2003), drug development (Weigl *et al.*, 2003) and tissue engineering (Khademhosseini *et al.*, 2006). Thus, μTAS research evolved over time from purely chemical-analysis, to a more interdisciplinary study of microfabricated physical, chemical, biochemical and biological systems (Weibel & Whitesides, 2006). These devices came to be referred to as 'lab-on-a-chip' (LoC) devices (Figeys & Pinto, 2000), in recognition of their potential to miniaturize entire laboratories, both in the chemical and life sciences, onto a chip. Microfluidics continued to be relevant for LoC development as it was for μTAS before it; this was acknowledged by van den Berg & Bergveld (2006) when they concluded, in a review article on the occasion of the 10th μTAS conference, that "microfluidics is the essential generic technology responsible for the broadening of the field and incredible variability of concepts and applications."

1.2 LoC's: Prototype to product?

The thriving academic communities, conferences and journals dedicated to microfluidics, demonstrate that overall field of LoC's has become a significant hub of research. Although this has resulted in a voluminous academic literature, the long-awaited transition from lab-tested prototypes to market-ready devices has largely not yet been achieved, especially when compared to micro-electrical-mechanical-systems (MEMS). Kamholz (2004) noted this when he observed that, while microfluidics *matched* MEMS in both number and rate of publications, "MEMS patents are still issuing with exponential growth, and with a substantially faster growth rate than those in the microfluidics area." He went on to point that this disparity "is largely explained by the commercial successes of MEMS-based products that have gone completely unmatched to date in microfluidics" (Kamholz, 2004). Consequently, microfluidics-based LoC devices do not yet impact our daily lives the way microelectronic devices do; we are yet to see "every patient monitor his or her condition using microfluidic home-test systems", for example (Whitesides, 2006). The

inkjet printer[6], the development of which preceded μTAS and LoC, remains the sole success story.[7]

1.2.1 Challenges

The barriers preventing microfluidic LoC's from replicating the inkjet printer's success are two-fold. The first barrier is commercialisation; businesses based on LoC devices, despite their considerable technological advantages, have largely failed to displace the incumbent macroscale technologies. The reasons for this are numerous: the lack of a true disruptive technology or 'killer app', inadequate standardisation of the functional parts of LoC's, and short life of the components have all been argued to be causal factors. The minutiae of this ongoing debate is outside the scope of this thesis work; the reader is directed to Holger Becker's series of articles for an overview of LoC commercialization (Becker, 2009*a*,*b*,*c*,*d*, 2010*a*,*b*,*c*,*d*, 2011).

The second barrier(s), more relevant here, are the deficiencies of existing LoC prototypes. Thus far, the discussion has been restricted to single-phase or continuous-flow microfluidic devices. These devices typically consist of a network of channels (etched onto a substrate) containing an aqueous solution on which fluidic operations need to be performed. The use of an aqueous solution (for e.g. water with dissolved salts) is popular because the majority of chemical and biological reactions occur in aqueous solutions, and they can be used with a broad variety of materials. These characteristics make aqueous solutions good 'working fluids' for LoC's, and they are commonly employed to carry the analyte/solute/reagent/biomolecule of interest. However, there are a few drawbacks associated with their use. Water is detrimental to semiconductor devices (such as embedded electrodes), leading to corrosion over time. As the sample or reagent is not physically separated from the surfaces, cross contamination can occur with chemically patterned surfaces. This can lead to spurious results if the target molecule is adsorbed onto the surface, as has been sometimes observed. This contamination can also affect the surface properties such as surface charge, which, for an electrically operated device, can modify the electric field and consequently the fluid flow in the device, leading to device

[6]The microfabricated inkjet print-head had a market volume of US$ 2.5 billion as of 2009 (Becker, 2009*b*)

[7]The modern day pregnancy and diabetes test strips as well as some environmental diagnostics systems can be brought up as counterpoints; while these inventions are impressive in their own right, none of them truly deliver on the promise of 'lab-on-a-chip'

degradation. Another drawback of single-phase devices is that implementing reagent mixing usually involves bringing reagent streams into contact. The mixing is therefore solely achieved by diffusion, which is inefficient.

The other crucial problem with single-phase (or continuous-flow) LoC's is that the size of the device scales almost linearly with the number of parallel experiments; therefore, the gains from parallelising are limited. This limitation in scalability limits the throughput that can be achieved from the device. The vast combinatorial spaces, that arise in the study of chemical, biochemical and biological systems, increasingly require high throughputs. For example, a pairwise interaction between all the genes in the human genome results in $\sim 10^9$ distinct gene combinations, a short polypeptide of 100 amino acids can have $\sim 10^{130}$ distinct sequences, and drug discoveries can routinely involve $\sim 10^{60}$ molecules (Kelly *et al.*, 2007). Such studies can, therefore, be only performed in highly parallel systems.

1.2.2 Drop microfluidics

In single-phase systems, parallelisation is usually achieved by fabricating separate chambers (Thorsen, 2002), and increasing the number of experiments requires adding more chambers. An alternative to increasing the size of the device to fit more chambers, is to shrink the size of the chamber to fit more chambers in a given device; this is, essentially, the motivation behind drop-based microfluidic devices. The idea is that each chamber can be reduced to an individual (aqueous) drop, which contains the solute of interest. There are two distinct drop-based technologies that have been invented almost entirely independently of each other. The first is 'digital microfluidics' (Fair, 2007), which uses arrays of drops resting on a planar surface (this system can be open to the air or closed), moved around by electrical variations in the interfacial tension force (see § 1.5.1). The second is 'droplet microfluidics' (Huebner *et al.*, 2008) where the aqueous drop is suspended in an immiscible oil phase and can be actuated by a variety of mechanisms, such as capillary or electrical forces. In this work, the term 'drop microfluidics' is used to describe both systems, as the results generated here are broadly applicable to both research streams. The term 'droplet' will, instead, be used to refer exclusively to the satellite drops in cases where a portion of the microdrop is separated/ejected.

The main features of drop microfluidics that make it so attractive are (Teh *et al.*, 2008; Theberge *et al.*, 2010):

- It provides discrete, monodisperse volumes in which the reaction or species of interest can be isolated.
- The nanometer to micrometer range drops have high surface to volume ratios, resulting in shorter diffusion distances, lower mass and heat transfer times and quicker reactions, with the added advantage of individual control of each reaction site.
- It offers the ability to conduct large numbers of experiments in an automated manner, which allows for batch processing and acquisition of large data sets efficiently.
- Because of the above advantages, it promises greater throughput and scalability, which has been a limitation of conventional LoC's.

Good reviews exist on different aspects of drop microfluidics. Günther & Jensen (2006) explored the flow characteristics of multiphase microfluidics, and provided a good overview of scaling of forces, fluid physics, and the flow regimes observed. Kelly *et al.* (2007) outlined the applications of microdrops to protein engineering. Shui *et al.* (2007) considered both stratified and disperse flows with a focus on interface stability. Teh *et al.* (2008) and Theberge *et al.* (2010) focused on the specific advantages of drop-based LoC's over single-phase devices, and detailed a range of applications. Baroud *et al.* (2010) provided an overview of the different techniques used to form, move and coalesce drops. Pompano *et al.* (2011) focused on droplet arrays, detailed their spatial indexing in one, two and three dimensions and provided applications for each setup. Zhao & Middelberg (2011) studied the effect of a number of parameters on the flow regimes for liquid-liquid and gas-liquid systems, and focused on drop formation and coalescence. Choi *et al.* (2012) summarised the latest developments in digital microfluidics, from device fabrication to applications. Seemann *et al.* (2012) reviewed aspects of drop generation and manipulation. Finally, Zhu & Fang (2013) compared analytical detection techniques for drop LoCs and listed their relative advantages and disadvantages.

1.3 Applications for microdrops

A survey of applications of drop microfluidics is provided below, covering both LoC devices and some noteworthy (non-LoC) ones. Note that the results of this thesis are not relevant to all of these applications; the intention here is to illustrate the diversity and scope of microdrop-based devices.

1.3.1 LoC-based applications

Knight (2002) framed the challenge for LoC development when he asked, 'could the equipment needed for everyday chemistry and biology procedures be shrunk to fit on a chip the size of a postage stamp?'. As elaborated below, microfluidic drops are a plausible means to achieving this miniaturization.

Drop as a chemist's flask

In single-phase devices for chemical analysis, the parabolic flow profiles of pressure-driven flow result in dispersion of the two reactant phases and, consequently, poor localization and control of the reaction sites. Drops, on the other hand, provide compartmentalisation of the individual reactants (Song *et al.*, 2003); reactions are induced by controlled coalescence of drops which provides accurate control over residence and reaction times. These advantages make drop microfluidics useful for chemical synthesis (Gerdts *et al.*, 2004), chemical kinetics (Bringer *et al.*, 2004) and clinical diagnostics (Srinivasan *et al.*, 2004) studies. Song *et al.* (2006) provide a good overview on reactions in microfluidic drops. In addition, by carrying out chemical and physical operations on suspended drops in a channel, it is possible to synthesize simple polymerised colloids (Xu *et al.*, 2005), as well as more complex soft-matter systems such as microcapsules (Zhang *et al.*, 2006), high-order emulsions (Shah *et al.*, 2008) and Janus particles (Chen *et al.*, 2009). This has applications to drug delivery; see Wang *et al.* (2011) for an overview on synthesis of advanced materials using microfluidic drops.

Drop as a Petri dish

In addition to microreactors, drops can be used to mimic biological environments, for applications involving cell cultures in biological assays (Yeo *et al.*, 2011). Cell growth assays are widely used because growth, which is calculated by measuring cell density, is a reliable indicator of a tested hypothesis on the target cells. Drops are advantageous for cell growth applications because of the drastically lowered volume needed,[8] along with the reduced risks of cross-contamination and fouling. Consequently, high throughput (drop-based) cell assays have been shown to use 1/1000th the assay volume of single-phase devices while still generating 500 times more throughput (Clausell-Tormos *et al.*, 2008). Recently, encapsulating a single cell in an emulsion drop has become possible (Joensson

[8] Guo *et al.* (2012) quantify this when they say 'the density of a single cell in a 10 μm drop is equivalent to that of a billion cells in a 1 μL well'

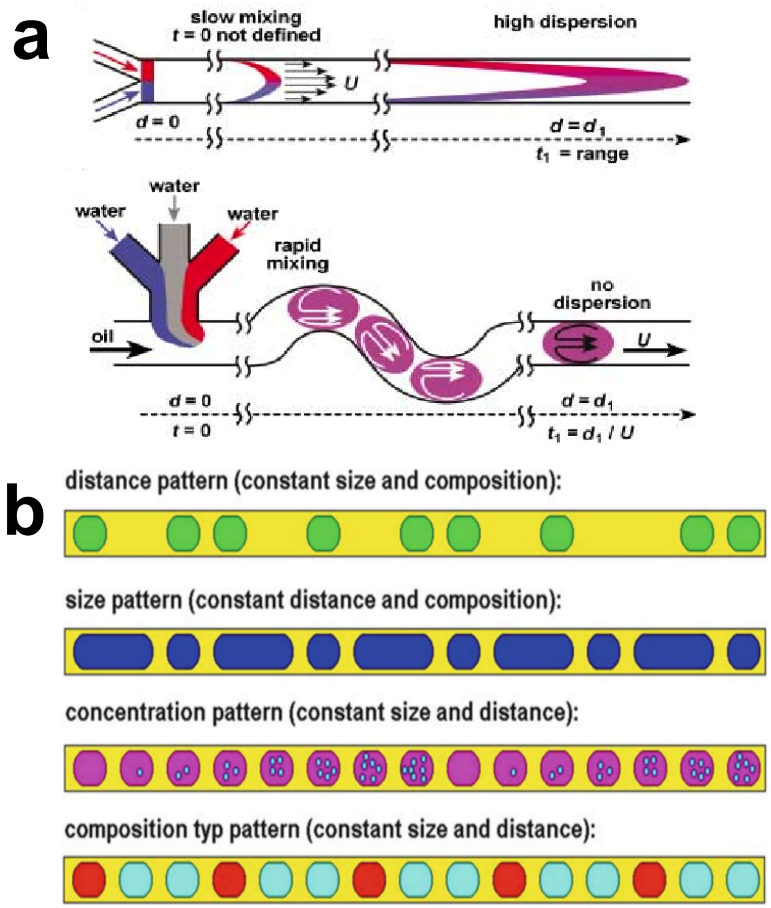

Figure 1.1: (a) Comparison of mixing of reagents in a pressure-driven channel for (top) single-phase and (bottom) microdrop systems. (b) The different types of desired drop distributions that can be achieved by LoC systems. Figures have been reproduced from Manz *et al.* (2012).

& Andersson, 2012); studying single-cell growth is relevant for applications involving rare growth events, such as viral epidemics or antibiotic resistance (Lecault *et al.*, 2011). In addition to cellular systems, the development of *cell-like* structures involving synthetic lipid bilayers (Funakoshi *et al.*, 2006) is valuable, with applications to high-throughput drug discovery.

Drop as a cell

At an even smaller scale, the compartmentalisation provided by drops can be used to mimic the boundary of a *single cell*. This creates a cell-free environment to carry out biochemical processes such as gene expression (Dittrich *et al.*, 2005) and ATP synthesis (Choi & Montemagno, 2006). Also, drop-based Polymerase Chain Reaction (PCR) systems for *in vitro* DNA amplification have been developed which encapsulate a single template copy of DNA in a drop. Zhang *et al.* (2004) showed that such systems, when compared to single-phase systems, provided higher performance with a simpler design. The smaller thermal mass of drops makes the thermal cycling (needed for PCR operation) more efficient. The isolation, or 'monoclonality', of the drops increases the amplification efficiency by preventing the production of unwanted recombination products. Consequently, the products of drop-based PCR are closer to the original composition of the genomic libraries, when compared to single-phase PCR (Williams *et al.*, 2006). Another application of cell-free *in vitro* compartmentalisation is to the *directed evolution* of proteins (Miller *et al.*, 2006). Using parallelised microdrops, it is now possible to screen 10^8 enzyme reactions using $< 150\mu$L of reagent, at a million-fold reduction in cost compared to single-phase alternatives (Agresti *et al.*, 2010).

1.3.2 Speculative applications

The precise control of microfluidic drops has applications outside of LoC devices: Here three of the more speculative drop-based inventions are highlighted.

Drop computer

Cheow *et al.* (2007), among others, developed microfluidic logic gates (AND, OR and NOT) where the presence or absence of a microdrop in a channel represented true or false, respectively. However, these methods were asynchronous, and therefore incapable of scaling up the complexity of logic operations as would be required in a computer. Katsikis *et al.* (2015) resolved these issues by pioneering the use of a rotating magnetic

field as a global 'CPU clock' which can synchronise an arbitrary number of ferrofluid microdrops. Using this system, they were able to construct cascadable logic gates using multiple synchronous gates (For e.g., two XOR/AND gates can be combined to form a NAND gate), and also incorporate memory into the system by ensuring drops stayed in the exact location when the system was switched off. Thus, they were able to design a device that could theoretically perform any operation that a conventional electronic computer can perform; effectively, they created a computer *that runs on water*. Though the operation times are predictably much slower than its electronic counterpart, the drop computer promises to be the first in a 'new class of computers that can precisely control and manipulate physical matter' (Katsikis *et al.*, 2015).

Drop jukebox

Existing drop formation systems can be used to generate drops at frequencies ranging from 1 to 20 kHz, which spans the audible range of human hearing. Tan *et al.* (2014*a*) developed a novel method to transduce drop production into sound tracks. They accessed the frequencies of a particular score[9] and converted them into corresponding voltage changes for electrostatic generation of drops. Then they were able to use image processing to recover the frequencies, and the score, with high fidelity. The small errors observed resulted from lags in switching response times for drops, and depended on the frequency range of the original score. The drop-based microfluidic chip, in effect, acts as a musical instrument. This has application to LoC monitoring as small changes in drop production can be monitored by *using the sound generated by the device.*

Drop digital copier

Guzowski *et al.* (2011) developed an automated microfluidic technique for nanolitre drop generation with a high degree of control over the volume, volume fraction, and distribution of the drops. They used four parameters to achieve this, the opening times of the two external valves used along with the flow rate of both phases. These parameters were calculated by an image processing algorithm which automatically set the length of the drops. As a demonstration of their technique, they encoded a 100 pixel x 100 pixel image using a sequence of 100 drops whose volumes were controlled by the opening time of the valves. They were then able to faithfully render the images by decoding the pixels from their measurements of the length of the drops. Their output replicas showed a high

[9] In the paper they use Beethoven's 9th Symphony (*Ode to Joy*) as a proof-of-concept (Tan *et al.*, 2014*a*).

degree of fidelity to the original image, thus they developed a microdrop digital copier.

1.4 Drop manipulation for microfluidic applications

Despite their apparent complexity, the diverse range of applications touched on in the previous section depend on a comparatively small set of fluidic operations. The key issues are control over the shape, size and location of the individual drops. The umbrella term *drop manipulation* is used to encompass all the operations needed to be performed. The three most important drop manipulations are:

- **Formation:** Drops need to be generated reliably on demand, at high rates ($\mathcal{O}$(kHz)), in a monodisperse manner, usually from an aqueous solution containing the solute of interest. Basaran (2002) has reviewed the history of drop formation, and concluded that one of the emerging areas of research is drop formation in liquid/liquid systems, which is poorly understood and has applications to drop microfluidics.
- **Fission:** Drops need to be subdivided, either in bulk or individually. Precise control is required over the size of the ejected *progeny* droplets. Fission is usually achieved by elongating the drop and splitting it using the Plateau-Rayleigh instability (Seemann *et al.*, 2012). A deeper understanding of the instability-driven drop-splitting process is crucial to improvements in this area.
- **Fusion**: Drops need to be coalesced on demand, with other drops or with its bulk fluid. Depending on the application, either complete coalescence (which results in a single drop), or partial coalescence (where a *residual* droplet is ejected), is desirable (Minardi *et al.*, 2013). A fundamental understanding of the coalescence process is necessary to control the coalescence outcome, both qualitatively and quantitatively.

Hence, performing these drop manipulations successfully requires a good understanding of the flow behaviour. This is particularly relevant for LoC's as the fundamental flow physics changes dramatically when the micrometer scale is approached in fluids; some phenomena which are prominent on the macro scale, such as inertial effects, all but disappear at the microscale and are replaced by other physical phenomena, such as interfacial tension, which gain importance. Also, boundaries are never too far in microfluidic devices and boundary effects influence the flow significantly (Squires & Quake, 2005). This means that fluid-actuation techniques - developed for macroscale flows - can be found wanting when

applied to microfluidics. An example of this is pressurized pumping, which is commonly used in macroscale water/oil pipelines, and was consequently used to transport fluid in early microfluidic devices (Brody *et al.*, 1996). A simple scaling law estimate[10] shows that, for a given flowrate, the pressure drop scales to the negative fourth power of the length scale. This implies that a relatively larger pressure drop is required as the channel dimensions are decreased, making pressure-driven flow inefficient at the microscale.

However, the length-scale dependence of microfluidic flow behaviour also allowed for the development of new techniques to exploit it. Acoustic, magnetic, thermo-capillary and electric forces have prominently been shown to successfully drive fluid flows for LoC applications; each alternative has its advantages. Acoustic streaming in general, and surface acoustic waves (SAW) in particular, can generate high velocities which are useful for mixing and transport (Friend & Yeo, 2011). However, they have low fluidic resolution and require specialised piezoelectric substrates for operation (Ding *et al.*, 2013); they are also ill-suited to the type of confined flow-chambers that are common in LoC's as standing waves are produced that prevent uni-directional flow (Yeo & Friend, 2014). Magnetic actuation relies on the Lorentz body force, resulting from the induced electromagnetic field, to propel the flow (Qian & Bau, 2009). Magnetic forces are not dependent on surface properties of the channels, do not induce heating, and are relatively inexpensive (Nguyen, 2012). However, they require the usage of specialised colloidal suspensions of magnetic particles, known as 'ferrofluids', which are not suitable for all applications. The magnetohydrodynamic Lorentz force generated also scales unfavourably with reduction of channel size, and is inappropriate for length scales ≤ 100 μm (Yang *et al.*, 2016). Thermocapillary techniques use the temperature dependence of interfacial tension to perform the required drop manipulations, by utilising thermal gradients induced by laser beams. Interfacial tension decreases with temperature, and the Maragoni effect dictates that the flow of liquid is directed towards regions of higher interfacial tension, i.e. lower temperature. Thermocapillary techniques have the advantages of being contactless, thus requiring no microfabrication. However, they require the generation of significant temperature gradients which can be difficult at the microscale. Also, sudden changes in temperature aren't suitable to a number of LoC applications (Delville *et al.*, 2009)

Despite their promise, the aforementioned alternatives have been unable to displace

[10] For a pipe of diameter d containing a fluid of viscosity μ, the pressure drop (Δp) over a length L (assuming $L \gg d$) required to generate a volumetric flow rate (Q), can be given as $\Delta p = \frac{12\mu LQ}{\pi d^4}$

electric fields as the most popular means of actuation (Squires & Quake, 2005). For single-phase flows, electric forces offer the advantages of simplicity, efficiency and reliability; as the working-fluid is usually aqueous, the application of electric fields is straightforward. For drop-based systems, where aqueous drops are suspended in oil, electric fields have an additional advantage as they selectively act on the (conducting) drop phase, without directly influencing the (non-conducting) oil phase; this is important for targeted drop manipulation. Consequently, electric fields have been the method of choice for drop based microfluidics, and have been used to form (Park *et al.*, 2007), breakup (Link *et al.*, 2004), coalesce (Zagnoni *et al.*, 2010) and mix (Song *et al.*, 2006) drops. While single-phase microfluidic devices relied primarily on electro-osmosis (§ 1.5.2), drop-based systems exploit a number of other electrical phenomena such as electrophoresis (§ 1.5.3), dielectrophoresis (§ 1.5.4), and electrowetting (§ 1.5.1) to achieve their goals; these phenomena are discussed in the next section.

1.5 Electrohydrodynamics

In this thesis, two simplifying assumptions relevant to drop-based LoC's are made: First, the focus is restricted to direct current (DC) electrohydrodynamics; second, only electrohydrodynamic phenomena in the electrostatic regime are studied, i.e. magnetic and radiative effects are ignored.

While studying electrostatic interactions in fluids, it is helpful to distinguish between *bound charge* and *free charge*. Bound charge refers to charges of equal magnitude, but opposite polarity, that are held together; consequently, they can only move atomic distances (≤ 1Å) (Kirby, 2010). A typical example of bound charge is the positive charge in an atomic nucleus and the negative charge of the surrounding electron cloud. An external electric field, if present, polarises the bound charge and reorients it in the direction of the field. The forces that result from polarization effects are denoted as *dielectric* forces. The detailed electrostatic interactions of bound charges are usually simplified by representing them with the continuum *electrical permittivity*. When an electric field is applied to a drop suspended in a medium (with a non-unity permittivity ratio between the two phases), for example, the resulting dielectric forces can deform the drop.

Free charge, on the other hand, refers to charge that is mobile over distances much larger than atomic lengths. A typical example of free charge is ions dissolved in an aqueous

solution. An external electric field, if present, conducts the free charge, producing electric forces that also act on the ion-containing fluid. The forces on the fluid that result from ion-motion effects are denoted as *electrokinetic* forces. When an electric field is applied to a drop with symmetric cations and anions, for example, the ion species are attracted to opposite sides of the drop, i.e. the top and bottom portions of the drop interface (parallel to the field). Depending on the interface portion chosen as reference, the positive and negative ion species are either attracted to that interface section (counter-ions) or repelled by it (co-ions). This leads to the formation of a diffuse charge layer adjacent to both interface sections of the drop. The thickness of the diffuse charge layer depends on the relative magnitudes of the electromigration and diffusion in the bulk of the drop.

Electrohydrodynamics is a vast field of study, encompassing both dielectric and electrokinetic effects; the origins and definitions of some of the relevant physical phenomena are provided below.

1.5.1 Electrocapillarity and Electrowetting

Throughout the 19th century, multiple experiments had confirmed that the interfacial tension at liquid-liquid interfaces, such as mercury-water, vary with time; this was usually attributed to the deposition of impurities. Gabriel Lippmann[11] showed that this interfacial tension variation was electrical in origin, and resulted from the potential difference between the two phases (Lippmann, 1875). He went on to perform experiments showing that the interfacial tension at phase boundaries can be varied by the application of an external electric field. He called this phenomenon *electrocapillarity* and used it to develop several applications, including an electrocapillary motor (Lippmann, 1875).[12] The last few decades has seen the development of *electrowetting*, a promising means of actuation of bubbles (Chung *et al.*, 2010) or drops (Nelson & Kim, 2012), that relies on electrocapillarity. Electrowetting is the primary means of drop manipulation for digital microfluidic devices. The basic principle of electrowetting, shown in Figure 1.2a, is that the contact angle between the bubble/drop and the interface can be varied by an electric field, in such way that the nonwetting configuration becomes wetting. This change in contact angle results in a change in the interfacial tension force (at the three phase

[11] Gabriel Lippmann would go on to win the Nobel prize in 1908 for inventing the first colour photography method.

[12] The reader is directed to the original paper for more details; it has been translated and appended to Mugele & Baret (2005)'s comprehensive review article.

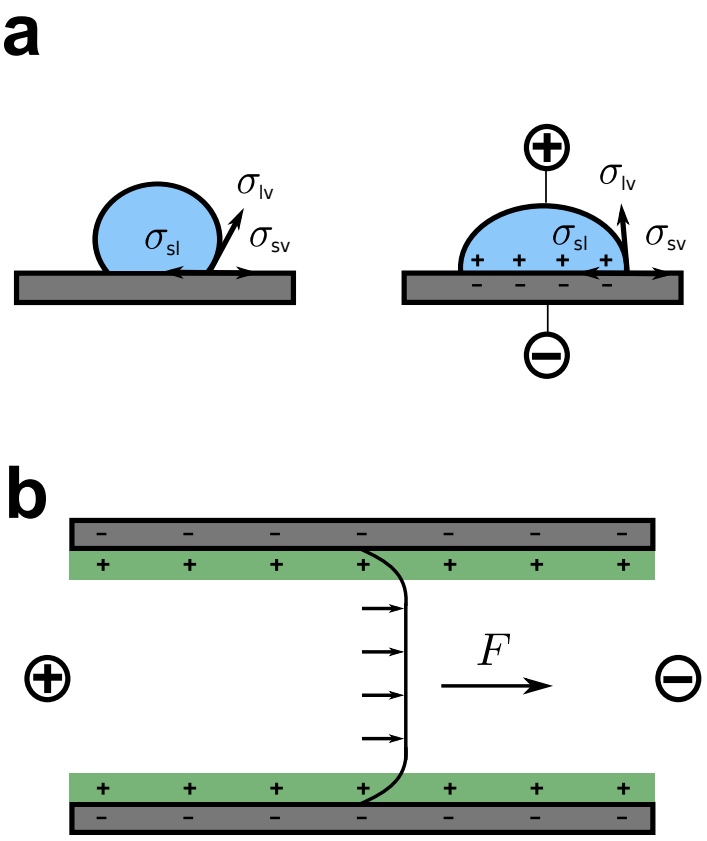

Figure 1.2: Illustrations of (a) electrowetting and (b) electro-osmosis. In (a), γ_{sv}, γ_{lv} and γ_{sl} represent the solid-vapour, liquid-vapour, and solid-liquid interfacial tensions, respectively. The application of an electric field decreases the contact angle of the drop (right), when compared to the case with no electrical forces (left). In (b), solid walls and particles are shown in dark grey. The liquid part of the double layers, containing a depleted level of co-ions, and a surfeit of counter-ions, is shown in green

contact line). If an electric field is applied in a preferential manner on one side of the bubble/drop, it is now possible to actuate motion using this interfacial tension force.

1.5.2 Electro-osmosis

The discovery of electro-osmosis is usually attributed to the experiments of Quincke (1861) who observed fluid motion while passing currents through glass capillaries filled with water. The phenomenon results because the presence of an electrolytic solution adjacent to the surfaces of a microchannel alters its chemical characteristics. This is achieved either by ion adsorption onto the surface or by ionization of covalently bonded surface groups. In either case, a surface charge is produced while adjacent counter-ions accumulate in the bulk liquid. This forms a diffuse charge layer, shown as a green bands (adjacent to channel walls) in Figure 1.2b. When an external field is applied along the channel, it exerts a body force on the fluid within the charge layers. This body force, in turn, induces a shear in the fluid outside the charge layer, thus creating a electro-osmotic force driving bulk liquid motion towards the electrode with the same polarity as the surface charge. The early single-phase LoC used electro-osmosis to control the flow; however it is sensitive to surface contamination effects which influence the surface charge distribution driving the flow.

1.5.3 Electrophoresis

In his quest to actuate a clay particle, Reuss used 92 silver rubles and an equal number of zinc plates to create an electric field in his experiments (Reuss, 1809; Frumkin, 1946). He successfully used this electric field to discover a linearity between the mobility of the particle and the applied field, known today as electrophoretic mobility. Electrophoresis is defined as the motion of a charged particle, immersed in a liquid, in response to an electric field. The particle is induced to move towards the electrode with the opposite polarity to its net charge. In this thesis, the electrophoresis of charged drops is considered. An example of the electrophoretic motion of a liquid drop is shown in Figure 1.3a. The drop has a net positive charge, and is consequently actuated in the direction of the field.

1.5.4 Dielectrophoresis

Pohl (1951) discovered that a particle is not necessarily required to carry a free charge in order to be induced to move in an electric field. He was able to move an electrically neutral particle by exploiting gradients in the electric field, using dielectric forces. In his bid to

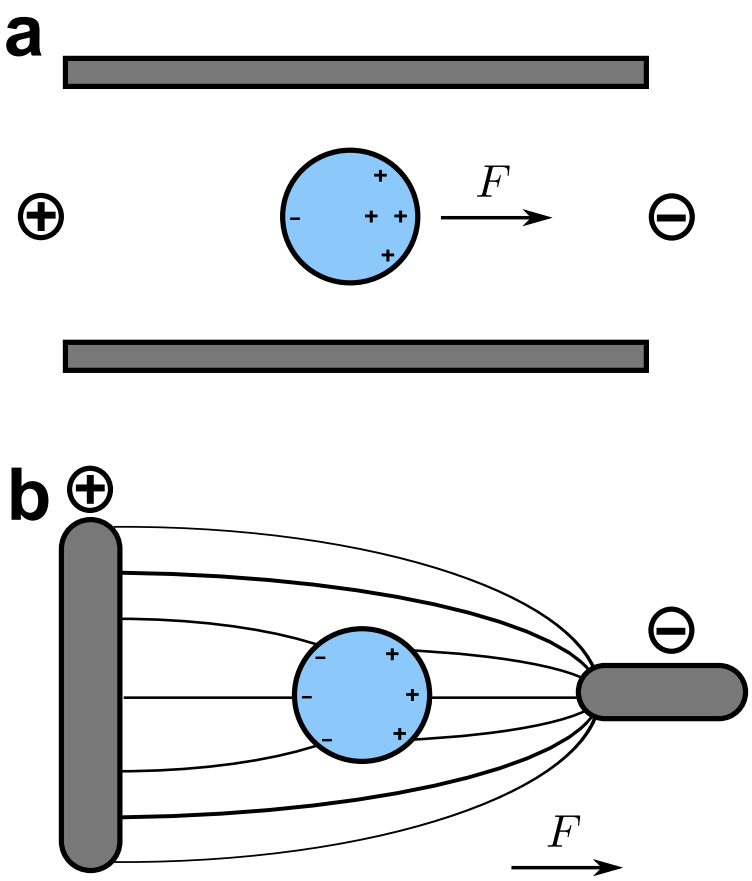

Figure 1.3: Illustrations of (a) electrophoresis and (b) dielectrophoresis. Solid walls are shown in dark grey, while the drop is shown in blue. In (a) the electrokinetic force due to the net charge and in (b) the dielectric forces due to the non-uniform electric field act to move the drop towards the negative electrode.

distinguish his discovery from electrophoresis while still remaining true to the common physical roots, he called this *dielectrophoresis*, defining it as 'the motion of suspensoid particles relative to that of the solvent resulting from polarization forces produced by an inhomogeneous electric field' (Pohl, 1951). In this thesis, the dielectrophoresis of drops is considered; the only requirement for dielectrophoresis is that the drop and the outer phase must have different dielectric constants or electric permittivities. An example is shown in figure 1.3b. By using electrodes of different dimensions, a non-uniform electric field is imposed on the drop. Consequently, it experiences a dielectrophoretic force in the direction of the applied field, causing it to move towards the negative electrode over time. Pethig (2010) provides a good overview of the physics of dielectrophoresis, as well as its applications to microfluidics.

1.6 Electrohydrodynamics of microdrop manipulation

The widespread deployment of electrohydrodynamic LoC devices requires the exploitation of the physical phenomena described in § 1.5 (electrophoresis, electrowetting, dielectrophoresis) to perform the drop manipulation operations listed in § 1.4 (formation, fission, and fusion). While there are hundreds of studies detailing proof-of-concept for individual applications (Huebner *et al.*, 2008), the development of general integrated systems has not been realised. This is because the standardisation of fluidic operations requires the characterisation of complex physics of microscale electrohydrodynamics at the smallest of scales, that of a single drop. The effects of a combination of the relevant physical/electrical/operation/design parameters, referred here as *tunable* parameters, is still not well understood. In particular, there are a number of unresolved issues:

- Electrohydrodynamic drop formation requires the ability to predict what combination of tunable parameters lead to drop breakup and ejection of progeny droplets.
- Electrohydrodynamic drop fission requires insight into the drop breakup process; a quantitative framework which can predict key output parameters of interest, such as the size and charge of progeny droplets, using the tunable (input) parameters, such as the applied electric field, is particularly relevant.
- Electrohydrodynamic fusion can produce complete or partial coalescence. For applications that require complete coalescence, it is important to be able to predict their occurrence in the tunable parameter-space. For cases where partial coalescence is desired, it is important to predict the size and charge of the residual droplets

formed.

Thus, the fundamental understanding of the problem of electrically induced deformation, breakup and coalescence of a single drop of water suspended in oil is important to the development of drop microfluidic devices. In particular, the qualitative and quantitative understanding of drop formation, fission, and fusion is crucial. Therefore, the goals of this work are to gain an understanding of the relevant physics of drop manipulation, characterize the complex behaviour into predictable patterns and explore interesting aspects of drop behaviour for varying tunable parameters, using simplified model problems.

There are technological challenges and high costs involved in fabricating and operating microfluidic LoC's, and a multiple-dimension parametric study of the kind proposed here would require thousands of individual experiments. As the mathematical principles underlying fluid dynamics are well-established, and have a universal nature, the problem is particularly suited to Computational Fluid Dynamics (CFD) simulations. CFD simulations have the ability to explore parameter spaces in a non-intrusive and inexpensive manner by employing mathematical modelling. In this thesis, CFD simulations are used to analyse drop behaviour. Whenever possible, comparisons are made with analytical, numerical, and experimental work to validate the model predictions.

1.7 Thesis statement

The thesis advanced herein is that *significant contributions to the theory of microscale drop electrohydrodynamics can be made using numerical simulations of drop deformation, breakup, and coalescence.* The aim of this dissertation is to demonstrate this assertion, and to explore its subsequent implications, for drops of electrolyte solution suspended in oil.

1.8 Outline of thesis

Chapter 2 explores the early history of drop electrohydrodynamics, touching on the seminal experimental studies that established the field. Subsequently, the contributions of G. I. Taylor, among others, in the development of analytical models is summarized. Then it traces the advent of computer modelling and simulation which allowed for extending the analytical framework. Finally, the reasons why these classical models do not adequately address applications involving microfluidic flow is emphasized. The chapter ends with the

introduction of an alternative approach involving a complete electrokinetic description of the charge inside the drop.

Chapter 3 details the governing equations underlying the electrokinetic model used in this work. The numerical implementation of this model is described in detail, including its evolution from a code designed to simulate multiphase flows through to the incorporation of novel schemes for interface tracking and electrokinetic flow modelling. Following some rigorous testing, an appropriate implementation of electric force formulation is selected for the model.

Chapters 4-6 outline the major results of this thesis work. Chapter 4 studies the electrohydrodynamics of an uncharged drop suspended in a dielectric liquid. The drop can be conducting or dielectric. Depending on the strength of the electric field and the drop ion concentration, either a steady state deformation (subcritical) or breakup (supercritical) is predicted. The parameter space delineating the stability boundary is studied. The types of breakup reported in the literature are studied and their relation to the predictions of the model are detailed.

Chapter 5 studies the transient electrohydrodynamics of the system from Chapter 4, for a wider range of tunable parameters. The dynamic behaviour of fluxes and forces inside the drop are studied for subcritical drops. For supercritical drops, the focus is on the drops ejected during breakup. Scaling laws are developed based on physical mechanisms to predict the size and charge of ejected drops. The range of validity for the two modelling approaches used, namely dielectric and electrokinetic models, is provided.

Chapter 6 considers the coalescence of charged drops. Two coalescence scenarios are studied; one is the coalescence of two drops or binary coalescence, and the other is the coalescence of a drop and a liquid interface, or drop-interface coalescence. As the drops are charged, they now translate under the influence of the electric field. In addition to complete and partial coalescence, new coalescence scenarios are observed, including cases where the drops bounce off each other (or off the interface). This is called 'non-coalescence' of charged drops. The underlying physical mechanisms are explored, and qualitative and quantitative criteria are developed to predict when this is likely to occur.

General conclusions, an overview of current ongoing work, and suggestions for future

research are given in Chapter 7.

2 Background

If you wish to make an apple pie from scratch, you must first invent the universe.

Carl Sagan

This chapter traces the history of drop electrohydrodynamics which can be divided into three sections. First, a few of the early experiments that established the field (§ 2.1) are described. Second, the later development of theory which helped understand the variety of phenomena observed (§ 2.2) is discussed. Third, the recent progress in numerical modelling which has allowed for a complete study of drop electrohydrodynamics for a wider range of parameters (§ 2.3), is outlined. Then, the limitations of the popular (simplified) electric-field model when applied to microfluidics is highlighted, and an alternative is suggested involving a full electrokinetic description of the forces within the drop (§ 2.4). The chapter concludes with an introduction of electrokinetic theory relevant to the model used in this thesis (§ 2.5).

2.1 The first act: Early experiments (1880s-1920s)

The breakthroughs in our scientific understanding of electrohydrodynamics can be traced to the Department of Physics at Cambridge University. In particular, the Cavendish Laboratory had a prominent role to play in the early experiments. The Cavendish laboratory was established by James Maxwell[1] whose research founded electrohydrodynamics as a field of inquiry. Maxwell was also the first Cavendish professor of Physics at Cambridge. His successor to the Cavendish Professorship, Lord Rayleigh[2], was motivated to study the capillary and electrostatic phenomena of relevance to droplet formation

[1] James Clerk Maxwell (1831-1879): Scottish physicist and mathematician, known for the formulation of the laws of electromagnetism (Maxwell's equations).

[2] John William Strutt, 3rd Baron Rayleigh (1842-1919, 1904 Physics Nobel Prize): English physicist, known for contributing to the understanding of several natural phenomena that bear his name, as well as the discovery of argon.

during thunderstorms. He developed the first analytical expression to predict the critical charge for Coulombic fission (i.e. breakup) of charged drops (Rayleigh, 1882), which came to be known as the *Rayleigh Limit*.

Though he did not perform much experimental work himself, Rayleigh expanded the Cavendish laboratory, which would be key to future developments in the field. His successor to the Cavendish Professorship, Sir J. J. Thomson[3], developed novel methods to test the electrical charge (Lenard effect) that appears when a drop of liquid splashes onto a plate coated by a film of the same liquid (Thomson, 1894). In addition to his pioneering experiments, he also supervised multiple research students, six of whom would go on to win the Nobel Prize. One of these future winners was C. T. R. Wilson[4] who developed a novel experimental setup to observe ionizing particles in a gas, which he named a *cloud chamber* (Wilson, 1911, 1912). A cloud chamber consisted of a sealed tank containing supersaturated alcohol, which condenses around ion trails left behind by ionizing radiation, thus forming 'clouds'.[5]

At the same time John Zeleny, one of J. J. Thomson's other students, was studying the electrical discharge from liquid menisci, and had developed a hydrostatic method to measure the electric potential at which a narrow jet was ejected (Zeleny, 1914). Using Wilson's cloud chamber apparatus, Zeleny was able to visually study the instability of the menisci formed by certain conducting liquids such as ethyl alcohol and glycerine, and obtain the first known photographs of drops suspended from a capillary tube as they disintegrated at high electric potential (Zeleny, 1917). The liquid interface, as seen in Figure 2.1 assumes a conical shape, with a jet being ejected from the apex. This phenomenon has subsequently come to be known as "cone-jet electrospraying". Zeleny (1917) also provided experimental evidence of the existence of different modes of breakup other than cone-jet formation, including dripping and pulsating modes.

This period when Zeleny conducted his experiments coincided with the arrival of G. I.

[3]Sir Joseph John Thomson (1856-1940, 1906 Physics Nobel Prize): English physicist, known for the discovery and identification of the electron.

[4]Charles Thomas Rees Wilson (1869-1959, 1927 Physics Nobel Prize): Scottish physicist, known for his experiments to detect ionizing radiation.

[5]The cloud chamber setup played a prominent role in early experimental particle physics, and is credited with the discoveries of the positron, muon and kaon.

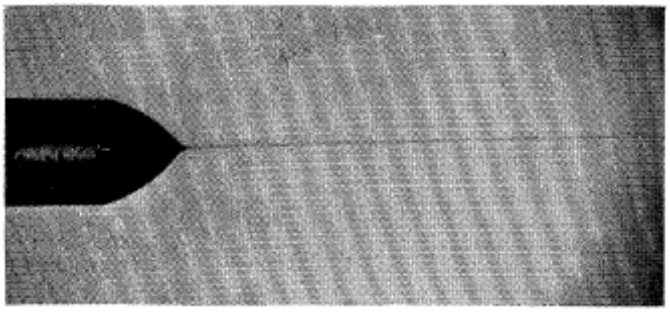

Figure 2.1: A reproduced image showing the formation of a glycerine jet of diameter 7 μm, ejected at velocity 3 m/s, under an external potential of 7000 V (Zeleny, 1917).

Taylor[6] at the Cavendish Laboratory to start his doctoral studies under J. J. Thompson; Taylor would go on to make seminal contributions to the study of electrically-induced drop breakup. His earliest work on this topic was a joint paper with C. T. R. Wilson which was motivated by, as with Rayleigh a few decades earlier, the breakup of charged rain drops in thunderstorms. They simplified the problem by studying bubbles instead of drops; the apparatus consisted of a soap bubble placed on a plate with a known potential difference from the plate above it. When the electric field was increased to a sufficiently high value, the bubble elongated to form a shape resembling 'the small end of an egg' (Wilson & Taylor, 1925). Eventually a filament formed and charge was ejected (Figure 2.2). This conical shape was similar to the shape observed by Zeleny in his experiments, which hinted at similarities in the underlying physics of electrified drops and bubbles.

Wilson & Taylor (1925) also formulated the first theoretical model to predict the breakup of a conducting bubble in an electric field. As the charge in the bubble is distributed on the interface, the condition for breakup was reduced to a simple normal stress balance between the external field, acting on the surface charge and deforming the drop, and the interfacial tension trying to prevent the drop from breaking up. They further concluded that, for bubbles of a given shape but different sizes, the density of charge was proportional to the external electric field, but independent of the drop radius.

[6]Geoffrey Ingram Taylor (1886-1975): British physicist, known for his contributions to turbulence and electrohydrodynamics, and widely regarded as one of the most influential fluid dynamicists of the 20th century (Batchelor, 1976).

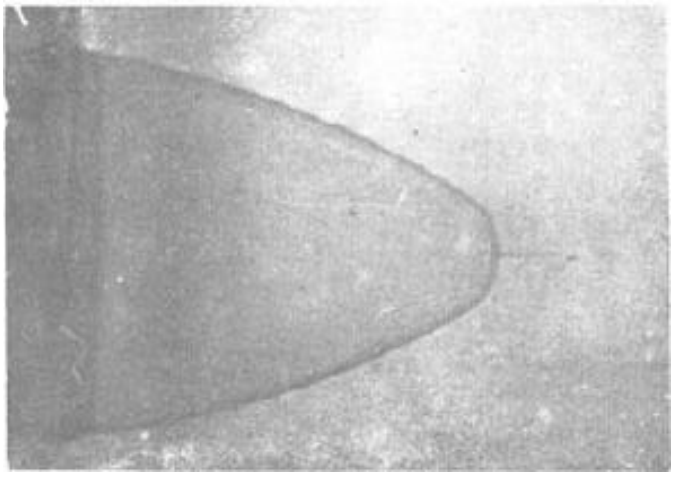

Figure 2.2: A reproduced image showing the formation of a filament on the bubble, due to the applied external electric field. (Wilson & Taylor, 1925).

The field that produces a given drop shape can be given by:

$$E \propto \sqrt{\frac{\gamma}{R}}, \tag{2.1}$$

where γ is the interfacial tension of the bubble, R is the undeformed radius of the bubble and E is the external applied electric field. They validated this inverse square-root relationship between electric field and drop radius by looking at the bubble-bursting field value for bubbles of different radii. When a drop rather than a bubble is considered, the electric field depends on an additional parameter, namely the permittivity of the drop. Therefore Equation 2.1 becomes:

$$E \propto \sqrt{\frac{\gamma}{\epsilon_\mathrm{d}\epsilon_0 R}}, \tag{2.2}$$

where ϵ_0 and ϵ_d are the vacuum permittivity and the relative permittivity of the drop, respectively. This proportionality constant in Equation 2.2 turned out to be an important dimensionless number, and is today commonly referred to in the literature as the Electric Capillary number[7] ($\mathrm{Ca_E}$) (Ha & Yang, 2000*a*).

$$E = \sqrt{\frac{\mathrm{Ca_E}\,\gamma}{\epsilon_\mathrm{d}\epsilon_0 R}}, \tag{2.3}$$

$$\mathrm{Ca_E} = \frac{\epsilon_\mathrm{d}\epsilon_0 R E^2}{\gamma}. \tag{2.4}$$

[7] $\mathrm{Ca_E}$ has also alternatively been called as Electric Weber number (Eow & Ghadiri, 2003) or Electric Bond number (Lin *et al.*, 2012).

Thus Ca_E is a comparison of the relative magnitudes of the electric forces and interfacial tension force, which are the two forces balanced to obtain the drop deformation.

There are two more experiments in this early period that have gained recognition. First, Nolan (1926) studied the effect of a transverse electric field on a falling, as opposed to stationary, water drop, to better mimic the drop formation in thunderclouds. He confirmed the critical electric field results obtained by Wilson & Taylor (1925) for bubbles, and further attempted to measure the charge contained in the fragments breaking off the main drop. Finally, Macky (1931) varied additional parameters including surrounding air pressure and orientation of electric field, and found a very similar stability limit to Wilson & Taylor (1925) for the break-up of a bubble.

2.2 The second act: Later analytics (1940s-1960s)

The investigations detailed in § 2.1 were limited to experiments because little theoretical understanding of interfacial electrohydrodynamics existed at that point. This section outlines the theoretical developments that occurred a few decades after the experiments described previously.

2.2.1 Perfect dielectric model

J.A. Stratton[8], in his iconic text 'Electromagnetic Theory' (Stratton, 1941), devoted chapters to the forces exerted on solid dielectrics and conductors by a electric field. One of the techniques he employed in his analysis was minimising the difference in energy of the electric field before and after the introduction of the dielectric/conducting body. Using these energy arguments he showed that, for a solid ellipsoid (isotropic) dielectric, the system would be at minimum energy when the longest axis is aligned with the direction of the electric field. O'Konski & Thatcher Jr (1953) were the first to apply this minimum-energy approach to liquids, analysing a dielectric drop of fluid (instead of a solid dielectric) suspended in a dielectric medium, with an applied electric field. They assumed the drop to be ellipsoidal and tried to derive the equilibrium shape of the drop. First, they used Stratton (1941)'s expression for the electrostatic energy (E_E) for

[8] Julius Adams Stratton (1901-1994): American electrical engineer, known for his contributions to electromagnetic theory and application, as well as his work for the US government which included helping plan the use of radar systems in the Normandy invasion of 1944.

a dielectric ellipsoid in a parallel electric field,

$$E_E = -2\pi R^3 E^2 \frac{(\epsilon_\mathrm{d} - \epsilon_\mathrm{c})(1 + (\epsilon_\mathrm{d} - \epsilon_\mathrm{c})(1 - e^2)(\ln[(1+e)/(1-e) - 2e]))}{6\epsilon_\mathrm{c} e^3}, \tag{2.5}$$

where e is the eccentricity of the ellipsoidal drop, and can be related to the semi-major (l) and semi-minor (b) drop axes by

$$l = R(1 - e^2)^{-1/3}, \tag{2.6}$$

$$b = R(1 - e^2)^{+1/5}. \tag{2.7}$$

Second, the surface energy (E_S) of the drop can be given as,

$$E_S = 2\pi R^2 \gamma (1 - e^2)^{1/3} \left(1 + \frac{\sin^{-1} e}{(1 - e^2)^{1/2}}\right). \tag{2.8}$$

The minimum-energy condition can then be imposed by differentiating the sum of the electrostatic (Equation 2.5) and interfacial (Equation 2.8) energies, and equating the result to zero. Upon expanding the resulting term in power series, O'Konski & Thatcher Jr (1953) solved and obtained different expressions for the equilibrium eccentricity depending on the order of the neglected terms. For illustration, the solution for the case where $e^2 \ll 1$ is:

$$e = 3|E(\epsilon_\mathrm{d} - \epsilon_\mathrm{c})| \frac{(\epsilon_\mathrm{c} R/\gamma)^{1/2}}{2(\epsilon_\mathrm{d} + 2\epsilon_\mathrm{c})}. \tag{2.9}$$

A visual inspection of Equation 2.9 shows that e is always positive, regardless of the permittivies of the two phases. Thus this model, known as the *perfect dielectric* model predicts the drop to *always* deform prolately. O'Konski & Thatcher Jr (1953) noted this and stated that for the perfect dielectric case, "it follows that *the droplet is elongated in the direction of the field whether its dielectric constant is greater or less than that of the surrounding medium* for the case where the surrounding medium can be regarded as perfect dielectric" (emphasis theirs). This conclusion was reached by other authors as well (Abbi & Chandra, 1956; Garton & Krasucki, 1964).

2.2.2 Perfect conductor model

O'Konski & Harris (1957) proceeded to study the deformation of a drop in an electric field where both phases were *conducting*. Once again, they relied on Stratton (1941)'s work on solid conductors to derive an expression for the equilibrium eccentricity of the ellipsoidal drop. For small values of e, their expression could be simplified to:

$$e = \frac{3E}{4}\left(\frac{\epsilon_\mathrm{c} R}{\pi\gamma}\right)^{1/2} \left[\frac{(\sigma_\mathrm{d} - \sigma_\mathrm{c})(\sigma_\mathrm{d}^2 + 7\sigma_\mathrm{c}\sigma_\mathrm{d} - 2\sigma_\mathrm{c}^2[1 + 3\,\epsilon_\mathrm{d}/\epsilon_\mathrm{c}])}{(\sigma_\mathrm{d} + 2\sigma_\mathrm{c})^3}\right]^{1/2}, \tag{2.10}$$

where σ_d and σ_c are the drop and continuous phase conductivities, respectively. For the case where the drop is conducting and the outer phase is a dielectric ($\sigma_\mathrm{c} = 0$), the term inside the square brackets in Equation 2.10 equals unity, and the expression simplifies to

$$e = \frac{3E}{4}\left(\frac{\epsilon_\mathrm{c} R}{\pi\gamma}\right)^{1/2}. \tag{2.11}$$

This is the expression for the equilibrium eccentricity of a *perfect conductor* drop in an electric field. Like the perfect dielectric limit (Equation 2.9), perfect conductor drops always deformed prolately. Allan & Mason (1962) independently arrived at the same analytical expressions for perfect dielectric and perfect conductors using a different method of balancing the electrical and interfacial tension forces. As has become common practice since, they characterised the deformation of the drop using a drop deformation parameter, D, (instead of eccentricity e) defined as

$$D = \frac{l - b}{l + b}. \tag{2.12}$$

Reformulating Equation 2.11 and Equation 2.9 using Equation 2.12 and Equation 2.4, we get the perfect conductor and perfect dielectric limits, respectively, as

$$D = \frac{9}{16}\,\mathrm{Ca_E}, \tag{2.13}$$

$$D = \frac{9}{16}\,\mathrm{Ca_E}\,\frac{(\bar{\epsilon} - 1)^2}{(\bar{\epsilon} + 2)^2}, \tag{2.14}$$

where $\bar{\epsilon}$ is the permittivity ratio ($\epsilon_\mathrm{d}/\epsilon_c$). Note that D is always positive (implying prolate drop deformation) for both perfect conductor (Equation 2.13) and perfect dielectric (Equation 2.14) limits, irrespective of the ratio of the permittivities of the two phases, consistent with the earlier expressions. Allan & Mason (1962) confirmed their deformation predictions experimentally for conducting drops suspended in dielectric liquids, for small field strengths. They also conducted experiments on dielectric drops suspended in dielectrics, and surprisingly observed *oblate* drop deformation in some cases (shown in Figure 2.3). This was contrary to previous experimental and theoretical work, which always predicted *prolate* drop deformation. They were unable to provide an explanation for this anomaly, and suggested that a closer examination of the formation of charges in both phases was necessary to understand this behaviour.

Continuing the study of equilibrium drop shapes in an electric field, Garton & Krasucki (1964) calculated that the maximum D value for subcritical, conducting drops, was

$D \simeq 0.3$, and verified it experimentally. Taylor (1964) obtained a value of $D \simeq 0.31$ and calculated the semi-vertical angle for the pointed end of a conducting drop at equilibrium.

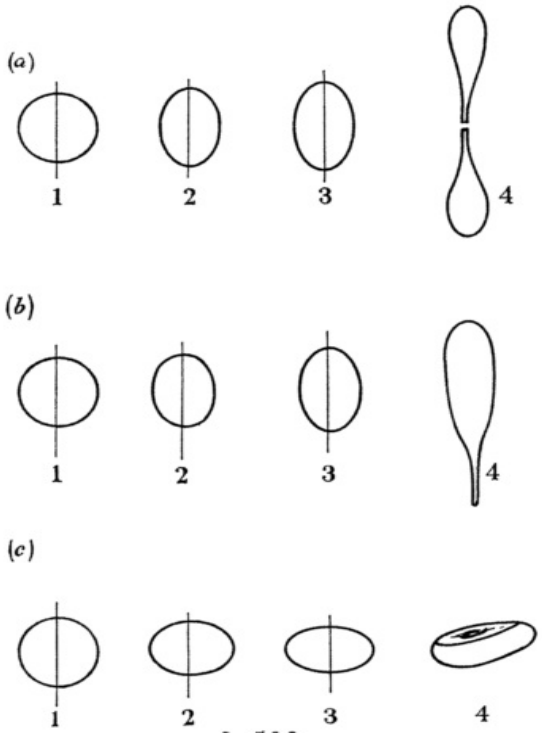

Figure 2.3: Allan & Mason (1962) showing expected prolate deformation for cases (a) and (b), but oblate deformation for case (c)

2.2.3 Resolution of anomaly

When an interface separating two immiscible liquids is acted on by an external electric field, the electric displacement field undergoes a sharp jump due to the difference in permittivities of the two liquids. This discontinuity in the electric displacement field results in the formation of an electric stress at the interface. For a drop, the curvature of its surface would result in the creation of electric stress gradients at the surface, which would deform it. The presence of free charge in either phase creates a surface charge distribution as well as diffuse regions of charge inside the phase, which would create tangential electric stresses and complicated deformation behaviour of the drop. As detailed in the last section, two different (simplified) limits, namely the perfect dielectric and the perfect conductor limits, gained popularity in the literature. Both these limits

ignore the presence of free charge.

In the case of the perfect dielectric approach, the two fluids were assumed to be dielectrics with zero conductivity. A feature of the perfect dielectric limit was that only the bound charge acting due to the difference in permittivities at the interface was considered. In the case of the perfect conductor approach, the drop was assumed to be perfectly conducting possessing infinite conductivity and the continuous phase is assumed to be perfectly dielectric with zero conductivity. The electric field inside the drop was zero. In both limits, due to the absence of free charge, the electric stress was normal to the interface and could be balanced by interfacial tension only. Thus, both limits assumed that the tangential electric stresses forming inside the drop near the interface are insignificant. Crucially these models also predicted *zero fluid flow inside the drop* at equilibrium, when the normal forces were balanced.

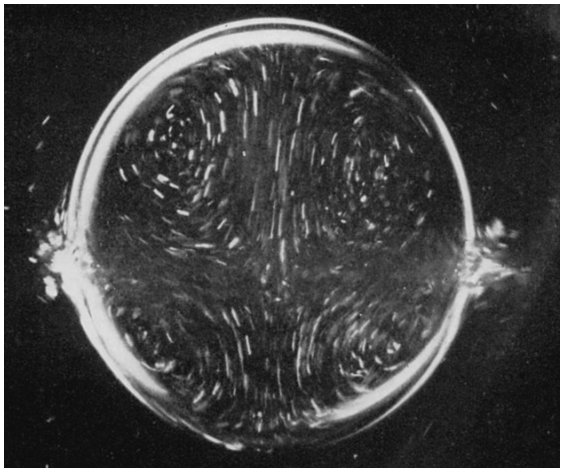

Figure 2.4: Fluid flow inside droplet. Reproduced from Taylor (1966)

In a seminal paper, Taylor predicted (and experimentally visualised) that significant quadropolar fluid flow existed inside the (hitherto considered dielectric) drop at equilibrium (Taylor, 1966). The key experimental image from his paper is reproduced in Figure 2.4. This meant that the assumption that the tangential electrical stresses could be considered insignificant needed re-evaluation. He therefore developed a model that assumed both phases to be slightly conducting, where the ensuing electric field in the two phases created a charge distribution at the interface between them, and resulted in tangential stresses. These tangential stresses could not be balanced by interfacial tension,

which always acted normal to the interface, and were instead balanced by viscous stresses, which allowed oblate equilibrium shapes to form (Melcher & Taylor, 1969) and fluid flow to exist at equilibrium. Although this model ignored the presence of free charge in the bulk phase, and assumed that charge was only present at the interface, it satisfactorily resolved the contradiction first observed by Allan & Mason (1962). The model posited a discriminating function which allowed the drop to deform both oblately and prolately depending on different combinations of conductivity, viscosity and permittivity ratios. This model, for drops with finite conductivity but without free charge in the bulk of the phase, has come to be referred to as the *leaky dielectric* (Saville, 1997) model. The predicted drop deformation for a leaky dielectric model can be stated as:

$$D = \frac{9}{16}\,\mathrm{Ca_E}\,\psi, \tag{2.15}$$

$$\psi = \bar{\epsilon}(\bar{\sigma}^2 + 1) - 2 + 3(\bar{\epsilon}\bar{\sigma} - 1)\frac{2\bar{\mu} + 3}{5\bar{\mu} + 5}, \tag{2.16}$$

where $\bar{\sigma}$ and $\bar{\mu}$ are the conductivity $(\sigma_\mathrm{d}/\sigma_\mathrm{c})$ and viscosity $(\mu_\mathrm{d}/\mu_\mathrm{c})$ ratios respectively. ψ is the discriminating function which allows the drop deformation parameter D to be negative (i.e. for the drop to deform oblately) depending on the drop and continuous phase properties, unlike the perfect dielectric and perfect conductor models. Note that if ψ is set to unity in Equation 2.15, the equation for a perfect conductor (Equation 2.13) is recovered. In general, Taylor's leaky dielectric model has proved very successful in qualitatively predicting drop deformations and there are several examples of successful comparisons with experiment (Torza *et al.* (1971); Tsukada *et al.* (1993)) and numerical results (Vizika & Saville (1991); Tsukada *et al.* (1993)). Ajayi (1978) extended Taylor's theory by including higher order terms to obtain greater quantitative agreement with empirical results. On the numerical front, most of the numerical studies on drop deformation have incorporated the leaky dielectric limit in their models, because it qualitatively replicates a large number of experimental results.

2.3 The third act: Recent numerics (1980s-present)

With the advent of computers and the exponential improvement in their processing power, numerical modelling has gained prominence in fluid dynamics research in general, and drop electrohydrodynamics in particular. In this section, the mathematical formulations of the three electrohydrodynamic models described earlier are outlined, and the relevant literature on the topic are reviewed.

2.3.1 Mathematical modelling

From a numerical perspective, it is assumed that the flow is governed by Navier-Stokes equations in both phases, with additional source terms added to account for the electrical forces and interfacial tension. The basic flow equations required for the model are:

$$\frac{\partial \rho \boldsymbol{u}}{\partial t} + \boldsymbol{u} \cdot \nabla \rho \boldsymbol{u} = \nabla p + \nabla \cdot [\mu(\nabla \boldsymbol{u} + \nabla \boldsymbol{u}^{\boldsymbol{T}})] + \boldsymbol{F}_{\mathrm{S}} + \boldsymbol{F}_{\mathrm{E}}, \tag{2.17}$$

$$\nabla \cdot \boldsymbol{u} = 0. \tag{2.18}$$

Here, $\boldsymbol{u}$ is the velocity vector, p the pressure, and $\boldsymbol{F}_S$ and $\boldsymbol{F}_E$ are the source terms for the interfacial tension and electric forces, respectively. Note that, for a Volume-of-Fluid type formulation (§ 3.2.2), Equation 2.17 is solved over the whole domain, including both phases and the interface. Equation 2.18 is the continuity equation that ensures mass conservation for an incompressible fluid. Depending on the treatment of electric charges, the formulation of $\boldsymbol{F}_E$ is what differentiates the three electric field models described earlier. In general, this term is calculated by taking the divergence of the Maxwell stress tensor ($\boldsymbol{\tau}_M$) (Melcher & Taylor, 1969; Saville, 1997):

$$\boldsymbol{F}_E = \nabla \cdot (\boldsymbol{\tau}_M) = -\frac{1}{2}\boldsymbol{E} \cdot \boldsymbol{E}\nabla\epsilon + q\boldsymbol{E} + \nabla(\frac{1}{2}\boldsymbol{E} \cdot \boldsymbol{E}\frac{\partial \epsilon}{\partial \rho}\rho), \tag{2.19}$$

$$\boldsymbol{\tau}_M = \epsilon \boldsymbol{E}\boldsymbol{E} - \frac{1}{2}\epsilon(\boldsymbol{E} \cdot \boldsymbol{E})\boldsymbol{I} \tag{2.20}$$

where q is the volumetric free charge density, and $\boldsymbol{E}$ is the electric field vector. The last term on the right hand side of Equation 2.19 is associated with changes in material density and is disregarded when the fluid is taken to be incompressible. Gauss' law states that $\boldsymbol{E}$ can be related to q by

$$\nabla \cdot (\epsilon \boldsymbol{E}) = q. \tag{2.21}$$

Also, for an irrotational electric field,

$$\nabla \times \boldsymbol{E} = 0. \tag{2.22}$$

Perfect dielectric model

The perfect dielectric model assumes that the conductivities of both phases are low enough for the effects of charge to be entirely disregarded. Using Gauss' law in the

absence of free charge, we get

$$\nabla \cdot (\epsilon \boldsymbol{E}) = 0. \tag{2.23}$$

Within each fluid, the permittivity is constant and this equation reduces to Laplace's equation when the field is rewritten in terms of electric potential ψ ($\boldsymbol{E} = \nabla\psi$). The absence of free charge (q) at the interface results in the boundary condition:

$$||\epsilon \nabla\psi \cdot \boldsymbol{n}|| = 0, \tag{2.24}$$

where $||(\cdot)||$ represents the jump of the quantity '$(\cdot)$' across the interface, and $\boldsymbol{n}$ is the unit normal to the interface. It is important to note here that any jump conditions specified in this section are implemented indirectly through variable properties between the phases, i.e. these conditions are embedded into the governing equations for flow in the entire domain including both phases and the interface. In this model, Equation 2.19 reduces to

$$\boldsymbol{F}_E = -\frac{1}{2}\boldsymbol{E} \cdot \boldsymbol{E}\nabla\epsilon. \tag{2.25}$$

This equation shows that the electric force in perfect dielectric models results from the permittivity jump at the interface.

Perfect conductor model

The perfect conductor model assumes that the electric field inside the drop is zero and the free charge migrates instantaneously to the interface, which is at a constant potential (ψ_0). This means that charge motion along the interface is effectively ignored as steady state is achieved instantly. The boundary condition at the interface in the presence of interfacial charge q_s is given by:

$$||\epsilon \nabla\psi \cdot \boldsymbol{n}|| = q_s. \tag{2.26}$$

The electric force in this model is given by

$$\boldsymbol{F}_E = -\frac{1}{2}\boldsymbol{E} \cdot \boldsymbol{E}\nabla\epsilon + q\boldsymbol{E}. \tag{2.27}$$

Leaky dielectric model

The leaky dielectric model assumes that the electric field inside the drop is non-zero, the free charge is distributed in a microscopic layer adjacent to the interface, and the electric current is continuous across the interface. The charge conservation equation can be expressed as:

$$\frac{\partial q}{\partial t} + \nabla \cdot (\sigma \boldsymbol{E}) = 0, \tag{2.28}$$

and the electric force is again given by

$$\boldsymbol{F}_E = -\frac{1}{2}\boldsymbol{E} \cdot \boldsymbol{E}\nabla\epsilon + q\boldsymbol{E}. \tag{2.29}$$

Preserving the continuity of the electric potential and the electric current at the interface, we get:

$$||\psi|| = 0, \tag{2.30}$$

$$||\sigma\nabla\psi \cdot \boldsymbol{n}|| = 0. \tag{2.31}$$

The normal and tangential component of the Maxwell stress tensor at the interface for an interfacial charge $q_s\boldsymbol{n}$ can be calculated as (Saville, 1997):

$$[\boldsymbol{\tau_M} \cdot \boldsymbol{n}] \cdot \boldsymbol{n} = \frac{1}{2}||\epsilon\epsilon_0(\boldsymbol{E} \cdot \boldsymbol{n})^2 + \epsilon\epsilon_0(\boldsymbol{E} \cdot \boldsymbol{t})^2||, \tag{2.32}$$

$$[\boldsymbol{\tau_M} \cdot \boldsymbol{n}] \cdot \boldsymbol{t} = q_s\boldsymbol{E} \cdot \boldsymbol{t}. \tag{2.33}$$

This tangential term (Equation 2.33) is zero for both the perfect dielectric model (because $q_s = 0$) and the perfect conductor model (because $\boldsymbol{E} \cdot \boldsymbol{t} = 0$). Unlike those two models, the leaky dielectric mode allows for charge motion on the same timescale as hydrodynamic effects, but only along the interface. The resultant non-zero tangential stress term in turn influences the hydrodynamics, resulting in fluid flow inside the drop.

2.3.2 Studies relevant to the above models

Using the models elaborated above, a vast number of numerical studies were published; a few are highlighted here. Brazier-Smith (1972) did away with the spheroidal drop shape assumption, and pioneered the use of Boundary Element Method (BEM) to calculate the aspect ratio, but obtained a similar equilibrium value of $D \simeq 0.29$, when compared to earlier analytical studies (Taylor, 1964; Garton & Krasucki, 1964). Sherwood (1988) employed BEM to solve Laplace's equation in the creeping flow regime, and demonstrated multiple breakup modes, but focused a narrow range of electrical properties for numerical convenience. Boundary element methods, although popular, cannot fully simulate breakup because the algorithm fails just as breakup occurs, and requires manual

intervention to effect the topological change if the simulation is to be continued. Feng & Scott (1996); Feng (1999) used the Galerkin Finite Element Method (FEM) to provide a more complete picture with a wider range of electrical properties, and concluded that inertial effects were irrelevant in the vast majority of cases. Other relevant numerical studies (Basaran & Scriven, 1989; Basaran & Patzek, 1995; Baygents, 1998; Stone *et al.*, 1999) explored drop deformation for a range of parameters, but not drop breakup.

Analytical	O'Konski & Thatcher Jr (1953), Abbi & Chandra (1956), Allan & Mason (1962), Garton & Krasucki (1964), Taylor (1966), Rosenkilde (1969), Sozou (1973), Saville (1974), Ajayi (1978), Sherwood (1999), Baygents & Saville (1990), Zholkovskij *et al.* (2002), Rhodes & Yariv (2010), Zhang *et al.* (2013*a*), Yariv & Rhodes (2013), Lanauze *et al.* (2013), Corson *et al.* (2014)
Experimental	Zeleny (1917), Wilson & Taylor (1925), Allan & Mason (1962), Torza *et al.* (1971), Vizika & Saville (1991), Ha & Yang (2000*a*,*b*), Eow *et al.* (2001*a*, 2003); Eow & Ghadiri (2003), Grimm & Beauchamp (2005), Adamiak & Floryan (2010), Salipante & Vlahovska (2010), Wang *et al.* (2012), Lee *et al.* (2013), Karyappa *et al.* (2014)
Numerical (BEM)	Brazier-Smith (1972), Sherwood (1988), Dubash & Mestel (2007*b*,*c*,*a*), Lac & Homsy (2007), Higuera (2008), Crowdy (2008)
Numerical (FEM/FVM)	Haywood *et al.* (1991), Feng & Beard (1991), Tsukada *et al.* (1993), Basaran & Patzek (1995), Feng & Scott (1996); Feng (1999), Collins *et al.* (2007*b*), Supeene *et al.* (2008), Hua *et al.* (2008), Adamiak & Floryan (2010), Esmaeeli & Sharifi (2011*b*), Paknemat *et al.* (2012), Ghazian *et al.* (2013), Halim & Esmaeeli (2013), Collins *et al.* (2013), Yao *et al.* (2015), Gong *et al.* (2015), Nganguia *et al.* (2016)

Table 2.1: Overview of analytical, numerical and experimental work

Lac & Homsy (2007) explored fluid flow coupled with electrostatic equations in axisymmetric coordinates, with both liquids considered to be leaky dielectrics and provided drop shapes for a wide range of conductivity, viscosity and permittivity ratios. Dubash & Mestel (2007*a*,*b*,*c*) looked at breakup scenarios for conducting drops in an inviscid medium, and later in a viscous medium. They formulated a critical electric capillary number above which breakup occurs. Hua *et al.* (2008) solved the full Navier Stokes equations using a Finite Volume Method (FVM) combined with front tracking to track the interface, for all three theoretical limits. Their model generally over predicted the deformation when compared to analytical and experimental results. Paknemat *et al.* (2012), employed the Ghost Fluid Method (GFM) to handle the jump of permittivities at the interface, as suggested by Bjørklund (2009), for perfect dielectric and perfect conductor limits. A complete picture of drop breakup requires the solving of the full Navier Stokes equations along with exploration of drop breakup scenarios. A common thread between these studies was that time dependent deformation has received little attention, and drop breakup has not been explored, usually due to computational limitations. An overview of the literature is given in Table 2.1.

On the experimental side, drop breakup has been receiving greater attention. Eow *et al.* published a number of studies (Eow *et al.*, 2001*a*; Eow & Ghadiri, 2003; Eow *et al.*, 2003) exploring the deformation and breakup of aqueous drops in dielectrics and showed the type of breakup to be qualitatively dependent on the viscosity ratio. Ha & Yang (2000*b*) explored this further for drops with a range of conductivities, from slightly conducting to highly conducting Newtonian and non-Newtonian drops. They found the leaky dielectric limit to be invalid when the viscosity of the drop was much less than the ambient fluid, even for small deformations. When compared to experimental data (Torza *et al.*, 1971; Vizika & Saville, 1991), the leaky dielectric model has been very successful in qualitatively predicting both oblate and prolate deformations (Baygents, 1998); quantitative discrepancies exist, especially at large deformations. Recent extensions to the leaky dielectric model to account for large drop deformations (Bentenitis & Krause, 2005) and finite charge-relaxation times (Zhang *et al.*, 2013*a*) have shown promising improvements in quantitative accuracy.

2.4 Electrohydrodynamics and electrokinetics

Electrokinetics, as a field of study, was established more than two centuries ago with the discovery of electrophoretic actuation of clay particles (Reuss, 1809). Electrokinetic studies were restricted to colloid science for the vast majority the 19th and 20th centuries (Lyklema, 2003). Recently, however, they have found application to microfluidic flows (Bruus, 2007). Electrokinetic phenomena can be defined as all those phenomena involving fluid motion adjacent to a charged surface (Delgado *et al.*, 2007), involving the formation a diffuse layer of charge (§ 2.5). This charge layer forms in response to polarisation near an interface; electrokinetic effects manifest in systems when electric fields and ions (in the charge layer) interact, and determine the resulting charge distribution. Given that conducting drops in electric fields contain charge, it is not unreasonable to expect that electrokinetics would have a role to play in their dynamic behaviour. However, despite studying the same problem of electrically-induced fluid motion, the fields of electrohydrodynamics and electrokinetics have developed separately, with little communication between the communities. Therefore, until very recently, the relationship between the leaky dielectric model (which ignores volumetric charge) developed by the electrohydrodynamic community, and an electrokinetic model (which considers volumetric charge) was not clear.

Baygents & Saville (1990) were the first to hypothesize that electrokinetic and leaky dielectric models might share common physical roots. They found complete agreement between the predictions of an electrokinetic and leaky dielectric model for the problem of circulation inside an electrified drop. They also introduced the asymptotic limit at which the electrokinetic model should reduce to a leaky dielectric formulation, but were unable to resolve the underlying mathematical issues. Schnitzer & Yariv (2015) were able to achieve this unification by building on Baygents & Saville (1990)'s work, and derived the leaky dielectric model at the large-field thin-diffuse-layer limit of the full electrokinetic equations. While this unification has uncovered new insights into the underlying similarity of electrohydrodynamic and electrokinetic phenomena (Bazant, 2015), it has also raised questions as to which approach is more suitable for the problems of interest in this work. The rest of this section focuses on answering this question.

2.4.1 Limitations of the leaky-dielectric approach

The leaky dielectric model has proven to be tremendously successful, and has served as the basis for investigations into a variety of electrohydrodynamic phenomena, including macroscale drop deformation (Supeene *et al.*, 2008; Zhang *et al.*, 2013*a*), breakup (Feng & Scott, 1996; Lac & Homsy, 2007), and electrohydrodynamic tip-streaming (Collins *et al.*, 2007*b*, 2013). Other applications include investigating the dynamics of electrified threads (Collins *et al.*, 2007*a*; Wang, 2012), confined drops (Esmaeeli & Behjatian, 2012; Mandal *et al.*, 2014) and fluid columns (Esmaeeli & Sharifi, 2011*a*); the stability of interfaces (Ozen *et al.*, 2006; Li *et al.*, 2007) and electrohydrodynamic patterning of thin films (Wu & Russel, 2009; Gambhire & Thaokar, 2012).

However, as the redistribution of mobile charge (due to the action of an external field) is the ultimate cause for the tangential Maxwell stresses forming at the interface, a complete description of transient drop dynamics requires an electrokinetic model (Supeene *et al.*, 2008). The leaky dielectric model, for all its merits, makes significant electrokinetic simplifications (Schnitzer & Yariv, 2015), such as the absence of volumetric charge (the bulk fluid is considered to be electrically neutral with an associated homogeneous conductivity), rapid electrical relaxation times, and the dominance of conduction over diffusion. At the microscale, electrokinetic phenomena gain importance and the bulk fluid conductivity can no longer be considered to be homogeneous when charge relaxation is disrupted by hydrodynamic motion (Saville, 1997). Instead, the appearance of diffuse charge layers adjacent to interfaces, in the presence of an electric field, is predicted (Zhao & Yang, 2012). At the microscale, the thickness of the diffuse charge layer, λ_{D} (Debye length), and the characteristic length scale of the system, R (drop radius) can be comparable (Stone *et al.*, 2004), and κ is finite ($\kappa = R/\lambda_{\mathrm{D}}$). In this case, the electrokinetic contributions to transient electrohydrodynamics cannot be neglected. This point is reinforced in the next section by a simple comparison of the relative timescales associated with the underlying forces.

2.4.2 Timescales for flow physics

The flow physics of drop breakup/coalescence is governed by the interplay between the electric, interfacial tension and viscous forces. It is useful to attempt to quantify the relative timescales over which the forces act to explore whether the timescales

are significantly affected by the transition to a micrometre length scale. Combining Equation 2.28 and Equation 2.21:

$$\frac{\partial q}{\partial t} + \nabla \cdot (\sigma \boldsymbol{E}) = \frac{\boldsymbol{D}q}{\boldsymbol{D}t} = \frac{\sigma}{\epsilon} q \tag{2.34}$$

$$q = q_0 e^{-(\sigma/\epsilon)t} \tag{2.35}$$

The time that the initial charge density takes to redistribute to a free charge density near an interface, namely the electric relaxation time (t_e), can be formulated from this equation. Similar relaxation times can be defined for the viscous (t_μ) and interfacial tension (t_γ) forces, respectively, as well:

$$t_\mathrm{e} = \frac{\epsilon_\mathrm{d}\epsilon_0}{\sigma}, \tag{2.36}$$

$$t_\mu = \frac{\rho R^2}{\mu}, \tag{2.37}$$

$$t_\gamma = \sqrt{\frac{\rho R^3}{\gamma}}. \tag{2.38}$$

	(s)		
$R(m)$	t_e	t_μ	t_γ
10^{-6}	7.1×10^{-6}	1.0×10^{-6}	6.33×10^{-7}
10^{-3}	7.1×10^{-6}	1.0×10^{0}	2.0×10^{-2}
10^{0}	7.1×10^{-6}	1.0×10^{6}	6.33×10^{2}

Table 2.2: Comparison of electric, viscous and interfacial tension relaxation times

The values of the relative timescales have been computed for a drop of water (ρ=10^3 kg/m^3, ϵ_d=80, μ=10^{-3} Pa-s, and γ= 0.0025 N/m) of various radii in Table 2.2. t_e is independent of length scale in question and hence remains constant. It is pertinent to note that the assumption of the leaky dielectric formulation is that charge redistribution occurs on a much shorter timescale than that of fluid motion, i.e. $t_\mathrm{e} \ll t_\mu, t_\gamma$. Though this assumption holds for millimetre size water drops (and larger), it is clear, from Table 2.2, that this is not applicable for a microfluidic drop as $t_\mathrm{e} \simeq t_\mu, t_\gamma$. This comparison of approximate timescales gives credence to the hypothesis that the effects of charge transport cannot be ignored for microfluidic drops.

2.5 Electrokinetics and diffuse charge layers

Electrokinetic phenomena manifest due to the presence of the *electric double layer* (EDL), which forms as a result of the interaction between the ions present in an electrolyte solution, and the static charges present on a surface in contact with the solution. These charges can form due to a variety of mechanisms, such as adsorption of charged species or ionisation of surface groups (Hunter, 1981). For example, when aqueous solution is brought into contact with silica, the silica surface hydrolyses to form silanol surface groups. These groups can be positively charged (Si-OH_2^+), neutral (Si-OH), or negatively charged (Si-O^-) depending on the pH of the solution. If the surface is positively charged, the negative ions in the solution, or counter-ions, are attracted to the surface. The positive ions, or co-ions, are repelled by it. While the solution together with the interface remains *globally* electroneutral, a charge distribution arises *locally* adjacent to the interface, as shown in Figure 2.5a.

Looking closely at Figure 2.5a, a small layer of co-ions can be seen immediately adjacent to the surface. This is known as the *Stern layer* (Stern, 1924), and its thickness depends on both the size of the ions and its chemical affinity to the surface. The Stern layer tends to be no larger than one ionic diameter (Zhang *et al.*, 2011). Molecular dynamics simulations have shown that the ions within the Stern layer experience a strong electrostatic attraction to the interface, which immobilizes them in contact with the surface (Lyklema *et al.*, 1998). As the Stern layer is immobile, the Stern layer potential (ζ) is used instead of wall potential in simulations. Thus, the Stern layer does not contribute to the transport of either liquid or ions. It is therefore neglected entirely in this thesis.

Beyond the Stern layer lies the *diffuse layer*, which, in contrast to the Stern layer, contains mobile ions. The equilibrium distribution of the ions depends on the competition between electromigration and diffusion. The thickness of this diffuse layer can be approximately predicted by the Debye length.[9] Diffuse layer electrohydrodynamics play a key role in the results obtained in this thesis, and electrokinetic phenomena in general. As Karniadakis *et al.* (2008) summarise, "the net charge contained in the diffuse layer is the primary reason for electrokinetic effects, where charged ions or particles can be mobilised by externally applied electric fields." Note that the diffuse layer is neglected

[9] The Debye length was originally called as the *Gouy length* (Gouy, 1910), but the latter term has fallen out of favour.

in the three simplified electric field models discussed earlier (perfect dielectric, perfect conductor, and leaky dielectric).

2.5.1 Thickness of diffuse layer

In this section, the thickness of the diffuse layer in one dimension (for the geometry given in Figure 2.5) for a symmetric, binary electrolyte solution, is derived from first principles. The governing equation for the continuum transport of ionic concentrations comes from the expression for chemical potential (ν) variation due to the addition of the last ion, given as (Bruus, 2007)

$$\nu(x) = \nu_0 + k_\mathrm{B}T \ln\left(\frac{n_\pm(x)}{n_0}\right) \pm ze\psi(x), \tag{2.39}$$

where ν_0 and n_0 are the chemical potential and ion number density in the absence of the surface, n_+ and n_- are the cation and anion number densities, k_B is the Boltzmann constant, and T is the absolute temperature, z is the valency, and e is the fundamental charge. In this subsection, the focus is on studying the ion distribution once it has attained equilibrium, i.e. once the system is at a constant chemical potential ($\nu(x) =$ constant). Therefore,

$$\frac{\partial \nu(x)}{\partial x} = 0. \tag{2.40}$$

Differentiating Equation 2.39, and then substituting Equation 2.40 we get,

$$k_\mathrm{B}T\frac{\partial P}{\partial x} = \mp ze\frac{\partial \psi(x)}{\partial x}, \tag{2.41}$$

where $P = \ln(n_\pm(x)/n_0)$. As indicated in Figure 2.5c, the bulk fluid is electroneutral, which is to say that the ion concentrations far away from the surface approach the initial value n_0. Also the surface potential is given by the Stern layer potential ζ. Therefore the boundary conditions are:

$$n_\pm(\infty) = n_0, \quad \psi(\infty) = 0, \quad \psi(0) = \zeta. \tag{2.42}$$

Now integrating Equation 2.41, we get,

$$n_\pm(x) = n_0 \exp\left[\mp \frac{ze}{k_\mathrm{B}T}\psi(x)\right]. \tag{2.43}$$

This results in a charge density ($q = ze(n_+ - n_-)$) of

$$q = -2zen_0 \sinh\left[\frac{ze}{k_\mathrm{B}T}\psi(x)\right]. \tag{2.44}$$

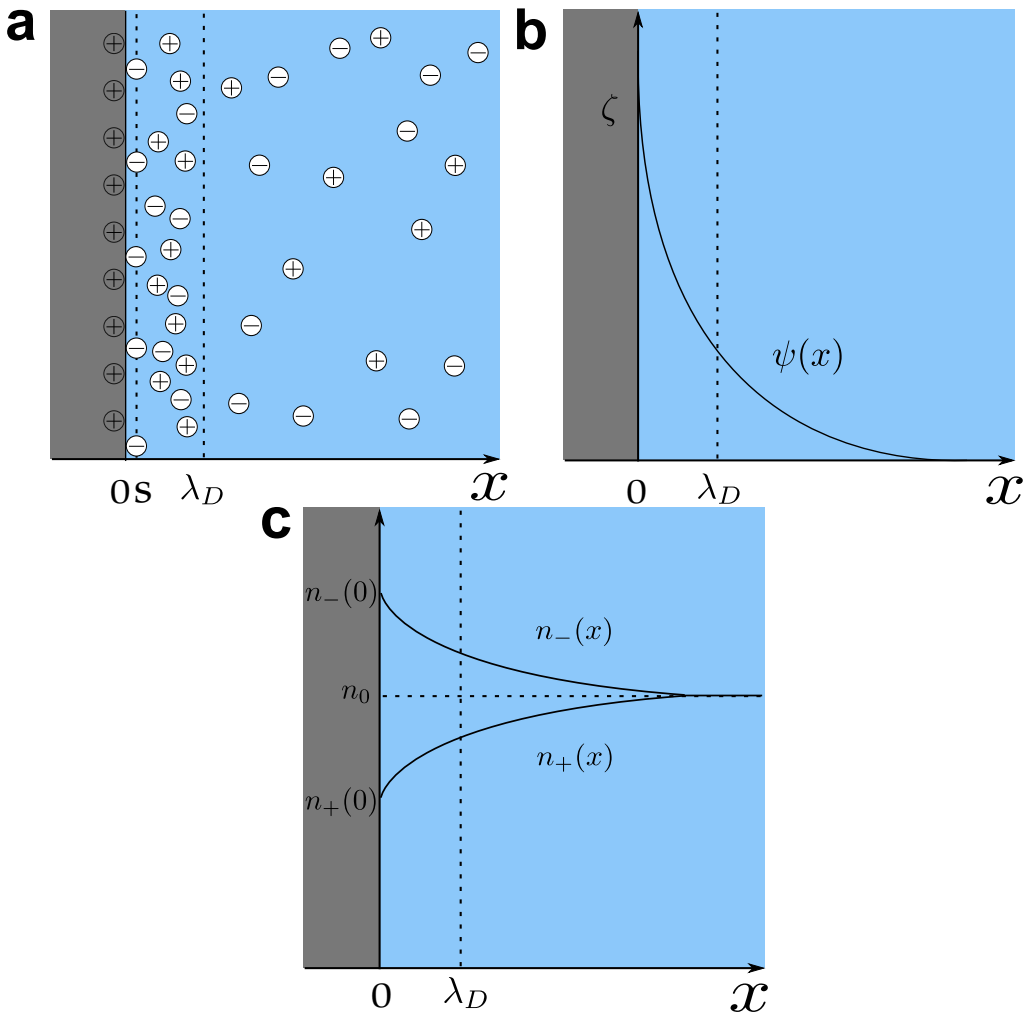

Figure 2.5: (a) The ionic structure of the Debye layer (in thermal equilibrium) in an electrolyte solution ($x > 0$) near a solid surface ($x \leq 0$), after charge transfer has taken place. The single layer of immobile counterions known as the Stern layer is depicted at $0 < x < s$. The diffuse charge layer, largely consisting of counterions, is depicted at $s < z < \lambda_D$. For $x > \lambda_D$, the electrolyte solution is electroneutral. (b) A simple continuous field model for the electric potential ($\psi(x)$) in the Debye layer. The potential at the surface ($x = 0$) is taken to be equal to the Stern layer potential ($\psi(0) = \zeta$), and the potential decays to zero in the bulk of the fluid. (c) The distribution of ionic densities $n_+(x)$ and $n_-(x)$ in the Debye layer.

Using the Poisson equation, given as

$$\nabla^2\psi = -\frac{q}{\epsilon\epsilon_0}, \tag{2.45}$$

we can derive the charge density in terms of potential leading to

$$\frac{\partial^2\psi(x)}{\partial x^2} = \frac{2zen_0}{\epsilon}\sinh\left[\frac{ze}{k_\mathrm{B}T}\psi(x)\right]. \tag{2.46}$$

This is called as the (1D) Poisson Boltzmann equation. When the electrical energy is small, i.e.

$$ze\zeta \ll k_\mathrm{B}T, \tag{2.47}$$

we can employ the Debye-Hückel approximation and use the Taylor expansion $\sinh(u) \sim u$. Hence, Equation 2.46 simplifies to:

$$\frac{\partial^2\psi(x)}{\partial x^2} = \frac{2z^2e^2n_0}{\epsilon k_\mathrm{B}T} \equiv \frac{1}{\lambda_D^2}\psi(x). \tag{2.48}$$

Thus, the Debye length ($\lambda_D = \sqrt{\epsilon k_\mathrm{B}T/2z^2e^2n_0}$) naturally appears in the equation for electric potential in diffuse charge layers, once the Debye-Hückel limit is utilised. Using the boundary conditions specified earlier (Equation 2.42), Equation 2.48 has the solution

$$\psi = \zeta e^{-x/\lambda_D}. \tag{2.49}$$

This solution confirms that the electric potential next to the surface decays exponentially from the initial value of ζ, on the scale of the Debye length, as illustrated in Figure 2.5.

2.5.2 Transition from solid/liquid to liquid/liquid interfaces

Though the previous section (and the bulk of electrokinetics research) has been directed towards single-phase or solid/liquid interfacial phenomena, such as electroosmotic/electroviscous flow adjacent to a surface, electrokinetic effects are faster at liquid/liquid interfaces due to the mobility of the interface, and can be used to generate, for example, higher velocities in microfluidic devices (Pascall & Squires, 2011). As discussed in the first chapter, liquid/liquid interfaces arise in lab-on-a-chip (LoC) devices that use drops (suspended in an immiscible medium) as microscale beakers, encapsulating a chemical/biological entity of interest. As with solid/liquid interfaces, interfacial charge can develop spontaneously at liquid/liquid interfaces when one of the phases is an electrolyte solution. This can occur via ion adsorption onto the interface (Creux *et al.*, 2009), or through direct contact with an electrode (Zhang *et al.*, 2013*b*). Once the interface is charged,

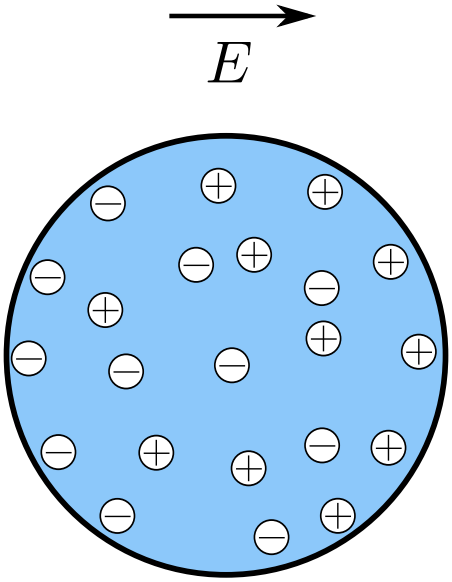

Figure 2.6: Illustration of a drop of electrolyte solution acted upon by an external electric field. The positive ions are conducted in the direction of the field, while the negative ions travel in the opposite direction, resulting in the formation of two 'effective' diffuse layers at the ends of the drop aligned with the field.

diffuse charge layers would spontaneously arise, and electrokinetic phenomena would result, as was the case with a solid surface. The thickness of the diffuse charge layer that forms can be characterized by the inverse dimensionless Debye length, defined for a drop radius R as:

$$\kappa = \frac{R}{\lambda_{\mathrm{D}}} = \sqrt{\frac{2z^2e^2n_0R^2}{\epsilon_0\epsilon_{\mathrm{d}}k_{\mathrm{B}}T}}. \tag{2.50}$$

As the inverse dimensionless Debye length (κ) is the ratio of the drop radius R to the EDL thickness λ_D (Equation 2.50), a high κ value implies a thin double layer, i.e. the charge is present in a smaller region near the drop interface. The electrokinetic model in a sense acts as a bridge between the perfect dielectric model, where the double layer is absent, and the leaky dielectric model, where the double layer exists, but is vanishingly thin (Zholkovskij *et al.*, 2002).

However, an interfacial charge isn't strictly necessary for a diffuse charge layer to form. Figure 2.6 illustrates a drop of electrolyte solution suspended in a dielectric fluid, subjected to an electric field. In this system, diffuse charge layers will form under the

action of an electric field, *in the absence of an interfacial charge*. This occurs because the electric field conducts the ions within the electroneutral drop bulk, transporting cations and anions in opposite directions. This results in charge separation within the drop as the concentration of ions changes locally, even though the drop on the whole remains electroneutral. Once the anion and cation concentration at the drop ends change, the mechanism will proceed *exactly* as for the case with the charged solid interface. The dynamics of these 'effective' diffuse layers will depend on electromigration and diffusion, where electromigration is driven by the field rather than a surface charge, and an equilibrium will result when the two effects are in balance. The thickness of the (symmetrical) diffuse layers will depend on the Debye length.

The model used in this thesis does not allow for interfacial charge formation, and the problem studied (for drop deformation and breakup) is the one described above. The exception is for coalescence studies where charged drops are considered. There, the charge is implemented by initialising the drop with a surplus/deficit of one ion species with respect to the other. In all cases, no interfacial charge is present.

The assumption of zero interfacial charge is justified because:

- In many cases, the presence of the interfacial charge does not affect the final steady state or transient drop behaviour. For example, the potential gradient induced by the external electric field tends to be far larger than that the corresponding potential gradient resulting from the small negative interfacial charge that develops at water/oil interfaces (Creux *et al.*, 2009).
- Ignoring interface charge allows us to isolate the effects of redistribution of free charge. Even for problems where the interfacial charge affects the drop dynamics significantly, there is value in generating insight using a simplified approach, as the literature on drop electrohydrodynamics using an electrokinetic model is sparse.[10]

2.5.3 Calculation of typical inverse Debye lengths

To calculate typical values for κ using Equation 2.50, we need an estimate of the range of initial ion number density in the drop (n_0). Conductivity values can be converted into an initial bulk ion number density ($/\mathrm{m}^3$) by using the formula (Masliyah, 2006),

[10] The consideration of the combined effect of free and interface charge will be the subject of future work utilising the recent extension of the code, as described in Davidson *et al.* (2016).

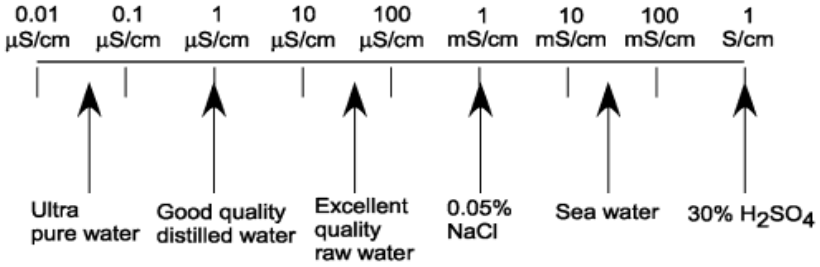

Figure 2.7: Electric conductivities of water under different conditions. Reproduced from Masliyah (2006)

$$n_0 = \frac{k_B T \sigma}{2 z^2 e^2 \bar{D}}, \tag{2.51}$$

where $\bar{D}$ is the diffusivity of ions in water (m^2/s). Water can have a range of conductivities depending on the concentration of impurities or dissolved salts. This is true of microfluidic water drops that are being modelled here. Figure 2.7 provides a summary. Using Equation 2.50 and Equation 2.51, values of κ for a range of water drop radii and drop conductivities are tabulated in Table 2.3. Due to computational limitations, an inverse Debye length greater than 25 is usually difficult to resolve numerically. Also, the higher the value of κ, the more accurate a simplified electric field model is going to be, as the charge would collect in increasingly small regions close to the interface. Table 2.3 reinforces the fact, both for physical and numerical reasons, the electrokinetic model described here is appropriate for simulating microfluidic drops and is probably unnecessary for larger drops or higher conductivity fluids.

	σ(S/m)		
R(m)	10^{-6}	10^{-3}	10^{0}
10^{-6}	1.19×10^{0}	3.76×10^{1}	1.19×10^{3}
10^{-3}	1.19×10^{2}	3.76×10^{4}	1.19×10^{6}
10^{0}	1.19×10^{4}	3.76×10^{7}	1.19×10^{9}

Table 2.3: Dimensionless inverse Debye lengths (κ) for a range of drop radii and conductivities

2.6 Summary

This chapter has summarised the history of drop electrohydrodynamics, covering the trinity of experiment, theory, and numerics. The development of the leaky dielectric model is a particular highlight of previous research, as it provides a bedrock for the study of macroscale electrohydrodynamic phenomena. Electrokinetics has been introduced, and the relationship between a full electrokinetic model and the leaky dielectric model has been discussed. It has been asserted that an electrokinetic model is uniquely suited to the topics of study in this work, namely microfluidic drop deformation, breakup, and coalescence. The next chapter outlines the electrokinetic model used in this work, covering the mathematical framework as well as its numerical implementation.

3 Model Formulation and Implementation

Essentially, all models are wrong, but some are useful.

GEORGE BOX

This chapter is divided into three sections. First, the governing equations of the electrokinetic model are listed, and the assumptions involved in their derivation are detailed (§ 3.1). Second, the numerical implementation of this model is described, starting from the origin of the code as a tool to simulate multiphase hydrodynamic flows, and covering its subsequent adaptation for electrokinetics and microfluidics (§ 3.2). Third, three alternate electric force formulations for the model are compared, and using rigorous validation, the appropriate model is selected for the rest of this thesis (§ 3.3). Finally, a summary is provided, along with a preview of the next chapter (§ 3.4).

3.1 Overview of model

3.1.1 Governing equations

In this section, the equations governing electrokinetic flow are outlined (Masliyah, 2006; Bruus, 2007; Chang & Yeo, 2010). The flow domain consists of two immiscible fluid phases. One phase, termed the 'disperse' phase, is assumed to be conducting, while the second phase, termed the 'continuous' phase, is assumed to be non-conducting or dielectric.[1] Both phases are considered to be incompressible. In this thesis, only electromagnetic phenomena in the electrostatic regime are considered; i.e magnetic and radiative effects are ignored. The Maxwell's electrostatic equations are (Bruus, 2007)

$$\epsilon\epsilon_0 \nabla \cdot \boldsymbol{E} = q, \tag{3.1}$$

$$\nabla \times \boldsymbol{E} = 0, \tag{3.2}$$

[1] In a microfluidic device, the disperse phase is commonly an electrolytic solution while the continuous phase tends to be an oil.

where q_e is the drop charge density. Equation 3.2 implies that the electric field is irrotational. Therefore the electric field in either phase can be represented in terms of a continuous electric potential (ψ):

$$\boldsymbol{E} = -\nabla\psi. \tag{3.3}$$

Using Equation 3.3, Equation 3.1 simplifies to the Poisson equation

$$\nabla^2\psi = -\frac{q_e}{\epsilon\epsilon_0}. \tag{3.4}$$

In the non-conducting phase, Equation 3.4 simplifies to Laplace's equation because of the absence of charge carriers. Within the conducting phase, the local charge density (for a binary, symmetric electrolyte solution) can be related to the local ion concentrations by using Gauss' law

$$q_e = ze(n_+ - n_-). \tag{3.5}$$

The local ion fluxes ($\boldsymbol{j}_\pm$) are described by the ion transport equation for both ion species:

$$\boldsymbol{j}_\pm = n_\pm\boldsymbol{u} - \bar{D}\nabla n_\pm \mp bzen_\pm\nabla\psi, \tag{3.6}$$

where b is the mobility, and $\bar{D}$ the diffusivity of the ion species. The terms on the right hand side of Equation 3.6 represent the advection, diffusion, and conduction of ions, respectively. In a dilute solution, b is given by Einstein's relation (Einstein, 1905; Peters, 1982):

$$b = \frac{\bar{D}}{k_\mathrm{B}T}, \tag{3.7}$$

where k_B is the Boltzmann constant and T is the absolute temperature. The total number of ions in the domain are conserved, as specified by the Nernst-Planck equation:

$$\frac{\partial n_\pm}{\partial t} + \nabla \cdot \boldsymbol{j}_\pm = 0. \tag{3.8}$$

As the phases are assumed to be incompressible, mass conservation is achieved by the continuity equation (as shown in Equation 2.18, repeated below)

$$\nabla \cdot \boldsymbol{u} = 0. \tag{3.9}$$

The velocity in the flow domain is determined by the Navier-Stokes equation, with additional terms to incorporate surface tension and electrical effects (as shown in Equation 2.17, repeated below),

$$\frac{\partial\rho\boldsymbol{u}}{\partial t} + \boldsymbol{u} \cdot \nabla\rho\boldsymbol{u} = \nabla p + \nabla \cdot [\mu(\nabla\boldsymbol{u} + \nabla\boldsymbol{u}^{\boldsymbol{T}})] + \boldsymbol{F}_\mathrm{S} + \boldsymbol{F}_\mathrm{E}. \tag{3.10}$$

Note that ρ and μ are uniform in each phase, with a jump at the interface. $\boldsymbol{F}_{\mathrm{S}}$ is the body force due to the interfacial tension, represented by the Continuum Surface Formulation (CSF) of Brackbill *et al.* (1992) (more details about the CSF implementation are provided in § 3.2.6):

$$\boldsymbol{F}_{\mathrm{S}} = \gamma k \delta(r) \boldsymbol{n}, \tag{3.11}$$

where k is the curvature, γ is the interfacial tension, $\delta(r)$ is the delta function that is zero everywhere except at the interface, and $\boldsymbol{n}$ is the unit normal to the interface, pointing into the disperse phase. The last term on the right-hand side in Equation 3.10 ($\boldsymbol{F}_{\mathrm{E}}$) is the electrical body force. The choice of $\boldsymbol{F}_{\mathrm{E}}$ in our simulations is elaborated in § 3.3.

3.1.2 Assumptions underlying model formulation

Continuum approximation

For most fluids of engineering interest, the standard continuum description of transport processes sufficiently captures the essential flow behaviour of the problem under consideration. Eijkel & van den Berg (2005) estimate that a continuum assumption for liquids is appropriate down to a characteristic length scale on the order of nanometres, and extended continuum models that can capture nanometre length-scale physics are being developed (Hansen *et al.*, 2015). As such, the micron-sized drops studied in this thesis can be safely considered to be in the continuum regime.

Newtonian fluids with spatially invariant physical properties

The conducting and dielectric phases are assumed to be Newtonian, which is to say that each has a constant viscosity, independent of the shear rate. There exist microfluidic applications involving non-Newtonian fluids; this includes physiological fluids such as blood, serum, and plasma (Srinivasan *et al.*, 2004) or polymer solutions (Ziemecka *et al.*, 2011). Numerical models have also been developed to simulate electrohydrodynamic flows for non-Newtonian drops (Lee & Li, 2006). However, the majority of microfluidic drop-based devices use a water-in-oil system (Huebner *et al.*, 2008) to which the results in this thesis will be applicable.

It is also assumed that the physical properties of the electrolyte solution used as a conducting phase in the simulations do not vary in response to the high electric fields and high ion concentrations. The density, viscosity, and permittivity are all assumed to be uniform throughout the disperse phase and continuous phases despite the high

variations in electric potential that can occur during the simulation.[2] This assumption is justifiable as experimental and numerical evidence suggests that changes in density (Lee *et al.*, 2012), viscosity (Bonthuis *et al.*, 2012), and permittivity (Bonthuis *et al.*, 2012) vary only in the Stern layer, and not in the diffuse charge layer.

Ideal electrolyte solution of a binary symmetric electrolyte

The electrolyte solution is assumed to be ideal, implying no ion-ion interactions. While the transport of ions is considered, the ions themselves are represented as species number densities. The ions therefore are assumed to have no mass or volume, and all electrostatic ion-ion interactions are ignored. There exists evidence from theoretical and numerical work that for aqueous, univalent electrolytes at 25 °C, ion-ion interactions are negligible for dissolved salt concentrations of up to 0.1 M (Carnie & Torrie, 1984; Carnie *et al.*, 1984).

The model considers only two ionic species (such as K^+ and Cl^-, for example) which are assumed to have identical diffusivities ($\bar{D}_+ = \bar{D}_- = \bar{D}$), valencies ($z_+ = z_- = z$), and electrical mobilities ($b_+ = b_- = b$). Any additional ionic species that are present in real aqueous solutions are ignored (Persat *et al.*, 2009*a*,*b*). The electrolyte is assumed to be symmetric. In addition Einstein's relation used to derive Equation 3.8 is invalid at high concentrations of solute (Peters, 1982), so the solution is assumed to be dilute.

Isothermal system with no chemical reactions

The system is assumed to be isothermal; temperature changes would result in additional physical (and consequently numerical) complications. For example, the conductivities depend on local temperature, which in turn would impact the electrohydrodynamics. The assumption of isothermality means that no heat energy is generated in the system.

It is also assumed that no chemical reactions occur at any point during the simulation. The dissolved salt ions are inert, and no electrode reactions are considered. While some reactions occur in all electrokinetic systems, numerical modelling of chemical reaction associated mass-transfer is generally not well-developed (Wörner, 2012). This means that the results presented here are less applicable where inducing a chemical reaction is the objective of the device being fabricated (Song *et al.*, 2006).

[2] Equation 3.1, for example, assumes that the permittivity is uniform in either phase.

No interfacial charge or gravitational forces

In this model, no kinetic mechanism for sorption or dissociation of ions is considered, Consequently, the interface is uncharged, and rather than the electric double layer (EDL) observed in electrokinetic flows, a non-equilibrium diffuse charge layer is induced by the application of the external electric field. As discussed in § 2.5.2, this model can be assumed to be a water-in-oil system where the induced electric field is far greater in magnitude than the (interfacial charge) generated electric field, and the latter can therefore be neglected entirely. The algorithm used in this thesis has been recently extended to allow for interfacial charge (Davidson *et al.*, 2014, 2016), and this model will be applied to relevant problems in the future.

3.2 Numerical implementation

The Computational Fluid Dynamics (CFD) models developed typically solve the macroscopic conservation laws for mass, momentum and, if necessary, energy. Broadly speaking, there are three types of numerical approaches in CFD: finite difference, finite element and spectral methods.[3] In this thesis, a special type of finite differencing, known as the Finite Volume Method (FVM) will be used.

3.2.1 Finite Volume Method

FVM methods require that the domain be subdivided into cells, or control volumes; these cells are contiguous and must completely fill the domain. A general solution procedure for FVM using CFD consists of the following three steps (Versteeg & Malalasekera, 2011):

- Integration: The governing equations are integrated over the numerical domain.
- Discretisation: The resulting integral equations are converted into a system of algebraic equations.
- Solution: The algebraic equations are solved by an iterative method

The first step, namely the control volume integration, distinguishes FVM from all other CFD techniques. In FVM, the integration is peformed over the volume (V) of each cell. The spatial derivative forms are converted to surface integrals over the cell surface

[3] For the sake of convenience, meshfree methods, such as Smoothed Particle Hydrodynamics which involve Lagrangian tracking of particles, are ignored in this classification.

S using Gauss' theorem. For a vector $\boldsymbol{T}$, this can be stated as:

$$\iiint_V (\nabla \cdot \boldsymbol{T})\, dV = \oiint_S (\boldsymbol{T} \cdot \boldsymbol{n})\, dS. \tag{3.12}$$

In Equation 3.12, the left and right hand sides represent a volume integral over the cell volume V and a surface integral over the boundary S of the cell volume V, respectively. Note that $\boldsymbol{n}$ is the outward normal in Equation 3.12. There are closely related theorems involving the gradient of a scalar and divergence of a tensor, that are used in the integration over a mesh cell in FVM (see appendix A5 in Bird *et al.* (2002) for more details). The resulting equations represent the exact conservation of relevant properties for each finite size cell. This formulation provides a clear relationship between the numerical algorithm and the underlying physical conservation principle, which is one of the main attractions of FVM. There exist many schemes to approximate the resultant surface integrals; the reader is directed to Versteeg & Malalasekera (2011) for additional details.

3.2.2 Volume of Fluid

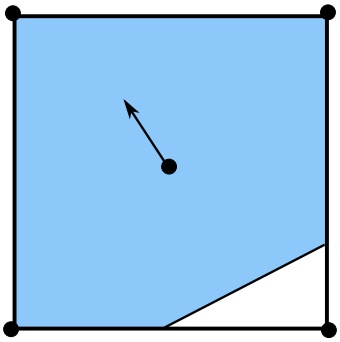

Figure 3.1: Schematic of a sample interface cell, with the phase being tracked coloured blue. The direction of the inward-pointing normal vector ($\hat{\boldsymbol{n}}$) is also shown.

For multiphase problems involving fluids, the interface between the fluids constitutes an additional complication; this interface is deformable, and can undergo topological changes during coalescence and breakup. The interface is classically considered to be a thin boundary layer, with properties distinct from either of the bulk fluids that it separates. Numerical methods for modelling interfaces can be divided as those which regard the interface thickness to be *zero* and those that consider it to be *finite* (Wörner,

2012). In this thesis, the focus is on diffuse interface numerical techniques. It is pertinent to note that the *numerical* interface thickness in diffuse interface methods is far larger than than the *physical* interfacial thickness suggested by the literature, which tends to be on the order of nanometres.

Prominent among diffuse interface methods is the Volume of Fluid (VoF) approach, pioneered by Hirt & Nichols (1981). VoF methods define a fractional volume or 'colour function' (ϕ) as the fraction of a numerical (mesh) cell that is filled by the fluid of interest (drop fluid in our case). This colour function is advected with the flow throughout the domain using the equation:

$$\frac{\partial \phi}{\partial t} + \nabla \cdot (\phi \boldsymbol{u}) = 0. \tag{3.13}$$

The colour function can assume any value between zero and unity; in the interior cells $\phi = 1$, in the exterior cells $\phi = 0$, and in the interface cells $0 < \phi < 1$. The interface curvature (k) and unit normal ($\boldsymbol{n}$) from the surface tension term of the Navier-Stokes equation (Equation 3.10) are determined numerically from:

$$\hat{\boldsymbol{n}} = \nabla \phi, \tag{3.14}$$

$$k = -\nabla \cdot \boldsymbol{n}, \tag{3.15}$$

$$\boldsymbol{n} = \frac{\hat{\boldsymbol{n}}}{|\hat{\boldsymbol{n}}|}. \tag{3.16}$$

where $\hat{\boldsymbol{n}}$ is the normal vector. In practice, this algorithm first determines the orientation of the interface in each interface cell from the normal vector (Figure 3.1), and then uses the ϕ value to place the (already-oriented) interface segment in the correct location.

Understanding the algorithms detailed in the next two subsections requires some familiarity with the computational grid used in this model, which is illustrated in Figure 3.2. The mass cell, shown within the solid lines in Figure 3.2, is centred on the location of the fluid pressures and ϕ (filled square). As the grid is staggered, the momentum cell, shown within the dashed boundary in Figure 3.2, is centered on the location of the velocity in the radial direction (open diamond). The momentum cell is therefore centered on the face of the mass cell in this setup. Hereafter, cell-centered and face-centered quantities are defined with respect to the mass cell.

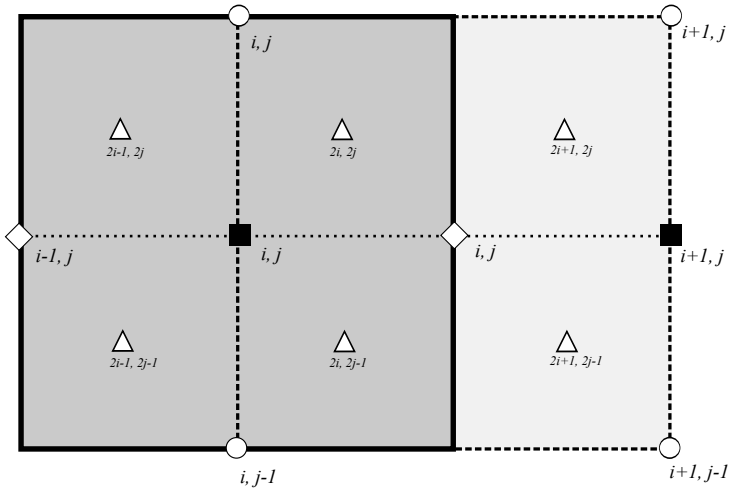

Figure 3.2: Schematic of the staggered computational grid. The mass cell (solid boundary) is centred on the location of the fluid pressures, electric potentials and ion concentrations (filled square). The u-momentum cell (dashed boundary), is centred on the location of the velocity in the r-direction (open diamond). The w-momentum cell (not shown) is centred on the location of the velocity in the z-direction (open circle). The colour function is located on the mass cell, but calculated on a mesh that is twice as fine (open triangle) as the mesh used to store all other variables (§ 3.2.5).

3.2.3 Advection of colour function ϕ

The fundamental challenge in solving the advection equation (Equation 3.13) is that upwind schemes tend to be diffusive which means that the interfaces smear out rapidly, while downwind schemes maintain a sharp interface but are unstable, and central or higher-order schemes struggle with preserving the boundedness of the solution. Using simple advection tests as a benchmark, Rudman (1997) found that the VoF method of Youngs (1982) outperformed the Simple Line Interface Construction (SLIC) of Noh & Woodward (1976), and the original VoF method of Hirt & Nichols (1981), as well as his own VoF approach. He attributed this to the fact that Youngs (1982) used a more accurate interface reconstruction than either Noh & Woodward (1976) or Hirt & Nichols (1981).

Therefore, in a subsequent paper (Rudman, 1998), the advection routine for ϕ was modified to emulate the approach of Youngs (1982), which is the algorithm used in

this model. While Youngs' VoF has some similarities to the Flux Corrected Transport algorithm for momentum advection described in § 3.2.4 such as the directionally-split advection updates, it is a significantly more complicated algorithm that can't be expressed as algebraic manipulations of upwind and downwind fluxes. The reader is directed to the Appendix of Rudman (1997) for more details. A brief summary of the 2D algorithm is provided below:

- The ϕ advection algorithm of Youngs' VoF rests on accurate estimation of the interface orientation angle υ within a cell. First, the upwind fluxes for ϕ are calculated at the faces of each cell following Equation 3.20, extended to two dimensions. This is accurate away from the interface when ϕ is constant. However, for each interface cell, the outward Youngs flux is calculated instead. Then the interface normals (n^x, n^y) in the cell are calculated at the cell centre (i, j) using:

$$n^x_{i,j} = \frac{1}{\delta x}(\phi_{i+1,j+1} + 2\phi_{i+1,j} + \phi_{i+1,j-1} - \phi_{i-1,j+1} - 2\phi_{i-1,j} - \phi_{i-1,j-1}), \quad (3.17)$$

$$n^y_{i,j} = \frac{1}{\delta y}(\phi_{i+1,j+1} + 2\phi_{i,j+1} + \phi_{i-1,j+1} - \phi_{i+1,j-1} - 2\phi_{i,j-1} - \phi_{i-1,j-1}). \quad (3.18)$$

- Next, υ can be calculated from

$$\upsilon = \tan^{-1}\left(-\frac{\delta x}{\delta y}\frac{n^x}{n^y}\right) \qquad (0 \leq \upsilon \leq \pi/2). \quad (3.19)$$

- Now, the interface cell can be rotated in such a way that υ lies in the range $0 \leq \upsilon \leq \pi/2$, such that there are only four possible interface configurations as shown in Figure 3.3. The interface cells can then be classified into I-IV based on the respective values of υ and ϕ
- Finally, the flux of ϕ through each face of an interface cell is then calculated geometrically using the interface reconstruction for that cell. Figure 3.4 illustrates the flux calculation in a typical interface cell. Please refer to Table V in Rudman (1997) for more information.

3.2.4 Momentum advection

As shown in Figure 3.2, the momentum fluxes are calculated at the faces of the mass cells. To prevent oscillations at density discontinuities, i.e. interfaces, Flux Corrected Transport (FCT) for momentum advection is implemented. As with advection of ϕ, upwind schemes for momentum advection tend to be diffusive, while downwind schemes are unstable.

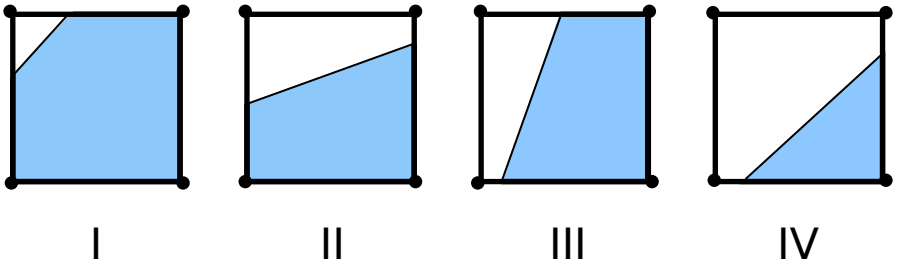

Figure 3.3: The four possible interfaces reconstructions for the VoF algorithm of Youngs (1982), with the phase being tracked coloured blue.

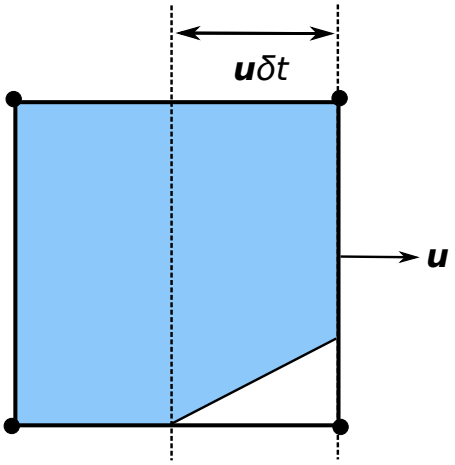

Figure 3.4: The estimate of the volume flux through the right-hand side of cell (i, j) is equal to the shaded volume bounded by the cell edges, the line that is a distance $\boldsymbol{u}\delta t$ from the cell edge and the approximate interface reconstruction in the cell.

The objective of a FCT algorithm is to design a suitable combination of upwind and downwind/higher-order fluxes that eliminates both the diffusiveness of the upwind scheme and the instability of the downwind/higher-order scheme. FCT was originally formulated by Boris & Book (1976). Zalesak (1979) generalised this approach and extended it to multiple dimensions. A basic 1D FCT procedure to advect a cell-centered quantity 'C' consists of the following steps (Rudman, 1998):

- First, the (diffusive) lower-order flux (F^U) for a timestep of δt and velocity u is calculated using first-order upwinding. For example, the flux at the cell face

$(i + 1/2)$ is given as

$$F^U_{i+1/2} = \begin{cases} u_{i+1/2}\,\delta t C_i & \text{if } u_{i+1/2} \geq 0, \\ u_{i+1/2}\,\delta t C_{i+1} & \text{if } u_{i+1/2} < 0. \end{cases} \tag{3.20}$$

- Second, an intermediate value of the parameter (C^*) is determined by a regular advection scheme. For mesh cell i and grid distance δx, this step can be represented as,
$$C^*_i = C^t_i - \frac{1}{\delta x}(F^U_{i+1/2} - F^U_{i-1/2}), \tag{3.21}$$
- Third, a higher-order upwind flux (F^H) is calculated as suggested by Zalesak (1979). An alternative to this would be using a downwind flux (Hirt & Nichols, 1981).
- Finally, an anti-diffusive flux is defined to correct the diffusion resulting from the upwind scheme. This anti-diffusive flux ($F^A_{i+1/2}$) is initially estimated to be the difference between the upwind and downwind flux approximations
$$F^A_{i+1/2} = F^U_{i+1/2} - F^H_{i+1/2} \tag{3.22}$$
- If this entire anti-diffusive flux were applied, the solution would become unstable. Instead correction factors (w) are used to limit the weight of the anti-diffusive flux in the advection calculation. The reader is directed to Zalesak (1979) for additional details. The final value of C at a new time (C^{t+1}_i) is obtained from:
$$C^{t+1}_i = C^t_i - \frac{1}{\delta x}(w_{i+1/2}\,F^A_{i+1/2} - w_{i-1/2}\,F^A_{i-1/2}). \tag{3.23}$$

Using this algorithm, Rudman (1997) coupled the FCT approach for momentum advection with the Youngs' VoF interface reconstruction to develop a new model (§ 3.2.5) for multiphase flow applications. The calculation of momentum fluxes was carried out at control volume edges, unlike Zalesak (1979). He also found that using Zalesak (1979)'s 2D algorithm resulted in unsatisfactory results. He instead employed an approach that swept the entire mesh in the x-direction with the 1D algorithm (Equation 3.20 - Equation 3.23), updated C, and then swept in the y-direction. To avoid systematic error, the order of the sweeps was interchanged at every time step. This 'direction-split' FCT was found to be significantly more accurate than the approach suggested by Zalesak (1979).

3.2.5 Fine Grid Volume Tracking

In addition to combining the Youngs' VoF advection of ϕ and FCT formulation of momentum fluxes, Rudman (1998) effected several key improvements, notably:

- Unlike the method of Youngs (1982), ϕ was advected on a grid twice as small as the ones used for momentum and pressure (see Figure 3.2). As the fluid properties such as permittivity an viscosity are functions of ϕ, this provided additional resolution to their calculations. Rudman (1998) termed this approach as Fine Grid Volume Tracking (FGVT).
- As a staggered grid was employed, the density and momentum fluxes were calculated at control volume edges, in a departure from Zalesak (1979). This helped prevent the checkerboard pressure pattern that can form in collocated grids.
- The surface tension algorithm was essentially the Continuum Surface Force (CSF) approach of Brackbill *et al.* (1992). The CSF formulation converts the stress jump across the interface into a volume force acting on both fluids in a small region adjacent to the interface. Reformulating the surface tension force as a volume force makes its implementation significantly easier in Eulerian codes. Also, a lower-order smoothing kernel (Monaghan, 1992) is used in calculating normals and curvature.
- A robust multigrid solver for the pressure-correction equation was also implemented, based on the Galerkin coarse-grid approximation method of Wesseling (1991).

This FGVT model could handle the merging and breaking-up of fluid naturally, without manual intervention. It has been used to study the flow regimes in splashing drops (Morton *et al.*, 2000); heat/mass transfer in multiphase flow (Davidson & Rudman, 2002); pinch-off of pendant drops for shear-thinning (Davidson *et al.*, 2004) and viscoelastic (Davidson *et al.*, 2006) fluids; parametric studies of drop deformation through a microfluidic contraction for Newtonian (Davidson *et al.*, 2005; Harvie & Davidson, 2005; Harvie *et al.*, 2006*b*) and non-Newtonian (Harvie *et al.*, 2006*a*, 2007, 2008*a*) fluids; and deformation of a surfactant-laden drop rising in a liquid (Davidson & Harvie, 2007*b*). Note that the models used for these studies have been modified from the original FGVT algorithm of Rudman (1998), in ways that *are not* relevant to the current thesis-work. However, they have been included here to illustrate the range of problems that have been successfully simulated using this base algorithm.

3.2.6 Implementation of Level Set

There are two key modifications to the FGVT model of Rudman (1998) that *are* relevant to the results presented in this thesis. First, the CSF formulation for the surface tension force in Rudman (1998), while more convenient, has a tendency to generate unphysical

currents for VoF schemes. These currents, known as 'parasitic currents', arise in regions adjacent to the interface, due to local errors in the CSF body force. The magnitude of parasitic currents increases with surface tension strength and can become large enough to affect the flow field velocities in certain cases. Harvie *et al.* (2006*c*) found the magnitude of these parasitic currents to be significant in some common physical systems, and, crucially, the generated currents did not decrease with increased mesh refinement and lowered computational time-stepping. An alternative to VoF is a zero-interface approach, such as Level Set (LS) which uses a signed distance function rather than ϕ to track the interface. LS methods are less susceptible to parasitic currents, and capture the interface effectively; unfortunately, they do not conserve mass well. However, by combining the VoF and LS approaches, in what is known as Combined Level Set Volume of Fluid (CLSVoF) method, both accurate surface tension force calculation and mass conservation can, in principle, be achieved. In the CLSVoF method, ϕ is advected using the VOF approach, while a LS function is used to compute the geometric properties (normal and curvature) of the interface. Harvie *et al.* (2008*b*) developed a CLSVoF version of Rudman (1998)'s algorithm, and demonstrated that the parasitic currents went to zero when the mesh was sufficiently refined. A brief summary of the algorithm is provided below. The reader is directed to Harvie *et al.* (2008*b*) for additional details.

The key difference in interface construction procedures between the VoF method outlined in § 3.2.2 and CLSVoF is that the interface normal ($\hat{\boldsymbol{n}}$) is not calculated from the colour function (ϕ). Instead, for interface cells the cell volume is divided into two regions by an interface, in the ratio $\phi/1-\phi$. Then a LS function (s) for the interface is defined in terms of distance (d) from the center of the cell ($\boldsymbol{x_c}$)

$$s = \hat{\boldsymbol{n}} \cdot \boldsymbol{x_c} - d, \tag{3.24}$$

Values of s calculated from Equation 3.24 are positive for $\phi > 1/2$, negative for $\phi < 1/2$, and zero for $\phi = 1/2$. As the gradient of s is required in subsequent steps, a value of s is needed in non-interface cells as well, which is calculated by

$$|\nabla s| = 1. \tag{3.25}$$

Equation 3.25 is solved iteratively, starting from the interface cells and sweeping outwards towards regions of higher $|s|$, and the numerical scheme is able to calculate s at large distances from the interface at relatively small computational cost. To ensure that the calculated values of s precisely satisfy Equation 3.25 in interface cells, a pseudo-transient improvement procedure is implemented to ensure that the s varies smoothly and

monotonically across the interface. For details about the calculation of s and subsequent iterative improvement, the reader is directed to Harvie *et al.* (2008*b*). Once the distance function (s) has been calculated accurately, the curvature (k) is calculated in the same manner as in § 3.2.2, by replacing ϕ by s

$$\hat{\boldsymbol{n}} = \nabla s, \tag{3.26}$$

$$k = -\nabla \cdot \boldsymbol{n}, \tag{3.27}$$

where $\boldsymbol{n}$ represents the unit normal for the level-set function.

3.2.7 Modifications for electrokinetics

The second important modification to the FGVT-CLSVoF model involves incorporation of electrokinetic effects, which is highly relevant to the present study. A separate single-phase version of the original FGVT-VoF code had been adapted by Davidson & Harvie (2007*a*) to calculate steady state solutions of the electrokinetic flow equations, with the expectation that the code would subsequently be extended to multiphase flows.[4] They used it to contrast the distribution of (electrical) parameters of interest in a rectangular contraction when compared to a straight channel. Davidson *et al.* (2008) studied electroviscous effects resulting from overlapping electric double layers, in both straight-channel and contraction geometries. Electroviscous effects manifest as an electrohydrodynamic resistance to the flow, resulting in an increased pressure-drop for a given flow rate. Electroviscous effects were subsequently studied for Newtonian liquids in a cylindrical contraction (Bharti *et al.*, 2008), non-Newtonian (power-law) liquids in a cylindrical channel (Bharti *et al.*, 2009), and non-Newtonian (shear-thinning) liquids in a cylindrical contraction (Davidson *et al.*, 2010). Finally, Berry *et al.* (2011*a*) analysed the electrokinetic development length for electroviscous flow in a contraction and developed an order-of-magnitude expression to predict it, while Berry *et al.* (2011*b*) showed that the development length could be controlled to some extent by modifying the wall permittivity.

The single-phase electrokinetic code and the multiphase hydrodynamic CLSVoF code were combined by Berry *et al.* (2013), who developed a multiphase electrohydrodynamic model for liquid/liquid interfaces. Their model allows for the coupled calculation of

[4] In fact Davidson & Harvie (2007*a*) state that the multiphase adaptation of the single-phase electrokinetic code "is convenient because the Rudman algorithm has already been used extensively by the authors for transient droplet deformation in non-electrokinetic flows, and the adapted code can be readily extended in the future to study such flows with electrokinetics included"

convective, conductive and diffusive ion transport, the electrical potential distribution, and the CLVoF-based flow dynamics of the liquid phases. This is the state-of-the-art model used in this thesis. While the reader is directed to Berry *et al.* (2013) for full details, a couple of novel aspects of this model are highlighted below.

Formulation of ion transport equation

The non-dimensionalised (§ 3.3.1) version of the ion-transport equation (Equation 3.6) can be represented as (after removal of any superscripts):

$$\boldsymbol{j}_{\pm} = n_{\pm}\boldsymbol{u} - \frac{1}{\mathrm{Pe}}(\nabla n_{\pm} \mp n_{\pm}\boldsymbol{E}), \tag{3.28}$$

where Pe is the Péclet number, defined as

$$\mathrm{Pe} = \frac{V_{\mathrm{ref}} R}{\bar{D}}. \tag{3.29}$$

Here V_{ref} is the velocity reference scale, to be defined later. The boundary condition for the ion transport equation at the interface between the fluids is given by (Castellanos & González, 1998):

$$\boldsymbol{n} \cdot ([\boldsymbol{j}_{\pm} - n_{\pm}\boldsymbol{u}]_{\mathrm{d}} - [\boldsymbol{j}_{\pm} - n_{\pm}\boldsymbol{u}]_{\mathrm{c}}) = 0, \tag{3.30}$$

where the subscripts 'd' and 'c' indicate disperse (conducting) and continuous (non-conducting) phase respectively. Combining the above equation with Equation 3.28 yields

$$\left[\frac{1}{\mathrm{Pe}}(\nabla n_{\pm} \mp n_{\pm}\boldsymbol{E})\right]_{\mathrm{d}} \cdot \boldsymbol{n} - \left[\frac{1}{\mathrm{Pe}}(\nabla n_{\pm} \mp n_{\pm}\boldsymbol{E})\right]_{\mathrm{c}} \cdot \boldsymbol{n} = 0. \tag{3.31}$$

As the continuous phase does not contain ions, this reduces to

$$\left[\frac{1}{\mathrm{Pe}}(\nabla n_{\pm} \mp n_{\pm}\boldsymbol{E})\right]_{\mathrm{d}} \cdot \boldsymbol{n} = 0. \tag{3.32}$$

Combining the above equation with the definition of a unit normal vector (Equation 3.16) we get

$$\left[\frac{1}{\mathrm{Pe}}(\nabla n_{\pm} \mp n_{\pm}\boldsymbol{E})\right]_{\mathrm{d}} \cdot \nabla\phi = 0. \tag{3.33}$$

Equation 3.33 sets the ion flux through the interface to be zero. Now while ions can be (algorithmically) present in either of the two phases, assuming that they do not (physically) pass through the interface is a reasonable assumption for the water/oil interfaces studied in this work as the oil phase is non-conducting. However, the numerical implementation

of Equation 3.33 at the interface is not straightforward because of the presence of the $\nabla\phi$ term. To mitigate this, Equation 3.33 can be combined with Equation 3.8 and Equation 3.6 to give

$$\frac{\partial \phi n_{\pm,\mathrm{d}}}{\partial t} + \nabla \cdot \phi n_{\pm,\mathrm{d}}\, \boldsymbol{u} = \frac{1}{\mathrm{Pe}}(\nabla \cdot [\nabla \phi n_{\pm,\mathrm{d}} \mp \phi n_{\pm,\mathrm{d}}\, \boldsymbol{E}] - [\nabla n_{\pm,\mathrm{d}} \mp n_{\pm,\mathrm{d}}\, \boldsymbol{E}] \cdot \nabla \phi). \quad (3.34)$$

Here the ion concentration ($n_{\pm,\mathrm{d}}$) is zero in the continuous phase by definition. A look at Equation 3.34 shows that for non-interface cells in the disperse phase, i.e. when $\phi = 1$, this equation reduces to the standard ion-transport equation (Equation 3.8). Also, in interface cells (when $\phi \neq 1$ and $\nabla\phi \neq 0$), the second term on the right hand side is identical to the charge boundary condition stated in Equation 3.33, and is consequently equal to zero. Therefore, for the interfacial zero ion-flux condition, Equation 3.34 simplifies to

$$\frac{\partial \phi n_{\pm,\mathrm{d}}}{\partial t} + \nabla \cdot \left[\phi n_{\pm,\mathrm{d}} \left(\boldsymbol{u} \pm \frac{1}{\mathrm{Pe}} \boldsymbol{E}\right)\right] = \frac{1}{\mathrm{Pe}} \nabla \cdot (\phi \nabla n_{\pm,\mathrm{d}}). \quad (3.35)$$

The implementation of this modified ion-transport equation (Equation 3.35) as opposed to the original equation (Equation 3.8) has two advantages:

- Equation 3.35 implicitly enforces the interfacial zero ion-flux condition, resulting in no numerical flux of ions between the phases, thus ensuring the conservation of ions in the conducting phase.
- This method can be applied over the whole domain, doing away with the need for special treatment for interface cells.

Numerical ion transport algorithm

Using implicit time-stepping, Equation 3.35 can be discretised as

$$\frac{(\phi n_{\pm,\mathrm{d}})^{t+1} - (\phi n_{\pm,\mathrm{d}})^{t}}{\delta t} + \nabla \cdot n^{t}_{\pm,\mathrm{d}}\, (\phi^{t} \boldsymbol{u}^{av}) \pm \frac{1}{\mathrm{Pe}} \left[\nabla \cdot n^{t}_{\pm,\mathrm{d}}\, (\phi^{t} \boldsymbol{E}^{t})\right] = \frac{1}{\mathrm{Pe}} \left[\nabla \cdot \phi^{t} \nabla n^{t}_{\pm,\mathrm{d}}\right], \quad (3.36)$$

where the superscripts '$t+1$', 't', and 'av' refer to end-of-timestep, beginning-of-timestep, and timestep-averaged values. Equation 3.36 is implemented in three steps as the advection, conduction, and diffusion updates are performed sequentially, starting with the advection update:

$$\frac{(\phi n_{\pm,\mathrm{d}})^{a} - (\phi n_{\pm,\mathrm{d}})^{t}}{\delta t} + \nabla \cdot n^{t}_{\pm,\mathrm{d}}\, (\phi^{t} \boldsymbol{u}^{av}) = 0, \quad (3.37)$$

where the superscript 'a' refers to values immediately after the advection step is completed. Equation 3.37 shows that the ion concentrations (n_{+}/n_{-}) are advected along with the

disperse phase volume fraction (ϕ). The ion concentrations are therefore stored at the cell centres, along with the disperse phase volume fraction, and are advected using a modified version of the direction-split FGVT algorithm (discussed in § 3.2.5) that is used to advect ϕ (Harvie *et al.*, 2008*a*). The advection update is followed by the conduction update, given by

$$\frac{(\phi n_{\pm,\mathrm{d}})^c - (\phi n_{\pm,\mathrm{d}})^a}{\delta t} + \pm\frac{1}{\mathrm{Pe}}\left[\nabla \cdot n^a_{\pm,\mathrm{d}}\,(\phi^t \boldsymbol{E}^t)\right] = 0, \tag{3.38}$$

where the superscript 'c' refers to values immediately after the conduction step is completed. The conduction step is implemented as an advection step with a pseudo-velocity $\phi^t \boldsymbol{E}^t$, which helps prevent the generation of unphysical ion concentrations (Biscombe *et al.*, 2012). This update uses the direction-split FCT method (described in § 3.2.4) that is used to advect the momentum fluxes. The final step in the ion transport algorithm is the diffusion update, given by

$$\frac{(\phi n_{\pm,\mathrm{d}})^{t+1} - (\phi n_{\pm,\mathrm{d}})^c}{\delta t} = \frac{1}{\mathrm{Pe}}\left[\nabla \cdot \phi^t \nabla n^c_{\pm,\mathrm{d}}\right], \tag{3.39}$$

This concludes the ion transport for a single timestep. In summary, the prominent features of the electrokinetic flow model used in this thesis are (Berry *et al.*, 2013):

- All models prior to Berry *et al.* (2013) assumed the electrical properties to be uniform in each phase, with the electrohydrodynamic coupling limited to the interface.
- However, as discussed in the section on electrokinetic theory, this is an oversimplification as the local electrokinetic phenomena depends on the local ion concentration. In the model described above, the local concentration of either ion species is a function of both space and time.
- In addition, the zero ion-flux boundary condition across the interface is implemented implicitly, requiring no special treatment for the interface cells.

It must be noted that López-Herrera *et al.* (2015) have since developed a numerical model that performs a similar function to that of Berry *et al.* (2013).

3.3 Choice of electric force formulation

3.3.1 Final model equations

The final model equations are provided here for completeness. The equations are normalized prior to being solved numerically. The characteristic length scale is undeformed

drop radius R, permittivity scale is ϵ_d, ion scale is n_0 and the electric field scale is $E_\mathrm{ref} = kT/zeR$. For the problems studied in this thesis - namely electrically-induced deformation, breakup, and coalescence of microfluidic drops - there is no external (imposed) velocity field. In the absence of an external forcing scale, the capillary thinning velocity ($V_\mathrm{cap} = R/\tau^V$) is an appropriate choice for the velocity scale (McKinley & Renardy, 2011), where τ^V is the viscocapillary time scale ($\tau^V = \mu R/\gamma$). This gives $V_\mathrm{ref} = \gamma/\mu_\mathrm{d}$.

All physical variables are non-dimensionalized to characterize the system,

$$x^* = \frac{x}{R};\ V^* = \frac{u}{V_\mathrm{ref}};\ \epsilon^* = \frac{\epsilon}{\epsilon_d};\ {n_\pm}^* = \frac{n_\pm}{n_0};\ E^* = \frac{E}{E_\mathrm{ref}}$$

The relevant non-dimensional numbers are:

$$\mathrm{Re} = \frac{\rho_\mathrm{d} V_\mathrm{ref} R}{\mu_\mathrm{d}};\ \mathrm{We} = \frac{\rho_\mathrm{d} V_\mathrm{ref}^2 R}{\gamma};\ \mathrm{Pe} = \frac{V_\mathrm{ref} R}{\bar{D}};\ \mathrm{B} = \frac{\rho_\mathrm{d} k^2 T^2 \epsilon_0 \epsilon_d}{2 z^2 e^2 \mu^2}$$

where Re is the Reynolds number, We the Weber number, Pe the Péclet number and B is a parameter that is fixed for a given liquid, in this case water, at a fixed temperature. The dimensionless equations governing the electrical field, the flow and ion concentration (after removing the '*') are:

$$\nabla \cdot \boldsymbol{u} = 0, \tag{3.40}$$

$$\frac{\partial \rho \boldsymbol{u}}{\partial t} + \nabla \cdot (\rho \boldsymbol{u}\boldsymbol{u}) = -\nabla p + \frac{1}{\mathrm{Re}} \nabla \cdot \boldsymbol{\tau}_V + \frac{1}{\mathrm{We}} \boldsymbol{F}_\mathrm{S} + \frac{2\,\mathrm{B}}{\mathrm{Re}^2} \boldsymbol{F}_\mathrm{E}, \tag{3.41}$$

$$\frac{\partial \phi n_\pm}{\partial t} + \nabla \cdot (\boldsymbol{u} \phi n_\pm) = \frac{1}{\mathrm{Pe}} \nabla \cdot (\phi \nabla n_\pm \mp \phi n_\pm \boldsymbol{E}), \tag{3.42}$$

$$\nabla \cdot (\epsilon \boldsymbol{E}) = \frac{1}{2} \kappa^2 q, \tag{3.43}$$

$$\frac{\partial \phi}{\partial t} + \nabla \cdot (\phi \boldsymbol{u}) = 0, \tag{3.44}$$

where $\boldsymbol{\tau}_V$ is the viscous stress tensor. $\boldsymbol{F}_\mathrm{S}$ and $\boldsymbol{F}_\mathrm{E}$ in Equation 3.41 are dimensionless forms of their counterparts in Equation 2.17 and Equation 3.10. Although κ (Equation 2.50) doesn't explicitly appear in any of the governing equations of the flow, it influences the flow via Equation 3.43 for the electrical potential ψ (recall that $\boldsymbol{E} = -\nabla\psi$). In summary, the governing equations are solved on a staggered, uniform mesh; fluid pressures, ion concentrations, and electric potentials are located at cell centers, while the velocity components are located at cell faces. The disperse phase volume fraction ϕ is located at the cell centers of a mesh that is twice as fine as the mesh used for all other variables.

The fluid properties (ρ, μ and ϵ) are functions of ϕ and are calculated on the fine mesh prior to being interpolated onto the coarser mesh.

3.3.2 Selection of appropriate electric force formation

In the final model equations listed above, the electric force term is represented by the divergence of the Maxwell electric stress tensor given by

$$\boldsymbol{F}_{\mathrm{E}} = \nabla \cdot \boldsymbol{\tau}_M = \nabla \cdot [\epsilon \boldsymbol{E}\boldsymbol{E} - \frac{1}{2}\epsilon(\boldsymbol{E} \cdot \boldsymbol{E})\boldsymbol{I}]. \tag{3.45}$$

An alternative formulation is the Maxwell body force, given by

$$\boldsymbol{F}_{\mathrm{E}} = \frac{1}{2}\kappa^2 q\boldsymbol{E} - \frac{1}{2}\boldsymbol{E} \cdot \boldsymbol{E}\nabla\epsilon. \tag{3.46}$$

The advantage of the Maxwell body force formulation (Equation 3.46) is that the two forces that contribute to the total electric force are represented as separate terms. The first term on the right-hand side of Equation 3.46 represents the contribution of the moving charge, referred to as *charge force* in this thesis. The second term represents the force resulting from the permittivity jump at the interface, referred to as *permittivity force* in this thesis. The difficulty with numerically implementing Equation 3.46, however, is that the jump in permittivities means that $\nabla\epsilon$ is discontinuous across the interface. Tomar *et al.* (2007) have shown that, the dielectric force term at the right hand side, $\boldsymbol{F}_{\mathrm{D}} = -(\boldsymbol{E} \cdot \boldsymbol{E}\nabla\epsilon)/2$, can be reformulated so as to make it continuous in a small region across the interface, analogous to the CSF approach discussed in § 3.2.5. To do this, they first rewrote the electric field in $\boldsymbol{F}_{\mathrm{D}}$ in terms of its normal and tangential components

$$\boldsymbol{F}_{\mathrm{D}} = \frac{1}{2}(-(\boldsymbol{E} \cdot \boldsymbol{n})^2\nabla\epsilon - (\boldsymbol{E} \cdot \boldsymbol{t})^2\nabla\epsilon). \tag{3.47}$$

Now multiplying and dividing the first term by ϵ^2 gives

$$\boldsymbol{F}_{\mathrm{D}} = \frac{1}{2}(-(\epsilon\boldsymbol{E} \cdot \boldsymbol{n})^2\ \nabla\epsilon\Big/\epsilon^2 - (\boldsymbol{E} \cdot \boldsymbol{t})^2\nabla\epsilon). \tag{3.48}$$

Equation 3.48 can now be rewritten as

$$\boldsymbol{F}_{\mathrm{D}} = \frac{1}{2}\left(- (\epsilon\boldsymbol{E} \cdot \boldsymbol{n})^2\nabla\left(\frac{1}{\epsilon}\right) - (\boldsymbol{E} \cdot \boldsymbol{t})^2\nabla\epsilon\right). \tag{3.49}$$

Equation 3.49 can be easily recast as an interfacial force in the limit of a infinitesimally small transition region

$$\boldsymbol{F}_{\mathrm{D}} = -\frac{1}{2}(\epsilon_1 - \epsilon_2)(\frac{(\epsilon\boldsymbol{E} \cdot \boldsymbol{n})^2}{\epsilon_1\epsilon_2} + (\boldsymbol{E} \cdot \boldsymbol{t})^2)\delta(r)\boldsymbol{n}. \tag{3.50}$$

In the absence of the free charge term, the surface force formulation (Equation 3.50) is only valid at the perfect dielectric and leaky dielectric limits. When ions are present, as is the case in an electrokinetic model, the resultant volume force is not continuous across the interface. However, López-Herrera *et al.* (2011) have shown that this model is quite accurate at the perfect dielectric limit. If the free charge term is included, Equation 3.50 becomes

$$\boldsymbol{F}_{\mathrm{E}} = \frac{1}{2}\kappa^2 q\boldsymbol{E} - \frac{1}{2}(\epsilon_1 - \epsilon_2)\left(\frac{(\epsilon\boldsymbol{E}\centerdot\boldsymbol{n})^2}{\epsilon_1\epsilon_2} + (\boldsymbol{E}\centerdot\boldsymbol{t})^2\right)\delta(r)\boldsymbol{n}. \tag{3.51}$$

Equation 3.51 is defined in this thesis as the Body Force (BF) approach, in contrast with the complete divergence stress tensor formulation (CDS) of Equation 3.45. In addition to the two formulations described, a third formulation for the electric force was defined by Davidson *et al.* (2016), which is a slight modification of CDS. The second term inside the bracket in Equation 3.45 is omitted altogether to yield

$$\boldsymbol{F}_{\mathrm{E}} = \nabla\centerdot[\epsilon\boldsymbol{E}\boldsymbol{E}]. \tag{3.52}$$

The missing term in Equation 3.52 is absorbed into the pressure gradient, resulting in a modified pressure term which incorporates part of the electrical force. This is referred to as Modified Pressure Divergence of Stress (MPDS). As the electric force and the pressure calculations are calculated in different parts of the code using different algorithms, this small change in the formulation results in a significant change in the numerical implementation of the electrical force. The goal of this section is to compare and contrast the three approaches, and conclude with showing why the CDS formulation is used in the rest of this thesis

3.3.3 Model validation problem

The problem used to validate the choice of electric force formulation is shown in Figure 3.5a. A drop is suspended in a continuous phase of infinite dimension, and acted upon by an electric field, which deforms it over time (Figure 3.5b). In § 3.3.4, the drop is assumed to be dielectric (only permittivity force), in § 3.3.5 the drop is assumed to be conducting (both permittivity and charge forces), and in § 3.3.6 the drop is assumed to be conducting with unity permittivity ratio (only charge force).

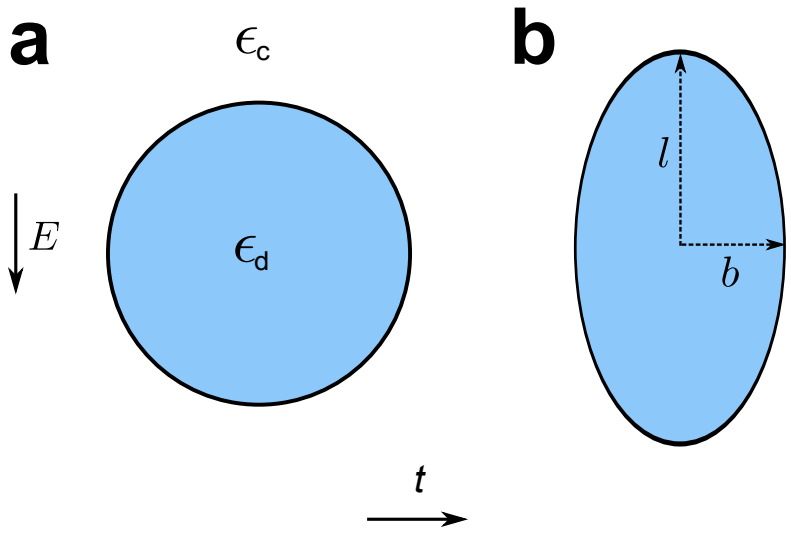

Figure 3.5: (a) Schematic of a drop with permittivity ϵ_d suspended in another immiscible liquid (oil) with permittivity ϵ_c of infinite dimension. An external electric field is applied in the vertical direction. (b) Schematic of drop post deformation under the action of the electric field. l and b are the semi-major and semi-minor axes of the ellipse formed.

3.3.4 Perfect dielectric drop results

The Minimum Energy Model (MEM) of Garton & Krasucki (1964), applicable only to drops without charge, is used for comparison with equilibrium drop deformation at the perfect dielectric limit. The MEM assumes that the drop takes on an ellipsoidal prolate shape, aligned with the electric field, with major and minor axes l and b, respectively (Figure 3.5b). The electric energy deforming the drop, and the surface energy opposing the deformation for this assumed shape, are calculated analytically. The drop is then assumed to take a shape that minimizes the sum of the energies yielding an equilibrium axial ratio $\Gamma = l/b$. The rescaled expression to solve for Γ is,

$$2\pi\left(\frac{(\Gamma+\frac{2}{\Gamma}+(\Gamma^2-4)\,(\vartheta/\sin(\vartheta))}{3(\Gamma^2-1)(\Gamma^{2/3})}+\frac{\xi(\Gamma)\,\mathrm{Ca_E}}{3}\left(\left(\frac{1}{1-\bar{\epsilon}}\right)-\left(\frac{\sqrt{\Gamma^2-1}(\Gamma-1)}{\Gamma\cos^{-1}(\Gamma)-\sqrt{\Gamma^2-1}}\right)^2\right)\right)=0, \tag{3.53}$$

where,

$$\xi(\Gamma) = \frac{3\Gamma\sqrt{\Gamma^2-1} - \cos^{-1}(\Gamma)(2\Gamma^2+1)}{(\Gamma^2-1)^{5/2}}, \tag{3.54}$$

$$\vartheta = \cos^{-1}(1/\Gamma). \tag{3.55}$$

In this subsection, the three formulations are compared to the MEM for cases where charge is absent and the only force deforming the drop is the electrical stress caused by the permittivity jump at the drop interface (permittivity force). For completeness, these comparisons are performed for different values of electric field, permittivity ratio, and mesh resolutions.

Small deformations

	Ca_E= 0.10	|Error%|(1.04)	Ca_E= 0.15	|Error%|(1.06)
BF (N/R = 16)	1.020	1.92	1.044	1.51
BF (N/R = 32)	1.026	1.35	1.044	1.51
CDS (N/R = 16)	1.021	1.83	1.039	1.98
CDS (N/R = 32)	1.022	1.73	1.045	1.42
MPDS (N/R = 16)	1.020	1.92	1.040	1.89
MPDS (N/R = 32)	1.022	1.73	1.043	1.60

Table 3.1: Drop axial ratio (Γ) comparison for $\bar{\epsilon} = 5$ and $Ca_E = 0.10$, 0.15 for all three formulations. The analytical result is listed in brackets next to '|Error%|'.

Berry *et al.* (2013) compared the predictions of the BF and CDS approaches with Taylor's analytical (leaky dielectric) model for very small deformations. They found that, while the approaches yielded identical results at low mesh resolutions, the CDS formulation was far more accurate at higher mesh resolutions. One of the early goals

of this work was to extend this validation to larger deformations. Table 3.1 lists equilibrium Γ values for all three formulations at low permittivity at electric field values ($\bar{\epsilon} = \epsilon_d/\epsilon_c = 5$ and $Ca_E = 0.10$ and 0.15). The predictions of the MEM (against which the comparisons are made) is provided in brackets next to '|Error%|'. There is little to separate the three formulations at the small-deformation limit, as error magnitudes are negligible and decrease at higher resolution, indicating that the correct solution is possibly being approached by all formulations.

	Ca_E= 0.05	|Error%|(1.06)	Ca_E= 0.10	|Error%|(1.13)
BF (N/R = 16)	1.074	1.32	1.362	20.53
BF (N/R = 32)	1.094	3.20	1.357	20.09
CDS (N/R = 16)	1.039	1.98	1.096	3.01
CDS (N/R = 32)	1.039	1.98	1.099	2.74
MPDS (N/R = 16)	1.039	1.98	1.093	3.27
MPDS (N/R = 32)	1.039	1.98	1.101	2.57

Table 3.2: Drop axial ratio (Γ) comparison for $\bar{\epsilon} = 50$ and $Ca_E = 0.05$, 0.10 for all three formulations. The analytical result is listed in brackets next to '|Error%|'.

Table 3.2 lists Γ values for all three models, at small Ca_E and a higher permittivity ratio of $\bar{\epsilon} = 50$. While the models are inseparable at $Ca_E = 0.05$, this is no longer true at $Ca_E = 0.10$. The predictions of BF starts diverging significantly from MPDS and CDS. This is presumably because the reformulation of the dielectric term as a surface force (Equation 3.47-Equation 3.50) results in inaccuracies when the gradient in permittivites across the interface is higher.

	Ca_E= 0.15	|Error%|(1.22)	Ca_E= 0.20	|Error%|(1.38)
BF (N/R = 16)	17.09	1300.82	7.658	454.93
BF (N/R = 32)	7.713	532.21	5.486	297.54
CDS (N/R = 16)	1.177	3.52	1.286	6.81
CDS (N/R = 32)	1.179	3.36	1.289	6.59
MPDS (N/R = 16)	1.177	3.52	1.295	6.16
MPDS (N/R = 32)	1.179	3.36	1.295	6.16

Table 3.3: Drop axial ratio (Γ) comparison for $\bar{\epsilon} = 50$ and $Ca_E = 0.15$, 0.20 for all three formulations. The analytical result is listed in brackets next to '|Error%|'.

Large deformations

In this section, larger equilibrium deformations ($\Gamma > 1.2$) are considered, for $\bar{\epsilon} = 5$ and $\bar{\epsilon} = 50$. Table 3.3 lists Γ $Ca_E = 0.15$ and 0.20 for $\bar{\epsilon} = 50$. It is clear that the BF predictions are wildly inaccurate. While they improve with resolution, the errors involved are too large for the BF to be a viable option. Additional tests (not listed here) showed that BF does poorly on any Ca_E greater than 0.05 when the permittivity ratio was $\bar{\epsilon} = 50$. As a result, BF predictions are excluded from subsequent tables. MPDS is slightly more accurate than CDS in both Table 3.2 and Table 3.3, but the differences are marginal.

Table 3.4 lists Γ comparisons (for just MPDS and CDS) for a lower permittivity ratio ($\bar{\epsilon}$) but higher electric fields ($Ca_E = 0.5$, 1.0). As earlier, the differences are marginal at best. Table 3.5 lists Γ comparisons (for just MPDS and CDS) very high electric fields ($Ca_E = 5.0$, 10.0). The results in Table 3.4 and Table 3.5 show that MPDS is slightly more accurate when directly compared to CDS directly. At $Ca_E = 10.0$ in Table 5, MPDS result for $N/R = 16$ is identical to the CDS result when $N/R = 32$. The MEM comparisons show that the BF formulation does poorly at low deformations for the higher

	Ca_E= 0.5	|Error%|(1.25)	Ca_E= 1.0	|Error%|(1.69)
CDS (N/R = 16)	1.191	4.72	1.535	9.17
CDS (N/R = 32)	1.209	3.28	1.579	6.57
MPDS (N/R = 16)	1.195	4.40	1.527	9.65
MPDS (N/R = 32)	1.209	3.28	1.583	6.33

Table 3.4: Drop axial ratio (Γ) comparison for $\bar{\epsilon} = 5$ and $Ca_E = 0.5$, 1.0 for all three formulations. The analytical result is listed in brackets next to '|Error%|'.

	Ca_E= 5.0	|Error%|(7.47)	Ca_E= 10.0	|Error%|(13.35)
CDS (N/R = 16)	6.298	15.69	11.50	13.85
CDS (N/R = 32)	6.770	9.37	12.15	8.99
MPDS (N/R = 16)	6.298	15.69	12.16	8.91
MPDS (N/R = 32)	6.836	8.49	12.89	3.45

Table 3.5: Drop axial ratio (Γ) comparison for $\bar{\epsilon} = 5$ and $Ca_E = 5$, 10.0 for all three formulations. The analytical result is listed in brackets next to '|Error%|'.

permittivity ratio used and the performance gets poorer the higher the Ca_E employed. It is only reasonably accurate for the small deformation limit. This implies that the surface force formulation is inaccurate compared to either of the divergence of stress formulations. Therefore, the BF formulation is not a viable option for the problems studied in this thesis.

3.3.5 Conducting drop results

It was concluded, after comparisons with MEM, that both the CDS and MPDS yielded essentially identical results. Now, all results considered so far have been for stable drops, i.e. with an equilibrium Γ value. However, when the electric field is increased, the drop becomes unstable, and ejects 'progeny' droplets from both ends. For unstable conducting drops, the predictions of these models starts diverging qualitatively, even if there is quantitative agreement. For example, a comparison of the two models for $\kappa = 5$ and $Ca_E = 0.30$ is shown in Figure 3.6. Figure 3.6a tracks the transient deformation parameter D (There is no equilibrium value as the drops will eventually break up). Consistent with earlier results, the deformation of the drops, as measured by D, is identical. However, a visual inspection of the drop shapes yields differences. The CDS case seems to form a bulge at the tip, while the MPDS case displays a parabolic profile. While this may seem like a minor difference, the shape of the drop prior to breakup significantly impacts the drop shape at breakup, which in turn determines the quantitative measurements of the progeny droplets ejected. As accurate measurement of progeny droplet properties is one of the goals of this thesis, determining which formulation produces the correct drop tip-shape is important.

3.3.6 Comparison of all three formulations with $\bar{\epsilon} = 1$

As there exist no analytical or experimental results involving microfluidic conducting drops with mobile ions, the only means of determining the appropriate model amongst CDS and MPDS is via comparison with the BF model. Now this might seem odd given the BF was shown to be extremely inaccurate outside of small deformation and small Ca_E regimes for non unity permittivity ratios. However, this results from errors in the surface force term in the BF formulation, which can be bypassed entirely by setting the permittivity ratio to 1. The complicated dielectric force term in BF is therefore set to zero as the gradient of permittivity across the interface is zero, and the formulation

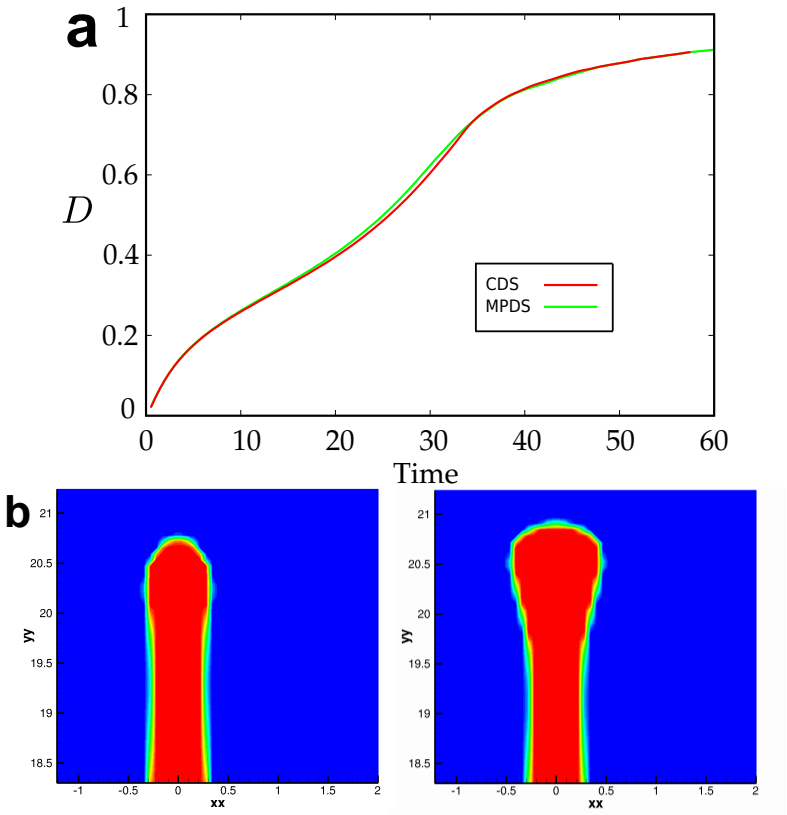

Figure 3.6: (a) Comparison of transient deformation of CDS and MPDS for $\kappa = 5$ and $\mathrm{Ca_E} = 0.30$ and (b) Visual comparison of tip shape before drop breakup.

simplifies to just the charge term (Equation 3.51). The predictions of this reduced BF is likely to be very accurate as it is the simplest of the three formulations (MPDS and CDS should give the same result in theory but the formulations themselves don't simplify as the contributions of the charge and permittivity are not explicitly provided).

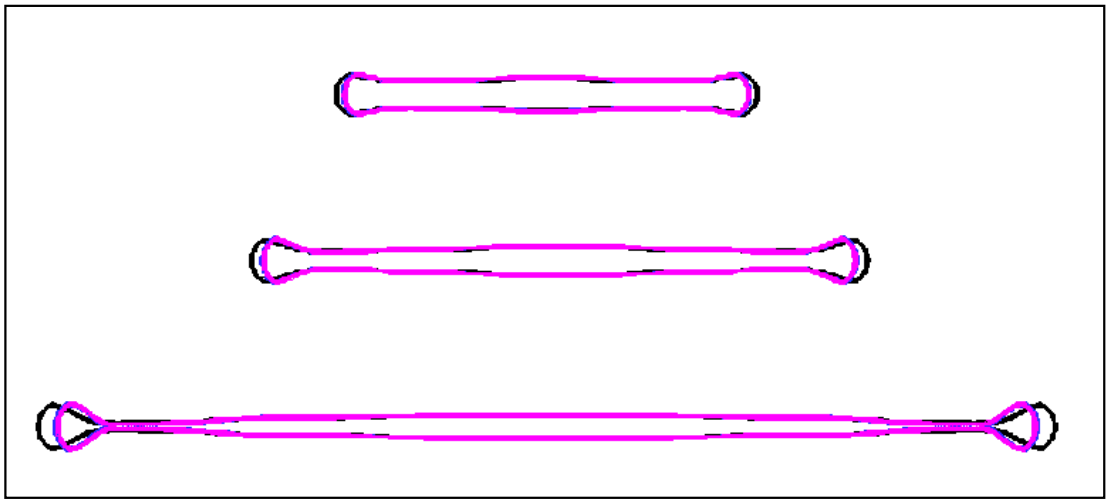

Figure 3.7: Comparison of drop shapes for all three formulations. The parameters are $\bar{\epsilon} = 1$, $\kappa = 25$ and $\mathrm{Ca_E} = 1.0$. Outline of BF is shown in blue, CDS in magenta and MPDS in black. The times are $t^* = 20$, $t^* = 25$ and $t^* = 30$ respectively

Figure 3.7 compares all three formulations for$\bar{\epsilon} = 1$, $\kappa = 25$ and $\mathrm{Ca_E} = 1.0$, at different snap shots in time as the drop breaks up. Even as early as in the first image when the neck of the lobe is beginning to differentiate from the body of the drop, the contours of MPDS case (black) are distinct from those of BF (blue) and CDS (magenta). This result is a validation for the charge based force term in the CDS routine, because the BF formulation is entirely different, yet provides near identical results. The progression of time shown in the two images under it shows further divergence between MPDS on the one hand, and CDS and BF on the other. In addition, the bulging of the tips is observed for both BF and CDS cases, and is absent only for MPDS. This confirms that the CDS formulation is probably the most accurate model for drop deformation among the three alternatives considered in this chapter.

A final check was undertaken to eliminate the possibility that the bulge seen at the

CDS tip results from grid influenced flattening. A simple way to test the impact of grid lines was to change the orientation of the electric field in such a way that it was no longer parallel to grid lines, but was instead at an angle of 45°. Figure 3.8 shows that the angle of orientation has no impact on deformation of drop and $D = 0.86$ in both cases. This shows that the drop shape is independent of grid structure. Consequently, the CDS formulation for electric force is used throughout this thesis.

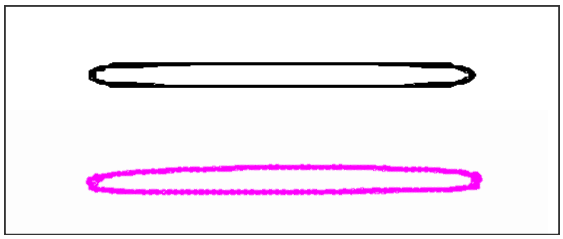

Figure 3.8: The steady state deformation for drop with parameters $\mathrm{Ca_E} = 1.0, \bar{\epsilon} = 50, \kappa = 0$. The black contour is for the regular drop and the magenta contour is from the drop subjected to an electric field at 45^o to the vertical. The equilibrium deformation ($D = 0.86$) is identical for both drops

3.4 Summary

This chapter started by providing a comprehensive review of the model equations, complete with underlying assumptions. Then, the numerical implementation is discussed, starting with an overview of the FGVT model developed by Rudman (1998). The two relevant modifications made to this model are the implementation of a CLSVoF method for tracking the interface (Harvie *et al.*, 2008*b*), and the addition of electrokinetic effects (Berry *et al.*, 2013). Both modifications are discussed in detail, and the key aspects of the ion transport algorithm are highlighted. Finally, the model equations are listed, and the process of choosing an appropriate electric force formulation from the three alternatives in the literature is described. The next chapter forms the first results chapter of this thesis, and studies the deformation and breakup of an isolated microfluidic drop in an electric field.

4 Isolated Drop: Deformation and Breakup

How water has tenacity in itself and cohesion between its particles. This is seen in the process of a drop becoming detached from the remainder, this remainder being stretched out as far as it can through the weight of the drop which is extending it; and after the drop has been severed from this mass the mass returns upwards with a movement contrary to the nature of heavy things.

LEONARDO DA VINCI[a]

[a]This is the first known description of what would come to be known as the Rayleigh-Savart instability that underpins all drop pinch-off phenomena

This is the first of two chapters studying the effect of an electric field on an isolated, conducting microdrop of electrolyte, suspended in non-conducting oil. This chapter characterises the drop deformation and breakup phenomena for applications where progeny droplet formation is undesirable; the focus is therefore on understanding the breakup process and providing a framework to predict when it occurs. This chapter starts by describing the importance of the problem studied and outlining the numerical setup (§ 4.1). Then, using the perfect dielectric approach, comparisons with past analytical and numerical results are presented (§ 4.2). The electrokinetic model is then used in the three subsequent sections: First the deformation behaviour of conducting drops is studied (§ 4.3), then a phase diagram of drop stability is compiled from results of multiple simulations (§ 4.4), and finally a comparison of the contribution of the dielectric and electrokinetic effects to the breakup process is investigated (§ 4.5). The chapter then concludes with a summary of the results and motivation for the slightly different focus of the next chapter of this thesis. (§ 4.6).

*This chapter is based on the author's paper R. Pillai, J. D. Berry, D. J. E. Harvie and M. R. Davidson, 'Electrolytic Drops in an Electric Field: A Numerical Study of Drop Deformation and Breakup', *Physical Review E*, 2015, 92, 013007

4.1 Relevance of problem

As discussed in chapter 2, the deformation and breakup of a conducting drop, suspended in a dielectric medium and subjected to an electric field, is a classical problem in electrohydrodynamics with a rich literature dating back to the late 19th century. Two modern examples are the use of electrically enhanced coalescence to separate water in oil emulsions (Eow & Ghadiri, 2002) and the role of water drops in dielectric breakdowns which has relevance to electrical power production (Dubash, 2007). The common numerical approach used to study these problems, called the *leaky dielectric* model, assumes that charge relaxation onto the interface is rapid, the Debye screening length is very small, and the electric field strength is sufficiently high for diffusive fluxes of ions to be negligible compared to conductive fluxes (Saville, 1997; Baygents & Saville, 1990). While the leaky dielectric approach yields excellent results at macroscales, electrically induced drop deformation is now mainly being studied at much smaller length scales (Teh *et al.*, 2008; Theberge *et al.*, 2010), where the underlying assumptions of the leaky dielectric model break down. The ratio of the width of the space charge regions to the drop radius increases and, consequently, diffusive fluxes gain importance at these scales (Theberge *et al.*, 2010). These facts taken together imply that diffuse ion layers are likely to evolve in microfluidic drops. In fact, concentration polarization (Mani *et al.*, 2009; Zangle *et al.*, 2009) and charge polarization (Berry *et al.*, 2011*b*) do occur in microfluidic devices and such variation in ion concentration can change the flow characteristics, including direction (García-Sánchez *et al.*, 2009), indicating that the physics of microscale flows are more sensitive to variations in local ionic concentrations (i.e. local conductivity) than macroscale flows.

Therefore, for microfluidic applications, the presence of charge carriers cannot be ignored as they contribute significantly to the drop physics, and the electrokinetic model detailed in chapter 3 is necessary. The history of electrokinetic studies of drops is quite short; the earliest work was an analytical formulation developed by Zholkovskij *et al.* (2002) for small drop deformations, employing a weak field approximation. López-Herrera *et al.* (2011) developed a numerical model to include spatially varying charge and conductivity using the Volume-of-Fluid (VoF) method. This model did not account for individual charge carriers which meant that the conductivity distribution had to be specified (They have since updated their model to include mobile charge effects (López-Herrera *et al.*, 2015)). In this and the subsequent chapters, the electrokinetic model of Berry *et al.* (2013)

is used to characterize the deformation and breakup behaviour of an isolated, conducting, initially spherical drop of electrolyte, suspended in an insulating oil phase, and subjected to an electric field. The model has previously been validated for small deformations (Berry, J. D., Davidson, M. R., & Harvie, 2012). Here the model predictions, at large deformations, are compared to analytical and numerical models commonly used in the literature.

4.1.1 Problem setup

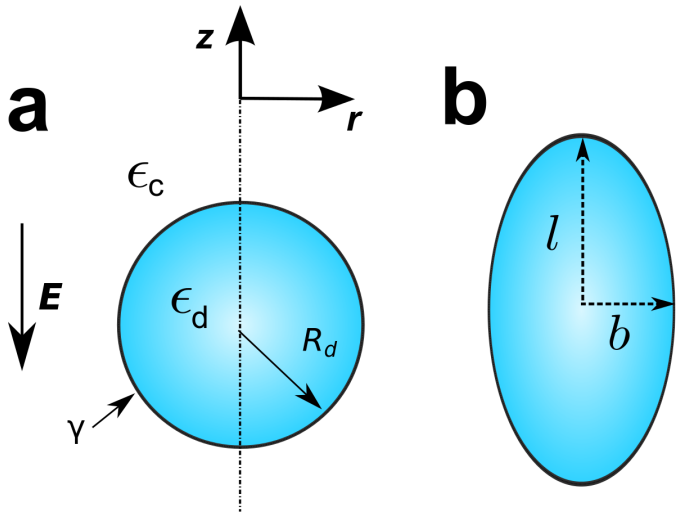

Figure 4.1: (a) Schematic of an electrolytic drop (with imposed axisymmetry and symmetry boundary conditions applied on the vertical centerline) suspended in another immiscible liquid (oil) of infinite dimension. An external electric field is applied parallel to the z direction. (b) Schematic of drop post deformation under the action of the electric field. l and b are the semi-major and semi-minor axes of the ellipse formed.

Figure 4.1 illustrates the problem analyzed in this chapter. An axisymmetric drop of undeformed radius R is considered, with permittivity ϵ_d (subscripts d and c are used to denote disperse and continuous phase properties respectively). The initial drop ion concentration, given by the geometric mean of the species ion concentrations ($n_0 = \sqrt{n_+ n_-}$) (Biscombe *et al.*, 2012), is uniform everywhere. n_0 is the bulk ion concentration in the drop before the electric field is activated. The drop is suspended in a dielectric medium of permittivity ϵ_c. The interface between the drop and continuous phase is assumed to have

a constant interfacial tension γ. To simplify the problem, the drop and continuous phase are assumed to have equal viscosity ($\mu_c = \mu_\mathrm{d}$) and density ($\rho_\mathrm{c} = \rho_\mathrm{d}$). The interfacial tension at the water-oil interface is assumed here to be 10^{-3} N/m.

The drop is assumed to be spherical initially, with its center located at the middle of a parallel-plate capacitor with a separation distance of $30R$. As the drop is electrically neutral, the axial electric field is set up to be equal (E^*_∞) at the top and bottom boundaries to satisfy Gauss' law in the domain. Zero normal field conditions are specified on the side boundaries. This corresponds to a uniform external field $\boldsymbol{E^*}$ parallel to the z axial direction at large distances from the drop. The drop is assumed to be symmetrical along the vertical centerline (as shown in Figure 4.1), and the calculations are performed in cylindrical polar coordinates. The width of the domain in the radial direction is $4R$, consistent with other studies (Hua *et al.*, 2008), to minimize boundary effects.

Two important dimensionless quantities for the discussion in this chapter are the dimensionless charge density (q) and the inverse dimensionless Debye length (κ), given as

$$q = n_+ - n_-, \tag{4.1}$$

$$\kappa = \sqrt{\frac{2z^2e^2n_0R^2}{\epsilon_0\epsilon_\mathrm{d}k_\mathrm{B}T}}. \tag{4.2}$$

As elaborated on in chapter 2, the strength of the electric field can be represented by the electric capillary number ($\mathrm{Ca_E}$),

$$\mathrm{Ca_E} = \frac{\epsilon_0\epsilon_\mathrm{c}R}{\gamma}E^{*2}_\infty. \tag{4.3}$$

The Ohnesorge number ($\mathrm{Oh} = \sqrt{\mathrm{We}}\big/\,\mathrm{Re} = \mu_\mathrm{d}/\sqrt{\rho_\mathrm{d}R_d\gamma}$), which is typically fixed for a given experiment, is also taken to be unity. This would occur, for example, for a drop of radius 1μm (typical for microfluidic devices), drop viscosity 10^{-3} Pa.s, drop density 10^3 kg/m^3 and interfacial tension 1 mN/m. Together $\mathrm{Oh} = \mathrm{Ca} = 1$ gives $\mathrm{Re} = \mathrm{We} = 1$ for all simulations conducted. The Péclet number (Pe) is taken to be 1000 for all simulations, a typical value for a water drop for the choice of Re. The permittivity of the electrolyte is greater than the surrounding oil ($\epsilon_\mathrm{d} > \epsilon_\mathrm{c}$).

Grid refinement showed that a mesh resolution of 16 cells per drop radius (R) was sufficient for the accurate prediction of the temporal and spatial variation of charge accumulation, electric force and electric field for all the parameters considered. However,

32 cells per R was necessary to accurately predict the drop shape, and it is this grid resolution that is used for all simulations described here. Initially, the ions are uniformly distributed in the drop in equal numbers ($n_+ = n_- = 1$). As seen on the right hand side of equation (3.42), the external electric field conducts the ion species in opposite directions. This results in the formation of regions of depletion of one ion species relative to the other, i.e. regions of charge. When the drop develops local nonzero free charge density (q), there are two electric forces deforming the drop. The first is the normal electric force formed at the interface due to the jump in permittivities from the drop phase to the continuous phase (opposed principally by the interfacial tension force) referred to in this work as the 'permittivity force'. The second is the force due to the formation of free charge in the drop referred to as the 'charge force'.

Though the electric force acting on the drop has been formulated using the Maxwell stress tensor (Equation 3.45), it can also be alternatively represented by the Maxwell electric force formulation,

$$\boldsymbol{F}_{\mathrm{E}} = -\frac{1}{2}\boldsymbol{E}\cdot\boldsymbol{E}\nabla\epsilon + \frac{1}{2}\kappa^2 q\boldsymbol{E}. \tag{4.4}$$

This formulation has the advantage of dividing the permittivity force and charge force (first and second terms on RHS of Equation 4.4, respectively) into separate terms, and can be used to reconstitute the approximate magnitude of the charge force inside the drop from the total force calculated, by integrating the second term on the right hand side of Equation 4.4 over the top (or bottom) half of the domain (note: $q = 0$ outside the drop). The permittivity force is then obtained by subtracting the charge force from the total force that is calculated by integrating Equation 3.45.

4.1.2 Characteristics of an electrokinetic model

It is important to remember that κ is also associated with the average concentration of ions inside the drop. For a fixed geometry and physical parameters, an increase in κ translates to an increase in the number density of ions inside the drop (n_0). In this thesis, κ can be considered as a dimensionless ion concentration as this lends itself to discussion of charge behaviour inside the drop, which is the goal of this work. The model used in this thesis has been previously validated for small deformations, by comparing against the perfect dielectric limit solution of O'Konski & Thatcher Jr (1953), and the leaky dielectric limit solution of Taylor (1964). As expected, the drop behaves like a perfect dielectric at low κ, and a leaky-dielectric model at high κ, as seen in Figure 4.2.

Note that the deformation of the drop is characterized by the deformation parameter D, defined as

$$D = \frac{l - b}{l + b}, \tag{4.5}$$

and the equilibrium deformation for a subcritical drop is given by D_∞.

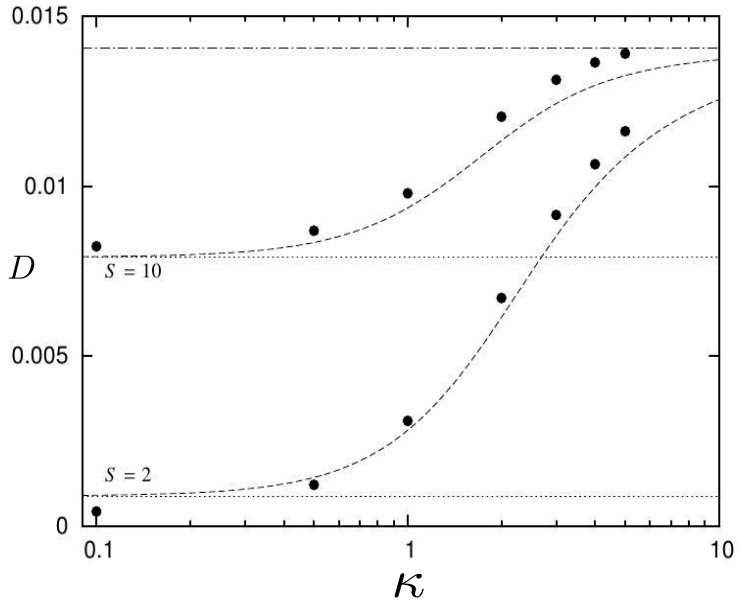

Figure 4.2: Taylor deformation parameter D_∞ as a function of dimensionless disperse inverse Debye length κ for a conducting drop in a perfect dielectric liquid, with viscosity ratio $\bar{\mu} = 1$ and electric capillary number $\mathrm{Ca_E} = 0.025$. The mesh density $N/R = 32$, Reynolds number $\mathrm{Re} = 0.1$, Weber number $\mathrm{We} = 0.1$, Peclet number $\mathrm{Pe} = 1$, and the electric body force is calculated using the complete divergence of stress implementation. The small $\mathrm{Ca_E}$ analytical solution of Zholkovskij *et al.* (2002) is given by the dashed line, and the results of the numerical simulations are given by the symbols. The dotted lines represent the perfect dielectric limit solution of O'Konski & Thatcher Jr (1953), and the dash-dotted line represents the leaky dielectric limit solution for an infinitely conducting drop of Taylor (1964). Reproduced from Berry *et al.* (2013).

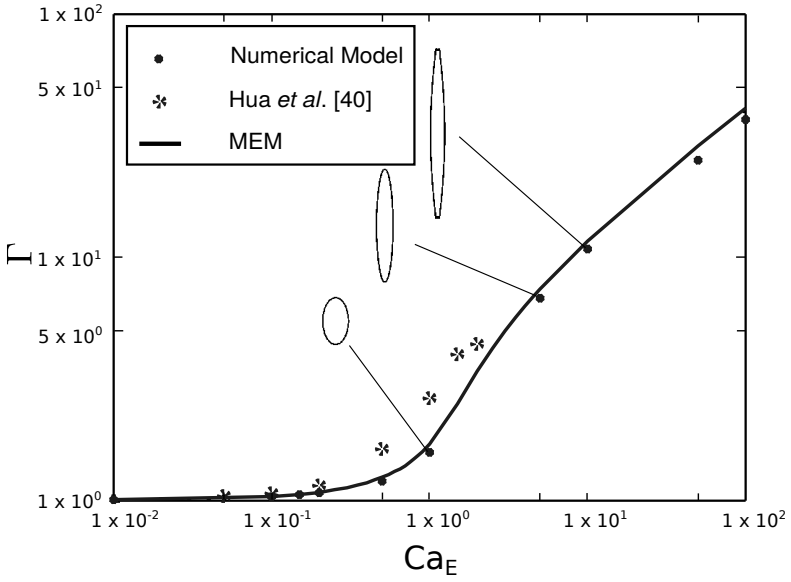

(a)

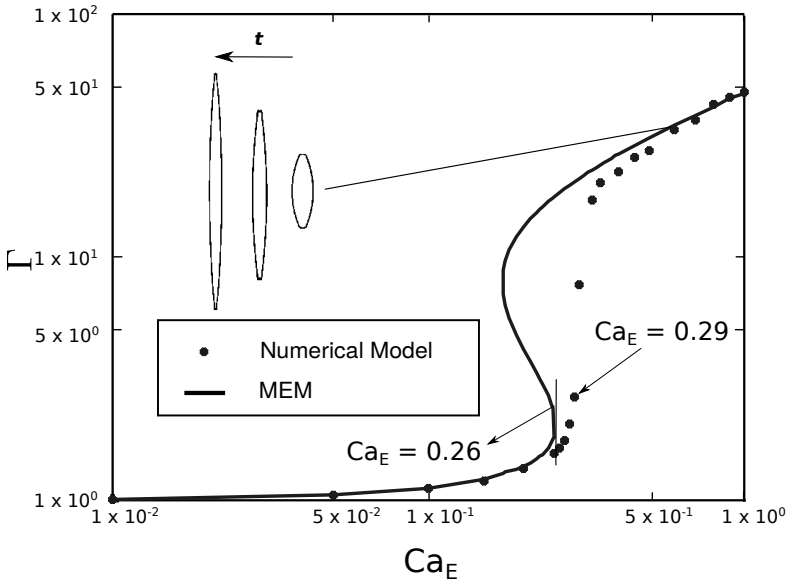

(b)

Figure 4.3: Comparison of axial ratio ($\Gamma = l/b$) predictions for this model (shown as black dots) with the Minimum Energy Model (Garton & Krasucki, 1964) for (a) $\bar{\epsilon} = 5$ and (b) $\bar{\epsilon} = 50$, for a range of $\mathrm{Ca_E}$. Results of Hua *et al.* (2008) are shown as black snowflakes.

4.2 Perfect dielectric drop behaviour

The model predictions are compared to the Minimum Energy Model for both low ($\bar{\epsilon} = 5$) and high ($\bar{\epsilon} = 50$) permittivity ratios, where $\bar{\epsilon} = \epsilon_d/\epsilon_c$. The MEM was originally developed for small deformations, but was found to give reasonable predictions for large deformations as well (Sherwood, 1988). An alternative, at the large deformation limit, is the slender body theory (Sherwood, 1999; Rhodes & Yariv, 2010; Dubash & Mestel, 2007*b*), which is not employed here. Figure 4.3a shows that the numerical model predictions for $\bar{\epsilon} = 5$ agree well with those of the MEM. In comparison, Hua *et al.* (2008)'s predictions, obtained employing VoF along with front tracking, are larger than both our simulations and the MEM results. Deviation from MEM predicted deformations (l/b) tend to occur when the drop shape is no longer ellipsoidal as that is a key assumption behind MEM (Dubash, 2007). The deviations observed at high ($Ca_E \geq 10$) values of applied electric field coincide with deformed drops having pointed tips, making them less ellipsoidal. This can be seen in the embedded drop deformation contours, which show the drop profile when steady state is reached at three values of Ca_E; $Ca_E = 1.0$, $Ca_E = 5.0$ and $Ca_E = 10.0$.

For the higher permittivity ratio selected ($\bar{\epsilon} = 50$), the behaviour of the MEM is somewhat different. When the permittivity ratio exceeds a critical value ($\bar{\epsilon} = 20.8$) (Sherwood, 1988), the MEM solution is no longer single valued as seen in figure 4.3b. Our large deformation simulations predict a sudden jump from a lower deformation trajectory to a higher one at around $Ca_E = 0.29$, compared to the MEM's predicted value of $Ca_E = 0.26$. A subcritical case from the higher branch would jump downward back to the lower branch, if the Ca_E was decreased. Multiple equilibria were not predicted by our simulations, i.e. irrespective of the starting point, the final deformed shapes could be plotted on one unique path, unlike the MEM which shows multiple possible solutions at certain values of Ca_E. This suggests that the hysteresis loop predicted by the MEM model is not present once the ellipsoidal drop shape assumption ceases to be valid. Note that, unlike the low permittivity case, there is no deviation from MEM at high Ca_E. A sample of the drop evolution and final shape for $Ca_E = 0.70$ are embedded in figure 4.3b.

Importantly, in all the cases studied, drop breakup was never predicted. This is in contrast with a study that predicts 'tip-streaming' - or jet-like shedding of droplets from the tip - for $\bar{\epsilon} = 50$ when $Ca_E \geq 0.33$ (Paknemat *et al.*, 2012). Those authors used the

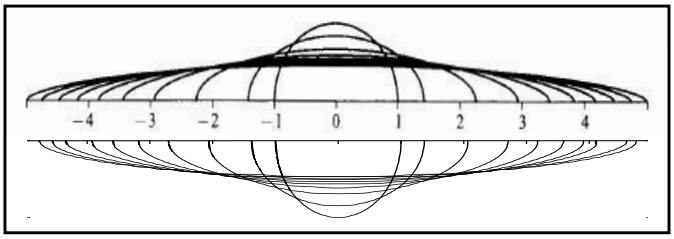

Figure 4.4: Composite equilibrium drop shapes for values of Ca_E from 1.0-9.0. Included results are Sherwood (1988) (top, reproduced with permission from Cambridge Press) and this model (bottom).

MEM curve in Garton & Krasucki (1964) to claim that no solutions exist beyond a critical Ca_E. But Garton & Krasucki (1964) only plotted values up to $l/b = 4$ at which point the high gradient means that the curve appears almost vertical, which would imply that no further solutions exist. However, as seen here, the MEM curve can be extended and a second branch is obtained at a higher value of Ca_E. Rather than a critical Ca_E for breakup, there exists a critical $Ca_E = 0.29$, beyond which a small increase in Ca_E results in a large increase in the predicted drop deformation, and this jump has been replicated by our model. Collins *et al.* (2013) suggest that tip-streaming is not possible in the absence of tangential stresses, as is the case in perfect dielectric drops, since the mechanism of tip-streaming require the presence of tangential electric stresses near the tip of the developing Taylor cone. These tangential stresses transfer the momentum inside the drop which destabilizes it. In the case of dielectric drops, the curvature of the tip is predicted to keep increasing as Ca_E is increased without droplets being ejected, consistent with our predictions.

The difficulty in comparing our method against studies which employ the infinitely thin layer of charge assumption is that $\kappa \to \infty$ cannot be replicated in our model as the κ parameter must have a finite value. If κ gets too large, the steep gradients of ion concentration that form at the drop interface cannot be resolved numerically. Hence the model predictions were compared, again for the perfect dielectric case, to the drop contours provided by Sherwood (1988), calculated using the Boundary Integral Method (BIM). The contours are for steady state deformation shapes, with increasing electric fields ($Ca_E = 1.0 - 9.0$) for $\bar{\epsilon} = 5$. The contours compare well with those calculated using this model, as shown in Figure 4.4. The model under predicts the deformation slightly at the higher values of Ca_E, which may be attributed to the fact that the BIM, which

only solves on the drop interface, can predict drop shape more accurately in regions of high curvature than models that solve the complete flow equations inside and outside the drop.

4.3 Conducting drop behaviour

Results are presented now for a microfluidic water drop immersed in oil of equal viscosity and density. The electric capillary number, representing electric field strength, is varied within $0.20 \leq \mathrm{Ca_E} \leq 0.30$ and the inverse dimensionless Debye length (κ), representing drop ion concentration, is varied between 1 and 10, which produces diffuse regions of charge under the influence of the electric field. A permittivity ratio of $\bar{\epsilon} = 50$, based on representative values for a water-in-oil system ($\epsilon_\mathrm{d} = 80$, $\epsilon_\mathrm{c} = 1.6$), is used for all the cases. When $\bar{\epsilon} \geq 1$, the drop always deforms prolately in the absence of ions. When ions are present inside the drop, both species are initially distributed equally and uniformly, ensuring electrical neutrality. However, the electric field imparts equal but opposite conductive fluxes to each species which results in anions migrating to one end of the drop and cations to the other. Depletion of either ion species from an initially neutral region leads to the formation of regions of charge (q) inside the drop. As the ions travel towards opposite ends of the drop, the regions of charge first develop at the drop tips. If the drop stayed spherical, and diffusion is ignored, these regions of charge would approach the centre as charge separation progressed and, eventually, the drop would be divided into two halves, each containing only cations or anions. The fact that the drop is deforming concurrently means that the effect of conduction is reduced by the convective fluxes resulting from the prolate drop deformation. The ion gradients formed by charge separation also give rise to opposing diffusion fluxes (equation (3.42)), which creates complex ion behaviour inside the drop.

The electric force due to the free charge (charge force) acts either towards or away from the direction of the field local to the charge, depending on the sign of the charge. This is not always aligned normally to the interface, as was the case for perfect dielectric models. Hence, tangential stresses can exist at equilibrium, leading to steady state fluid flow. Increasing the electric field strength increases the deformation of the drop and not just because of the increase in the permittivity force. It also increases the conductive fluxes of the ions, resulting in greater concentration of charge at the tips and therefore greater

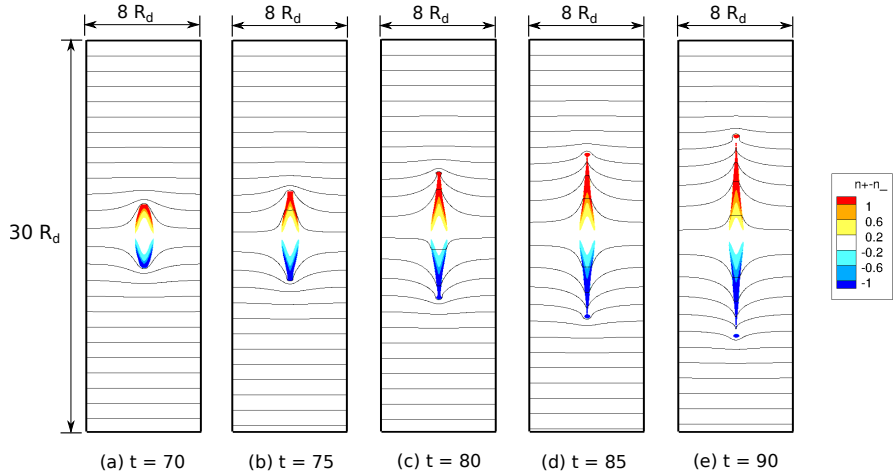

Figure 4.5: Images of a supercritical drop with $\mathrm{Ca_E} = 0.24$ and $\kappa = 7$ for $t = 70, 75, 80, 85$ and 90. Charge contours are embedded inside the drop and lines of constant potential are also shown.

charge force. However, it is also possible to increase the effect of charge, and thus only the charge force, without increasing the electric field. This can be achieved by increasing the ion concentration inside the drop. For a given electric field, a higher κ implies that there are a larger number of ions, which increases the number of ions redistributing themselves in response to the electric field. This results in a larger number of ions conducting towards opposite ends and, consequently, a larger charge force acts on the drop.

Unlike in the case without ions, the tangential stresses resulting from this additional electric force component can destabilize the drop, when the charge force is sufficiently high. A sample breakup case at $\mathrm{Ca_E} = 0.24$ and $\kappa = 7$ is shown in Figure 4.5. The contours of charge density magnitude are overlaid inside the drop, along with those of electric potential. The lines of potential are closest together near the tips of the drop, indicating that the potential gradient and therefore the electric field is highest near the drop surface. As a consequence, electric force inside the drop peaks near the interface. Because the permittivity ratio selected here is large, and the electrical displacement field is continuous at the drop interface (as the interface is uncharged), the magnitude of the electric field inside the drop is much smaller than the corresponding value outside the drop. Consequently, the electric potential contours inside the drop are not visible at the scale chosen. The charge separation process resulting in charge buildup at the tips is shown in 4.5b. Unlike in the subcritical case, the charge forcing in this case is sufficient to change

the curvature of the drop end, as can be seen in 4.5b, and lobes containing charge of opposite species are formed at each end (4.5c). These charge containing lobes, being near the interface of the drop, experience the highest electrical force in the drop. This leads to the acceleration of the lobes at a faster pace than the parent drop, which in turn increases the electric force acting on it as greater lines of potential get compressed together near the lobe tips. This process culminates in the breaking off of the lobes from the rest of the drop in 4.5e. This is repeated with the remaining charge inside the drop, until sufficient charge has been shed by the drop in the form of progeny droplets to ensure that the remaining parent drop can achieve the steady state force balance as seen in the subcritical case, with the effective κ for the subcritical parent drop now being insufficient for breakup.

4.3.1 Initial drop dynamics

The initial deformation behaviour ($t \leq 20$) is studied both for fixed $\mathrm{Ca_E} = 0.26$ and various κ in Figure 4.6a. Charge force increases with κ, so that the higher the κ, the more the drop will deform as is observed. However, the effects of increasing κ are insignificant until $t = 5$, and the curves only start diverging away from the perfect dielectric case ($\kappa = 0$) after this initial period. In fact $\kappa = 2$ is close to the perfect dielectric case until the end of the period plotted. This is in contrast to the results obtained in Figure 4.6b where a change in $\mathrm{Ca_E}$ affects the drop deformation curves from the beginning. These results can be explained by comparing the initial values of the permittivity and charge forces when the electric field is introduced. The permittivity force which is dependent only on the electric field and the permittivity jump (Equation 4.4), begins to deform the drop instantaneously. The increases in the permittivity force, by increasing $\mathrm{Ca_E}$, are therefore apparent immediately in the drop deformation. The charge force, in contrast, depends on the accumulation of free charge near the drop interface, a process that requires the positive and negative ions to be conducted in opposite directions by the electric field. The timescale for charge separation is larger than that for drop deformation since Pe is large (1000 for this study). Thus there is an initial period of drop deformation where the charge has not yet had time to separate, before the curves for different κ diverge from each other.

The z-averaged mean ion location for each ion species (scaled with respect to the vertical half length of the domain) can be calculated from the expression

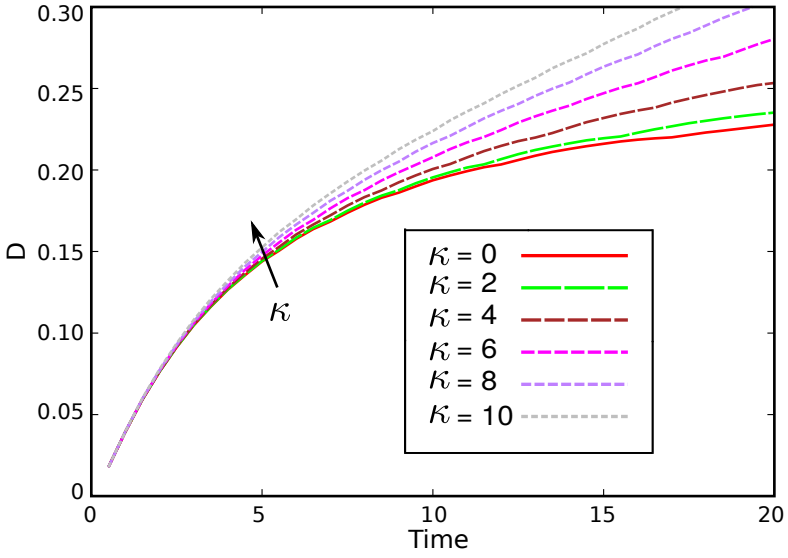

(a)

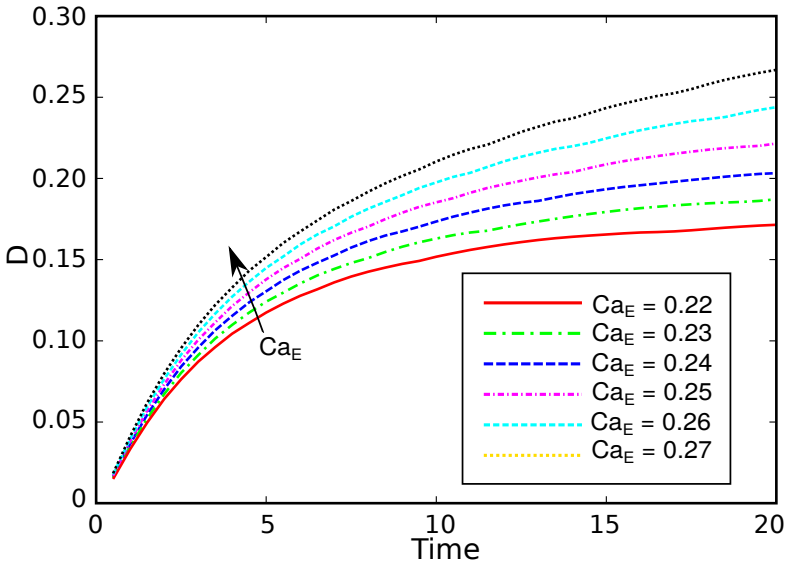

(b)

Figure 4.6: Evolution of drop deformation with time for (*a*) $\mathrm{Ca_E} = 0.26$ and $\kappa = 0 - 10$ (Only the $\kappa = 0$ case is subcritical) and (*b*) $\kappa = 3$ and $\mathrm{Ca_E} = 0.22 - 0.27$ (Only the $\mathrm{Ca_E} = 0.22$ case is subcritical).

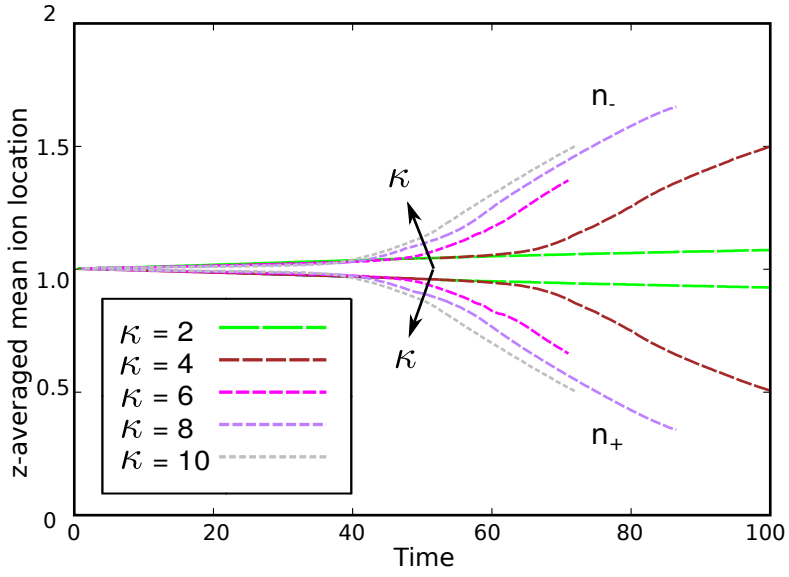

(a)

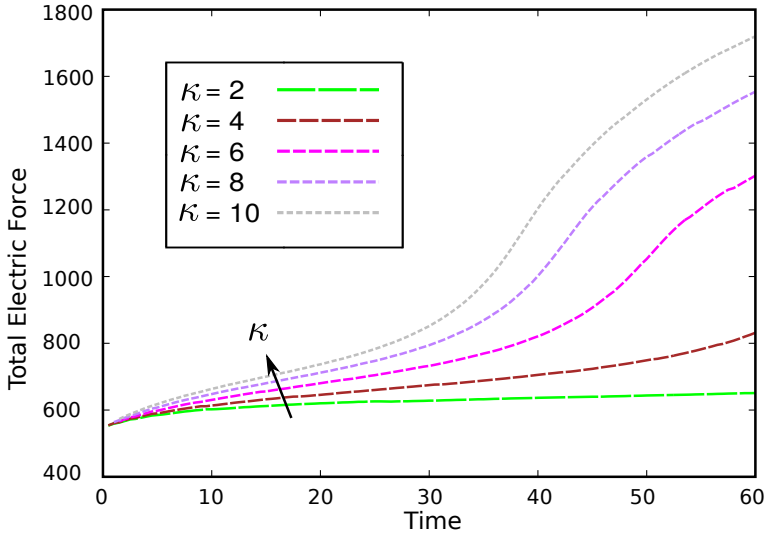

(b)

Figure 4.7: (*a*) Evolution of z-averaged mean ion location (equation (4.6)) with time and (*b*) Total electric force comparison, for $\mathrm{Ca_E} = 0.26$ and $\kappa = 1 - 10$ (Only the $\kappa = 0$ case is subcritical).

$$\frac{\int z\phi n_{\pm} dz}{\frac{L}{2}\int \phi n_{\pm} dz}, \tag{4.6}$$

which is integrated over the entire vertical axis of symmetry, where $n_{\pm}$ and L are the ion species and the vertical length of the domain, respectively. In equation (17) and hereafter, z denotes the vertical axis coordinate. Based on the scaling, this expression equals 1 at the centre of the domain (corresponding to uniform distributions), and equals 0 and 2 at the bottom and top, respectively. These cases would correspond to all the ions being at the bottom of top of the domain, respectively. Figure 4.7a plots this quantity for $\mathrm{Ca_E} = 0.26$ and shows that, for both species, it tends to be clustered around the centre until $t = 40$, regardless of κ. In fact, the permittivity force constitutes the majority of the total force deforming the drop until $t = 5$, independent of κ, due to the time lag associated with charge separation, as outlined earlier. The charge force, in contrast is zero initially and increases gradually over the course of drop evolution. Figure 4.7b shows the evolution of the total force with κ. The curves only diverge away from each other after $t = 30$.

4.4 Phase diagram of parameter space

To explore and characterize the drop dynamics, a phase diagram has been created with the phase boundary separating the subcritical and supercritical regions (Figure 4.8). The axes represent the effects of electric field strength and ion concentration, represented here by $\mathrm{Ca_E}$ and κ respectively. The subcritical regime is the parameter space for which the drop attains a deformed subcritical shape at steady state without breaking up. Anywhere in the supercritical regime, no equilibrium solutions exist and the drop breaks up. Selected results along the phase diagram are embedded as drop contours. The stability limit of $\mathrm{Ca_E} = 0.22$ approached for high κ agrees well with the value obtained numerically (0.22) by Lac & Homsy (2007) using a leaky dielectric model in the limit of highly conducting drops, and is close to the value obtained by experiment (0.214) by Ha & Yang (2000*a*) when studying breakup of highly conducting Newtonian drops. Interestingly, as is common in experiments, Ha & Yang (2000*a*) observe asymmetries in drop breakup. This is not possible in our model as the drop is assumed to be axisymmetric. The fact that the $\mathrm{Ca_E}$ values compare well suggests that the phase map would not change much if an axisymmetric drop shape was not assumed.

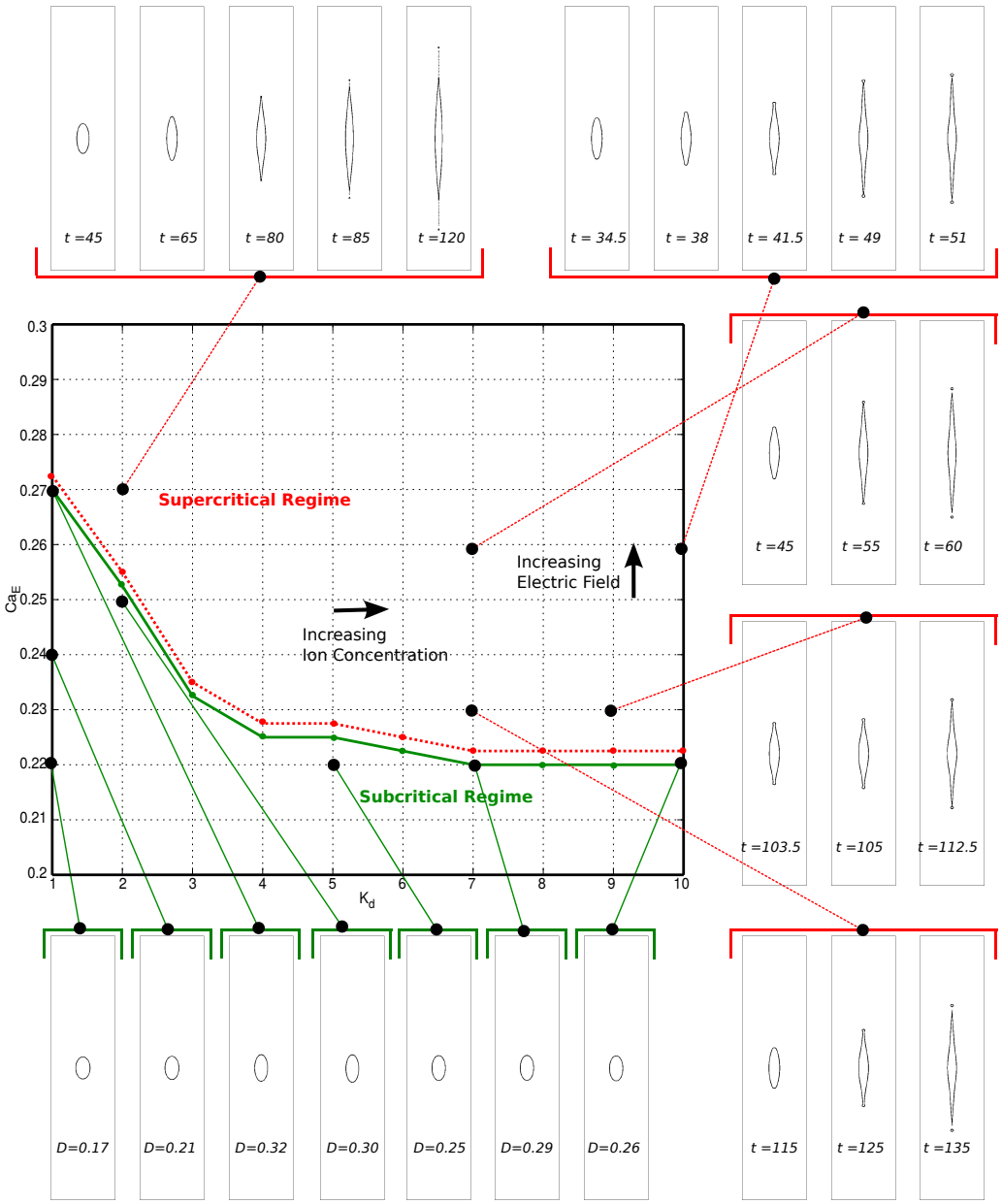

Figure 4.8: Phase diagram for overall drop deformation behaviour. The subcritical and supercritical boundaries have been drawn connecting the cases to direct the reader's eyes.

In the subcritical regime, longer subcritical drop shapes are attained with increasing κ for a fixed $\mathrm{Ca_E}$, as can be seen from the values of D_∞ for the embedded drop shapes for $\kappa = 1, 5$ and 10 when $\mathrm{Ca_E} = 0.22$. Analogously, for a fixed κ, increasing $\mathrm{Ca_E}$ also results in increasing D_∞ for subcritical drops, this can be seen by comparing the cases for $\mathrm{Ca_E} = 0.22, 0.24$ and 0.26 at $\kappa = 1$. This is consistent with the explanation that an increase in the total force acting on the drop, achieved through increasing either the permittivity or charge force, results in greater deformation prior to equilibrium being attained. However, the deformation of the subcritical drop on the boundary (D_{cr}), decreases with κ. For example, $D_{\mathrm{cr}} = 0.32$ for $\kappa = 1$ and $D_{\mathrm{cr}} = 0.26$ for $\kappa = 10$. This is due to the fact that the permittivity force does not destabilize the drop in the absence of free charge, as seen in the case of perfect dielectric drops. The charge force necessary to destabilize the drop depends on both the electric field and κ. For cases with lower κ, this means that achieving the necessary charge force for breakup requires compensating for the smaller contribution of κ with a higher electric field. As the electric field also acts on the permittivity jump, this means that for low κ the drop deforms more before sufficient charge separation is achieved and the drop is destabilized. The higher the κ, the lower the $\mathrm{Ca_E}$ required to destabilize the drop. The lower $\mathrm{Ca_E}$ results in a lower contribution of permittivity force in the resulting drop deformation.

In the supercritical regime, the non-dimensional times are provided for the individual snapshots of transient cases. The time to breakup decreases when two cases along one axis are compared, for e.g. $\mathrm{Ca_E} = 0.23$ and $\mathrm{Ca_E} = 0.27$ for $\kappa = 7$ and $\kappa = 6$ respectively, which show similar breakup shapes occurring at $t = 60$ and $t = 135$. This can be understood as a result of the increased total forcing due to the higher electric field accelerating the breakup of the drop relative to the lower field case. The phenomenon of greater interest is the variation in drop shape at breakup, between the $\kappa = 2$ for $\mathrm{Ca_E} = 0.27$ and $\kappa = 10$ for $\mathrm{Ca_E} = 0.26$ images. One shows a stream of tiny droplets exiting from the tip of the drop, while the other exhibits the aforementioned lobe formation prior to break off, and the size of the lobes appears to be increasing with κ. The former also displays a much pointier end, similar to perfect dielectric drop images embedded in Figure 4.3a and Figure 4.3b, and distinct from the rounded tips of the latter. In fact these two breakup modes have been observed in both experimental and numerical studies and are referred to as *tip-streaming* (Paknemat *et al.*, 2012) and *pinch-off* (Ha & Yang, 2000*a*) in the literature, respectively. It is understood that drops with high permittivity breakup via tip streaming and those with high conductivity breakup via pinch-off, but the physics

underlying this drop behaviour has received scant attention (Sherwood, 1988).

Using an electrokinetic model with varying conductivity helps shed light on the behaviour of charge inside the drop and trace its evolution as it exits the drop, ejected as progeny droplets. The difference between the modes of breakup lies in the shape prior to charge accumulation and the number of ions being redistributed inside the drop ($\kappa = 10$ case has 25 times the number of ions as that of $\kappa = 2$). When few or no ions are present inside the drop, the drop assumes pointed tips as it deforms due to the dominance of normal stresses at the drop interface. The higher curvature of the pointed end causes the charge that does form in regions near the tip to accelerate to the interface during tip-streaming. On reaching the interface, the small packet of charge is ejected in the form of a tiny droplet. This process is repeated in quick succession as the ejection is followed by accumulation of charge at the still pointed interface. This results in breakup via release of several tiny droplets or tip-streaming. As the number of ions in the drop increases, the amount of charge forming near the tip at the same time increases, which means that pointed tips do not form. Instead, a larger area containing charge forms a neck at the top of the drop. This allows charge buildup to occur without the early ejection associated with the pointed end. Larger amounts of charge collect in the tips with increasing κ, allowing lobes to form eventually and the charge to exit the drop via a progeny droplet as opposed to a stream of tiny droplets. The phase diagram shows how tip-streaming behaviour can smoothly morph into pinch-off due to changes in tip curvature caused by the amount of charge collecting near the tips. A comparison is provided in Figure 4.9a.

4.5 Balance of permittivity force and charge force

Using the Maxwell electric force formulation (Equation 4.4), the evolution of the permittivity and charge forces over time for the entire phase diagram can be studied. When $\kappa < 5$, the breakup is mainly due to the permittivity force, which constitutes more than 60% of the total force at the point of breakup. When, $\kappa \sim 5$, the values of both permittivity and charge forces are close to each other at breakup. Cases where the charge force is the dominant contributer to breakup occur at high κ values. The transition from zones of high permittivity force of the phase diagram (Figure 4.8) to those of high charge force do not neatly map onto the two types of breakup observed; even for a low $\kappa = 2$,

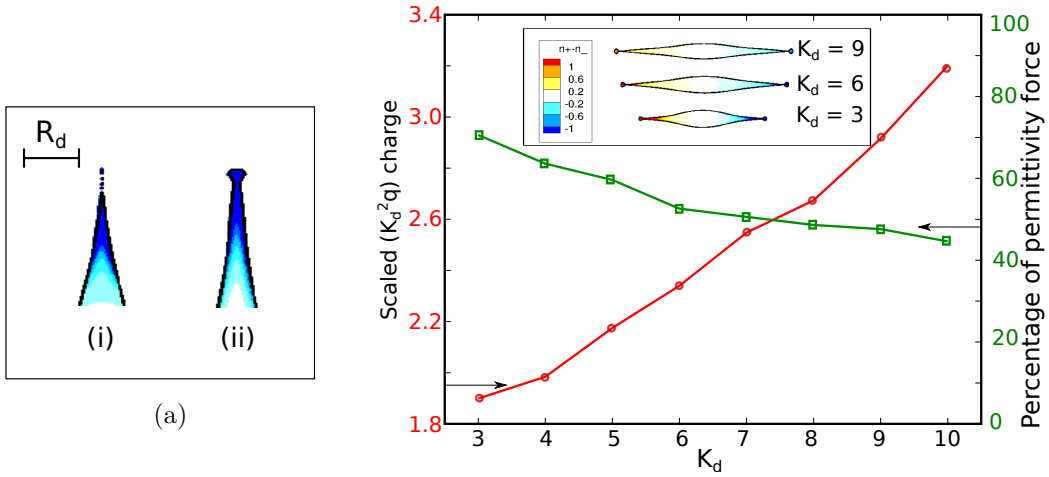

Figure 4.9: (*a*) Comparison of breakup modes ((i) tip-streaming and (ii) pinch-off) for $\kappa = 1$ and $\kappa = 10$ for $\mathrm{Ca_E} = 0.28$ (scale for charge contours shown in (b)) and (*b*) Charge in first drop ejected (red circles) and permittivity force as a percentage of total electric force at breakup (green squares) vs κ for $\mathrm{Ca_E} = 0.25$ (all supercritical cases). Drop profiles just prior to breakup for selected κ with embedded charge contours are also included.

which is in the high permittivity force zone, a mixture of pinch-off and tip-streaming modes start to appear, where a small lobe is formed and breaks off, followed by quick ejection of small droplets resembling tip streaming.

4.5.1 Higher charge force breakup

The scaled charge ($\kappa^2 q$) contained in the first drop being ejected is tracked for different κ values (at $\mathrm{Ca_E} = 0.25$) in Figure 4.9b. The scaled charge increases linearly with κ. This is consistent with the predictions made in section 4.2 regarding greater charge accumulation being made possible at the tips with increasing κ, due to a decrease in tip curvature. The drop shapes just prior to breakup for $\kappa = 3, 6$ and 9 with overlaid unscaled charge contours are also embedded. Though the time to breakup decreases with increase in κ, as seen in the phase diagram, the main drop gets longer before breakup and the lobe size also increases. This result is due to the greater charge force, which not only breaks up the drop faster, but also deforms it further. The value of the permittivity force as a percentage of total force, plotted on the same figure, is indicative of that as it decreases from $\sim 70\%$ to $\sim 45\%$ as κ increases from 3 to 10 (Figure 4.9b).

To illustrate this, the evolution of the reconstituted charge and permittivity force until breakup with time for selected cases is provided in Figure 4.10a, one of which is in the high permittivity force regime ($\kappa = 3$). The small fluctuations in the post processed calculation of the field inside the drop is due to the errors in the calculation of the charge force. These possibly result from the interface cells where no charge is present on the non-conductive side, which result in fluctuations in the calculations of the charge force from one time step to the next. However, the trends in the force balance plot are still qualitatively significant and are useful in probing the force dynamics inside the drop. The relative importance of charge force increases as κ increases from 3 to 10. The time to breakup is much higher for the $\kappa = 3$ case than the others as expected.

The rate of charge separation inside the drop, which affects its deformation behaviour, is shown in Figure 4.10b. It shows the change in percentage of total ions present in one half of the drop (in this case, the top half) over time, which served as a representation of the charge separation process. Due to the orientation of the field negative ions are conducted into the top half while positive ions are conducted out of the top half as seen in the figure for all κ. Differences exist in the extent of the charge separation. The curve

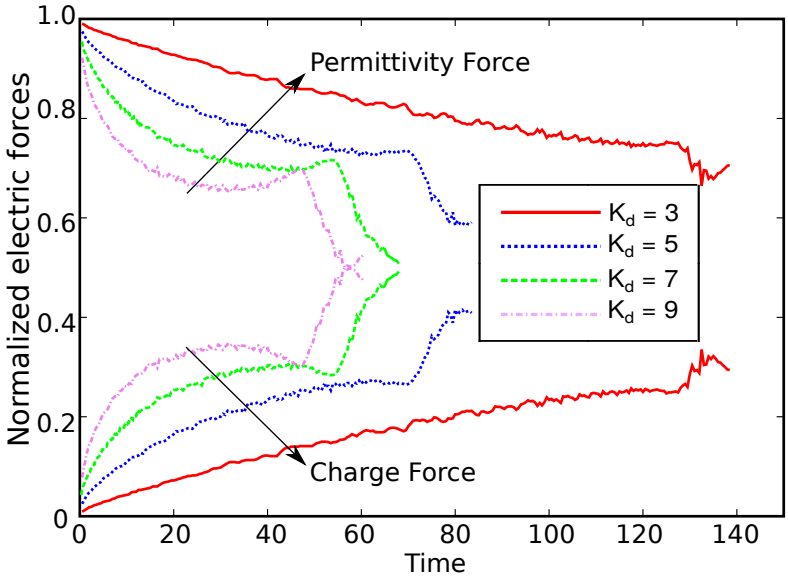

(a)

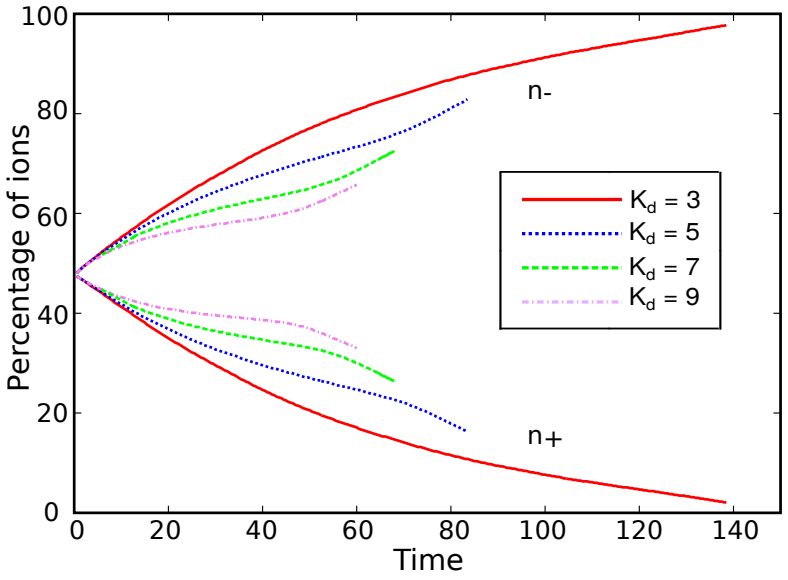

(b)

Figure 4.10: (*a*) Evolution of permittivity and charge force (equation (4.4)) as a ratio of total electric force for selected κ (all supercritical cases) at $\mathrm{Ca_E} = 0.25$ with time and (*b*) Evolution of percentage of both ion species in the top half of drop with time for selected dimensionless ion concentration κ (all supercritical cases) at $\mathrm{Ca_E} = 0.25$.

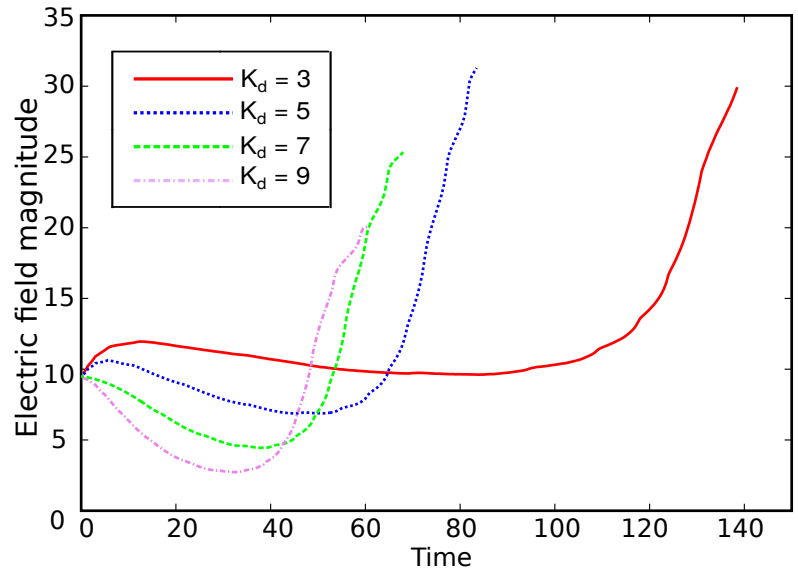

(a)

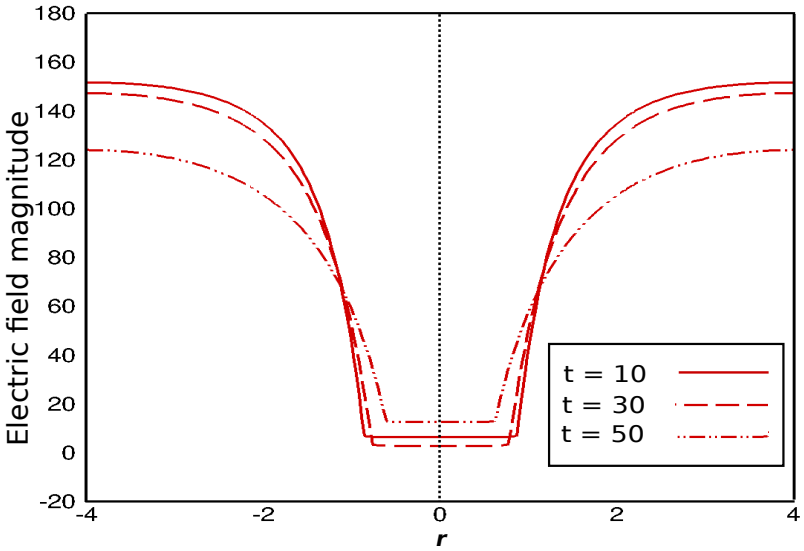

(b)

Figure 4.11: (*a*) Evolution of electric field magnitude at centre of drop with time for selected dimensionless ion concentration κ (all supercritical cases) at $\mathrm{Ca_E} = 0.25$ and (*b*) Evolution of the electric field magnitude with time across the horizontal centerline in the domain for $\mathrm{Ca_E} = 0.25$ (all supercritical cases) and $\kappa = 9$. The black dotted line indicates the vertical line of symmetry.

for $\kappa = 3$ eventually reaches 100% at which point there are no negative ions remaining in that half and all charge has been separated. For the other cases, the drop breaks up before the charge separation is complete.

Note that even though the charge force is proportional κ^2, it does not scale linearly with κ^2 because the electric field does not remain the same inside the drop. The moving charge inside the drop screens the externally imposed electric field, reducing the net electric field inside the drop over time. This is illustrated in Figure 4.11a, which plots the electric field magnitude at the center of the drop. After $t = 10$, the electric field decreases initially at different constant rates (up to $t = 80$ for $\kappa = 3$ and $t = 40$ for $\kappa = 5, 7, 9$) for all κ as ions are conducted. The effect is more marked at higher κ values because more ions are redistributed. Indeed, the curve for $\kappa = 9$ gets close to zero, after which the ions would stop conducting; increasing κ would have no effect, as the drop would behave like a perfect conductor in the absence of a field inside the drop. However, between $t = 40$ and $t = 80$ the field begins to increase inside the drop. To explore this, the field across the horizontal centerline of the domain is plotted for different times (for the $\kappa = 9$ case) in Figure 4.11b. First, the electric field varies minimally along the radial axis inside the drop at any given time. This can be seen in the figure, where the flat region in the centre of all curves represents the drop interior. The reason the length of the flat section varies with time is because the drop itself is deforming. Second, the field outside and away from drop is higher due to the permittivity ratio but decreases as it approaches the drop interface. The electric field magnitude in the center of the drop decreases from $t = 10$ and $t = 30$ for $\kappa = 9$ in Figure 4.11a. Comparing the curves for $t = 10$ and $t = 30$ in Figure 4.11b shows that the electric field also decreases outside the drop with time. However, when the field increases after $t = 30$, it can be seen from the $t = 50$ curve in Figure 4.11b that the increase, with respect to time, in the electric field inside the drop is accompanied by a large decrease outside the drop, which remains to be explained.

4.5.2 Higher permittivity force breakup

The drop size at breakup increases with increasing $\mathrm{Ca_E}$ due to the effect of the increased total force. Figure 4.12 shows that the charge contained in the first ejected drop for $\kappa = 4$ interestingly decreases linearly with $\mathrm{Ca_E}$. This is unlike the case with increasing κ. A possible explanation is that the increased $\mathrm{Ca_E}$ and consequent increased total electric force breaks up the drop earlier in the charge separation process, which means

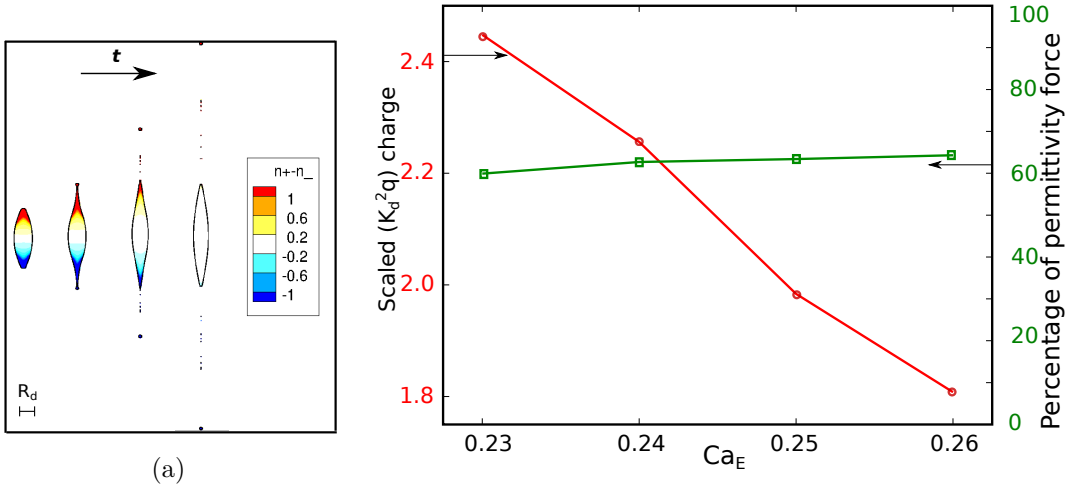

Figure 4.12: (*a*) Evolution of drop deformation of $Ca_E = 0.26$ ($\kappa = 4$) with time (with embedded charge contours) and (*b*) Charge in first drop ejected (red circles) and permittivity force (Equation 4.4) as a percentage of total electric force at breakup (green squares) vs Ca_E for $\kappa = 4$ (all supercritical cases)

that less of the charge has collected in the lobe near the tip at breakup. This effect is more pronounced for higher Ca_E values. The selected drop shapes for $Ca_E = 0.26$ with overlaid charge contours show that over the course of breakup, most of the visible charge contained in the drop is ejected after the first drop has broken off. There is little visible charge left in the drop in the last image, as most of it exits the drop at breakup. The charge separation plot (Figure 4.13a) shows that for all the cases considered, the charge separation at the centreline reaches completion (100%). Greater charge separation, a result of the low κ and longer breakup time associated with tip-streaming, results in most of the charge contained in the drop exiting the tip. Simultaneously, the increase in total force with Ca_E is sufficient to destabilize the drop earlier, resulting in the first ejected droplet containing less charge. This case is indicative of how pinch-off merges into tip-streaming as the size of the first drop decreases.

A force balance over time is shown in Figure 4.13b for the same cases studied above. Though increasing the Ca_E increases the total force deforming the drop, it does not change the relative balance of the permittivity and charge forces. The changes that do appear only do so just before the drop breaks up. This is because the increased electric field inside the drop increases the conduction flux of the ions, and hence the charge force,

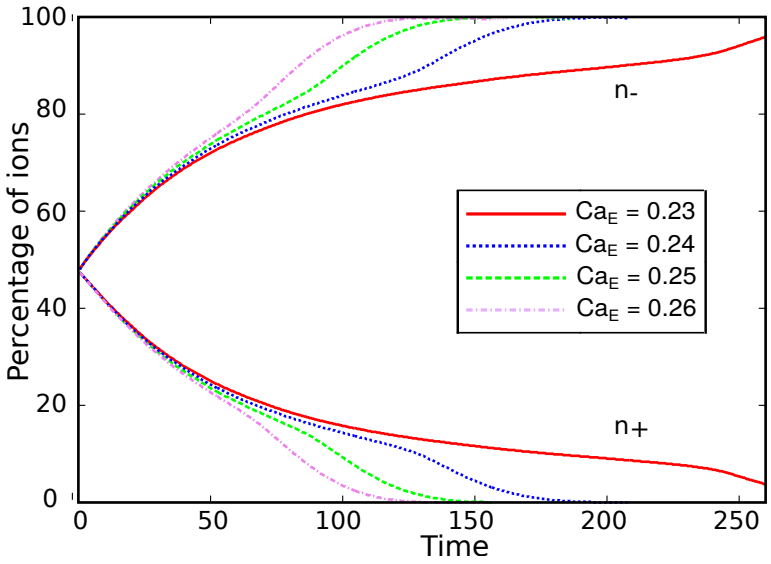

(a)

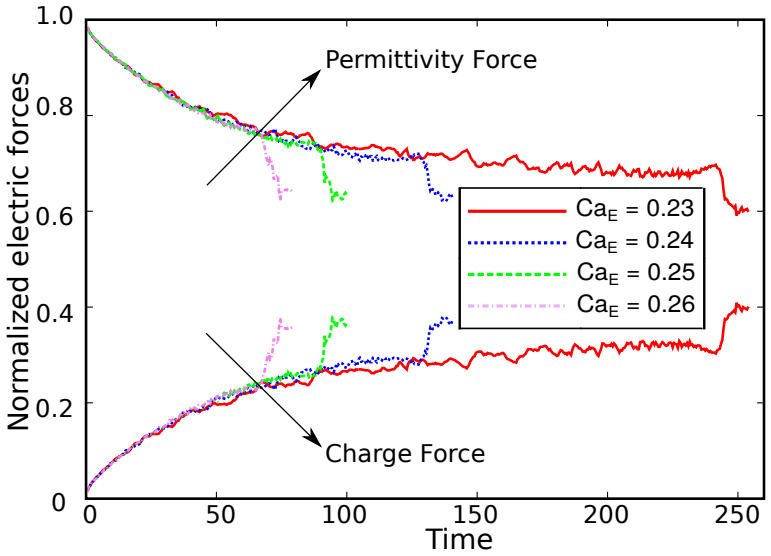

(b)

Figure 4.13: (a) Evolution of percentage of both ion species in the top half of drop with time for selected Ca_E (all supercritical cases) at $\kappa = 4$ (b) Evolution of permittivity and charge force (Equation 4.4) as a ratio of total electric force with time for selected Ca_E (all supercritical cases) at $\kappa = 4$.

and the permittivity force at the interface, which appears to maintain the relative balance of the two forces for the cases studied. The force balance is only affected by changes in κ which increases the charge force, without affecting the permittvity force.

Figure 4.14a plots the mean ion location until breakup and shows that the ions are slightly closer to the centre at breakup when the Ca_E is higher. Figure 4.14b shows the electric field at the centre of the drop and the behaviour is qualitatively similar to the $\kappa = 3$ case from figure 4.11a, with slow prolonged decrease as the charge separates. The gradient of the electric field is similar for the different Ca_E values. However, as the permittivity jump is the dominant force for these cases, we see that although the electric field inside the drop decreases as ions are conducted, the effect is far more gradual than that oberved in high charge force cases. This underlines the key distinction between high permittivity force breakup and high charge force breakup. Cases of the former tend to slowly deform due to the electric field acting on the permittivity jump. They breakup after most of the charge, which has collected near the tip of the already deformed drop, destabilize it. This results in a quicker breakup process with the drop dimensions changing relatively little in the time after the first droplet has left the main drop and before the rest of the charge exits the drop. High charge breakups however are realized because a significant amount of charge contained in the drop collects relatively quickly near the interface, deforming it, and then destabilizing it. However, as charge separation has not neared completion yet, the breakup process itself continues for a longer duration and the main drop keeps lengthening after ejecting the first droplet.

4.6 Conclusions

The impact of an electric field on an isolated, axisymmetric, conducting drop was investigated in this chapter. The continuous phase, oil, and the drop interface are uncharged while the drop was a symmetric 1:1 electrolyte. The simulations were conducted for a wide range of electric capillary numbers (Ca_E) and dimensionless inverse Debye lengths (κ) and the drop deformation behaviours for both steady state and transient cases were studied. The contribution of the charge force on drop deformation was reconstituted from knowledge of the total force, and compared against the permittivity force.

The numerical results showed that the breakup process does not occur in the absence

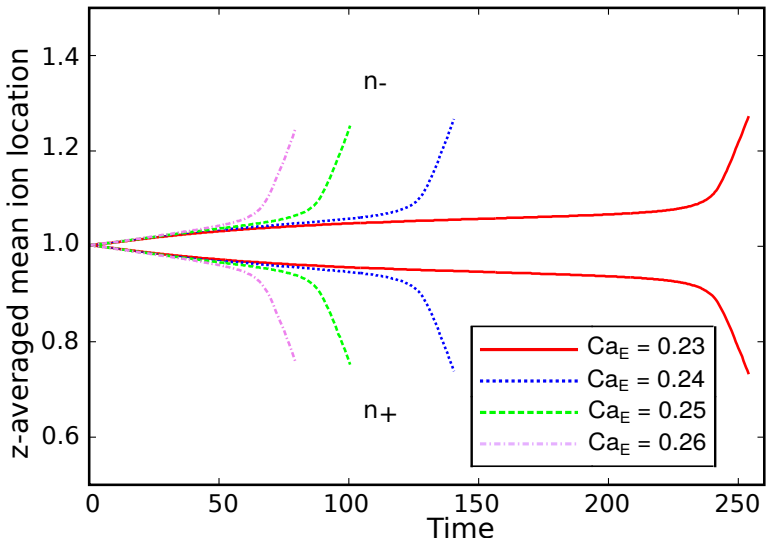

(a)

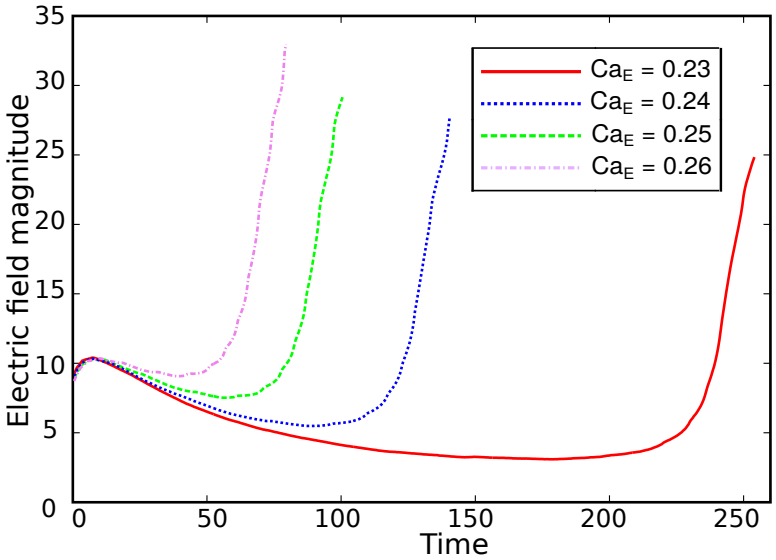

(b)

Figure 4.14: (a) Evolution of z-averaged mean ion location (Equation 4.6) with time for selected Ca_E (all supercritical cases) at $\kappa = 4$ (b) Evolution of electric field magnitude at centre of drop with time for selected Ca_E (all supercritical cases) at $\kappa = 4$.

of tangential stresses associated with the presence of charge. Hence, the tip curvature of perfect dielectric drops kept increasing as the electric field increased, without breakup. When ions were present in the drop, separation of anions and cations occurred under the influence of the electric field, and they conducted to opposite ends of the drop. The subsequent charge accumulation at each end of the drop resulted in an additional electric force component due to the electrical field acting on the collected charge. If the total force was sufficient, the electric force overcame the interfacial tension and a neck was formed, where charge started to collect. Due to charge accumulation in the neck, the electric force acting on it was higher relative to the rest of the drop. This eventually caused a lobe to form which breaks off and accelerate away from the main drop. The size of the lobe depended on the charge contained in it and determines whether the breakup mode would be classified as 'pinch off' or 'tip streaming'.

Differences in drop dynamical behaviour between drops with high permittivity and those with high conductivity could be explained by examining the charge behaviour inside the drop. The permittivity force is the majority component in the early stages of deformation, with the charge force only playing a role later. This is due to the fact that the permittivity force acts instantaneously as soon as the field is introduced whereas there is a time delay associated with the process of charge separation (due to the choice of a high Pe) and accumulating of charge at the tips of the drop. The relative importance of the ion forcing increases steadily over the course of drop evolution. Both the permittivity and charge forces increase with increasing electric field. Hence, increasing $\mathrm{Ca_E}$ has similar effects on charge and permittivity forces and does not affect the relative balance of the forces. Increasing the dimensionless ion concentration κ, however, only affects the charge force.

Two important behaviours occurred when either the charge force or permittivity force are dominant, based on the relative values of the forces at breakup, or at final steady state. Drops with higher permittivity force, when deforming to a subcritical equilibrium, were characterized by longer drop shapes. This is because the stability of the drop depends on the charge force whereas the deformation depends on the total force acting on the drop. When the former is small enough so as the destabilizing stresses are small and the latter is maximised, longer drop shapes can form. This is consistent with the results of perfect dielectric drops where long subcritical drop shapes are observed (up to $D_\infty = 0.93$ in the cases tested) as opposed to a maximum of $D_\infty = 0.32$ for

conducting drops. For higher κ, an increase in the $\mathrm{Ca_E}$ means that the destabilization limit for the ion forcing is reached faster, resulting in a smaller maximum subcritical shape.

For supercritical cases in the higher permittivity force regime, the charge contained in the first ejected drop is smaller than corresponding cases in the high charge regime. Also, the charge contained in the first drop decreases with $\mathrm{Ca_E}$. Breakup occurs when a highly deformed drop ejects most of the charge that has separated so as to occupy regions near the tip. High charge regime drops have greater charge accumulation in the lobes at each end, and the progeny droplet released has higher charge which increases with κ. The electric field inside the drop decreases as ions are conducted towards the drop tips and this effect is exaggerated when the ion number density inside the drop is increased. Breakup occurs when a portion of the charge deforms and destabilizes the interface, and this process continues as charge separation continues inside the drop.

In this chapter, the drop and continuous phases are assumed to have the same viscosity and density, and all the cases are run for a fixed value of permittivity ratio ($\bar{\epsilon} = 1$) and interface tension ($\mathrm{Oh} = 1$). In the next chapter, the restriction on these parameters will be relaxed and the effects on drop dynamics for a range of alternative physical scenarios will be documented. Second, the analysis in the present chapter is largely qualitative in nature and therefore limited to applications where progeny droplets are undesirable. For applications where this is not the case, however, a deeper and more quantitative understanding of the breakup process is necessary; in particular fine control over the size and charge of the ejected progeny droplets would be valuable. The goals of the next chapter are to extend this work to include a wider parameter space and develop general quantitative criteria to predict progeny droplet characteristics.

5 Isolated drop: transient effects and scaling laws

The surface of a small solid is comparatively greater than that of a large one.

GALILEO GALILEI[a]

[a]This is the first known statement describing a scaling law (Peterson, 2001).

This is the second of two chapters studying the effect of an electric field on an isolated, conducting microdrop of electrolyte, suspended in non-conducting oil. This chapter characterises the drop deformation and breakup phenomena for applications where progeny droplet formation is desirable. The focus is on studying a wide parameter space and developing quantitative criteria to predict the size and charge of progeny droplets ejected. This chapter begins with an introduction to the problem studied (§ 5.1). The effects of varying interfacial tension is subsequently explored, and the impact of the relative timescales of the different forces on subcritical drop deformation is outlined (§ 5.2). This leads into a general discussion of transient drop deformation, including a review of the literature on this topic, and the formulation of a simple analytical expression to accurately describe the transient drop deformation behaviour (§ 5.3). Next, supercritical drops are studied: a qualitative description is provided (§ 5.4), followed by quantitative study of the charge and size of the ejected droplets. This culminates in the formulation of universal scaling laws to predict these quantities (§ 5.5).

5.1 Introduction

An isolated drop of liquid - suspended in an immiscible fluid medium - will take the form of a sphere to minimize its surface area. As discussed in the last chapter, if a vertical

*This chapter is based on the author's papers R. Pillai, J. D. Berry, D. J. E. Harvie and M. R. Davidson, 'Electrokinetics of isolated electrified drops', *Soft Matter*, 2016, 12, 3310 and R. Pillai, J. D. Berry, D. J. E. Harvie and M. R. Davidson, 'Effect of interfacial tension and electric field on charge separation dynamics inside stable and unstable microdrops', *19th Australasian Fluid Mechanics Conference*, 2014

external electric field is then applied, the mismatch of permittivities at the drop interface results in the formation of a *normal* electric stress, which is the origin of the permittivity force. As the electric field magnitude (and electric stress magnitude) tends to be highest adjacent to the top and bottom interfaces, the drop deforms in the direction of the electric field (prolately). A steady state shape is obtained when the increased interfacial tension force of the (deformed) drop balances the electric stress. If the drop is conducting, i.e. if it contains ions, there are additional normal and *tangential* electric stresses generated by the mobile charge, resulting in the charge force. Toroidal circulations are observed inside and outside the drop, and a tangential viscous stress forms inside the drop in response to the tangential electric stress. Depending on the choice of physical and electrical parameters, the drop can be either subcritical (i.e., achieve a steady state deformation), or supercritical. In the latter case, the tangential electrohydrodynamic stresses destabilise the 'primary' drop, culminating in the ejection of 'progeny' drops from both tips, analogous to the Coloumbic fission of perturbed charged drops (Gu *et al.*, 2007).

In this chapter, the numerical study the electric-field induced electrokinetic effects on a conducting, initially spherical drop of electrolyte, suspended in an insulating oil phase, for finite κ ($1 \leq \kappa \leq 25$) is continued. The focus is on the effect of varying physical and electrical parameters on both the transient deformation behaviour of subcritical drops, as well as the electrohydrodynamic instabilities formed in supercritical drops. For subcritical microfluidic drops, electrokinetics affects the relative timescales of electrical and hydrodynamic effects. This information is important for designing micromixers, for example (Link *et al.*, 2004). The dynamics of the charge motion inside these stable drops is studied. The relative importance of fluxes and forces are characterized. For supercritical microfluidic drops, the precise behaviour of charge inside the drop influences the progeny drop formation. The study of the size and charge of ejected progeny drops, which is relevant to a range of applications like electrocoalescence in de-emulsifiers (Eow *et al.*, 2001*a*), inkjet printing (Lee *et al.*, 2013) and microfluidic chemical analysis systems (Livak-Dahl *et al.*, 2011), is studied. Using scaling laws, it is shown that the electrohydrodynamic breaking up of drops is analogous to ubiquitous capillary pinch-off phenomena.

5.1.1 Overview of problem

Following the initialization of the uniform DC electric field (oriented vertically in this work, see Figure 4.1), the difference in permittivities of the two phases results in dielectric

polarization at the interface (due to the jump in displacement field) creating a deforming electric force or *permittivity force*. This force develops over the dielectric polarization timescale ($\sim 10^{-12}$ s (Kirby, 2010)), that is effectively instantaneous. Simultaneously, the electric field acts on the ions inside the conducting drop, resulting in the formation of a charge distribution, creating a second deforming electric force or *charge force*. This force develops over the charge relaxation timescale ($t_e = \epsilon_d \epsilon_0 / \sigma$), where σ is the drop conductivity. The drop deforms under the action of the two electrical forces until equilibrium is reached when electrostatic effects are balanced by hydrodynamic effects. The hydrodynamic timescale depends on a balance of inertial, viscous and interfacial tension effects. The simplified electric field models detailed in chapter 2 usually make assumptions about the relative magnitudes of the charge relaxation timescale and the hydrodynamic timescale. For the length scales studied here, the charge and hydrodynamic timescales can be comparable (Lim *et al.*, 2010), and no assumptions of relative insignificance (for either timescale) can be made.

As discussed previously, in an electrokinetic model, the fluid flow inside the drop arises from the diffuse charge layers that form adjacent to the interface. In contrast to simplified electric-field models where σ is assumed to be constant, we specify an initial ion number density by choosing κ, and the local conductivity arises as a direct consequence of local ion concentration. Both ion species are initially distributed equally and uniformly inside the drop, to ensure electroneutrality. The electric field, however, imparts equal but opposite conductive fluxes to each species, resulting in anions migrating to one end of the drop and cations to the other. Depletion of either ion species from an initially neutral region leads to the formation of diffuse regions of charge (q) inside the drop. The field simultaneously acts on the charge, giving rise to electric forces on the fluid, and fluid flow, inside the drop. Diffusive ion fluxes also result from the gradients of charge that form (Equation 3.42), resulting in complex non-linear charge dynamics.

The drop's evolution towards steady state deformation depends on its physical properties. The liquid flow inside the drop results from the presence of the charge and permittivity forces, which are highest at the tips of the drop. The normal component of the electrical stress is opposed by capillary pressure. This results in a pressure decrease at the tips (relative to the drop bulk) driving fluid motion motion towards the tips. This liquid flow stretches the drop, increasing the curvature of the tips; a restoring capillary force results in the region. These capillary effects take place over times on the order of

$t_\gamma = \sqrt{\rho_\mathrm{d} R^3/\gamma}$. If viscous effects balance capillary effects, a typical timescale of motion would be $t_\mu = \mu_\mathrm{d} R/\gamma$ ($t_\mu = t_\mathrm{ref}$). An estimate of their relative contributions gives,

$$t_\mu/t_\gamma = \sqrt{\mathrm{We}}\Big/\,\mathrm{Re} = \mu_\mathrm{d}\Big/(\sqrt{\rho_\mathrm{d} R\gamma})\,. \tag{5.1}$$

This non-dimensional quantity, known as the Ohnesorge number (Oh) (McKinley & Renardy, 2011), is used to characterize our simulations from this chapter onwards. The value of Oh determines the primary forces influencing drop deformation. For a small Oh, inertio-capillary effects play a greater role, and viscous effects gain importance as Oh increases. Based on our scalings, Oh can be interpreted as the inverse square root of interfacial tension, for a fixed drop radius. Instead of selecting a constant value of external electric field for varying interfacial tension (when Oh is varied), we use a constant electric capillary number ($\mathrm{Ca_E}$), defined earlier as a measure of the relative importance of electrical to capillary forces,

$$\mathrm{Ca_E} = \frac{\epsilon_0 \epsilon_\mathrm{c} R}{\gamma} E_\infty^{*2}. \tag{5.2}$$

Using the definition of B (Equation 3.40) and Oh (Equation 5.1), this is recast as

$$\mathrm{Ca_E} = 2\,\mathrm{B}\,\mathrm{Oh}^2\,E_\infty^2. \tag{5.3}$$

This implies that the external electric field is adjusted to balance any changes in interfacial tension, consistent with other studies on the topic (Collins *et al.*, 2013). The advantage of this approach is that it allows us to study transient deformation of subcritical drops exclusively (as shown in chapter 4, for $\mathrm{Ca_E} < 0.22$, the electroneutral drop is always subcritical), for varying interfacial tension (or Oh). Here, the effect of Oh is studied for $0.10 \leq \mathrm{Ca_E} \leq 0.20$. The drop conductivity is varied by changing κ ($3 \leq \kappa \leq 25$) corresponding to changing ion concentration.

5.2 Effect of varying Oh

In this section, the effects of varying interfacial tension for a water drop suspended in oil, is studied. The permittivity ratio $\bar{\epsilon} = \epsilon_\mathrm{d}/\epsilon_\mathrm{c} = 50$. For practical applications involving microfluidic water-in-oil systems, the interfacial tension of a water/oil interface in the absence of surface-active agents is $\mathcal{O}(10^{-2})$ N/m, but, in their presence, can be reduced to $\mathcal{O}(10^{-5})$ N/m (Hashimoto *et al.*, 2008). Here, three values of interfacial tension are used, $\gamma = 10^{-2}$, 10^{-3} and 10^{-4} N/m which correspond to $\mathrm{Oh}^2 = 10^{-1}$, 10^0, and 10^1

respectively. As Ca_E is constant, the external electric field varies inversely with Oh as seen in Equation 5.3.

Figure 5.1 traces the deformation with time for the three cases outlined earlier. The drop deformation behaviour is faster the lower the Oh (higher electric field and interfacial tension). The plotting continues until the drop has reached stability or has broken up. The behaviour of the $Oh^2 = 10^0$ and $Oh^2 = 10^1$ cases appear largely similar, with a gradual increase preceding a steep rise at the tail end of the curve. This deformation behaviour is associated with the formation of lobes at both ends of the drop. These lobes then accelerate and pinch-off from the main drop to form droplets as the main drop breaks up. However the deformation curve for $Oh^2 = 10^{-1}$ does not display similar acceleration and instead stabilizes to a constant value. The embedded final drop shapes show the drop has attained a stable shape. The other two cases, in contrast, achieve breakup. Among the cases that have broken up it can be seen that the droplet breaking off in the $Oh^2 = 10^1$ case is slightly flatter than that ejected by the $Oh^2 = 10^0$ case. This could be because the higher interfacial tension for the $Oh = 10^0$ case helps the ejected droplet retain its spherical shape.

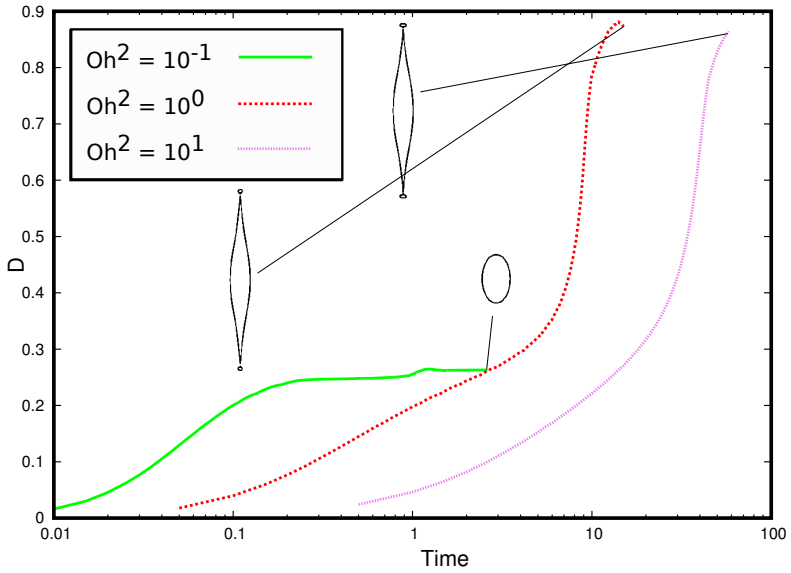

Figure 5.1: Comparison of deformation curves for $Oh^2 = 10^{-1}$, 10^0 and 10^1. Embedded images show final drop shape ($Oh^2 = 10^{-1}$) and shapes at breakup after which data is no longer plotted ($Oh^2 = 10^0$, 10^1) respectively

5.2.1 Stable and unstable drops

As discussed in chapter 4, drops which do not contain ions cannot breakup via ejection of droplets at both ends. The destabilization and breakup of the drop in this manner requires the presence of tangential stresses created by the moving charge inside the drop. As Figure 5.1 shows, for identical ion concentrations, drops can either be stable or unstable depending on the relative strength of the electric field and interface tension. This indicates that the charge separation dynamics inside the drop is affected by the choice of Oh. To investigate this further, the variation of the percentage of ions of each species in one half of the drop with time is plotted in Figure 5.2. This can be treated as a measure of the charge separation process inside the drop. The charge behaviour is symmetrical across the horizontal centerline. Since the top half of the drop is considered, the anions conduct into the half and cations conduct out of the half. Consequently, the percentage of anions increases while that of cations decreases and this is true for all cases considered.

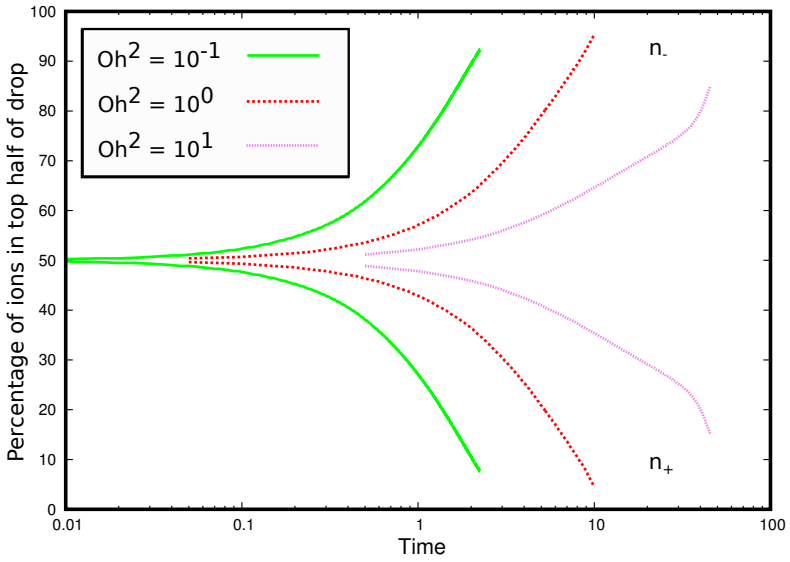

Figure 5.2: The percentage of cations (bottom group) and anions (top group) in top half of the drop for $\mathrm{Oh}^2 = 10^{-1}$, 10^0 and 10^1

The charge separation rate (Figure 5.2) appears to be qualitatively similar for all three values of Oh^2. This is despite the fact that $\mathrm{Oh}^2 = 10^{-1}$ case is stable while $\mathrm{Oh}^2 = 10^0, 10^1$ cases are unstable, and that charge separation is the driver for the electrical force acting

at the drop tips and resulting in drop breakup. It can also be seen that the rate of charge separation does not appear to be decreasing with time. No equilibrium appears to have been reached between the conductive, convective and diffusive fluxes governing ion transport inside the drop for the cases considered. Note that the drop dimensions for $\mathrm{Oh}^2 = 10^{-1}$ have stabilized but conduction of charge across the centerline continues.

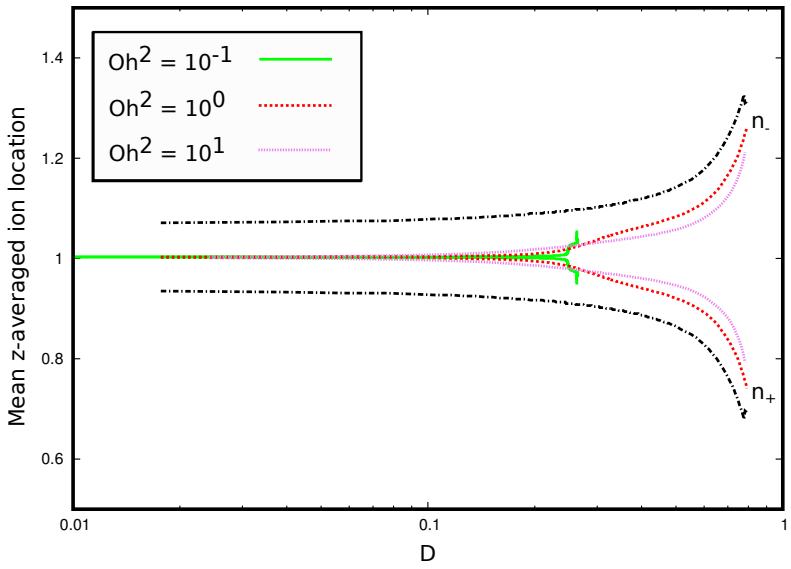

Figure 5.3: Comparison of mean ion location curves (Equation 4.6) for cations (bottom group) and anions (top group) for $\mathrm{Oh}^2 = 10^{-1}$, 10^0 and 10^1. The black lines show the location of the drop tips.

The fact that the $\mathrm{Oh}^2 = 10^{-1}$ case is stable implies that the charge separation isn't sufficient to destabilize drops for the lowest value of Oh^2 considered. To probe the dynamics of the charge separation further, the mean ion location in the drop along the Z axis (using Equation 4.6) is plotted for all three cases considered in Figure 5.3. In order to account for the temporal differences in deformation behaviour between the cases, the ion location is plotted against the transient deformation parameter D ($D = D(t)$). In this plot 1 is the centre of the domain and drop while 0 and 2 are the bottom and top of the domain respectively. The location of the drop tips is also included and the variation of drop tip with D is the same for all drops. Here the differences between the stable and unstable cases become clearer. First, the two unstable drops have similar profiles. The section between $D = 0.1$ and $D = 1$ is where some differences appear as the drops transition from well under the stability limit ($D = 0.1$) to unstable ($D \to 1$). It can

be seen that the mean ion location shows the greatest variation in this region for both the unstable cases. The mean location is affected by the motion of regions of drop as it breaks up, implying that a significant amount of the charge separated is concentrated in the lobe that accelerates and breaks away from the main drop. In contrast, the mean location of the ions for $\mathrm{Oh} = 10^{-1}$ is much closer to the centre of the domain. This shows that even though the charge separation when measured at the centre of the drop appears to be similar for stable and unstable drops, the location of the ions is different because in unstable drops, the bulk of the charge destabilizes the drop tip and breaks off from the main drop. The mean ion location for the $\mathrm{Oh}^2 = 10^0$ case is further from the centre of the domain than the $\mathrm{Oh}^2 = 10^1$ case. This implies that a greater volume of charge separation is required to achieve the same deformation value for the $\mathrm{Oh}^2 = 10^1$ case, possibly because of the higher interfacial tension resisting the formation of a lobe on the surface of the drop. This is consistent with the ejection of the slightly larger droplet for the $\mathrm{Oh}^2 = 10^1$ case at breakup in Figure 5.1.

The mean ion curve for the stable case (Figure 5.3) has interesting features. The deformation of the drop attains a maximum value of $D_\infty = 0.263$ and hence the curve does not extend to the right end of the plot. However, this does not imply that the charge separation inside the drop has achieved a steady equilibrium. As seen here, despite the dimensions of the drop being stable, the mean ion location continues to move steadily away from the centre as indicated by the small vertical lines for fixed D_∞ (Figure 5.3). This implies that the process of conduction of ions followed by accumulation of charge at the ends of the drop has not ceased consistent with the charge separation results. Note that the total force F_T deforming the drop seems to be stable because the drop dimensions have attained steady state values. This aspect of stable drop dynamics wherein the electric force associated with charge F_C is increasing but F_T is constant, is interesting and warrants further study. It can be concluded that for $\mathrm{Oh} = 10^{-1}$, the timescale for charge separation is significantly greater than the timescale for drop deformation. This results in the drop stabilizing before the charge dynamics inside the drop have reached an equilibrium. It therefore cannot be stated with complete certainty that the drop is stable at all, as ongoing charge dynamics inside the drop can possibly destabilize it at a later time.

5.2.2 Forces and fluxes in the drop.

In the last section it is seen that if Oh ≥ 1, the charge force controls the drop deformation; which is to say that once the charge separating inside the drop achieves equilibrium (F_{C} becomes constant), F_{T}, which is the total electric force deforming the drop, also equilibrates, and the drop achieves steady state. For Oh < 1, the charge and permittivity forces are found to be comparable inside the drop when it achieves an equilibrium elongation. However, unlike the case for Oh ≥ 1, the charge separation inside the drop is not at steady state at this point. The question arises: *if the charge separation is ongoing, and consequently the charge force is increasing, why does the drop not continue to deform?*

To probe this apparent inconsistency, the evolution of the permittivity force and the charge force (both scaled with F_{T}) is plotted for $\mathrm{Ca_E} = 0.1, \kappa = 10$ and Oh $= 0.316$ in Figure 5.4a. The deformation parameter D is also plotted and plateaus at $t \simeq 15$. The axial F_{T} measured inside the drop, is also effectively constant at this point (not shown here). Figure 5.4a shows that the charge force, however, continues to increase till the end of the plotted time period. However, the drop shape continues to be at equilibrium because, surprisingly, the permittivity force decreases at roughly the same rate (post $t \simeq 15$, when F_{T} is constant) as the charge force increases, thus maintaining a constant D ($D = D_\infty$). A simple mechanism is proposed to explain this: as charge separates and reaches the interface, it modifies the local electric field, reducing the net electric field magnitude near the drop interface. This lowers the permittivity force ($F_{\mathrm{P}} \propto \boldsymbol{E^2}$) (Equation 4.4). Though the charge force is also affected ($F_{\mathrm{C}} \propto \kappa^2 q\boldsymbol{E}$), the effects of the decreasing electric field are outweighed by the increasing charge separation (q). Steady state is achieved ($t \simeq 15$) when this decrease in the permittivity force is balanced by the corresponding increase in the charge force.

A related observation, based on Figure 5.4a is that the charge force variation (electrokinetic effects) is successfully captured by our choice of timescale ($t_{\mathrm{ref}} = t_\mu$). The conductivity σ in the charge relaxation timescale (defined earlier as $t_{\mathrm{e}} = \epsilon_{\mathrm{d}}\epsilon_0/\sigma$) can be rewritten in terms of initial ion number density (n_0) (Masliyah, 2006),

$$\sigma = \frac{2z^2e^2\bar{D}n_0}{k_{\mathrm{B}}T}. \tag{5.4}$$

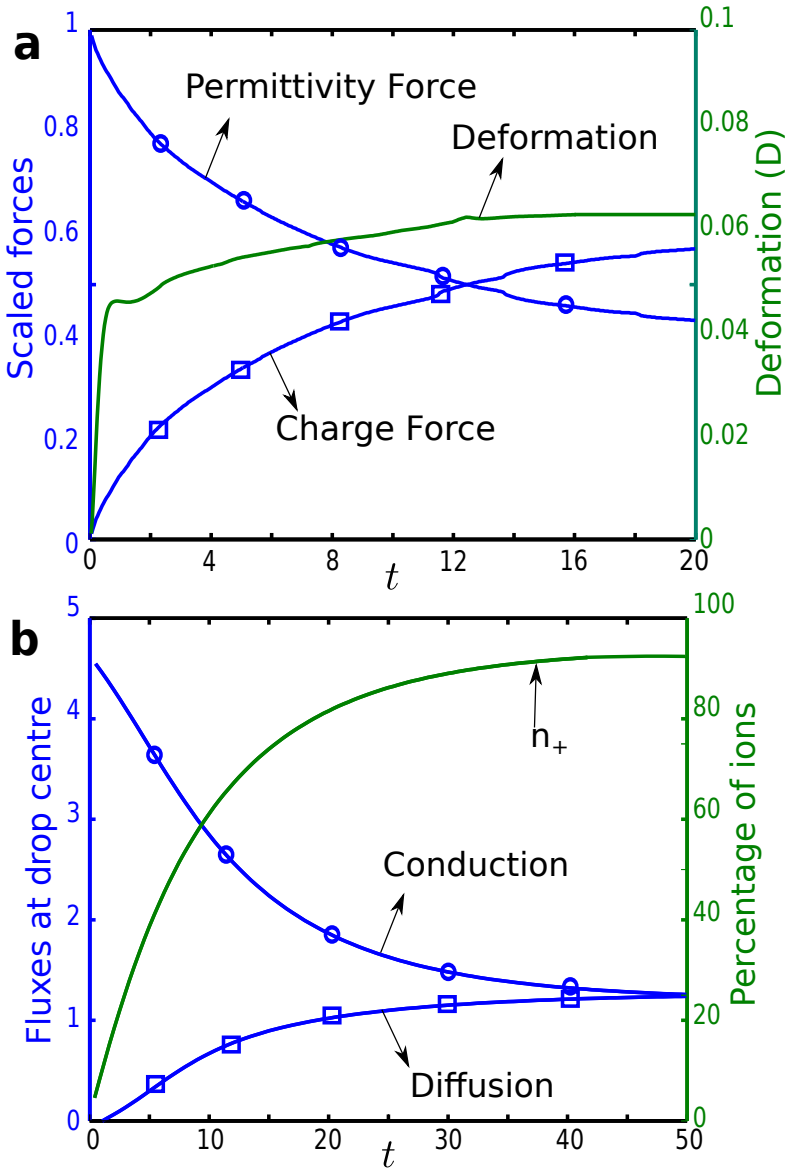

Figure 5.4: (a) Scaled permittivity force (blue line with overlaid circles), charge force (blue line with overlaid squares) and deformation parameter (D, green line), for $\mathrm{Ca_E} = 0.1, \kappa = 10, \bar{\epsilon} = 20$ and $\mathrm{Oh} = 0.316$. (b) Temporal evolution of conductive (blue line with circles) and diffusive (blue line with squares) fluxes measured at the centre of the drop along with the number of cations (green line) in the bottom half of the drop for $\mathrm{Ca_E} = 0.1, \kappa = 3, \bar{\epsilon} = 1$ and $\mathrm{Oh} = 1$

Modifying the charge relaxation timescale for our model using Equation 5.4, we obtain

$$t_e = \frac{\mathrm{Pe}}{\kappa^2} t_\mu. \tag{5.5}$$

Therefore the non dimensional ratio $\psi = t_e/t_\mu$ depends on electrokinetic effects (Pe/κ^2). Based on Equation 5.5, $\psi = 10^2$ in Figure 5.4a, which shows good agreement with our model given that the charge force hasn't equilibrated at $t = 20$. In contrast the permittivity force acts effectively instantaneously as the associated timescale is much smaller (chapter 4). Equation 5.5 also shows that, for a fixed κ, $\psi \propto 1/\mathrm{Oh}^2$ (Given our scalings, $\mathrm{Pe} \propto 1/\mathrm{Oh}^2$), implying that the charge separation gains importance with increasing Oh. This is because viscous forces dissipate the momentum created by the charge force (charge layers initially form adjacent the interface), while the permittivity force being an interfacial force, does not depend on viscosity. Therefore as Oh decreases, the importance of viscous forces to drop deformation decrease (as inertial and capillary forces dominate), and consequently the importance of electrokinetic effects to drop deformation also decrease (ψ decreases). Consequently, a lower Oh is consistent with less charge separated (F_C) at steady state, and continuing charge separation after. In contrast, for $\mathrm{Oh} \geq 1$, viscous forces are dominant and the electrokinetic and hydrodynamic timescales are comparable ($\psi \simeq 1$), and consequently, charge equilibrium is achieved alongside steady state deformation (F_C is steady). Note that as interfacial tension increases (Oh decreases), the electric field increases as well (fixed $\mathrm{Ca_E}$), which increases the permittivity force ($\propto \boldsymbol{E^2}$), compared to the the charge force ($\propto \kappa^2 q\boldsymbol{E}$) (Equation 4.4).

To estimate the relative importance of diffusive and conductive ion fluxes inside the drop, magnitude estimates of these effects are calculated by integrating the axial diffusion ($\phi\nabla n_\pm$) and conduction ($\phi n_\pm \boldsymbol{E}$) terms from (Equation 3.42) across the horizontal centerline of the drop. In Figure 5.4b, the evolution of these fluxes is plotted for a higher Oh than in Figure 5.4a, permittivity ratio ($\bar{\epsilon} = 1$), and a lower κ ($\mathrm{Ca_E} = 0.1$, $\kappa = 3$, $\mathrm{Oh} = 1$ and $\psi \sim 10^2$). Also included in Figure 5.4b is the evolution in the the number of cations (n_+) contained within the bottom half of the drop, which is a measure of the charge separation inside the drop (when the rate at which ions enter the lower half of the drop becomes negligible, the charge can be assumed to be fully separated).

Figure 5.4b shows that charge separation plateaus out (at $\sim 93\%$ around $t = 45$, when equilibrium is reached ($\kappa = 3$, $\mathrm{Oh} = 1$). The plateauing of ion migration (i.e. completion of charge separation) also coincides with the convergence of the decreasing (estimated)

conductive ion fluxes (blue line with overlaid circles) with the increasing (estimated) diffusive fluxes (blue line with overlaid squares), as predicted. The conductive fluxes decrease as the field inside the drop decreases following charge separation, while the ion gradients created by conduction result in a gradual increase in diffusive fluxes. For lower Oh, the conductive fluxes are larger (due to higher $\boldsymbol{E}$), while the diffusive fluxes are independent of the electrical field. Consequently, it would take longer for the field inside the drop to decrease sufficiently for the conduction fluxes to be balanced by the diffusive fluxes, and equilibrium to result.

5.3 Transient drop deformation.

The early analytical studies on transient drop deformation focused on perfect dielectric and perfect conductor electric field models paired with Stokes flow based hydrodynamics (Haywood *et al.*, 1991). Recently, Esmaeeli & Sharifi (2011*b*) showed that the deformation history of a leaky dielectric drop can be represented by the following equation:

$$D = D_\infty(1 - e^{-\tilde{t}/t_c}), \tag{5.6}$$

where D and D_∞ are the transient and steady state drop deformation parameters, respectively (In their solution, D_∞ is obtained from G. I. Taylor's classic expression (Taylor, 1966)). t_c, the timescale that governs these dynamics is given as

$$t_c = t_\mu \frac{\bar{\mu}(19\bar{\mu} + 16)(2\bar{\mu} + 3)}{40(\bar{\mu} + 1)}. \tag{5.7}$$

The form of Equation 5.6 is such that the transient deformation (D) will monotonically approach its steady state value (D_∞). Figure 5.5a shows that Equation 5.6 (shown as back dots) predicts the qualitative deformation behaviour well for cases where Oh ≥ 1. However, by neglecting the inertial terms in the momentum equations, it cannot predict the type of non-monotonic, oscillatory behaviour seen for the (lower) Oh $= 0.1$ case in the same figure. Non-monotonic evolution towards steady state deformation has been reported elsewhere in the literature (Supeene *et al.*, 2008; Paknemat *et al.*, 2012; Lanauze *et al.*, 2013). Lanauze *et al.* (2013) highlighted the importance of Oh and suggested inertia and charge relaxation as likely causes of the oscillatory behaviour, with charge relaxation sometimes causing a prolate-oblate deformation transition prior to overshoot. They measured the impact of the charge relaxation through a dimensionless quantity

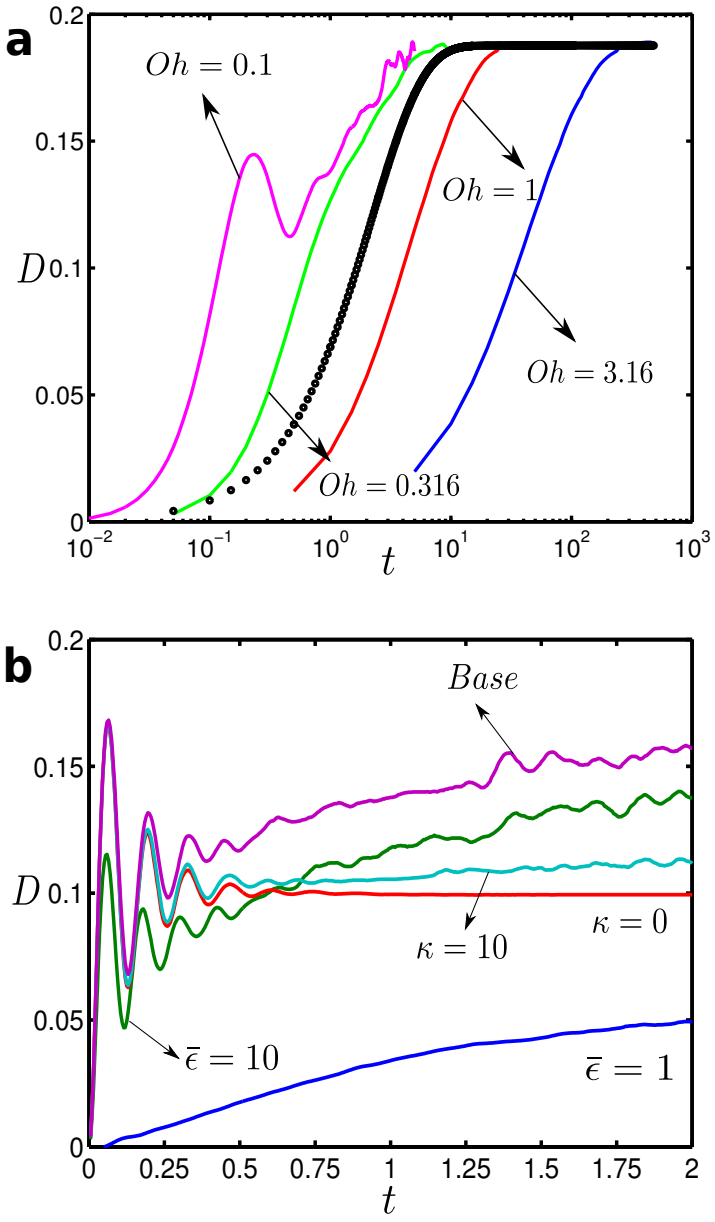

Figure 5.5: (a) Temporal evolution of drop deformation for Oh = 0.1 (magenta line), Oh = 0.316 (green line), Oh = 1 (red line) and Oh = 3.16 (blue line). $Ca_E = 0.2, \bar{\epsilon} = 20, \kappa = 25$ for all cases. In addition, the predictions of Equation 5.7 are shown as black dots. (b) Temporal evolution of drop deformation for Oh = 0.0316. Base case is $\bar{\epsilon} = 20$, $\kappa = 25$, $\bar{\mu} = 1$ (magenta). Others are $\bar{\epsilon} = 1$ (blue), $\kappa = 0$ (red), $\bar{\epsilon} = 10$ (green) and $\kappa = 10$ (cyan).

which they named as 'Saville' number (Sa) (Saville, 1997), given as a ratio of charge relaxation and momentum diffusion (t_{V}) timescales. Using Equation 5.4, we reformulate Sa as:

$$\mathrm{Sa} = t_{\mathrm{e}}/t_{\mathrm{V}} = \left(\frac{\epsilon_{\mathrm{d}}\epsilon_0}{\sigma}\right) \Big/ \left(\frac{\rho_{\mathrm{d}} R^2}{\mu_{\mathrm{d}}}\right) = \mathrm{Pe} \Big/ (\mathrm{Re}\,\kappa^2)\ . \tag{5.8}$$

For the cases considered in Figure 5.5a, Sa is fixed (Sa = 1.6) as κ is not varied and the ratio of $\mathrm{Pe}/\,\mathrm{Re} = 1000$ for all our simulations. As Sa is independent of Oh, charge effects cannot explain the deformation behaviour seen in Figure 5.5a. Hence, we conclude that inertia alone produces non-monotonic transient deformation (Lanauze *et al.*, 2013). As discussed in the previous section, decreasing Oh in our model results in reduced importance of electrokinetic effects on drop deformation. This supports the hypothesis that the oscillations are inertial and result from the deformation induced by dielectric polarization, as they manifest for cases of lower Oh (see Equation 5.1).

A parametric study of the oscillations for Oh = 0.0316 shown in Figure 5.5b confirms their inertial origin. In the absence of dielectric forces, no oscillations are seen for the $\bar{\epsilon} = 1$ case (blue line) and the transient deformation resembles the Oh ≥ 0.316 cases from Figure 5.5a. Also, for $\bar{\epsilon} = 20$, the variation in κ has negligible impact initially as expected. The cases for $\kappa = 25$ (magenta line), $\kappa = 10$ (cyan line) and $\kappa = 0$ (red line) completely overlap until $t = 0.2$. The results described here differ from the existing literature on the topic in two ways. First, Lanauze *et al.* (2013), in part due to the restrictions of their approach (analytical formulation of the unsteady Stokes equations), were limited to small amplitude oscillations (at small deformations, $D_\infty < 0.05, \mathrm{Ca_E} \ll 1$). In contrast, the results shown in Figure 5.5a depict oscillatory behaviour that is significantly larger in magnitude. A second, equally important distinction is that, for simplified perfect conductor/leaky dielectric approaches (Supeene *et al.*, 2008; Lanauze *et al.*, 2013), charge relaxation occurs on the same timescale as dielectric polarization (i.e. instantaneously). This means that, in those cases, all electrostatic effects are fast relative to the oscillation of the drop. The drop, therefore, oscillates in response to the combined effect of charge and permittivity jump. Consequently, following this temporary transient behaviour, a steady state deformation of roughly half the amplitude of the initial, undamped wave is obtained (the qualitative deformation of drops always resembles the dielectric case $\kappa = 0$ from Figure 5.5b). In contrast our model predicts an initial oscillatory transient behaviour ($t \leq 4$) driven by dielectric-inertio-capillary effects (F_{P}), damped by viscosity

and followed by charge induced deformation (F_{C}) towards a final steady deformation independent of Oh ($D_\infty \sim 0.187$ for all cases in Figure 5.5a).

Analytical approaches to characterizing the deformation of oscillating drops, excited by acoustic (Marston, 1980), inertial (Subramanyam, 1969) or electrostatic (Saville, 1974) means, usually involves small deformation perturbation analysis. Rayleigh (1879) pioneered this approach and performed a linear stability analysis to determine the natural oscillation frequency of an inviscid liquid drop, suspended in an inviscid medium. He showed that a drop of radius R, when excited by external means, would oscillate according to,

$$\omega_{\mathrm{n}} = \sqrt{\frac{\gamma n(n+1)(n-1)(n+2)}{R^3(\rho_{\mathrm{c}} n + \rho_{\mathrm{d}}(n+1))}} \tag{5.9}$$

where ω_{n} is the angular frequency of oscillation for mode number n. Basaran (1992) found that the $n = 2$ harmonic, which is the lowest order harmonic possible for an incompressible drop with no variation in centre of mass, sufficiently captures most of the oscillatory behaviour of a viscous drop. Substituting $n = 2$ in Equation 5.9, we get

$$\omega_2 = \sqrt{\frac{24\gamma}{R^3(2\rho_{\mathrm{c}} + 3\rho_{\mathrm{d}})}} \tag{5.10}$$

The reciprocal of this natural (angular) frequency allows us to recover the characteristic timescale of the oscillations. If the phases can be assumed to have equal densities, then this timescale is $1/\omega_2 \sim t_\gamma \big/ \sqrt{5}$. This shows that the inertia-dependent oscillatory behaviour is appropriately scaled by the capillary timescale (t_γ). However, Equation 5.9 does not contain a mechanism for the oscillations to be dampened. Prosperetti (1980) showed, analytically, that the frequency of (infinitesimal) oscillations was damped monotonically as viscous effects become important, as seen in Figure 5.5a and Figure 5.5b. Subsequent authors (Scott *et al.*, 1990; Whitaker *et al.*, 1998) have shown that, an approximate expression (for a perfect dielectric) can be obtained analytically by expressing the damping rate (ξ) in a power series in terms of the square roots of the viscosities (for the two lowest powers),

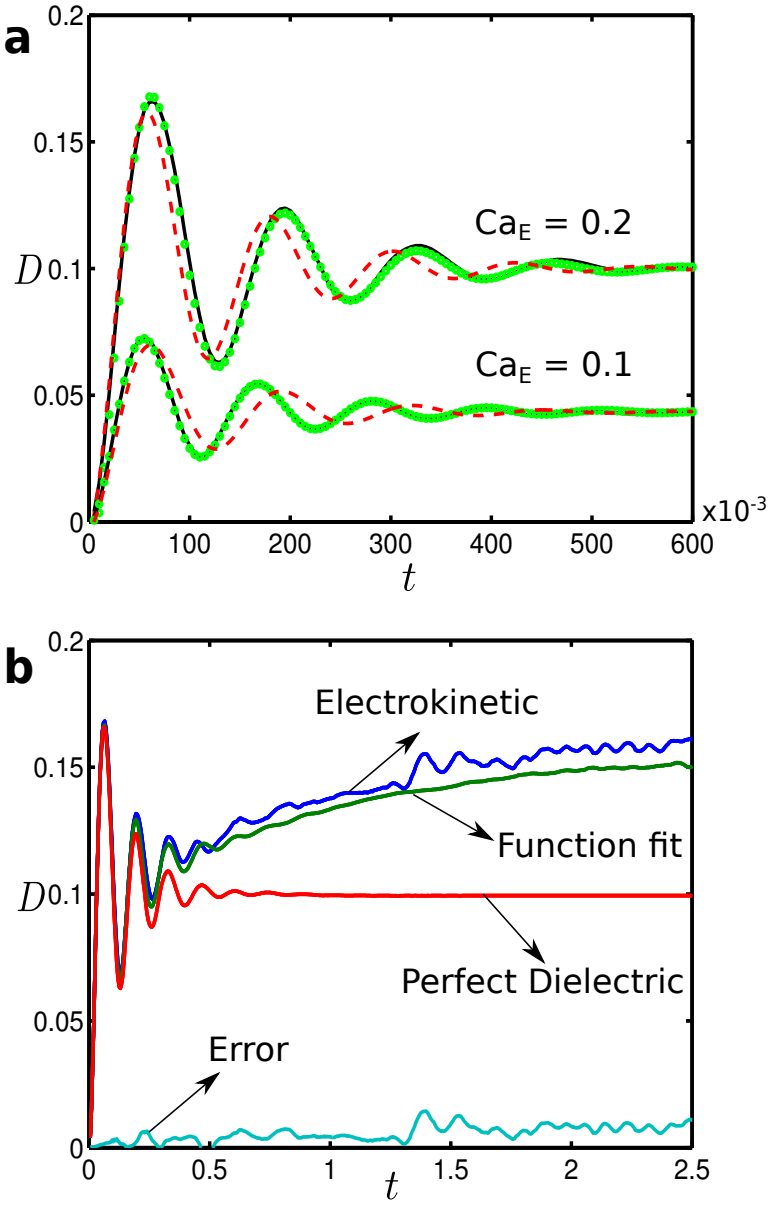

Figure 5.6: (a) Temporal evolution of oscillatory behaviour for Oh $= 0.0316$ and $\bar{\epsilon} = 20$ for two values of electric field ($\mathrm{Ca_E} = 0.1, 0.2$) for a perfect dielectric drop, $\kappa = 0$ (black lines). The predictions of the analytical model (Equation 5.11 and Equation 5.13, red dashed lines) and the curve fit (Equation 5.14, green dots) is also plotted. a $= 0.0079$ and b $= 0.0552$ for $\mathrm{Ca_E} = 0.1$; a $= 0.0073$ and b $= 0.0476$ for $\mathrm{Ca_E} = 0.2$. (b) Temporal evolution of drop deformation for $\mathrm{Ca_E} = 0.2, \bar{\epsilon} = 20,$ Oh $= 0.0316$. The four cases are a perfect dielectric case ($\kappa = 0$, red line), an electrokinetic case ($\kappa = 25$, blue line), a curve fit based on Equation 5.15 (green line) and an error curve (cyan line).

$$\xi \simeq \frac{(2n+1)^2(\omega_n \mu_c \mu_d \rho_c \rho_d)^{1/2}}{\chi\sqrt{2}} - \frac{(2n+1)^4 \mu_c \mu_d \rho_c \rho_d}{\chi^2} + \frac{(2n+1)[2(n-1)(n+1)\mu_d^2 \rho_d + 2n(n+2)\mu_c^2 \rho_c] + (2n+1)\mu_d \mu_c[(n+2)\rho_d - (n-1)\rho_c]}{R\chi[(\mu_c \rho_c)^{1/2} + (\mu_d \rho_d)^{1/2}]}, \tag{5.11}$$

where χ is given by,

$$\chi = 2R[n\rho_c + (n+1)\rho_d][\sqrt{\mu_d \rho_d + \mu_c \rho_c}]. \tag{5.12}$$

The natural frequency in the presence of viscous damping (ω_d) is given by Scott *et al.* (1990),

$$\omega_d = \omega_n - \frac{(2n+1)^2\sqrt{\omega_n \mu_d \rho_d \mu_c \rho_c}}{2\sqrt{2}R(n\rho_c + (n+1)\rho_d)(\sqrt{\mu_d \rho_d + \mu_c \rho_c})}. \tag{5.13}$$

These expressions were simplified by assuming equal viscosity and density for the two phases and $n = 2$. To test the accuracy of this model, we first compare it to the predictions of a perfect dielectric case (no ions, $\kappa = 0$). The analytical model predictions (red) are compared to our numerical predictions (black) in Figure 5.6a, for two values of electric field ($Ca_E = 0.1$ and $Ca_E = 0.2$). In addition, an equation describing a damped oscillator,

$$D = D_\infty(1 - e^{-at}\cos(bt)), \tag{5.14}$$

was also plotted (green dots) where a and b are the decay rate and angular frequency, respectively. These unknowns were calculated using a least-squares-fit algorithm in MATLAB. As seen in Figure 5.6a, the analytical model reasonably captures the frequency and damping rate; but discrepancies exist, possibly arising from the high deformations seen here. In contrast, the curve fit agrees very well with the data, capturing all the smaller amplitude oscillations. Note that a viscous liquid drop suspended in a viscous continuous phase possesses a natural oscillation frequency that is a function of multiple parameters, including physical and electrical properties, drop size, and the interfacial tension. However, this analysis shows that for a perfect dielectric drop with sufficiently low Oh, the oscillatory deformation behaviour of an electrically excited drop can be accurately represented by a (curve-fitted) exponentially decaying cosine wave equation.

If ions (i.e. electrokinetic effects) are considered, the deformation behaviour becomes more complex, and cannot be represented by a simple decaying cosine wave. The separating charge both influences the deformation directly, via the charge force, but also

indirectly, via the screening of the electric field inside the drop, resulting in significant nonlinear effects. But, given the fact that the charge force scales as t_e ($\sim t_\mu$ for the cases studied in this chapter, as shown earlier), and the permittivity force scales as t_γ (for the oscillations, Equation 5.10), could a choice of low Oh (Oh $= t_\mu/t_\gamma$) create a scenario where the two forces act on such disparate timescales, that they can be effectively considered independent of each other? Given that charge driven deformation evolves monotonically towards a steady state value, using the principle of superposition, a combined electrokinetic-dielectric (approximate) transient deformation equation can be formulated,

$$D = D_{\mathrm{ek}} + D_{\mathrm{dc}}, \tag{5.15}$$

where D_{ek} and D_{dc} are the electrokinetic and dielectric contributions, described by equations 5.6 and 5.14 respectively. Figure 5.6b shows the behaviour of this combined equation (green line) compared with both a full electrokinetic model (blue line) and the perfect dielectric model (red line). There is good agreement initially, for small electrokinetic effects, but this is less true once viscous effects become significant ($\tilde{t}/t_\mu = t > 1$). The combined equation does a reasonable job in capturing the overall trend, but does not capture the small-amplitude irregular oscillations seen in the electrokinetic model's predictions. These oscillations only occur for drops when both charge and permittivity forces are present ($\kappa \neq 0$ and $\bar{\epsilon} \neq 1$). Further, they only occur when Oh < 1, suggesting that inertia plays a significant role. The origins of these small-amplitude oscillations are yet to be established.

5.4 Supercritical dielectric and conducting drops

A second series of simulations was conducted for supercritical drops, i.e. drops which deform, destabilize, and then eject progeny droplets from the tips. The key results from these simulations are outlined in this section. The destabilizing of a supercritical drop principally results from the motion of mobile ions inside the drop over time. To illustrate this, the deformation behaviour of two drops, one dielectric (without ions, $\kappa = 0$) and the other conducting (containing ions, $\kappa = 25$), is contrasted in Figure 5.7. We find that the electric forces deforming the drop are roughly comparable in magnitude when the electric capillary number of the dielectric case ($\mathrm{Ca_E} = 0.6$) is chosen to be twice that of the conducting case ($\mathrm{Ca_E} = 0.3$). As seen in Figure 5.7a, this results in both drops attaining a similar deformation ($D_\infty \sim 0.9$) at $t = 40$. However, qualitative differences exist, as seen in the (selected) drop contours in Figure 5.7b. Due to the disparity in timescale of

action of the forces, the permittivity force acts faster, as expected. As the dielectric drop is acted on by a field that is effectively twice that acting on the conducting drop, the initial deformation ($t < 30$) is higher. This can be seen when comparing the first three sets of drop contours ((i)-(iii) in Figure 5.7b and Figure 5.7c).

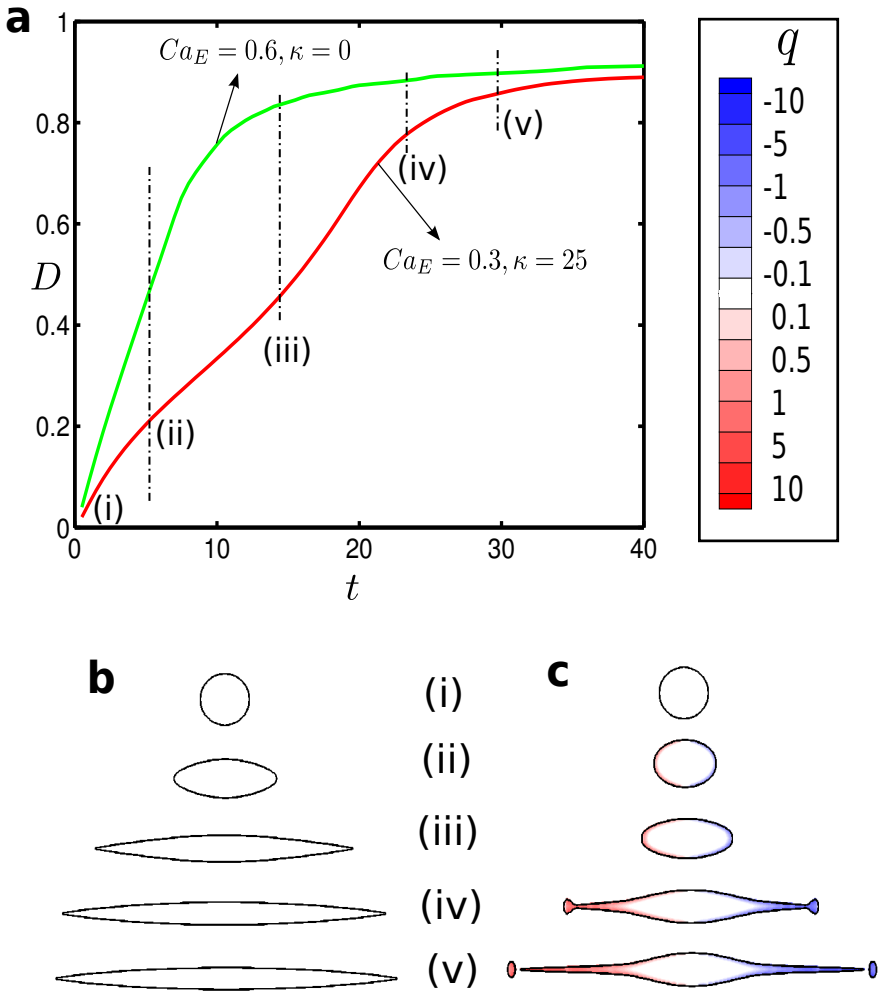

Figure 5.7: (a) Deformation curves for two drops, one dielectric and one conducting, respectively. Drop contours for $t = 0, 6, 15, 25, 30$ for (b) dielectric and (c) conducting drops respectively. Oh $= 1$ and $\bar{\epsilon} = 50$ for both cases. Charge contours have been overlaid for the case in (c).

An interesting feature is the formation of pointed tips on the dielectric drop, apparent in the bottom three frames of Figure 5.7b starting with (iii). This high-curvature drop

tip (known as a Taylor cone (Taylor, 1964)) results due to the spherically symmetrical acceleration of the fluid, when the (deforming) normal dielectric force (F_{P}) is continuously balanced by the (resisting) normal interfacial tension. For dielectric drops with a permittivity ratio greater than 17.6 (note $\bar{\epsilon} = 50$ in fig Figure 5.7), the drop tip continues to sharpen indefinitely (Ramos & Castellanos, 1994) , as seen in frames (iv) and (v), resulting in what is known as a conic cusping singularity (Zubarev, 2005). Importantly, this singularity implies that no ejection of progeny droplets is observed, even for high electric fields.

In contrast, the conducting drop deforms more slowly, as the charge takes a finite time to separate (see charge contours embedded). However, frame (iv) of Figure 5.7c for the conducting drop shows the formation of lobes at both ends, connected to the primary drop via threads. In frame (v), as a consequence of the Rayleigh-Plateau instability, the thickness of the thread goes to zero and the progeny drops break off. Being charged, the progeny drops are subsequently electrophoretically conducted away from the primary drop (not shown here). This phenomenon can be explained by the conduction of the ions inside the drop, adjacent to the interface, resulting in the tangential electric shear stress. The viscous stresses that arise in response transfer the axial momentum inwards (Collins *et al.*, 2007*b*), which increases the centerline velocity. This flow into the drop tips results in formation of lobes at both ends (Figure 5.7c -(iv)), which then accelerate away from the primary drop, on account of the greater charge force experienced by the charged lobes relative to the primary drop. As the breakup is mediated by both conductive and capillary effects, it is useful to define a ratio of their associated timescales (using Equation 5.4):

$$\alpha = t_{\mathrm{e}}/t_{\gamma} = \left(\frac{\epsilon_{\mathrm{d}}\epsilon_0}{\sigma}\right) \Big/ \left(\frac{\rho_{\mathrm{d}}^3 R^3}{\gamma}\right) = \mathrm{Pe} \Big/ (\mathrm{Oh}\,\mathrm{Re}\,\kappa^2)\,. \tag{5.16}$$

This resulting non-dimensional parameter (α) has been shown to determine the size of the progeny droplets for both Coulombic fission arising from infinitesimal perturbations of charged drops (Burton & Taborek, 2011) and electrical field induced cone-jetting of thin films (Collins *et al.*, 2007*b*), and shown to influence the growth rate of axisymmetric perturbations on electrified jets (López-Herrera *et al.*, 2005) (for e.g., $\alpha = 1.6$ in figure Figure 5.7(c)). Converted into the present scalings, the presence of Pe and κ indicates electrokinetic effects influence the progeny drop formation process. The perfect dielectric limit can now be interpreted as a limiting case when conduction of ions is too slow to have

any impact on the hydrodynamics, i.e. $t_e \to \infty$ (consequently $\alpha \to \infty$ as well). This has been referred to as the 'glued charge' limit (López-Herrera *et al.*, 2005), the implication being that the charges are glued to their location and are passively convected by the flow. No breakup occurs at this limit, when t_e is far larger than any of the other timescales (as shown in figure Figure 5.7b). It has been similarly shown that no breakup occurs when t_e is far smaller than the other timescales in the system either ($t_e, \alpha \to 0$). In this case, ionic conduction is instantaneous, and the drop behaves like a perfect conductor, with perfect charge screening and consequently no internal electric field. Any charge formed is instantly transported to the interface and the normal electric force inside the drop now incorporates both dielectric and charge effects. A quasi-steady balance with interfacial tension again results, and conic cusps form (Collins *et al.*, 2007*b*). For finite values of α, the charge transport along the interface, rather than towards it, gains importance (as the internal field is now nonzero). Consequently, electrohydrodynamic instability, and progeny drop ejection, results. This parameter space is studied in the next section.

5.5 Scaling laws for progeny drop radius.

The effect of α on the radius of progeny drops ejected $\widetilde{r_\mathrm{p}}$ is studied in figure Figure 5.8. Here $\widetilde{r_\mathrm{p}}$ is the dimensional (equivalent) radius of the progeny drop, scaled to the radius of the primary drop R. The results are plotted for a range of Ohnesorge numbers ($10^{-1} \leq \mathrm{Oh} \leq 10^{1}$). The base cases, represented by red squares in the figure, have $\kappa = 25$, $\bar{\epsilon} = 20$ and $\bar{\mu} = 1$. Cases with varying κ ($5 \leq \kappa \leq 25$), physically realizable by changing the conductivity of the drop, are shown as pink diamonds. Cases with varying viscosity ($0.1 \leq \bar{\mu} \leq 1$) and permittivity ($10 \leq \bar{\epsilon} \leq 50$), physically realizable by selecting different oils for the outer phase, are represented by green stars and blue triangles, respectively. Results involving varying the density ratio were shown to have negligible effects on progeny drop ejected, and are hence not shown. In addition, the results of Collins *et al.* (2007*b*), for drops ejected during cone-jetting of a liquid, leaky dielectric film in air, have been represented by black circles. The plot symbols in subsequent figures are consistent with these choices. Fig Figure 5.8 shows an increase in progeny drop size with α. Notably, the cases with varying drop conductivity, κ (magenta diamonds), are outliers to this trend. Though the trend is replicated in the results of Collins *et al.* (2007*b*), the progeny drops seen here are about two orders of magnitude larger. The electrohydrodynamic atomization/electrospray/tip-streaming phenomenon studied by Collins *et al.* (2007*b*) is characterized by emission of a cloud of drops in quick succession (Gañán-Calvo *et al.*,

1997) (Collins *et al.* (2007*b*) measure the first ejected drop), which are individually negligible in size compared to the primary drop. In contrast, the drops seen here are considerably larger. For example, the progeny drop ejected in figure Figure 5.7c has an equivalent radius of $\widetilde{r_\mathrm{p}} \sim 0.24R$.

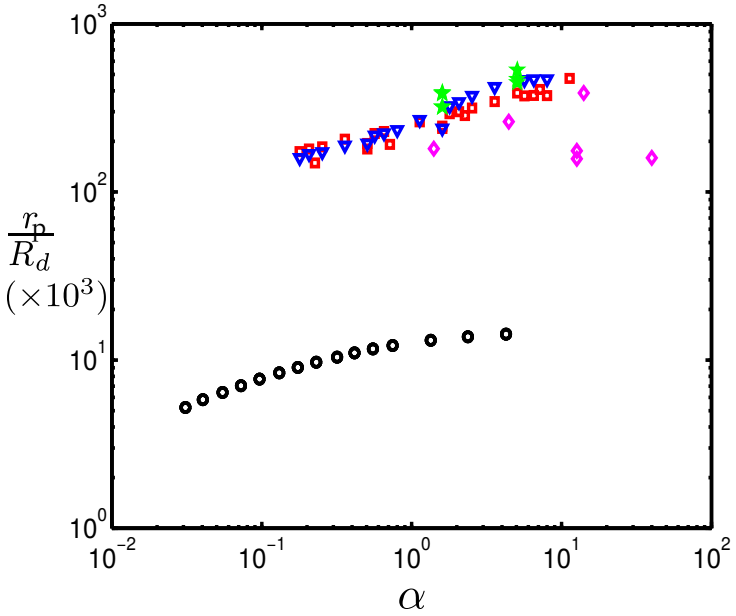

Figure 5.8: Equivalent radius of progeny drop for varying α. The coloured symbols represent results from simulations where only Oh has been varied (base cases, red squares), only $\bar{\epsilon}$ has been varied (blue triangles), only $\bar{\mu}$ has been varied (green stars), or only κ has been varied (pink diamonds). Results of Collins *et al.* (2007*b*) (figure 4a in their paper) have been represented by black circles.

In a follow up paper, Collins *et al.* (2013) numerically study the related problem of electrohydrodynamic tip-streaming of liquid drops suspended in air. They argue that, given the disparity of length scales between the primary and progeny drops, the drop formation process ought to be self-similar and amenable to the formulation of universal scaling laws. However, the disparity in scales, referenced in the capillary pinch-off literature, refers to the local time and length scales of the thinning liquid thread connecting the (primary and progeny) drops as it approaches the singularity, when compared to the respective global scales of the problem (Chen *et al.*, 2002). Indeed, the choice of terminology - 'pinch-off' - itself hints at a family resemblance to the kind of breakup seen

in figure Figure 5.7c. So the size of the progeny drop (which is of the order of the global length scale in our case) does not necessarily preclude the existence of scaling laws. This self-similar dynamical process only requires a non-uniform deforming force forming a slender thread connecting the drops, before interfacial tension drives flows that shrink the neck, leading to pinch-off (Eggers, 1993).

The non-uniform force driving thread formation can be varied in origin; expanding on the physical problem, typical examples include gravity on a dripping faucet (Subramani *et al.*, 2006), viscous stresses generated in a co-axial flow during microscale flow focusing (Anna & Mayer, 2006) and inertia in a jet emanating from a nozzle (Eggers & Villermaux, 2008). While the thinning thread approaches a singularity, the size of the progeny drops themselves can be quite large, approaching the global length scale in pendant drops (Zhang & Basaran, 1995), for example. In the problem studied here, the non-uniform charge force (F_{C}) drives the formation of a lobe, connected to the drop by a liquid thread, prior to pinch-off. The advantage of analysing electric field induced breakup by focusing on the capillary pinch off phenomena is that it allows for two simplifications; firstly, the local description of the motion in the thread near the point of breakup depends on the pinch-off length, $l_{\mathrm{po}} = \mu_{\mathrm{d}}^2 \rho_{\mathrm{d}} / \gamma$. Secondly, the time taken for the neck to shrink towards zero scales with the pinch-off time (Eggers, 1997), $t_{\mathrm{po}} = \mu_{\mathrm{d}}^3 \rho_{\mathrm{d}} / \gamma^2$. These scales, which only depend on the properties of the drop, can be readily obtained by a simple order of magnitude balance between the contributing terms in the Navier-Stokes equations (Lister & Stone, 1998). Following the lead of Collins *et al.* (2013), we nondimensionalise the progeny drop radius using the pinch-off length (l_{po}),

$$r^* = \tilde{r_{\mathrm{p}}} / l_{\mathrm{po}} \ , \tag{5.17}$$

and define the nondimensional quantity (β) as the ratio of the charge relaxation and capillary pinch-off timescales (using Equation 5.4),

$$\beta = t_{\mathrm{e}} / t_{\mathrm{po}} = \left(\frac{\epsilon_{\mathrm{d}} \epsilon_0}{\sigma} \right) \Big/ \left(\frac{\mu_{\mathrm{d}}^3 \rho_{\mathrm{d}}}{\gamma^2} \right) = \mathrm{Pe} \Big/ (\mathrm{Oh}^4 \, \mathrm{Re} \, \kappa^2) \ . \tag{5.18}$$

Note that the arguments made about the limiting case behaviour for α also apply to β, i.e. $\beta \to 0$ and $\beta \to \infty$ can be interpreted as the perfect conductor and perfect dielectric limits, respectively ($\alpha / \beta = \mathrm{Oh}^3$).

The simulations from figure Figure 5.8 are re-plotted using r^* and β in figure Figure 5.9a, using the same colour scheme. Good agreement is obtained with the results of

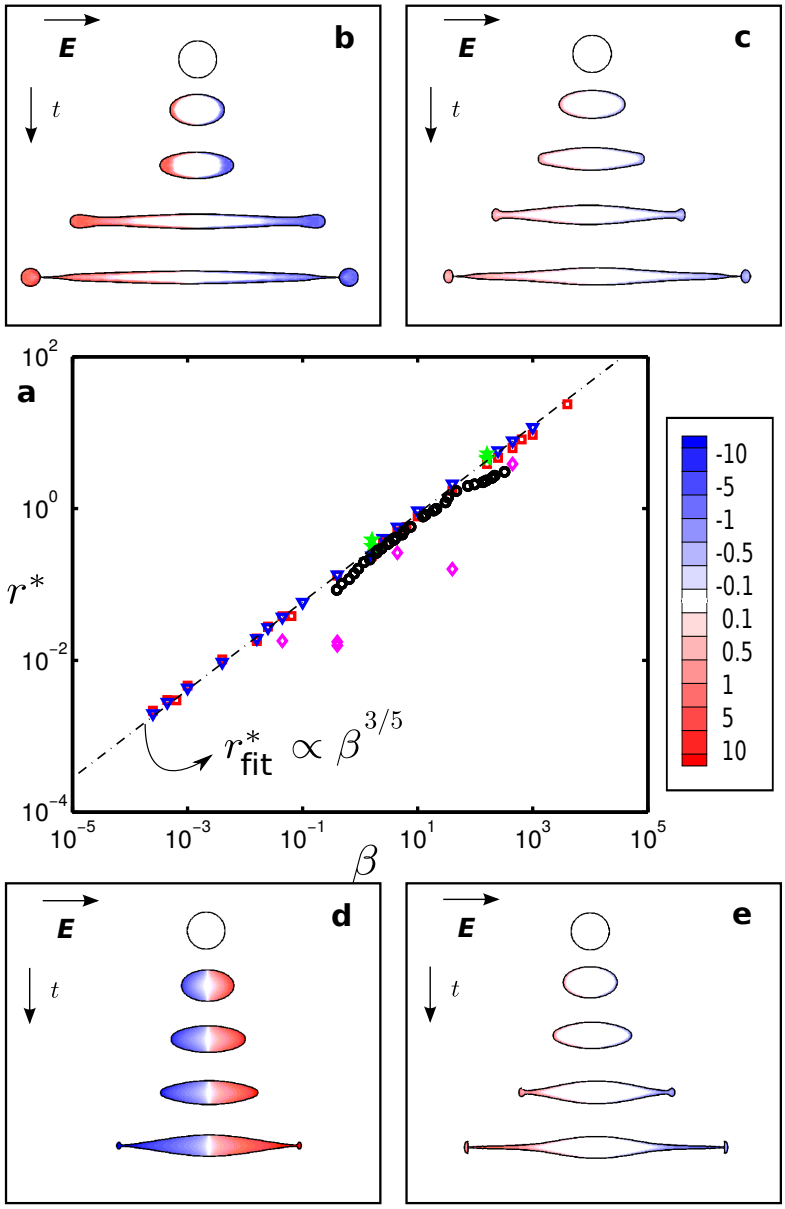

Figure 5.9: Clockwise (a) scaling law for r^* (Equation 5.17), employing the same colour scheme as figure Figure 5.8. Drop contours for selected cases are embedded, for (b) Oh $= 10^{-1}$, $\kappa = 25$ for t =0, 0.5, 1, 2, 2.3, (c) Oh $= 10^{0}$, $\kappa = 25$ for t =0, 7.5, 12.5, 17.5, 23.5, (d) Oh $= 0.316 \times 10^{1}$, $\kappa = 5$ for t =0, 80, 180, 220, 280 and (e) Oh $= 0.316 \times 10^{1}$, $\kappa = 25$ for t =0, 37.5, 75, 112.5, 150. The charge contours shown here are also used for Figure 5.10. Note that charge is normalized by zen_0, so a visual (quantitative) comparison between (d) and (e) does not represent physical charge.

Collins *et al.* (2013). This agreement is achieved despite the vast disparity in progeny drop radius noted in figure Figure 5.8, supporting the claim that the chosen scaling parameters provide a 'universal' solution. This is not entirely unanticipated; in fact we have previously shown, using the same electrokinetic model, that tip-streaming is observed in cases involving low conductivity ($\kappa \leq 3$) along with high electric field ($\mathrm{Ca_E} \gg \mathrm{Ca_{Ecr}}$) where $\mathrm{Ca_{Ecr}}$ is the electric field necessary to nudge the drop from a subcritical to a supercritical regime. Tip-streaming can be considered, therefore, to be a small progeny drop limit for capillary pinch-off. Collins *et al.* (2013) identify three distinct scaling regimes, $r^* \propto \beta^{2/3}$ for $\beta < 5$, $r^* \propto \beta^{1/2}$ for $5 < \beta < 50$, and $r^* \propto \beta^{1/3}$ for $50 < \beta < 200$. Because $\beta \propto 1/\sigma$ ($\beta \propto 1/\kappa^2$ in our scalings), these three regimes correspond to drops of high, medium and low conductivity, respectively. In contrast, we find a single scaling regime of $r^* \propto \beta^{3/5}$, which is closest to the value obtained by Collins *et al.* (2013) for low β ($r^* \propto \beta^{2/3}$), or highly conducting drops. Note that the outliers, as was the case in figure Figure 5.8, are the cases with varying drop conductivity (κ). This has been expanded on subsequently, in the section on modified scaling laws.

The transient drop evolution of selected cases has been illustrated in figures Figure 5.9(b-e), with overlaid charge contours. We first compare cases Figure 5.9d and Figure 5.9e, which have identical parameters except for different drop conductivities with $\kappa = 5$ and $\kappa = 25$, respectively. In addition to causing a lower conductivity, a lower κ also results in a thicker diffuse charge layer adjacent to the interface, as can be observed while comparing the panels 5.9d and 5.9e. The progeny drop size (and charge contained) also decreases slightly with decreasing κ, consistent with the findings in chapter 4. For panels 5.9b, 5.9c and 5.9e, the Ohnesorge number increases ($\mathrm{Oh} = 10^{-1}, 10^0$ and 0.316×10^1, respectively), i.e. β decreases (Equation 5.18). For capillary pinch-off, two types of behaviour can be outlined based on the value of Oh: if $\mathrm{Oh} < 1$, the thread formation results from a balance of interfacial tension and inertia, while for $\mathrm{Oh} > 1$, a balance of viscous forces and interfacial tension become more important (Burton *et al.*, 2004). It follows that for Figure 5.9b ($\mathrm{Oh} = 10^{-1}$), the higher inertia of the flow results in greater accumulation of mass (and charge) in the drop tips, before the (higher) interfacial tension pinches off the progeny drop. Note that the lower viscosity means that significant charge buildup is necessary before the axial momentum from the electric force, arising from the electric field acting on the diffuse charge layers adjacent to the interface, is transferred inwards. The flow into the tips is then initiated, resulting in even more charge formation (visible in Figure 5.9b). The relatively higher interfacial tension also smoothes regions of

high curvature, resulting in more rounded primary and progeny drops. In contrast, for Figure 5.9e, the higher viscosity means comparable charge buildup does not occur, as momentum is transferred inward relatively efficiently, and the relatively lower interfacial tension pinches off the thread more slowly (compare times in Figure 5.9b and Figure 5.9e) but still before the progeny drop in Figure 5.9e can grow to the size seen in Figure 5.9b, resulting in a smaller drop which contains less charge. The lower interfacial tension means that the drops are more deformable, and the primary drop appears tapered at breakup, while the progeny drop is flatter.

5.5.1 Dripping-jetting transition.

The dynamical behaviour of drops after the ejection of the first progeny drop is explored in Figure 5.10. Cases (a) and (b) are for Oh $= 10^{-1}$ ($\beta = 1.6 \times 10^{4}$) and Oh $= 3.16$ ($\beta = 1.6 \times 10^{-2}$), respectively, with all other parameters held constant. For case (a) the ejection of the first progeny drops (frame 2) is followed by retraction of the primary drop neck (frame 3) due to the higher interfacial tension (low Oh). Then as charge continues to accumulate at the ends, the process repeats itself with a smaller lobe (frame 4) resulting in the ejection of smaller progeny drops (not shown here). This behaviour is analogous to the dripping of water from a faucet. The key difference is that due to the continuous flow rate (from the faucet), the size of successive drops formed during dripping is either constant or follows a periodic pattern (Clanet & Lasheras, 1999). In contrast, each ejected progeny drop here is smaller than the preceding one. This is because the rate of charge-induced liquid flow is not constant, due to constraints of decreasing primary drop charge and volume following each instance of dripping.

The dynamics for case (b), for higher Oh, are qualitatively different. Once the progeny drop is ejected (frame 2), the locations of breakup (i.e. the necks of the primary drop) continue to move under the influence of the charge force. They appear to follow the moving progeny drops (frame 3). No retraction of the necks is observed as the interfacial tension is too low to retard the inertia of the moving tips. These tips form long, narrow jet-like structures before breaking up into multiple satellite droplets (frames 4 and 5), which are slightly larger in diameter than the cylindrical jet itself. This resembles the 'jetting' of a faucet when the flow rate is increased (Clanet & Lasheras, 1999). Oh, therefore acts as a means of controlling the liquid flow rate due to charge; the flow transitions from dripping at low Oh to jetting at high Oh. The ionic conductivity also plays a role as illustrated in

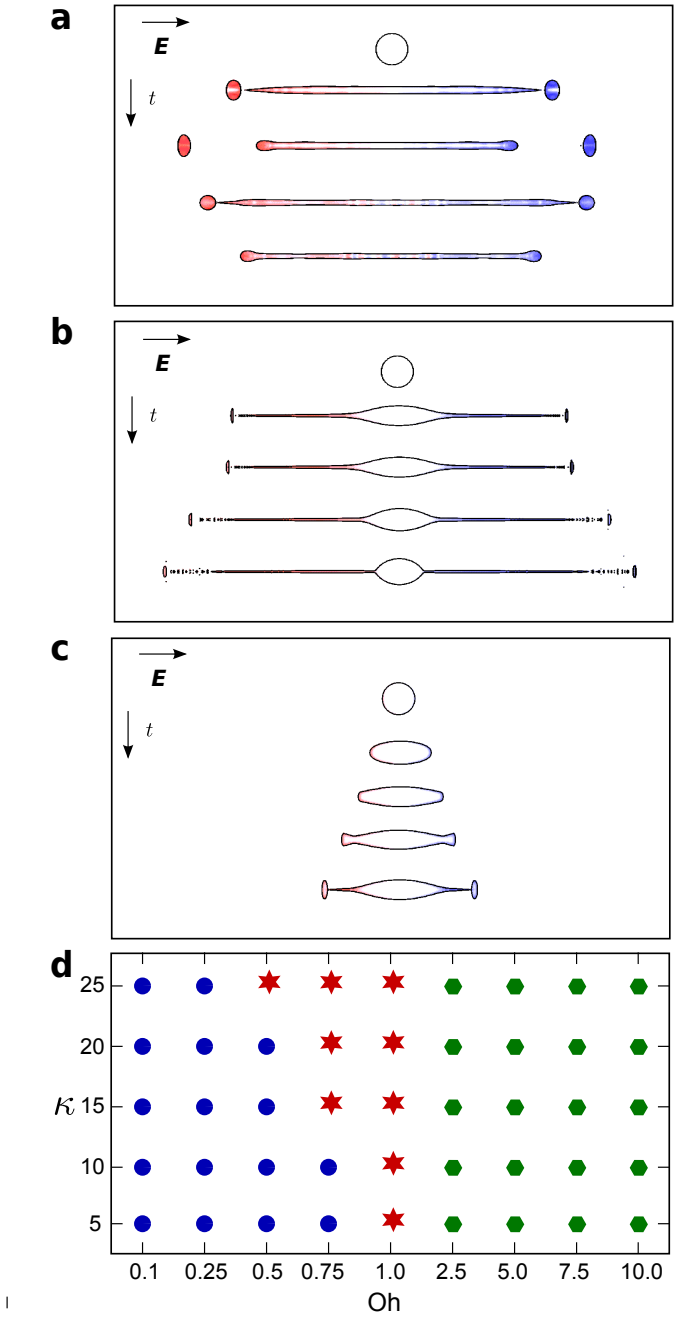

Figure 5.10: Case (a) $\mathrm{Ca_E} = 0.4$, $\kappa = 25$, $\bar{\epsilon} = 20$, $\mathrm{Oh} = 10^{-1}$, $\bar{\rho} = 0.1$ for times t =0, 1.19, 1.43, 2.22, 2.41, dripping. Case (b) $\mathrm{Ca_E} = 0.4$, $\kappa = 25$, $\bar{\epsilon} = 20$, $\mathrm{Oh} = 3.16$, $\bar{\rho} = 0.1$ for times t =0, 560, 580, 740, 940, jetting. (c) $\mathrm{Ca_E} = 0.30$, $\kappa = 25$, $\bar{\mu} = 0.1$ for times t =0, 75, 110, 125, 155. (d) $\mathrm{Oh} - \kappa$ phase map showing regions of dripping (blue circles), transition regime (red stars) and jetting (green hexagons).

the drop formation phase-map in Figure 5.10d. The study of electrohydrodynamic effects on drop breakup have focused on the latter jetting/electrospraying regime (Gañán-Calvo *et al.*, 2007; Collins *et al.*, 2007*b*, 2013). However jetting is unsuitable for microscale drop formation as resulting drop sizes can be unpredictable, and the contents polydisperse (Utada *et al.*, 2005). Instead, microfluidic devices use dripping for drop formation. Dripping is usually induced without an electric field by a variety of techniques like flow focusing, co-axial flow and T junctions (Baroud *et al.*, 2010). The velocities of both phases play a role in drop formation (Utada *et al.*, 2007), and the drop sizes can be manipulated with great precision (Fu *et al.*, 2012). We have shown here that there exists an analogous dripping regime ($\mathrm{Oh} < 1$) for electrokinetic drop formation that has not been explored in the literature. We also observe complex dripping behaviour, i.e. dripping accompanied by satellite droplet formation (Ambravaneswaran *et al.*, 2004) as well as dripping that transitions into jetting, for intermediate values of Oh, shown as red stars in Figure 5.10d.

5.5.2 Effect of physical parameters.

Among the physical parameters studied, density had minimal effect on (primary/progeny) drop shape, while drop permittivity variations had a small impact as shown in Figure 5.9a. The effect of viscosity ratio is under represented in the drop electrohydrodynamics literature, prominent exceptions being Lac & Homsy (2007) and Karyappa *et al.* (2014). We have shown, in Figure 5.9a, that the size of progeny drops is largely independent of viscosity ratio (for $0.1 < \bar{\mu} < 1$). Figure 5.10c shows the transient deformation of a case with identical parameters as the case in 5.7c, except a higher outer phase viscosity ($\bar{\mu} = 0.1$). Thus far, two types of drop deformations, pointed ends (for dielectric drops) and rounded lobe formation (for conducting drops), have been predicted. Here we see a third type of deformation, i.e. lobes with flat ends (see frame 3 onwards in Figure 5.10c). This results from the higher viscous resistance in the outer phase to drop deformation (compare times for Figure 5.10c and Figure 5.7c) resulting in a visible flattening even prior to lobe formation (frame 3). Consequently, the lobe formed has a relatively lower centerline velocity. This creates a more uniform flow profile in the lobe, resulting in a flatter progeny drop ejected, and a stouter primary drop, post-breakup. This is consistent with the findings of Karyappa *et al.* (2014). Given the slower breakup (compare times 5.7c and 5.10c), one would expect that the progeny drops shown here would contain greater charge.

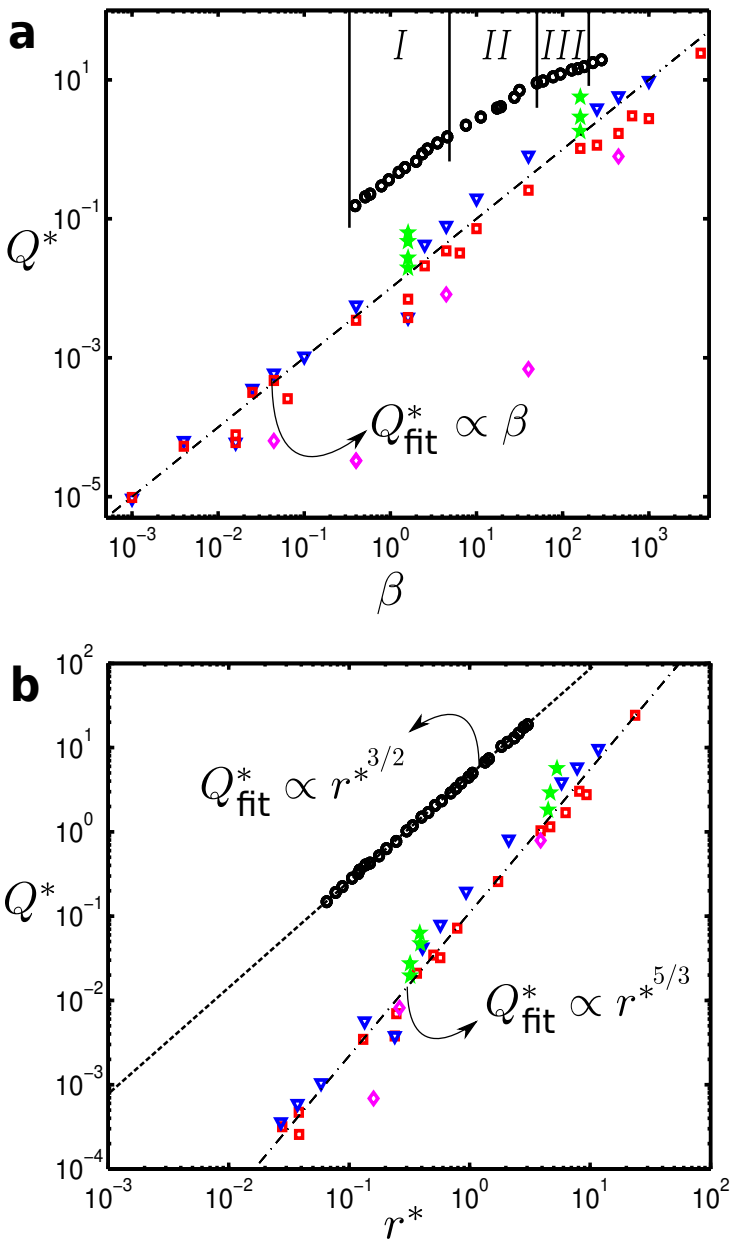

Figure 5.11: Scaling laws for (a) variation of scaled drop charge (Q^*, Equation 5.19) with (a) β and (b) r^* (Equation 5.17). Same colour scheme as figures Figure 5.9a and Figure 5.8 employed.

5.5.3 Charge contained in progeny drops.

It was noted earlier that, despite significant global agreement, rather than the three scaling regimes for scaled progeny drop radius (r^*) reported by Collins *et al.* (2013) for leaky dielectric drops, we only find a solitary relation in our electrokinetic simulations ($r^* \propto \beta^{3/5}$). Collins *et al.* (2013) also found three corresponding distinct scaling regimes for charge (Q^*) contained in progeny drops, where:

$$Q^* = \widetilde{q} \Big/ (\epsilon_c \gamma l_{po}^3)^{1/2} \, . \tag{5.19}$$

We have plotted the results of our simulations (using this scaling) along with those of Collins *et al.* (2013) in Figure 5.11a. Our results considerably under-predict the charge-to-mass ratio of the progeny drops when compared to the results of Collins *et al.* (2013). It must be noted that Collins *et al.* (2013), by virtue of the model used (leaky dielectric), measure interfacial charge, whereas we measure the bulk charge contained within the progeny drops. Also, the pinch-off process studied here produces significantly larger drops than those obtained by tip-streaming. Collins *et al.* (2013) again find three scaling regimes, $Q^* \propto \beta$ for $\beta < 5$, $Q^* \propto \beta^{3/4}$ for $5 < \beta < 50$, and $Q^* \propto \beta^{1/2}$ for $50 < \beta < 200$. These scaling regimes are identified respectively by roman numerals I, II and III in Figure 5.11a. For $\beta > 200$, they find that their scalings for r^* and Q^* no longer hold. However, significantly, the charge scaling relation in our simulations (see Figure 5.11a), $Q^* \propto \beta$ for all β, matches the relation obtained by Collins *et al.* (2013) for low β (region I in 5.11a), or highly conducting drops. This parallels the progeny radius scaling law ($r^* \propto \beta^{3/5}$) obtained earlier, which was close to the value obtained by Collins *et al.* for low β ($r^* \propto \beta^{2/3}$). Combining these sets of overlapping scaling regimes for Q^* and r^*, Collins *et al.* formulate what they refer to as 'the most fundamental scaling law of electrospraying', $Q^* \propto (r^*)^{3/2}$. Despite differences in magnitude of charge contained, we formulate a quite similar scaling law, $Q^* \propto (r^*)^{5/3}$, shown in Figure 5.11b. Additionally, our scaling laws apply to the entire range of simulations performed in this study.

It is useful here to re-introduce the Rayleigh limit (Rayleigh, 1882), which is the maximum charge that can be contained on a spherical drop above which is unstable to infinitesimal perturbations, given as,

$$\widetilde{Q}_R = (64\pi^2 \epsilon_c \gamma r^3)^{1/2} . \tag{5.20}$$

Using our scalings, we can define a ratio of progeny drop charge ($\tilde{q}$) to the Rayleigh limit,

$$\frac{\tilde{q}}{\widetilde{Q}_R} = Q^* \left[\left(\frac{V_e}{V_d} \right) \frac{\kappa^2 \, \mathrm{B} \, \mathrm{Oh}^2}{72} \right]^{\frac{1}{2}} \tag{5.21}$$

where V_e and V_d are the progeny and primary drop volumes, respectively. A progeny drop with $\tilde{q}/\widetilde{Q}_R > 1$ is expected to be Coulombically unstable and hence supercritical. Collins *et al.* (2013) found $\tilde{q}/\widetilde{Q}_R = 0.44$, independent of progeny drop radius. Instead of a constant $\tilde{q}/\widetilde{Q}_R$, a power-law relationship is found between the relative size of progeny drop and $\tilde{q}/\widetilde{Q}_R$ as shown in Figure 5.12. Note that, in our case, the charge forms layers adjacent to the interface rather than accumulating on the interface itself.

5.5.4 Modified scaling laws.

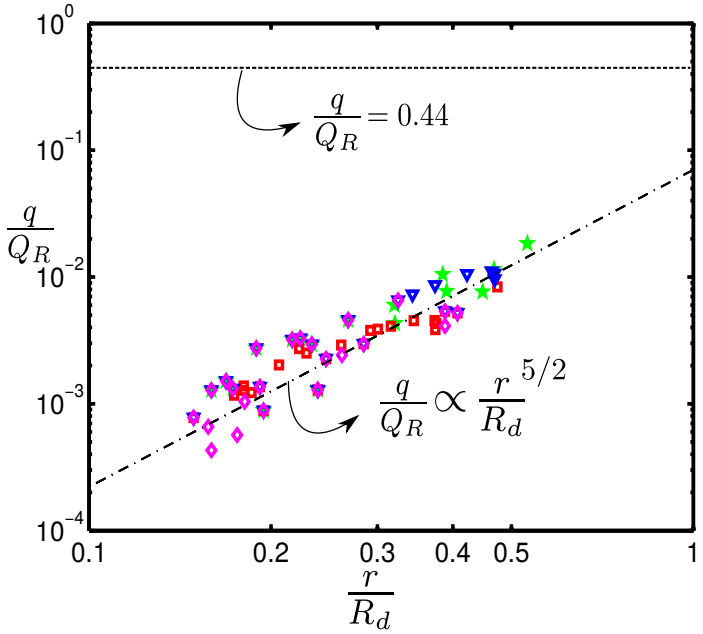

Figure 5.12: Plot showing relationship between relative progeny drop radius and ratio of progeny drop charge to the Rayleigh limit. The limit obtained by Collins *et al.* (2013) is shown as a dotted black line.

While experimentally studying Coulombic fission of charged drops, Hunter & Ray (2009) found that the size of progeny drops increases with decreasing conductivity, and underlined the importance of surface conduction in the process. Burton & Taborek (2011)

approached this problem numerically using a combined bulk and surface conduction model (for an inviscid drop), and found a similar increase in both progeny drop size and elongation of the primary drop at breakup. They attributed these to 'the reduced rate of charge transport to the pointed tips'. We see both of these features (elongation and increasing progeny drop size) when β is increased (i.e. effective conductivity decreased) by decreasing Oh ($\beta = \mathrm{Pe}\big/(\mathrm{Oh}^4\,\mathrm{Re}\,\kappa^2)$). Comparing drop shapes in Figure 5.9b and Figure 5.9c confirms that our predictions are consistent with the aforementioned studies.

However, crucially, we do not see this behaviour when the β is increased by decreasing κ (instead of Oh), which if the scalings were accurate, should have the same effect. Instead, comparing Figure 5.9e and Figure 5.9d (identical except for κ of 25 and 5, respectively), a decrease in drop elongation is seen, while the progeny drop size remains comparable. This is consistent with the findings in chapter 4, and is the reason why the outliers to the best-fit scales in Figure 5.9b and Figure 5.11a (which use β) are the cases with varying κ or drop conductivity (magenta diamonds). In an electrokinetic model, κ is associated with both the concentration of ions, as well as its distribution: A drop with a lower κ has a lower ion concentration (or conductivity), but also wider diffuse charge layers. Hence, the effect of the lower ion concentration is partially mitigated by the smaller momentum diffusion required for flow into the drop tips to be induced, and the charge transport into the tips is not reduced to the extent predicted by the scaling. This indicates that the charge relaxation timescale (used to formulate β), while still useful in a global sense (it can be used to estimate whether electrokinetic effects are important (Lim *et al.*, 2010), for example) is inadequate for describing local electrokinetic effects. In the absence of a suitable alternative, we propose a purely hydrodynamic scaling (Eggers & Villermaux, 2008). We have shown earlier that electrokinetic effects can be captured by the viscocapillary timescale ($t_\mu = \mu_\mathrm{d} R/\gamma$). When scaled with the pinch-off timescale (t_po) we get,

$$t_\mu/t_\mathrm{po} = \left(\frac{\mu_\mathrm{d} R}{\gamma}\right)\Big/\left(\frac{\mu_\mathrm{d}^3}{\rho_\mathrm{d}\gamma^2}\right) = 1\big/\,\mathrm{Oh}^2 \tag{5.22}$$

Using the inverse of Oh^2, we re-plot the scaling relations for Q^* and r^* in Figure 5.13. Comparing 5.9a and 5.13a, better agreement with the (least-squares) best-fit line is observed for cases with varying conductivity (magenta diamonds). Figure 5.13b shows that cases with lower conductivity have a lower charge-to-mass ratio compared to the base cases. Note that our scaling implicitly assumes that for the variations in drop ion

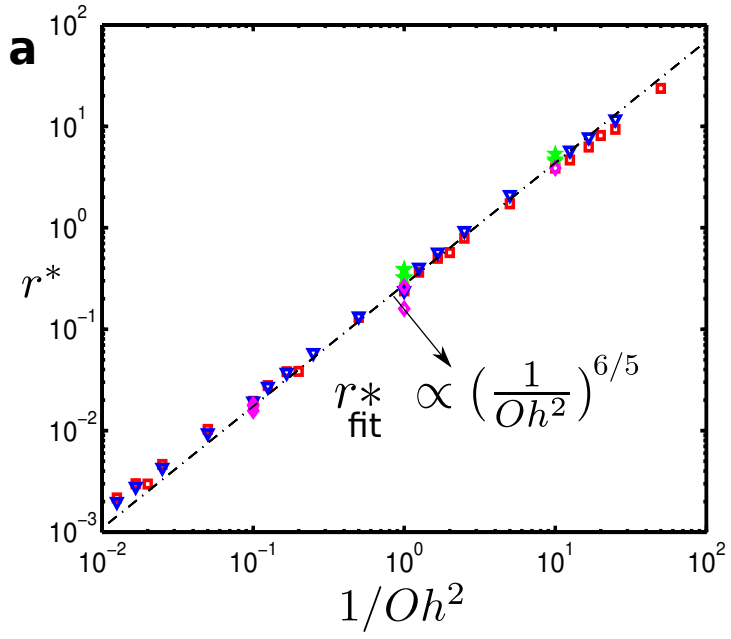

(a)

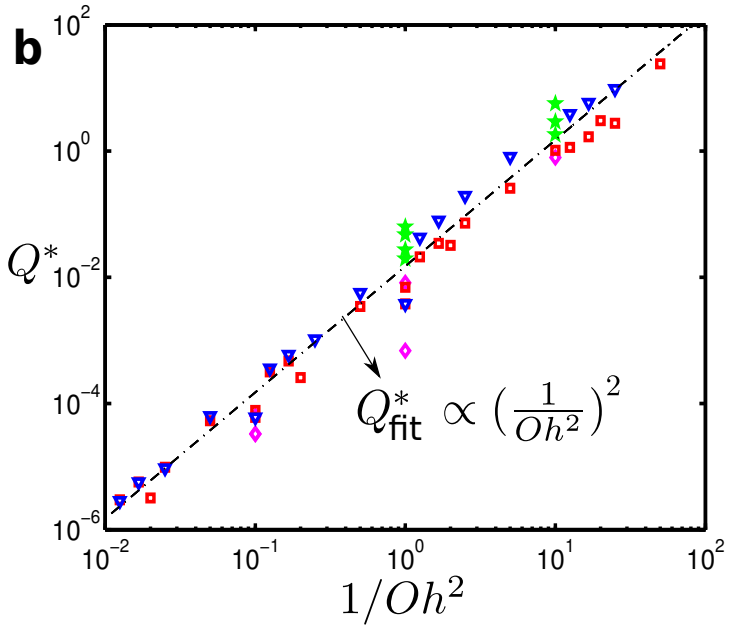

(b)

Figure 5.13: Scaling laws for (a) Q^* (Equation 5.19) and (b) r^* (Equation 5.17) with $1/\mathrm{Oh}^2$ Same colour scheme as figures 5.9a, 5.8 and 5.11 is employed.

concentration considered here ($5 < \kappa < 25$), effects of greater ion concentration are balanced by a more distributed charge force, yielding no net effect. The size variation in progeny drops can now be interpreted using only the definition of Oh in combination with the relative importance of permittivity and charge forces as Oh is varied, for a fixed Ca_E. Looking at 5.13b, it can be seen that changes in viscosity (see green stars) result in a larger charge-to-mass ratio, as predicted by the discussion regarding Figure 5.10c. Also, decreasing the permittivity ratio (blue triangles) results in greater charge contained in progeny drops. This follows from the fact that the F_C/F_T ratio is increased, resulting in greater charge-induced flow into the lobes and larger progeny drops being ejected for lower $\bar{\epsilon}$. Note that, by combining these scaling laws (figures 5.13a and 5.13b), we recover the fundamental scaling relationship for the electrokinetic effect induced pinch-off, $Q^* \propto (r^*)^{5/3}$ as shown in Figure 5.11b. Since this work was completed, Gañán-Calvo *et al.* (2016) have discovered the existence of similar scaling relationships for electrosprays.

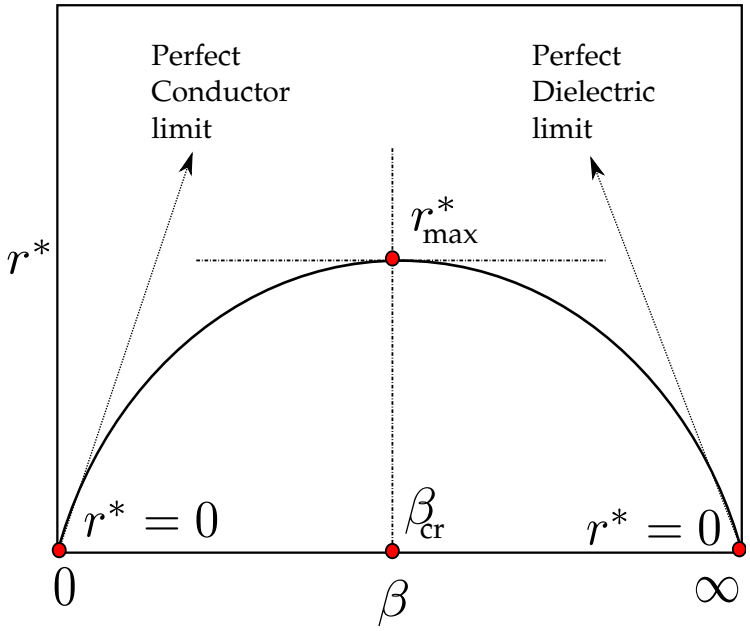

Figure 5.14: Qualitative map of (expected) progeny drop radius (r^*) variation based on known values ($r^* = 0$) at the perfect conductor ($\beta \to 0$) and perfect dielectric ($\beta \to 0$) limits

One unreported aspect of the variation of r^* with β requires comment; if both $\beta \to 0$ and $\beta \to \infty$ limits are characterized by no progeny drop formation ($r^* = 0$), then surely

the scaling law presented in Figure 5.9a only applies to the positive slope beginning near the perfect conductor limit (A qualitative illustrative is provided in Figure 5.14). This raises some interesting questions. *What is the maximum progeny drop ($r^*_{\max}$) size (at the inflection point) and associated critical ($\beta_{\rm cr}$) value? What scaling law best describes the downward slope of progeny drop size from $\beta_{\rm cr}$ to the perfect dielectric limit?* According to the limiting case behaviour, both $\beta \to 0$ and $\beta \to \infty$ would be characterized by conic cusping, giving way to progeny drop formation for finite β. Figure 5.14 assumes the slopes to be symmetrical around $r^*_{\max}$ for illustrative purposes. It is strongly suspected that these slopes aren't, in fact, symmetrical. Instead it is expected that the downward slope (from $r^*_{\max}$ to $\beta \to \infty$) is much steeper. Unfortunately, due to numerical constraints, this problem could not be probed further. As Oh is decreased (β increased) past the region displayed in Figure 5.9a, the lower viscosity, combined with less charge formation, results in less momentum transfer, resulting in a smaller lobe. However, as elaborated in the section on subcritical drops, a smaller Oh results in electrokinetic effects taking longer to impact the drop deformation. The relatively higher dielectric force stretches the drop significantly in the time period, consequently, which requires a larger domain to eliminate wall effects. Additionally, the long threads formed in this elongation are much more sensitive to small variations in capillary pressure, resulting in asymmetrical breakup. In this chapter, attention has been, therefore, focused to the region between the perfect conductor ($\beta \to 0$) and peak progeny drop $\beta = \beta_{\rm cr}$ limits.

5.6 Conclusions

The problem of transient electrohydrodynamics of a liquid drop containing ions is considered for an axisymmetric, conducting drop, subjected to an external electric field. Two electric forces act on the drop; the first force is due to charged regions formed by ion migration (charge force) while the second force results from a mismatch of permittivities at the drop interface (permittivity force). For subcritical drops, the charge force scales with the viscocapillary timescale ($t_\mu = \mu_{\rm d} R/\gamma$), while the permittivity force scales with the inertio-capillary timescale ($t_\gamma = \sqrt{\rho_{\rm d} R^3/\gamma}$). The relative importance of these forces on the drop deformation process is characterized by the Ohnesorge number ($\mathrm{Oh} = t_\mu/t_\gamma$). For $\mathrm{Oh} \geq 1$, the charge force controls the drop deformation, and steady state is achieved when charge separation is completed. For $\mathrm{Oh} < 1$, the permittivity force is more important, and can cause non-monotonic oscillatory deformation behaviour, and ongoing charge dynamics following steady state deformation.

For supercritical drops, the size of progeny drops ejected was scaled successfully using the capillary pinch-off time and length scales, as suggested by Collins *et al.* (2013). Scaling laws were obtained relating the progeny drop size and progeny drop charge. It was shown that electrokinetic effects cannot be reliably predicted by the ubiquitous charge relaxation timescale. Instead, a hydrodynamic timescale based on viscocapillary effects was proposed, which fit our simulations better. As opposed to the three scaling relations proposed by Collins *et al.* (2013) for leaky dielectric drops, we find a single universal scaling relation that holds across a wider range of parameters. It was also shown that Oh controls the liquid flow rate due to charge inside the drop. Progeny drops are formed in a dripping regime at low Oh, and in a jetting regime at high Oh.

A common aspect connecting our sections on subcritical and supercritical drops is the diminished importance of electrokinetic effects when the Oh is small, for the permittivity ratios ($\bar{\epsilon} \geq 10$) and inverse dimensionless Debye lengths ($5 \leq \kappa \leq 25$). For subcritical drops, the early oscillatory behaviour can be effectively separated from the viscous and electrokinetic effects, and a linear superposition of the two is effective at describing the drop behaviour. For supercritical drops, no electrohydrodynamic breakup is observed below $\mathrm{Oh} < 0.1$, as dielectric forces deform the drop too quickly for charge induced lobes to form at both ends. This indicates that an electrokinetic model is probably unnecessary for $\mathrm{Oh} < 0.1$ as the pertinent timescale of interest, that of drop deformation, can be simulated using the much simpler perfect dielectric approach. A similar limit probably exists for high Oh as well, when a perfect conductor assumption is valid; however, this regime is inaccessible using the current approach because the double layers beyond $\kappa = 25$ are too thin to be resolved numerically. For the regime in between these limits, the general electrokinetic model yields significantly different transient drop dynamics from approaches that assume homogeneous bulk conductivities. The results in this chapter will inform future applications involving microscale two-phase electrohydrodynamic flow and be instructive to experimental design.

This chapter concludes the study of isolated-drop systems. For microfluidic devices, most experimental work tends to involve moving drops as opposed to stationary drops. In other cases, more complicated drop scenarios, such as drop-drop coalescence and drop-interface coalescence, are studied. Consequently, the next chapter focus on studying (simplified) coalescing-drop systems. It, however, builds on the fundamental physical

understanding of isolated drop electrohydrodynamics gained thus far.

6 Coalescence of charged drops

> *In the land of splashes, what the scientist knows as Inertia and Surface Tension are the sculptors in liquids, and fashion from them delicate shapes none the less beautiful because they are too ephemeral for any eye.*
>
> Harold Edgerton and James Killian

This chapter studies the effect of an electric field on the coalescence process of a charged microdrop of electrolyte solution, suspended in non-conducting oil. The goals of this chapter are to explore interesting aspects of coalescence behaviour for drop-interface and drop-drop systems, and further develop quantitative criteria to characterise the results. This chapter begins with an introduction to the mechanism of drop charging and its relevance to LoC devices (§ 6.1). Next, the model modifications necessary to simulate charged drops are outlined (§ 6.2). Then the model is used to study two different systems: The first is the coalescence of a charged drop into an electroneutral bulk liquid (§ 6.3). The second is the coalescence of two oppositely-charged drops (§ 6.4). In both cases, we are able to qualitatively replicate existing results in the literature, discover new phenomena, and develop a quantitative understanding of the underlying physics.

6.1 Introduction

When an initially electroneutral drop comes into contact with an electrode, it acquires a net charge (Jung *et al.*, 2008). While the precise mechanisms underlying contact charging have not yet been established (Im *et al.*, 2011), it is understood that the drop is, post charging, electrophoretically conducted away from the electrode by the electric field. This

This chapter is based on the author's papers R. Pillai, J. D. Berry, D. J. E. Harvie and M. R. Davidson, 'Electrophoretically mediated partial coalescence of a charged microdrop', *Chemical Engineering Science*, 2017, 169, 273-283, 'Electrohydrodynamic deformation and interaction of microscale drop pairs', *International Journal of Computational Methods and Experimental Measurements*, 2016, 4, 33-41, and R. Pillai, J. D. Berry, D. J. E. Harvie and M. R. Davidson, 'Electrophoretic effects on satellite droplet formation during electrocoalescence of microdrops', *11th International Conference on CFD in the Minerals and Process Industries*, 2015

phenomenon, known as Contact Charge Electrophoresis (CCEP) (Drews *et al.*, 2015) (alternatively Electrophoresis of a Charged Drop (ECD) (Im *et al.*, 2015)), can be used to perform the precise drop manipulation required in microdrop based lab-on-a-chip (LoC) devices (Jung & Kang, 2009). The key advantage of this approach is that the direct charging of microdrops is efficient compared to alternative approaches, which makes the subsequent electrophoretic actuation stronger and more consistent (Im *et al.*, 2013). These devices treat each drop as a microreactor encapsulating a chemical/biological entity of interest (Theberge *et al.*, 2010), which is subsequently transported and analyzed. The contents of the drop are extracted by coalescing it into a bulk liquid (Fidalgo *et al.*, 2009).

Oppositely-charged microdrops can interact during CCEP/ECD LoC device operation (Link *et al.*, 2006); recent experiments have shown that fascinating physical phenomena can occur under specified conditions for oppositely-charged *macrodrop* coalescence (Ristenpart *et al.*, 2009). Thus, the fundamental understanding of electrically induced coalescence of charged microdrops, for both drop-interface and drop-drop systems, is both intrinsically interesting, and relevant for designing LoC devices (Zhao & Middelberg, 2011). It is also pertinent to a host of industrial applications, including electrohydrodynamic inkjet printing (Choi *et al.*, 2008) and electrical demulsification (Eow *et al.*, 2001*b*). However, it has received scant attention in the numerical modelling literature, in part due to the complexities involved in modeling two-phase electrophoretic flow (Pagonabarraga *et al.*, 2010). By means of a minor modification to the electrokinetic model discussed in previous chapters, a model for *charged* drops is developed in the next section.

6.2 Model overview

The drop can acquire net positive/negative charge which is physically achievable through direct contact with a positive/negative electrode (Jung & Kang, 2009). Here, the charge is implemented by initializing the drop with a uniform deficit of anion/cation density (n_-/n_+), such that $\Delta q > 0/\Delta q < 0$, where Δq is the (initial) dimensionless average charge density within the impacting drop ($\Delta q = n_+|_{t=0} - n_-|_{t=0}$). Note that the water/oil interfaces are taken to be uncharged; in practice these interfaces tend to assume a small negative charge (Creux *et al.*, 2009). A steady (DC) electric field $\boldsymbol{E}$ is imposed along the negative z axial direction. The interface between the water and oil is taken to have

a constant interfacial tension γ. To simplify the problem, the phases are assumed to have equal viscosities ($\mu_c = \mu_d$), densities ($\rho_c = \rho_d$) and relative permittivities ($\epsilon_c = \epsilon_d$). We see little effect of varying density on drop deformation behaviour, and note that oils with viscosities (Teh *et al.*, 2008) and dielectric constants (Ha & Yang, 2000*a*) close to that of water have been employed in microfluidic devices. The width and height of the computation domain were $4R$ and $20R$, respectively. The height of the bulk fluid (when present) was $5R$. Tests were undertaken ($\pm 2R$) to ensure that the domain size (including height of bulk fluid) was sufficiently large to contain the shapes of interest as well as minimize boundary effects in each case. Grid refinement showed that increasing the mesh resolution from 16 cells per drop radius (R) to 32 cells per R resulted in insignificant changes to the measured charge and size ($< 2\%$) of residual drops, and it is the latter grid resolution that is used for all simulations described here.

6.3 Case I: Coalescence of a charged drop and a bulk liquid

Surface energy arguments indicate that complete coalescence is energetically favoured when an *uncharged* drop contacts its bulk liquid as it minimizes the total surface area (Charles & Mason, 1960*b*). Sometimes, incomplete or partial coalescence can occur, resulting in the pinching-off of a 'residual droplet'. This is temporary as the newly-formed residual droplet subsequently proceeds to coalesce with the bulk liquid (Aryafar & Kavehpour, 2006). When a *charged* drop is conducted towards its bulk liquid in the presence of an external electric field, electrohydrodynamic effects can induce a similar partial coalescence phenomenon (Aryafar & Kavehpour, 2009). However, unlike the hydrodynamic case, the residual droplet moves away from the interface (towards the top electrode) indicating that it has switched charge during the coalescence process (Mousavi-choubeh *et al.*, 2011*a*). Despite the charge transference occurring, remarkably, the size and charge of the residual droplet was found to be independent of the ionic conductivity of the original charged (macroscale) drop (Hamlin *et al.*, 2012). Instead, residual droplet formation, for a fixed electric field, was understood to be a pure inertio-capillary process, with convection determining the quantity of charge transferred.

Depending on the application, either complete or partial coalescence can be desirable in microfluidic devices (Minardi *et al.*, 2013). Predicting and controlling the coalescence outcome requires insight into the physics of charge-transfer during microdrop coalescence. As the width of the space charge regions becomes significant in comparison to the drop

size (Masliyah, 2006) for microdrops, charged microdrop dynamics differs in important ways from its macroscale counterpart. To date, the phenomenon of charged drop coalescence (into an electroneutral bulk liquid) has been studied exclusively in the context of macroscale drops (Charles & Mason, 1960*a*; Aryafar & Kavehpour, 2009; Mousavichoubeh *et al.*, 2011*a*; Hamlin *et al.*, 2012), where the charge can be assumed to be located entirely on the interfaces; conduction dominates and diffusion can be assumed to be negligible. In contrast, for microdrops, an electrokinetic model that accounts for the diffusive, conductive and advective transport of individual ion species, is needed to accurately capture the essential physics (Delgado *et al.*, 2007). In this section, the electrophoretic coalescence of a charged microdrop into its electroneutral bulk liquid is studied, using a recently developed multiphase electrokinetic model (Berry *et al.*, 2013). We focus on the transition between complete and partial coalescence. In particular, we seek to shed light on the fundamental questions: *when do residual droplets form and what affects their size and charge?*

Results are presented here for a charged drop coalescing into its bulk liquid. Based on the problem setup (Figure 6.1), the drop is intialised at a distance $\bar{S}$ ($\bar{S} = S/R$) above the bulk liquid interface. The drop has a finite (dimensionless) average charge density ($\Delta q > 0$), while $\Delta q = 0$ initially in the electroneutral bulk liquid. The drop is otherwise identical to the bulk liquid. As the drop is positively charged, it is conducted in the direction of the electric field, i.e. towards its bulk liquid (Figure 6.2); it is thus induced to coalesce into its bulk liquid.

6.3.1 Complete coalescence

A complete coalescence case is studied in figure (6.2), where $\mathrm{Oh}^2 = 1$, $\mathrm{Ca_E} = 0.20$, $\kappa = 10$, $\Delta q = 0.1125$ and $\bar{S} = 1$, with overlaid charge contours. The ions are present both inside the drop, and in the bulk phase. As both ion species are initially distributed equally and uniformly in the bulk liquid (to ensure electrical neutrality), it is colourless in the first frame. The drop, on the other hand, is positively charged, and the excess cations are uniformly distributed initially. However, the electric field imparts equal but opposite conductive fluxes to each ion species (in both drop and bulk liquid) which results in anions migrating to one end of the drop and cations to the other. In the bulk liquid, depletion of cation species from the initially neutral region (just below the interface) leads to the formation of regions of negative charge (frame b). A symmetric region of positive charge also forms within the bulk liquid, at the lower boundary of the computational

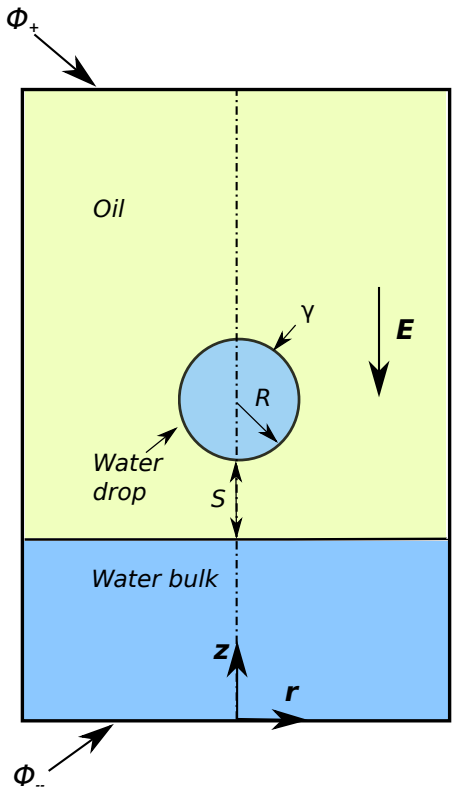

Figure 6.1: Schematic of an axisymmetric, positively charged drop of water (symmetry boundary conditions are applied on the vertical centerline), suspended in oil, and acted on by a downward-acting external electric field parallel to the z direction. The electric field electrophoretically conducts the drop towards its bulk liquid at the bottom of the domain.

domain (not in the frame).

As the ions travel towards opposite ends of the drop, the regions of charge first develop at the drop tips, forming bands next to the upper and lower interfaces. The thickness of these bands is governed by the choice of κ. The electric field acts on the charged regions, resulting in a deforming electric force which stretches the drops, as seen in the third frame. As seen in chapter 4 and chapter 5, had the drop had been electroneutral (and the bulk liquid was absent), the regions of charge would continue to form at both ends, but the centre of the drop would stay stationary as it deformed. However, as the drop has a net charge, it moves and approaches the interface as it deforms (frame 6.2c), and eventually makes contact with it (frame 6.2d). Because the bulk

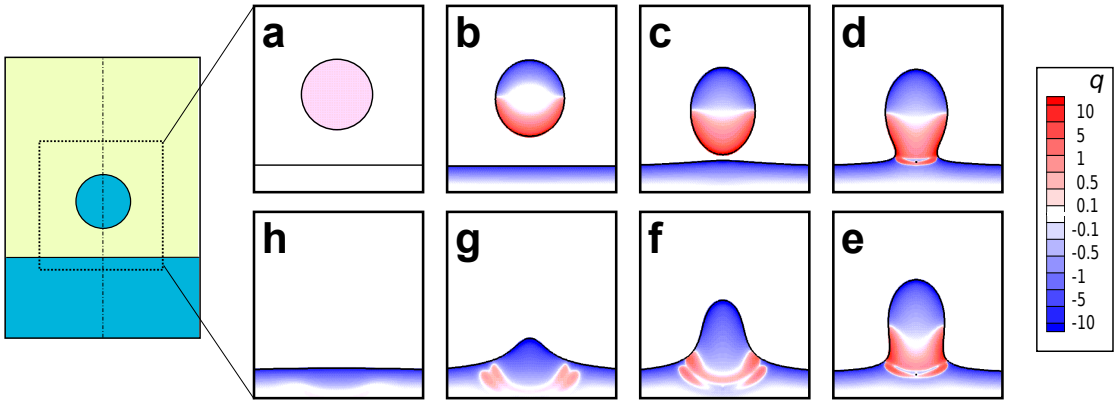

Figure 6.2: Left: schematic of numerical domain with box showing region of interest. Center: time lapse images (clockwise, starting from top left) of a water drop ($\mathrm{Oh}^2 = 1$, $\mathrm{Ca_E} = 0.20$, $\kappa = 10$, $\Delta q = 0.1125$ and $\bar{S} = 1$) undergoing complete coalescence, $t = 0, 20, 95, 102.5, 105, 110, 115, 145$. Right: charge ($\Delta q$) contour scale for relevant figures in this section.

surface and the approaching drop interface are oppositely charged, they experience an electrostatic attraction which lifts the bulk interface upwards prior to contact (frame 6.2c).

In the absence of an electric field, a contacting drop - planar interface would take a finite time to coalesce, which would occur once the interfacial film of oil separating them had ruptured. But the electric field (and corresponding electrical force) creates an attractive force between the inner tip of the drop and the upper surface of the bulk liquid, which accelerates the drainage of the oil film and the coalescence event happens almost instantaneously (Aryafar & Kavehpour, 2009). Here, we observe the coalescence occurring in the transition from frames 6.2c and 6.2d, 7.5 time units apart. At this point, the curvature of the impacting drop is far greater than that of the bulk liquid. Hence, the capillary pressure inside the drop approximately exceeds the corresponding value in the bulk by the Laplace pressure of $2\gamma/R$. The analysis of Anilkumar *et al.* (1991) shows that the interfacial energy of the drop is of order $R^2\gamma$, and this energy is converted into kinetic energy of order $\rho_\mathrm{d} R^3 u^2$ post interfacial film rupture, which facilitates the drop penetration into the bulk. When the two energies are equated, the velocity of the drop penetration just after film-rupture is estimated to be $u \sim \mathcal{O}(\sqrt{\gamma/\rho_\mathrm{d} R}) = 1$ m/s. For the case shown here, we calculate velocities of ~ 0.5 m/s, which are comparable. An interesting feature is the temporal development of the region of bulk phase surrounded

by drop phase (first visible as a curved slit near the bottom of the drop in frame 6.2d), which gradually leads to the separation of the drop charge into two narrow wavelike structures with large rounded ends (frames 6.2f - 6.2g), prior to dissipation (frame 6.2h).

6.3.2 Transition to partial coalescence

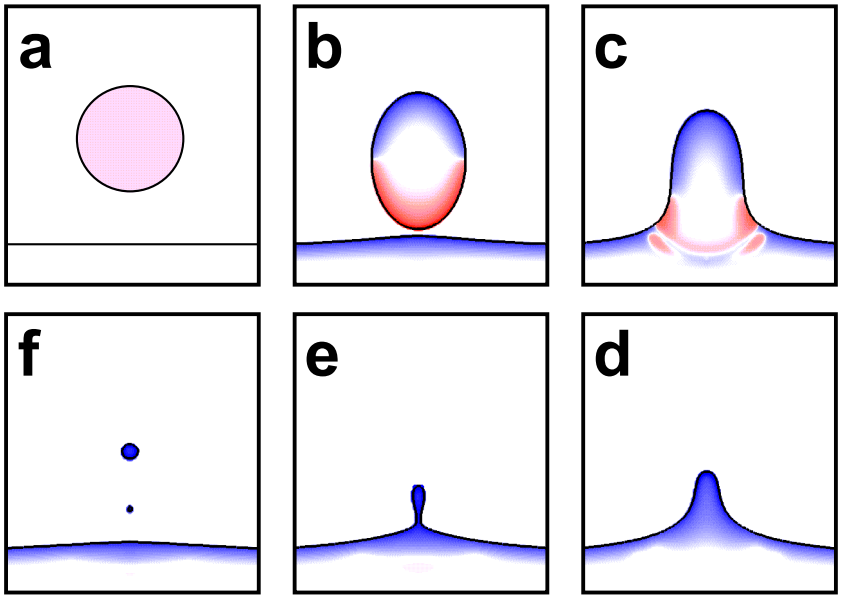

Figure 6.3: Time lapse images (clockwise, starting from top left) of a water drop ($\mathrm{Oh}^2 = 1$, $\mathrm{Ca_E} = 0.20$, $\kappa = 15$, $\Delta q = 0.05$ and $\bar{S} = 1$) undergoing partial coalescence ($a/R = 0.003$), $t = 0, 60, 70, 80, 86, 95$. The overlaid charge contours employ the same scale as figure (6.2).

In figure (6.3), the coalescence process of a drop with a higher bulk ion concentration ($\kappa = 15$) than the case in Figure 6.2, is illustrated. Note that the dimensional charge in the impacting drop (Q) can be related to the average (dimensionless) charge density (Δq) by

$$Q = \left(\frac{\epsilon_0 \epsilon_\mathrm{d} k_\mathrm{B} T V}{2 z e R^2} \right) \kappa^2 \Delta q, \tag{6.1}$$

where V is the volume of the drop. Note that $Q \propto \kappa^2 \Delta q$, if physical parameters except for the bulk ion concentration are held constant. Therefore, in order to maintain constant (dimensional) overall drop charge ($\kappa^2 \Delta q = 11.25$) as κ is increased, the average (dimensionless) charge density Δq is decreased from 0.1125 (Figure 6.2) to 0.05 (Figure 6.3).

The higher ion concentration (measured by κ) means that the drop deforms faster, as there is greater charge separation at both ends of the drop (even though the *net* dimensional drop charge is the same for the cases in figures (6.2) and (6.3)). This enables the drop to reach the interface and coalesce into the bulk liquid faster as well (see t values in respective figure captions). The higher κ also results in a narrower diffuse charge layer adjacent to the interface, plainly observable when comparing the cases (frame b of Figure 6.3 against frame c of Figure 6.2). However, unlike the case in Figure 6.2, the drop fluid pinches off to eject a residual droplet, i.e. partial coalescence is observed. This residual droplet then breaks into two droplets (frame 6.3f), which move vertically away from the interface (not shown here). The equivalent radius of the residual droplet (a), calculated from its measured volume, is 0.3 % of the radius of the original drop ($a/R = 0.003$).

Mechanism of partial coalescence

The high velocity of drop penetration into the bulk in Figure 6.3 begs the question as to why complete coalescence *isn't* observed. The answer lies in the nuanced role interfacial tension plays in the coalescence process, along with the role of charge. In the absence of gravitational effects (as is the case here), the coalescence process is controlled by a competition between vertical and horizontal rates of collapse, both driven by interfacial tension. The vertically downward acting collapse, resulting from the capillary pressure difference between the drop and the bulk liquid outlined earlier, usually dominates over the inward horizontal collapse, driven by the capillary pressure arising from the azimuthal curvature of the neck. This means that the vertical collapse tends to prevail (as was the case in figure (6.2)), and the drop tends to coalesce into the bulk (Blanchette & Bigioni, 2006).

For the horizontal collapse to prevail, and pinch off of the drop to occur, the vertical collapse must be sufficiently delayed by a suitable mechanism. For larger drops with sufficiently high interfacial tension ($\mathrm{Oh}^2 \leq 10^{-4}$), the convergence of capillary waves at the drop summit provide a suitable hydrodynamic mechanism (Blanchette & Bigioni, 2009). In the case studied here, with $\mathrm{Oh}^2 = 1$, this mechanism is absent. As such, upon application of an external electric field, it is the electrophoretic lift force generated by the negative charge near the upper drop interface, interacting with the downward electric field, that acts as a delaying electrohydrodynamic mechanism. While the positive charge at the lower interface is convected into the bulk liquid (frames 6.3b - 6.3c), the influence of the near-symmetric negative charge formed at the upper drop interface opposes this

convective fluid drainage into the bulk, delaying it until horizontal collapse occurs, and resulting in pinch-off and the formation of a residual droplet.

This residual droplet is subsequently electrophoretically conducted away from the interface, indicating the switch in net charge from positive to negative. This switch is a consequence of the positive charge being convected out of the bottom of the drop, resulting in a residual droplet containing (primarily) the residual negative charge. The coalescence process can therefore be understood as a competition between the electrophoretic force acting upward at the top of the drop and the capillary force acting downward; charged drops coalesce completely below a critical bulk ion concentration (figure (6.2), lower electrophoretic lift force), and partially above it (figure (6.3), higher electrophoretic lift force). This understanding is consistent with the macroscopic drop study of Hamlin *et al.* (2012), who found a similar critical ionic conductivity separating regimes of partial coalescence (lower electrophoretic lift force), and non-coalescence or 'bouncing' (higher electrophoretic lift force). This is relevant to microscale flows as the bulk ion concentration of the electrolytic solution, which is used to produce the drops employed, is adjustable; experimentally, this is achieved by varying the concentration of ionic salts (KCl, for example (Sadri *et al.*, 2013)) in the electrolyte solution. Consequently, the desired coalescence outcome can be achieved by choosing an appropriate value of κ.

Effect of drop charge

In addition to bulk ion concentration, the dimensional charge (Q) in the drop can also be adjusted; Q can be related to the dimensionless anion-deficit density (Δq) using Equation 6.1. The numerical value of Q, achieved experimentally by contacting the electrode, is approximated by,

$$Q = \eta Q_{th}, \tag{6.2}$$

where η is determined empirically and Q_{th} is the amount of charge transferred onto a perfectly conducting sphere by an infinite planar electrode (Zhang *et al.*, 2013*b*), given as,

$$Q_{\mathrm{th}} = 2\pi^3 R^2 \epsilon_{\mathrm{c}} \boldsymbol{E} \big/ 3 \; . \tag{6.3}$$

As η has been shown to vary from 0.25 to 4 depending on the type (Ahn *et al.*, 2013) and alignment (Ahn *et al.*, 2015) of the electrode used, the study of impacting-drop charge variation on the coalescence outcome is relevant to the design of electrodes in

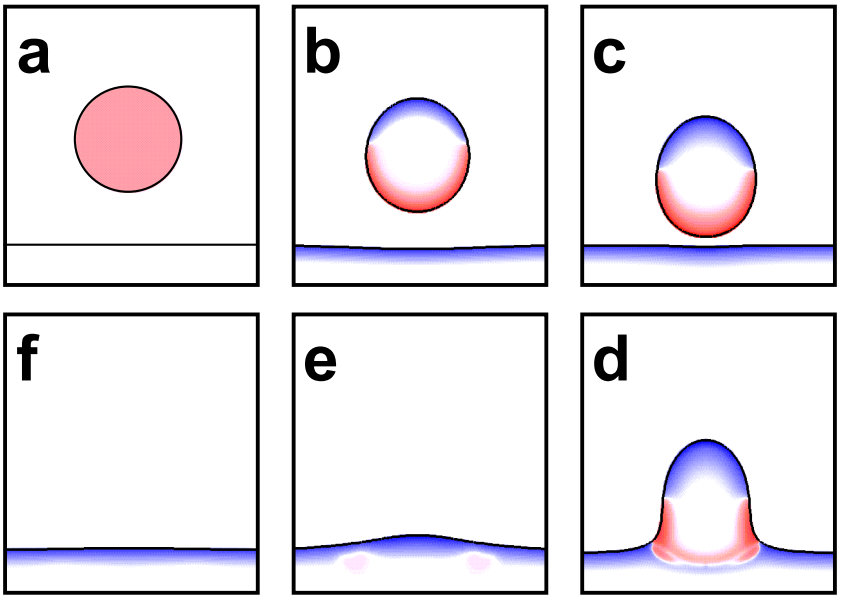

Figure 6.4: Time lapse images (clockwise, starting from top left) of a water drop ($\mathrm{Oh}^2 = 1$, $\mathrm{Ca_E} = 0.20$, $\kappa = 15$, $\Delta q = 0.20$ and $\bar{S} = 1$) undergoing partial coalescence, $t = 0, 10, 30, 40, 50, 70$. The overlaid charge contours employ the same scale as figures (6.2) and (6.3).

LoC devices. Note that, in the last subsection, as ion concentration (κ) was varied, the (dimensional) drop charge was kept constant ($\kappa^2\Delta q = 11.25$ for figures 6.2 and 6.3). Here, the drop charge ($Q \propto \kappa^2\Delta q$) is increased by varying Δq for a fixed κ. In figure (6.4), the coalescence process of a drop with a larger initial drop charge ($\Delta q = 0.20$, see darker-tinted drop in frame 6.4a), with all other parameters identical to the case in figure (6.3), is studied. This increased charge results in a larger translational force acting on the drop. Therefore, the drop approaches the interface faster (compare times for frame c in figure (6.4) with frame b in figure (6.3)). However, due to this greater drop velocity, there is less time for ions to be conducted to the drop tips, and less charge separation occurs inside the drop. Consequently, the drop is far less deformed when it contacts the interface, which happens much earlier than the case in figure (6.3). The electrophoretic lift force developed at the top of the drop (after contact is made) is therefore not sufficient to delay the vertical collapse, and partial coalescence does not occur.

A surprising implication of this result is that complete coalescence becomes *more likely* when the net charge in the drop is *larger* (for fixed drop ion concentration, and hence fixed κ). One possibility is that this (counter-intuitive) result is a consequence of our choice of using a deficit of anions (n_-) to create a positive charge on the drop rather than a surplus of cations (n_+); anions determine the magnitude of the upward-acting electrophoretic force, and a case with greater charge results in a drop initiated with fewer anions than a corresponding lower charge case. To test the sensitivity of the coalescence outcome to this assumption, additional simulations were conducted. It was found that, for the parameter ranges employed in this work, the coalescence outcome (partial or complete) was independent of whether the charge on the drop ($\Delta q = 0.20$ and $\kappa = 15$ in this case) was implemented via a deficit of anions ($n_+|_{t=0} = 1.0, n_-|_{t=0} = 0.8$) or a surplus of cations ($n_+|_{t=0} = 1.2, n_-|_{t=0} = 1.0$). In either case, the velocity of the drop before it contacted interface (determined by Δq for fixed κ) was key to determining the coalescence outcome.

Phase maps for coalescence transitions

In figure (6.5), the qualitative impact of relevant parameters on the coalescence transition is illustrated using phase maps. For the numerical model employed in this paper, the Ohnesorge number represents the importance of electrokinetic effects as discussed in the last chapter; Oh is also a key parameter for understanding both hydrodynamic

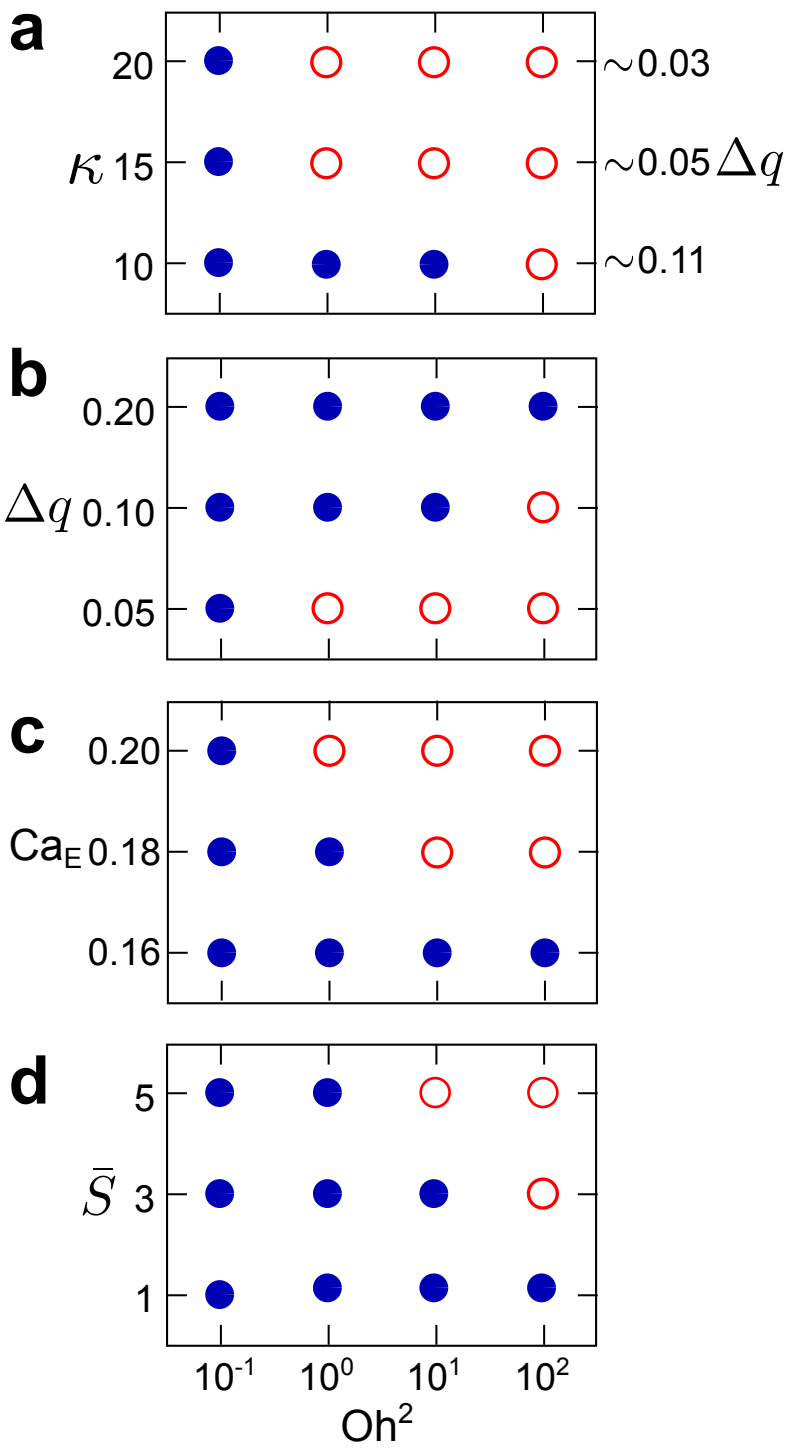

Figure 6.5: Phase maps showing type of coalescence observed by varying Oh^2 and (a) bulk ion concentration (κ) for $\kappa^2\Delta q = 11.25$, $\mathrm{Ca_E} = 0.20$ and $\bar{S} = 3$; (b) drop charge (Δq) for $\mathrm{Ca_E} = 0.20$, $\kappa = 15$ and $\bar{S} = 1$; (c) electric field strength ($\mathrm{Ca_E}$) for $\kappa = 20$, $q = 0.0281$ and $\bar{S} = 3$; and (d) separation distance ($\bar{S}$) for $\mathrm{Ca_E} = 0.20$, $\kappa = 10$ and $q = 0.1125$. Complete coalescence is depicted by solid blue circles, and partial coalescence by open red circles.

(Gilet *et al.*, 2007) and electrohydrodynamic (Aryafar & Kavehpour, 2009) coalescence phenomena. Hence, the impact of these parameters are studied for varying Oh^2. Cases where complete coalescence was the final outcome are represented by solid blue circles, and those where partial coalescence was observed by open red circles. Note that partial coalescence is never observed for $\mathrm{Oh}^2 < 1$ in our simulations; this is consistent with previous experiments on this topic (Aryafar & Kavehpour, 2006, 2009). As Oh^2 is increased, partial coalescence becomes more likely for all parameters, because charge separation becomes faster relative to drop deformation, resulting in the generation of a stronger upward-acting lift force, delaying coalescence.

Figure (6.5)a and b show that partial coalescence becomes more likely as the bulk ion concentration (for fixed drop charge $Q \propto \kappa^2 \Delta q$) and charge (for fixed κ) of the drop are increased and decreased, respectively, for reasons outlined previously. In addition, we identify two more parameters that impact the transition from complete to partial coalescence, namely the strength of the external electric field (represented by $\mathrm{Ca_E}$) and the initial separation distance ($\bar{S}$) of the drop from the bulk interface. The impact of $\mathrm{Ca_E}$ is particularly relevant to LoC device operation, where the electric field can be adjusted by varying the voltage across the electrodes. As the first term on the right hand side of Equation 3.46 shows, the delaying electrophoretic force (at the drop summit) depends on both the separated net charge in the region and the electric field acting on it. By decreasing the electric field, this force is weakened, and complete coalescence becomes more likely. In our simulations, complete coalescence is always observed for $\mathrm{Ca_E} \leq 0.16$. The distance between electrodes can be small (relative to channel dimensions) in CCEP LoC devices (Drews *et al.*, 2013); hence, the impact of $\bar{S}$ on coalescence outcome is pertinent to device design. A case with higher (initial) separation distance thus represents a drop that has contacted the electrode further away, and consequently undergoes CCEP over a longer distance before contacting its bulk liquid interface. As shown here, partial coalescence becomes more likely as the initial separation distance is increased. This is because for a higher separation distance, the impacting drop takes longer to contact the interface; this results in greater charge separation prior to contact, and a greater likelihood of partial coalescence occurring.

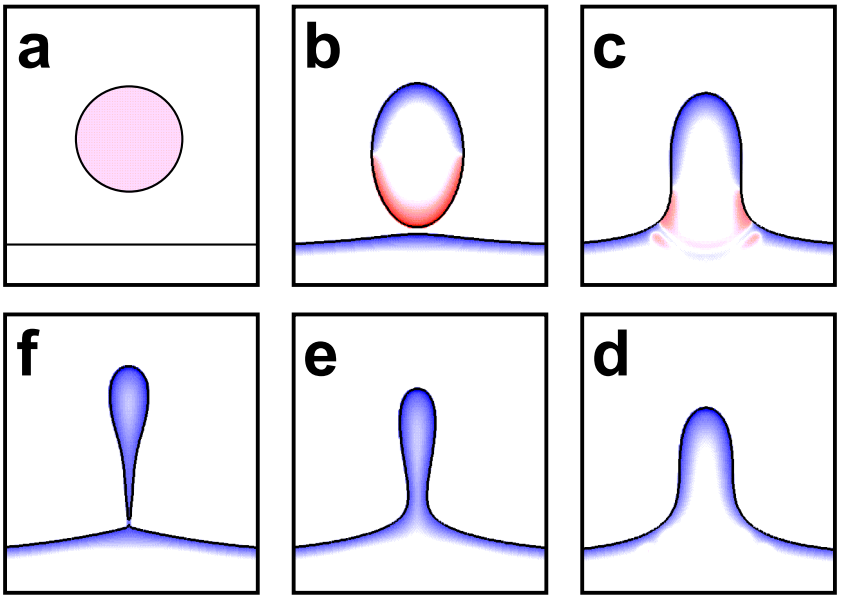

Figure 6.6: Time lapse images (clockwise, starting from top left) of a water drop ($\mathrm{Oh}^2 = 1$, $\mathrm{Ca_E} = 0.20$, $\kappa = 20$, $\Delta q = 0.028$ and $\bar{S} = 1$) undergoing partial coalescence ($a/R = 0.11$), $t = 0, 50, 60, 65, 75, 80$. The overlaid charge contours employ the same scale as figures (6.2), (6.3) and (6.4).

Effect of increasing bulk ion concentration

It has been shown that complete coalescence is observed for $\kappa = 10$ (figure (6.2)), while partial coalescence is observed for $\kappa = 15$ (figure (6.3)). In figure (6.6), the coalescence process of a drop with an even higher bulk ion concentration of $\kappa = 20$ for the same net drop charge ($\Delta q = 0.028$, $\kappa^2 \Delta q = 11.25$) as the cases in figures (6.2) and (6.3), is illustrated. The first three frames appear superficially similar to the corresponding ones in figure (6.3) (the times are selected in order to allow for a convenient comparison). However, on closer examination of frame c of both figures, the peak of the drop appears to be higher here compared to the case in figure (6.3). This implies that the drop has undergone greater deformation than the case in figure (6.3). The bottom frames (d-f) in figure (6.6) depart significantly from the corresponding frames in figure (6.3). The drop summit is higher (frames 6.6d - 6.6e) and the residual droplet formed in frame 6.6f is larger ($a/R = 0.11$ here compared to $a/R = 0.003$ for figure (6.3)). The charge contained is higher as well. This differs from the findings of Hamlin *et al.* (2012) who, while experimentally studying macroscale drop coalescence, found the size and charge of residual droplets to be independent of ionic conductivity, for a fixed value of electric field (The electric field is the same for the cases in figures (6.3) and (6.6), $\mathrm{Ca_E} = 0.20$). To probe this difference, the dynamics underlying the size of (and charge contained in) the residual droplets formed during partial coalescence is studied in the next section.

6.3.3 Characteristics of residual droplets

The residual droplets for drops with different (initial) separation distances ($\bar{S} = 1, 3$ and 5, respectively) for three values of bulk ion concentration ($\kappa = 15, 20$ and 25), have been compared in figure (6.7). First, we look at frames a, d and g of figure (6.7), where κ is increased while the separation distance is fixed ($\bar{S} = 1$). The significant variation between the frames a and d, noted earlier, can be directly contrasted. However, increasing the ion concentration additionally by the same amount (frame g, $\kappa = 25$, $a/R = 0.152$), does not result in a similar increase in droplet size, though the bulb of the droplet is still slightly bigger when compared to $\kappa = 20$ case (frame 6.7d, $a/R = 0.11$). Note that the diffuse charge layers are narrower in frame 6.7g compared to frames 6.7a and 6.7d, due to the higher κ. The charge ($\propto \kappa^2 \Delta q_\mathrm{r}$) contained in the residual droplet, where Δq_r is the residual droplet average charge density, increases significantly in magnitude from $\kappa = 15$ ($\kappa^2 \Delta q_\mathrm{r} = -10.575$) to $\kappa = 20$ ($\kappa^2 \Delta q_\mathrm{r} = -55.2$), but a much smaller difference is observed for a commensurate increase from $\kappa = 20$ to $\kappa = 25$ ($\kappa^2 \Delta q_\mathrm{r} = -55.625$).

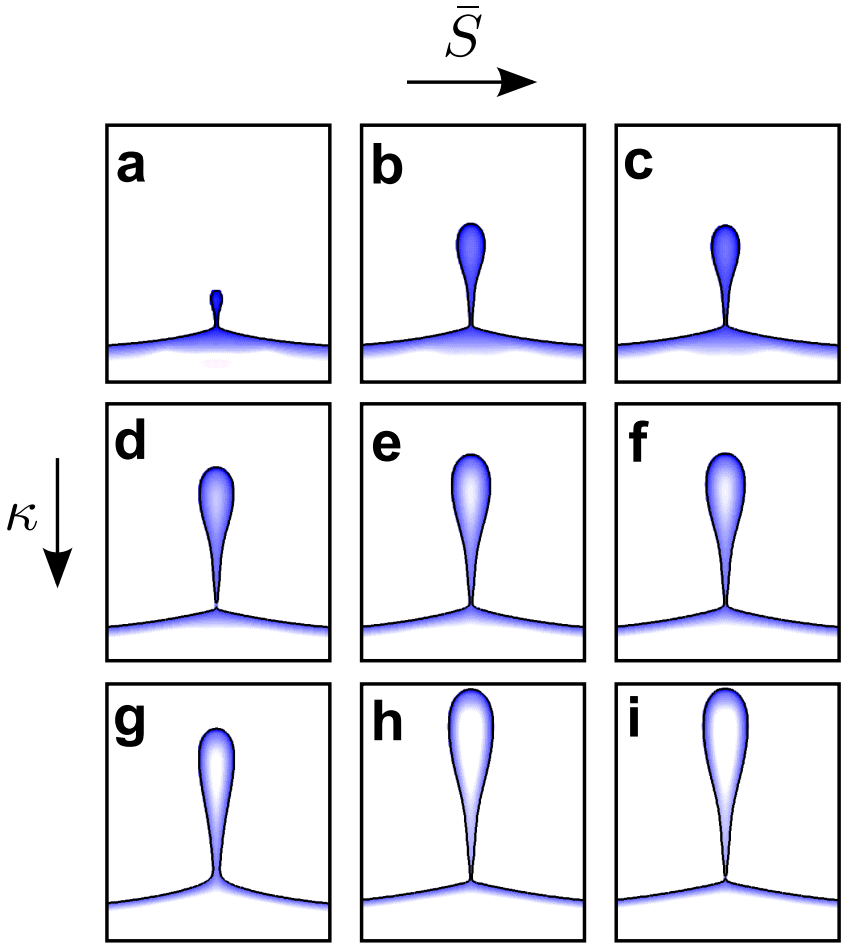

Figure 6.7: Residual droplet comparison for $\mathrm{Oh}^2 = 1$, and $\mathrm{Ca_E} = 0.2$, for increasing separation distance ($\bar{S}$) bulk ion concentration (κ); $\kappa = 15$ for (a) $\bar{S} = 1$, (b) $\bar{S} = 3$ and (c) $\bar{S} = 5$; $\kappa = 20$ for (d) $\bar{S} = 1$, (e) $\bar{S} = 3$ and (f) $\bar{S} = 5$; $\kappa = 25$ for (g) $\bar{S} = 1$, (h) $\bar{S} = 3$ and (i) $\bar{S} = 5$. The residual droplet ratios for frames a-i are a/R=0.003, 0.053, 0.053, 0.11, 0.162, 0.162, 0.152, 0.272 and 0.272, respectively. The overlaid charge contours employ the same scale as figures (6.2), (6.3), (6.4) and (6.6).

In addition, we can also observe how increasing the separation distance, for a fixed ion concentration, impacts droplet size. Once again, significant variation in droplet size is observed when the separation distance is increased from frames a ($\bar{S} = 1,\ a/R = 0.003$) to b ($\bar{S} = 3,\ a/R = 0.052$), while negligible variation is seen when the separation distance is increased further in frame c ($\bar{S} = 5,\ a/R = 0.052$), all for $\kappa = 15$. This (initial increase followed by a levelling-off) is mirrored in the droplet charge values as well ($\kappa^2 \Delta q_\mathrm{r} = -10.575, -37.125, -37.575$ for $\bar{S} = 1, 3, 5$). This effect can be observed by visually tracing any row in figure (6.7). Therefore, the physical process controlling the residual droplet size changes with separation distance and ion concentration, but asymptotes to a near-constant value as $\bar{S}$ or κ are increased further. It bears repeating that these observations are unique to impacting microdrops, and are not observed for the impacting (millimetre-sized) drops studied by Hamlin *et al.* (2012).

Electrokinetic effects on the electrophoretic lift force generated

The discrepancies (between our observations and the experiments of Hamlin *et al.* (2012) noted in the preceding section possibly arise from the differences between the charge separation dynamics, and consequent charge transfer dynamics, of (impacting) macroscale and microscale drops. In the case of macrodrops, diffuse space charge layers adjacent to the interface are infinitesimally thin, and the charge can be assumed to be completely located at the interface (Saville, 1997). In this case, as the macrodrop approaches the interface, the positive charge is practically located entirely at the lower, or leading, drop interface. Similarly, the negative charge is located entirely at the upper, or trailing drop interface. Hence, when the drop contacts the interface of its bulk liquid, the entire positive charge is transferred almost instantaneously, while the entire negative charge is left contributing to the electrophoretic lift force at the drop summit (Hamlin *et al.*, 2012). In this system, the actual pinching-off process is solely driven by capillary forces, with charge dynamics not varying when the drop ionic conductivity or initial separation distance is varied. Consequently, the size and charge of ejected residual droplets would be independent of ionic conductivity and separation distance, for a fixed experimental setup (i.e., constant interfacial tension and electric field).

However, the high surface-to-volume ratios of microdrops means that the ratio of space charge layer dimension to the drop radius (R) is higher, with the diffuse charge occupying

a significant region adjacent to the drop interface (these diffuse layers can be observed in figures (6.2)-(6.4) and (6.6)-(6.7)). Thus κ has a finite value for microdrops (but $\kappa^{-1} \to 0$ for macrodrops). Also, the ion distributions may not necessarily be in steady state when the drop contacts the interface, as the conductive and diffusive fluxes inside the drop might not have achieved equilibrium. The ongoing charge-separation dynamics after contact can result in ongoing charge-transfer dynamics during the coalescence process. This means that all the positive charge is not instantaneously transferred out of the leading end, and the negative charge driven electrophoretic lift force is not constant at the trailing interface, post coalescence.

We can use this understanding of impacting microdrop charge behaviour to explain the observed variation in residual droplet size and charge. The time lag associated with charge separation means that the further the initial location of the drop is from the bulk liquid, the more time there is for charge-separation to occur. For the three cases (6.7a, 6.7d and 6.7g), the positive charge is completely convected out of the drop ($|n_+| \sim 0$ in the residual droplet). However, the greater charge-separation that occurs (as $\bar{S}$ is increased) results in greater negative charge in the residual droplets formed. Similarly, the higher the drop ion concentration, the more ions there are in the drop to contribute to charge-separation at both ends. We find evidence of incomplete charge-separation as κ is increased, as some positive charge is found in the residual droplet for $\kappa = 25$ ($|n_+| = 0.047$), and none for the lower $\kappa = 15$ case ($|n_+| = 0$).

In both these cases (increasing $\bar{S}/\kappa$), the transient electrophoretic lift force is higher at the drop summit when compared to a case with lower κ or lower $\bar{S}$. Consequently, capillary-driven convection into the bulk is delayed to a greater extent, prior to horizontal collapse. This process then culminates in the pinching off of a larger residual droplet, as a smaller proportion of the drop volume is convected into the bulk liquid. This explains how the size and charge of residual droplets are dependent upon the transient charge separation in the drop. The charge separation, in turn, is a function of the five parameters discussed in figure (6.5). An implication of this is that the (constant) size of residual droplets ejected at macroscales is probably represented here by the limiting case of high κ, rather than a self-similar physical phenomenon as suggested by Hamlin *et al.* (2012).

6.3.4 Transition from passive to active partial coalescence

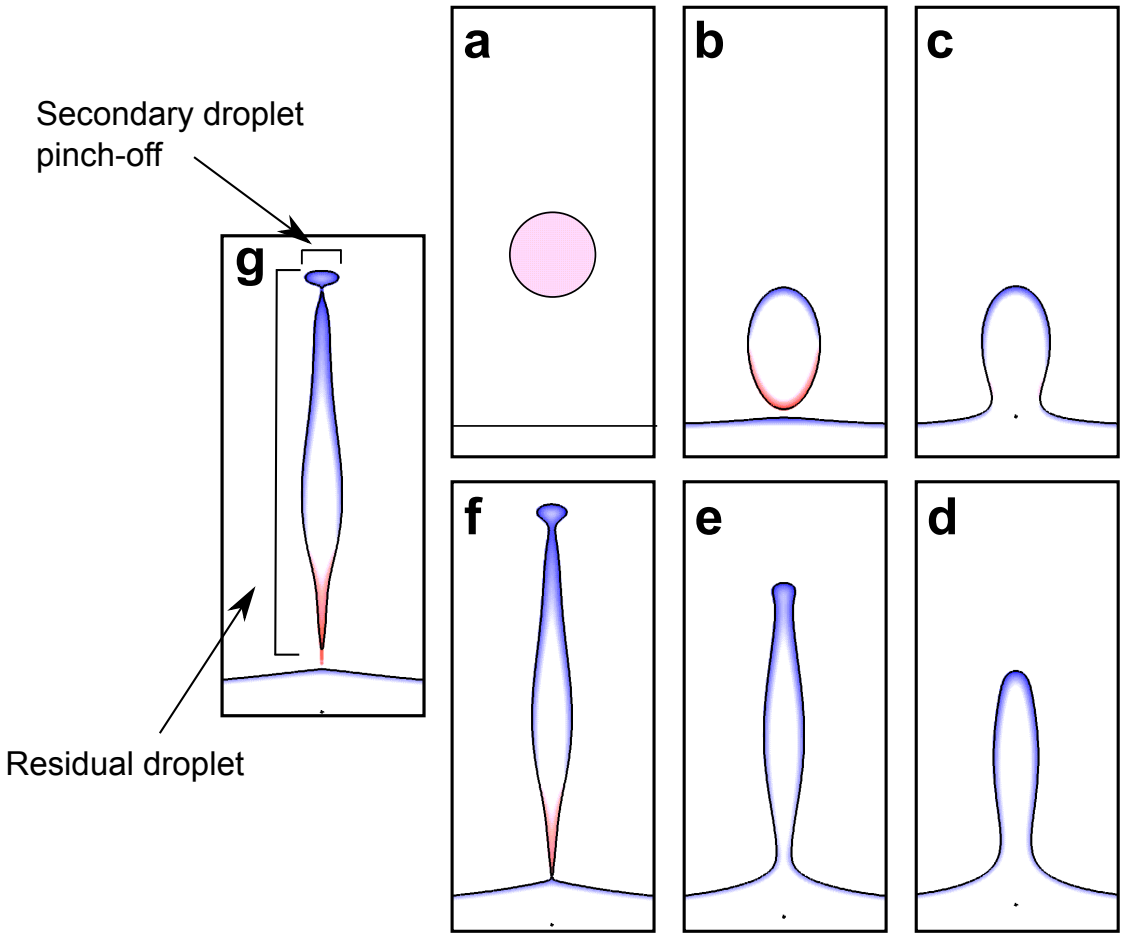

Figure 6.8: Time lapse images (clockwise, starting from top left) of a water drop ($\mathrm{Oh}^2 = 10$, $\bar{S} = 3$, $\kappa = 25$ and $\Delta q = 0.018$) undergoing partial coalescence ($a/R = 0.578$), $t = 0, 650, 700, 800, 850, 900, 950$. The overlaid charge contours employ the same scale as figures (6.2), (6.3), (6.4), (6.6) and (6.7).

In this section, the impact of varying Oh^2 simultaneously with other parameters, is studied. Figure (6.8) illustrates the coalescence process of an impacting drop with higher Oh^2 ($\mathrm{Oh}^2 = 10$), higher separation distance ($\bar{S} = 3$) and a higher bulk ion concentration ($\kappa = 25$) than the case in figure (6.3). All three parameters act to increase the amount of charge separated inside the drop before it impacts the interface, and the drop is consequently highly deformed at contact (frame 6.8b). This results in a narrower neck formed for the conjoined drop-interface system; importantly, the width of the neck does

not exceed the diameter of the drop at its centre, unlike the cases in the earlier sections (compare frame 6.8c with the corresponding frames of figures (6.3), (6.4) and (6.6)).

At this point, the charge separated at the drop summit is sufficiently high to create an actuating electrophoretic force, rather than simply a delaying force; this induces the drop tip to be electrophoretically driven away from the interface *while* the drop fluid is being convected into the bulk (frame 6.8d). As a result, part of the fluid in the (relatively higher pressure) neck is convected vertically upward. This increases the rate of fluid flow out of the neck, as flow occurs simultaneously upwards and downwards, thus *accelerating* the horizontal collapse, and culminating in the pinch-off of the residual droplet (frames 6.8e - 6.8f). The residual droplet formed is far larger ($a/R = 0.578$) than those studied in figure 6.7. Because the convection of the drop fluid into the bulk is hindered, the positive charge does not completely leave the drop. Therefore, the residual droplet is, unlike in preceding cases, not predominantly negatively charged; positively charged regions are visible at the bottom of the residual droplet in frame 6.8g. The contours of the residual droplet qualitatively resemble a 'Worthington jet' ejected when a drop splashes into a bulk liquid at high velocity (Worthington, 1882).

This process can be termed as *active* partial coalescence, compared with the *passive* partial coalescence phenomena observed thus far, where the electrohydrodynamic forces act to only delay coalescence, and do not influence the pinch-off process. In contrast, active partial coalescence is characterised by the generation of an actuating electrophoretic force which stretches the drop, and induces pinch-off to occur earlier. As opposed to the negatively-charged residual droplets formed during passive partial coalescence, the ejection of a residual droplet with a positively-charged lower tip is observed. Such (large) residual droplets have been observed in experiment by Mousavichoubeh *et al.* (2011*b*) for cases with low interfacial tension (see Figure 6.9). Active partial coalescence results from the dominance of electrohydrodynamic forces over capillary forces; it can manifest either when the capillary forces are weakened (by the addition of a surfactant (Mousavichoubeh *et al.*, 2011*b*)) or when electrokinetic effects are enhanced (as is the case here). Note that the upper tip of the residual droplet deforms and forms a lobe, connected to the remainder of the droplet by a (cylindrical) neck (frame 8e). When the height of this cylindrical neck section formed exceeds its circumference, the Rayleigh-Plateau instability acts to shrink the neck (Tomotika, 1935), resulting in a second, separate, pinch-off phenomena (frame 6.8f) which splits the residual droplet at the top to produce another (negatively-charged)

droplet (frame 6.8g).

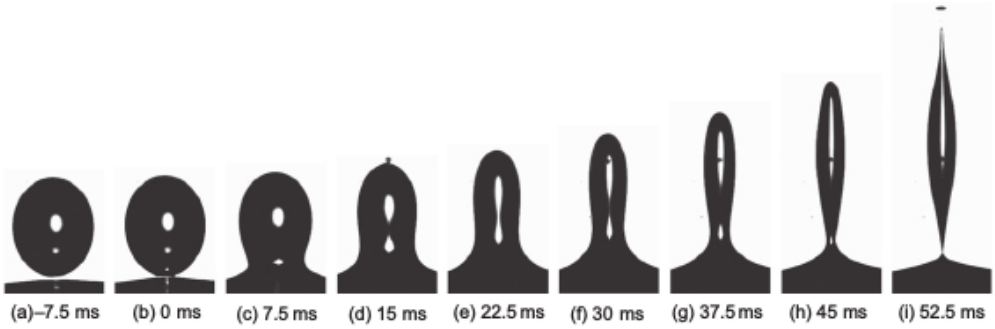

Figure 6.9: Residual droplet detaching in the presence of 1 g/L Tween 20 in dispersed phase for a drop with diameter of 1196 mm under electric field strength of 232 V/mm. Reproduced from Mousavichoubeh *et al.* (2011*b*)

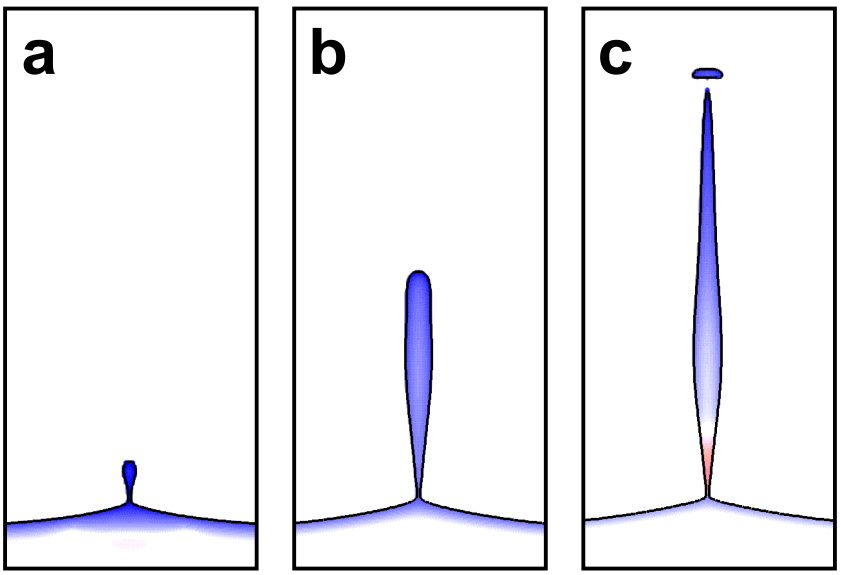

Figure 6.10: Residual droplet comparison for $\kappa = 15$, $\kappa^2 \Delta q = 11.25$ and $\bar{S} = 1$, for three values of Oh^2; (a) $\mathrm{Oh}^2 = 1$, (b) $\mathrm{Oh}^2 = 10$ and (c) $\mathrm{Oh}^2 = 10^2$. The times for the frames a-c are t = 86.5, 450 and 3250, respectively. The residual droplet ratios for frames a-c are a/R =0.003, 0.118 and 0.175, respectively. The overlaid charge contours employ the same scale as figures (6.2), (6.3), (6.4), (6.6), (6.7) and (6.8).

In frames a-c of figure (6.10), the effect of Oh^2 on the residual droplet size is isolated

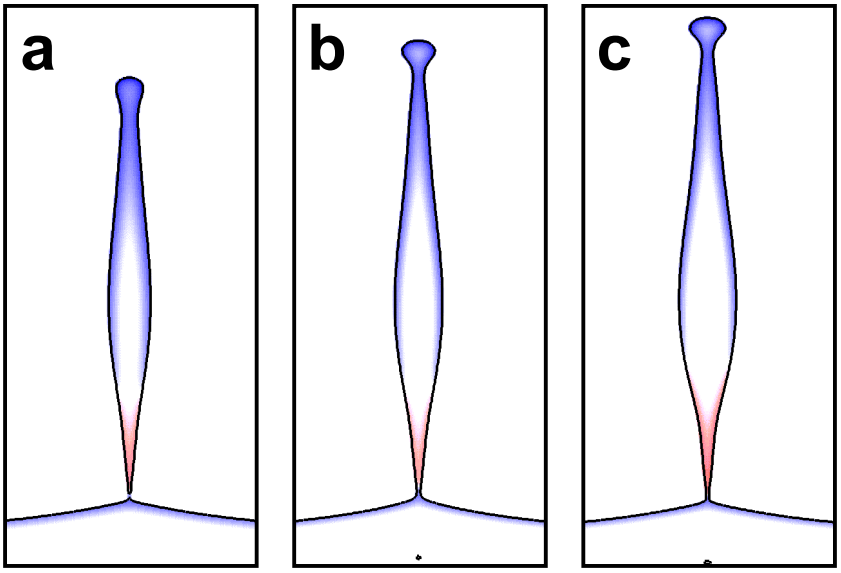

Figure 6.11: Residual droplet comparison for $\mathrm{Oh}^2 = 10$, $\kappa^2 \Delta q = 11.25$ and $\bar{S} = 3$ for (d) $\mathrm{Ca_E} = 0.20$ and $\kappa = 20$ ($\Delta q = 0.028$), (e) $\mathrm{Ca_E} = 0.20$ and $\kappa = 24$ ($\Delta q = 0.020$), and (f) $\mathrm{Ca_E} = 0.22$ and $\kappa = 24$ ($\Delta q = 0.020$). The times for the frames a-c are t = 950, 887.5 and 745, respectively. The residual droplet ratios for frames a-c are $a/R = 0.421$, 0.549 and 0.772, respectively. The overlaid charge contours employ the same scale as figures (6.2), (6.3), (6.4), (6.6), (6.7), (6.8) and (6.10).

by keeping other parameters fixed. The transition from passive (frame 6.10a, $\mathrm{Oh}^2 = 1$) to active partial coalescence (frames 6.10c, $\mathrm{Oh}^2 = 10^2$) is still observed here, as manifested by the positive charge accumulation at the lower tip of the residual droplet in frame 6.10c. However, the difference between the residual droplet sizes in frames 6.10c, where only Oh^2 is varied, ($a/R = 0.175$) and 6.11c where parameters other than Oh^2 are also varied ($a/R = 0.772$) is still significant. This indicates that while Oh^2 controls the *qualitative* transition from passive to active partial coalescence (active partial coalescence is not observed for $\mathrm{Oh}^2 = 1$), the other (physical and electrical) parameters influence the *quantitative* size of the residual droplet ejected.

6.3.5 Scaling laws for residual droplet size and charge

The development of an analytical framework to predict residual droplet size and charge is challenging, due to the fact that the charge distribution inside the drop is dynamic and continues to vary throughout the coalescence process. Mousavichoubeh *et al.* (2011*b*) examined video recordings of partial coalescence experiments (of macrodrops) and concluded that the horizontal and vertical collapses were described by the electric capillary number ($\mathrm{Ca_E}$) and the Ohnesorge number (Oh), respectively. By defining a new dimensionless number that was a product of these two quantities (WO= $\mathrm{Ca_E} \times \mathrm{Oh}$), they were able to obtain a reasonable fit for the residual droplet sizes obtained in their experiments. However, WO was related by a convex function to residual droplets formed by passive partial coalescence, and a (different) concave function for residual droplets formed by active partial coalescence; unification of the entire dataset was not achieved (Mousavichoubeh *et al.*, 2011*b*). This dimensionless quantity (WO) was predictably poor at scaling the residual droplets simulated in this paper, as the size of these drops has been shown to depend on multiple parameters other than $\mathrm{Ca_E}$ and Oh.

Hamlin *et al.* (2012) developed a scaling relationship based on an electrophoretic-inertial force balance. They note that the electrophoretic force acting on the drop must scale with $Q_\mathrm{r}E$, where Q_r and E are the (dimensional) residual droplet charge and external electric field, respectively. As convection drives the drop contents into the bulk liquid, the instantaneous inertial force on the drop at any instant can be given by $\rho_\mathrm{d} u^2 r^2(t)$ where u is given by Anilkumar *et al.* (1991)'s expression ($u \simeq \sqrt{\gamma/\rho_\mathrm{d} R}$). Under the assumption that inertia balances the electrophoretic force acting on a residual droplet of

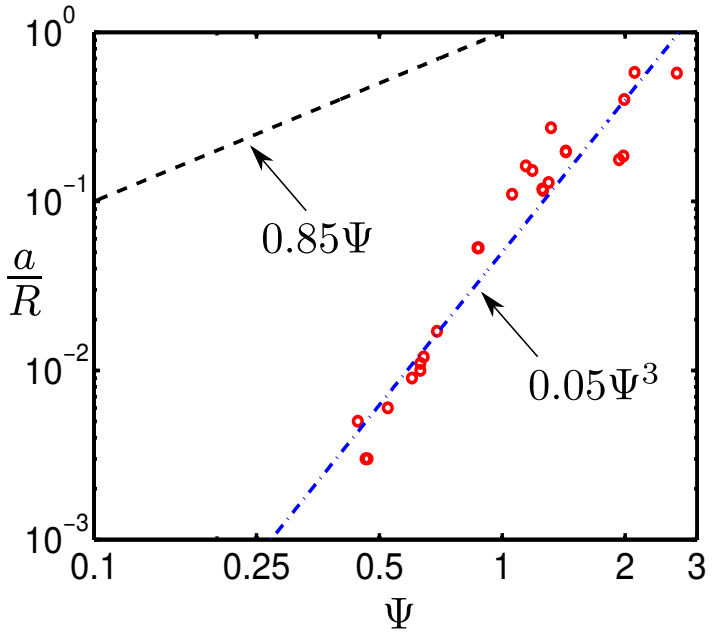

Figure 6.12: Scaling law relating the residual droplet ratio (a/R) to Ψ (equation 6.6). The results obtained by our simulations are depicted as open red circles, the relationship obtained by Hamlin *et al.* (2012) is shown as a black dashed line, and the best fit curve for our results is shown as a blue dotted-and-dashed line.

radius a, Hamlin *et al.* (2012) obtained,

$$\frac{a}{R} \sim \sqrt{\frac{Q_{\mathrm{r}} E}{\gamma R}}. \tag{6.4}$$

Rewriting this expression using our (electrokinetic) scalings, we get,

$$\frac{a}{R} \sim \Psi, \tag{6.5}$$

where

$$\Psi = \sqrt{\frac{4\pi \Delta q_{\mathrm{r}}\, \mathrm{B}\, \mathrm{Oh}^2\, \kappa^2 |E|}{3}}, \tag{6.6}$$

where Δq_{r} is the residual droplet charge. This relationship is not predictive in nature as the residual droplet radius (a) and charge (Δq_{r}) are both unknown *a priori*. However, it does shed some light on how these two quantities (residual droplet size and charge) relate to each other.

In figure (6.12), we have plotted the results of our simulations (using the scaling relation formulated in Equation 6.6, along with the results obtained by Hamlin *et al.* (2012). Our simulated cases are depicted as open red circles, the best fit curve for our results is shown as a blue dotted-and-dashed line, and the relationship obtained by Hamlin *et al.* (2012) is shown as a black dashed line (they used a prefactor of 0.85 to fit their simulations). It can be seen that our model predicts a higher residual droplet charge (for a fixed residual droplet radius) compared with that of Hamlin *et al.* (2012). It must be noted that Hamlin *et al.* (2012) studied macroscale drops with infinitesimally-thin (diffuse) charge layers, while we measure the bulk charge contained in the residual droplet. Rather than the linear relationship ($a/R \sim c_1 \Psi$, where $c_1 = 0.85$) observed by Hamlin *et al.* (2012), we find that an power-law curve of the form $a/R \sim c_1 \Psi^{c_2}$ fits our results reasonably ($c_1 = 0.05$, $c_2 = 3$ in figure (6.12).

6.3.6 Conclusions

The coalescence of a charged microdrop undergoing Contact Charge Electrophoresis (CCEP) (Drews *et al.*, 2015) with a electroneutral bulk liquid, is numerically studied in this section. The aim of the section was to shed light on two questions: first, under what conditions does the coalescence outcome transition from complete coalescence (where the drop is completely convected into the bulk liquid after impact) to partial coalescence (where a residual droplet is ejected)? And, second, for the cases where partial coalescence

is observed, what determines the size and charge of residual droplets?

Partial coalescence occurs when the upward-acting electrophoretic force (at the trailing tip of the impacting drop as it approaches the interface) is sufficiently high to prevent the the downward-acting capillary forces from convecting the contents of the drop into the bulk (once the drop has made contact) for long enough for the inward-acting capillary forces at the neck to pinch-off the residual droplet. There are five parameters, relevant to the application of lab-on-a-chip devices, that are shown to influence the strength of this electrophoretic lift force; these play a role in the coalescence transition. First, the external electric field ($\mathrm{Ca_E}$), which can be adjusted by increasing the voltage across the electrodes, must exceed a threshold ($\mathrm{Ca_E} > 0.16$) for partial coalescence to occur, consistent with Mousavichoubeh *et al.* (2011*a*). Second, increasing the Ohnesorge number, $\mathrm{Oh} = \mu_\mathrm{d}/(\rho_\mathrm{d}\gamma R)$, is shown to make partial coalescence more likely, consistent with Aryafar & Kavehpour (2009). Third, the impacting-drop bulk ion concentration (κ), which can be adjusted experimentally by the addition of ionic salts, determines the amount of charge separated at drop contact. It is shown that there is a critical ion concentration separating the regimes of complete and partial coalescence, analogous to the limit reported by Hamlin *et al.* (2012) between the partial coalescence and the non coalescence (or 'bouncing') regimes. Fourth, the drop charge (given by Δq for fixed κ), which is influenced by the type (Ahn *et al.*, 2013) and alignment (Ahn *et al.*, 2015) of electrodes used in LoC devices, controls its velocity as it approaches the interface. This velocity increases with Δq, allowing for less time for charge separation to occur at higher Δq, resulting in a weaker electrophoretic lift force post-contact. Hence, complete coalescence becomes more likely as Δq is increased. Fifth, the initial separation distance ($\bar{S}$), which depends on the distance between the electrode (where drop charging occurs) and its bulk liquid, was shown to influence the time to coalescence. For higher $\bar{S}$, the drop deforms for a longer time prior to impacting the interface, which allows for more charge separation to occur and a stronger electrophoretic force to be generated. Thus, partial coalescence becomes more likely with increasing $\bar{S}$.

The external electric field (once $\mathrm{Ca_E} > 0.16$) and interfacial tension (Oh) influence the size and charge contained in the residual droplet, consistent with previous studies (Hamlin *et al.*, 2012; Mousavichoubeh *et al.*, 2011*b*). However, it is shown here that the residual droplet size and charge increases with both $\bar{S}$ and κ, differing from Hamlin *et al.* who found the residual droplet and charge to be fixed at a particular electric

field, for fixed interfacial tension. This increase in residual droplet size and charge levels off at higher values of $\bar{S}$ or κ. This discrepancy is explained as resulting from the distinct charge separation dynamics, and consequent charge transfer dynamics, of microdrops. For macrodrops, the charge is entirely located close to the interfaces, and the electrophoretic force does not change as the coalescence process unfolds. In contrast, the charge separation process is dynamic for microdrops, and the charge distribution on the drop tips varies throughout the coalescence process. Therefore, parameters that affect the rate (κ) and amount ($\bar{S}$) of charge separated impact the strength of the electrophoretic force, thus allowing for variation in size of residual droplet ejected. For cases when the charge separation process is completed, the microdrop behaves like a macrodrop; i.e. and residual droplet size depends only on electric field and the dependence on $\bar{S}$ and κ is lost. The findings of Hamlin *et al.* (2012) can therefore be interpreted as limiting cases for high κ and high $\bar{S}$, where the charge distribution has achieved steady-state equilibrium prior to the drop contacting the interface.

Increasing the Oh^2 of the system results in the transition from 'passive' partial coalescence, where the electrophoretic force delays coalescence until horizontal pinch-off occurs, to 'active' partial coalescence. Active partial coalescence is characterised by an actuating electrophoretic force that stretches the drop vertically upwards, accelerating the horizontal collapse of the neck, and pinching-off the drop before all the positive charge can leave the drop. The residual droplets, that are pinched off as a result, are larger than those observed at lower Oh^2, and their size is shown to be influenced by electrical and setup parameters. Finally, using a scaling analysis formulated by Hamlin *et al.* (2012), a scaling relation between residual droplet charge and size is obtained.

6.4 Case II: Coalescence of two oppositely-charged drops

This chapter is motivated by CCEP/ECD applications; microdrop manipulation technologies that involve charging the microdrop by contacting the surface of an electrode, prior to using the electric field for actuation. Section 6.3 focused on the coalescence of a charged drop with an electroneutral bulk fluid. However, oppositely-charged microdrops can interact during CCEP/ECD LoC device operation (Link *et al.*, 2006), but their subsequent coalescence process has received little attention. This section is focused on studying the coalescence of two oppositely charged drops, physically this is realisable by

the drops contacting opposite electrodes prior to coalescence.

In most cases, when oppositely-charged liquid drops are induced to come into contact by an electric field, they tend to coalesce into a larger drop, thus minimizing the total interfacial area. If the attractive force between the drops were to be enhanced by increasing the electric field, intuition would suggest that the coalescence process would be faster. However, Ristenpart *et al.* (2009) showed that, on the contrary, there exists a critical electric field strength above which the drops appear to bounce-off each other, rather than coalescing. Mugele (2009) captured this tension between our intuition and this phenomenon when he said "Just as we may be guided by a sense of 'more is more' in our daily lives, so physicists often use this principle as a good first guess to explain physical phenomena. For example, in a situation as simple as two objects with electrically opposite charges, the expectation is that the more strongly charged the objects are, the more they should attract each other. In the case of liquid drops, we would expect them to bump into each other and coalesce into one larger drop, and that, the higher their charge, the quicker this would happen. It seems that the simpler a situation is, the more stunned we are if nature 'refuses' to follow our expectations".

The mechanism for this 'non-coalescence' can be explained thus: under the influence the electric field, the drops deform and form conical projections known as Taylor cones (Fernández de la Mora, 2007) at the inner-facing tips prior to contact, due to a combination of electrophoretic and dielectrophoretic effects. If the Taylor cones are sufficiently pronounced, i.e. if the cone angle (β) is sufficiently high ($\beta_{\mathrm{cr}} \sim 31°$), the azimuthal curvature around the meniscus that forms when the drops contact is sharper than the axial curvature of the meniscus. This results in higher fluid pressure in the meniscus when compared to the drop centres; consequently, capillary forces act to shrink it. This creates a flow away from the meniscus, resulting in fluid drainage followed by breakup. In effect, the system behaves like an unstable thread and breaks up due to the Rayleigh-Plateau instability (Bird *et al.*, 2009).

As the cone angle is proportional to the electric field, the transition from coalescence to non-coalescence at high electric fields can be explained by the increased probability of the drops forming cone angles unfavourable for coalescence. In this Taylor cone angle model (TCAM), the electric field only sets the cone angle for the approaching drops. The coalescence dynamics after contact is determined by capillary effects, with charge

transport playing no role (Ristenpart *et al.*, 2009; Bird *et al.*, 2009; Helmensdorfer & Topping, 2013). The TCAM has been successful in explaining observed non-coalescence phenomena at macro (Ristenpart *et al.*, 2009), micro (Thiam *et al.*, 2009) and nano (Wang *et al.*, 2015) length scales, demonstrating its universality. However, in some non-coalescence cases, the meniscus between the drops widens to form a neck, prior to shrinking (Mhatre *et al.*, 2015; Guo & He, 2014). This cannot be explained by the TCAM, which predicts that the meniscus shrink as soon as charge is transferred; further study is needed to characterise this phenomena.

In this section, the transition from coalescence to non-coalescence of microdrops is investigated, a problem that has not yet been numerically studied using a continuum approach. There are several novel aspects to this work. First, as discussed in the previous section, charged microdrop dynamics differs from its macroscale counterpart, because the width of the diffuse charge regions becomes significant in comparison to the drop size. The electrokinetic model employed here allows for the transfer of charge to be tracked as the coalescence process unfolds. Second, using this model, a regime of non-coalescence phenomena is found which depends on both charge and capillary effects, and cannot be predicted by the TCAM. In addition, a number of factors which affect charge separation are shown to influence the coalescence transition. Third, a hitherto unexplored intermediate 'partial coalescence' regime is discovered.

The system studied is illustrated in figure 6.13a. Two conducting, electrolytic drops of equal radii ($R_1 = R_2$) are suspended in immiscible outer phase (oil), separated by an initial separation distance S. A steady (DC) electric field $\boldsymbol{E}^*$ is imposed along the vertical axis. Figure 6.13b illustrates the dynamic behaviour of the system considered here. The initially electroneutral drops 1 and 2 get charged by the positive and negative electrode, respectively (frame 1), thus acquiring the same net polarity as the adjacent electrode (frame 2). Note that the outer phase is a dielectric and does not contain ions, while the charging of the drops is achieved numerically by initializing the drops 1 and 2 with a deficit of anions and cations, respectively. Consequently, the electric field electrophoretically conducts each drop to the electrode with the opposite polarity to its charge, thus setting the drops on a collision course (frame 3).

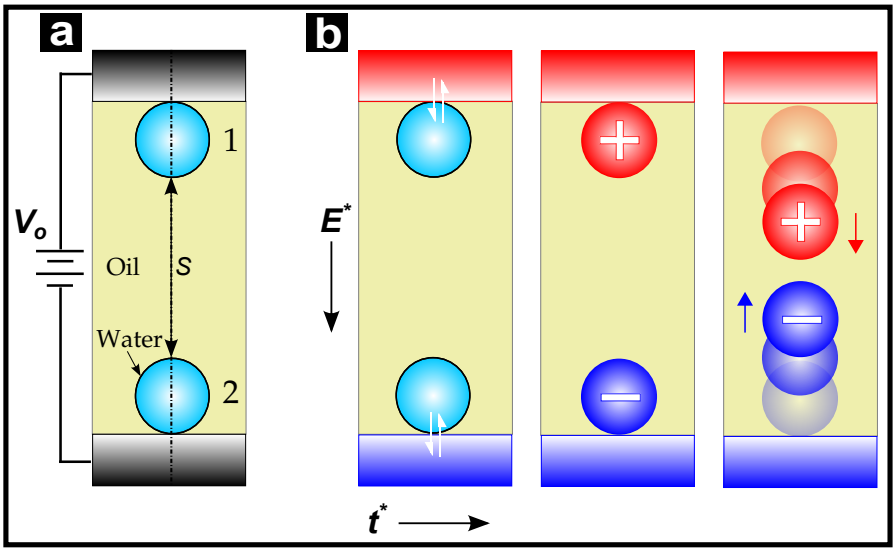

Figure 6.13: (a) Schematic of problem. (b) The drops get oppositely charged by contacting the electrodes, following which they are induced to move towards each other.

6.4.1 Types of coalescence phenomena

Three distinct behaviours are observed as shown in figure 6.14. Figure 6.14a shows the temporal evolution for drops with small Oh (Oh = 0.5), i.e. when charge effects are relatively less important. The drops are initialised in the first frame with equal and opposite net charges ($\Delta q_1 = 0.05, \Delta q_2 = -0.05$). The electric field imparts opposite conductive fluxes to both ion species (in both drops), resulting in anions and cations migrating to opposite ends within the drops. The regions of bulk charge that form are visible in frame 2. Due to the imposed imbalance in ion densities, the net electrophoretic force acts to translate the drops towards each other. In addition, the dielectrophoretic force increases with decreasing separation ($F_D = 24\pi\epsilon_c R^6 \boldsymbol{E}^2/S^4$ for two equal sized conducting drops in a dielectric medium (Atten, 1993)). This causes the inner tips of the approaching drops to project outward and form Taylor-cone like structures (frame 2). Note that actual pointed ends don't form for charged drops, as discussed in Chapter 4. Once the outer phase between the drops is squeezed out, the drops contact, and the interfacial film ruptures. The bulk charge, which sandwiched the interfacial film pre-rupture, is conducted to the ends of the now-conjoined drop (frame 3). Capillary forces push fluid into the neck, widening it, and the drop relaxes into an equilibrium shape (frames 4-7).

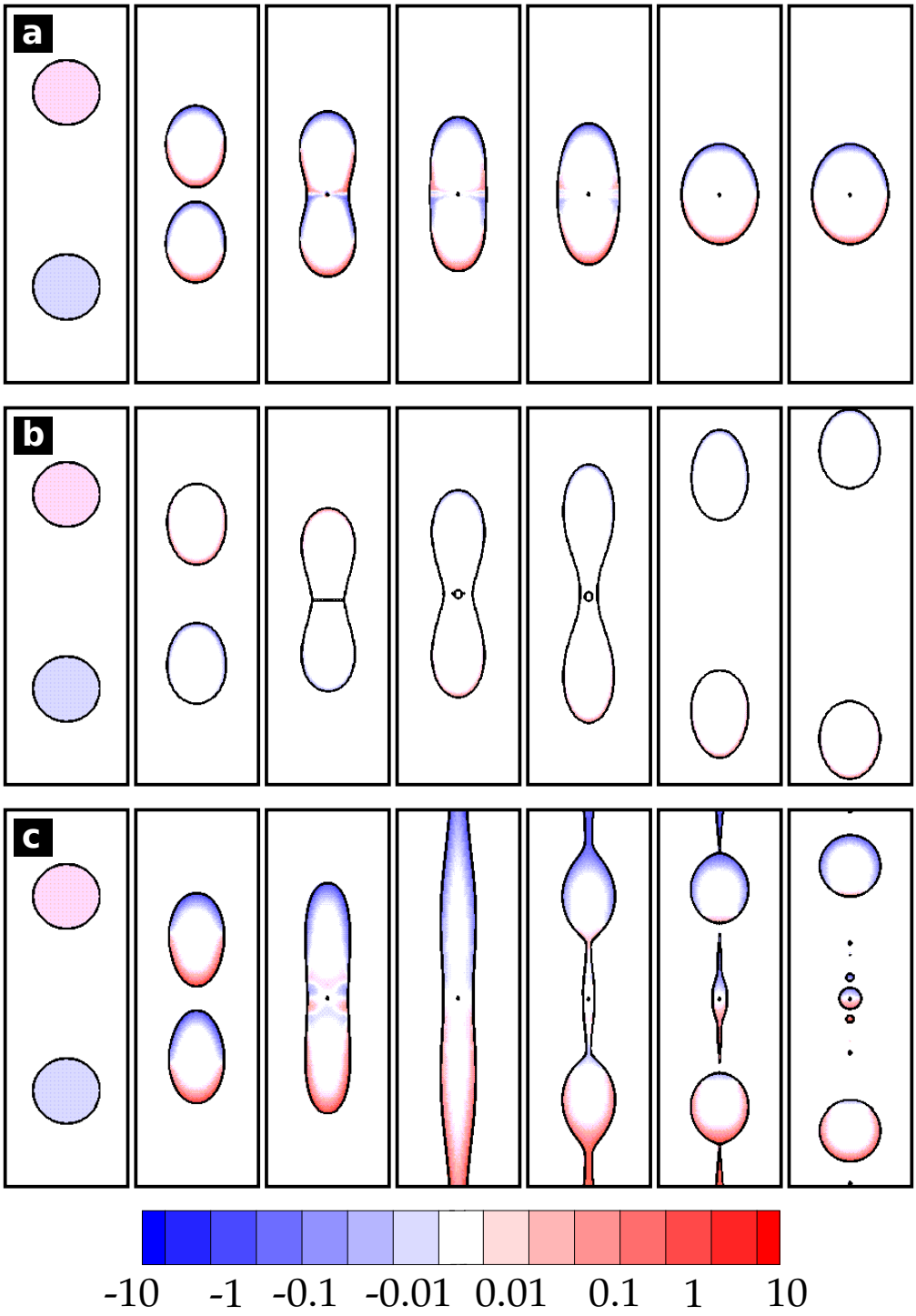

Figure 6.14: Time lapse images with overlaid charge (q) contours for (a) Ca = 0.15, κ = 25, Oh = 0.5 for times t = 0, 20, 22.5, 25, 27.5, 45, 60, complete coalescence. (b) Ca = 0.15, κ = 25, Oh = 5 for times t = 0, 7.5, 15, 30, 90, 150, 180, non-coalescence. (c) Ca = 0.20, κ = 15, Oh = 1.0 for times t = 0, 35, 50, 80, 115, 120, 140, partial coalescence. $\Delta q = 0.05$, $S = 4$ and $Q = 10$ for a-c.

In figure 6.14b, Oh is increased by an order of magnitude (Oh = 5), resulting in a slower deformation process (compare the times for corresponding frames in figure caption). This temporal difference allows greater charge to accumulate near the interface, resulting in a narrower diffuse charge layer adjacent to the interfaces compared to 6.14a (frame 2), and a stronger electrophoretic attractive force. Once the drops contact (frame 3), the portion of the interfacial film adjoining the sides of the drops ruptures first and a small drop of oil is encapsulated at the centre (frame 4) as observed in experiments (see figure 3 in Mhatre *et al.* (2015)). Following charge conduction to the outer tips of the conjoined drop, the electrophoretic force there becomes strong enough to separate the drops. The drops proceed to move away from each other, indicating the switch in net charge achieved during the brief contact (frames 5-7). Thus, the transition from coalescence (6.14a) to non-coalescence (6.14b) is obtained by increasing the Oh number, which effectively increases the relative importance of electrokinetic effects to the deformation of the drops.

The first three frames of 6.14c, with an intermediate Oh (Oh = 1) and a higher electric field (Ca = 0.20), qualitatively resemble the corresponding frames in 6.14a. However, there are quantitative differences because of the increased charge separation; the inner tips are significantly more deformed in frame 2 and the conjoined drop is more elongated in frame 3. This results from the larger attractive electrophoretic force pre-contact and the larger electrophoretic deforming force once charge is conducted to the outer tips after contact. Unlike the case in fig 6.14a, the deforming force is able to overcome the resisting interfacial tension and stretch the drop (frame 4) until the lobes form a dumbbell structure (frame 5). Then, capillary pinch off occurs in multiple locations simultaneously (frame 6), resulting in a partial coalescence event with multiple satellite droplets separating the two larger drops which continue to move apart (frame 7).

6.4.2 Electrohydrodynamics of partial coalescence

The temporal evolution of the pressure distribution (for a partial coalescence case) is shown in figure 6.15. As the drops approach each other, the pressure is lowest at the inner tips despite the high curvature (frame 1), due to the attractive electrical forces. Once the drops have undergone a topological transition to a unified conjoined drop, the pressure in the neck is lower compared to the bulk (frame 2). This initially results in fluid flow into the neck, widening it (frame 3). Then, the electrophoretic separation forces stretch the outer tips (frame 4), thus increasing the Taylor cone angle gradually. The

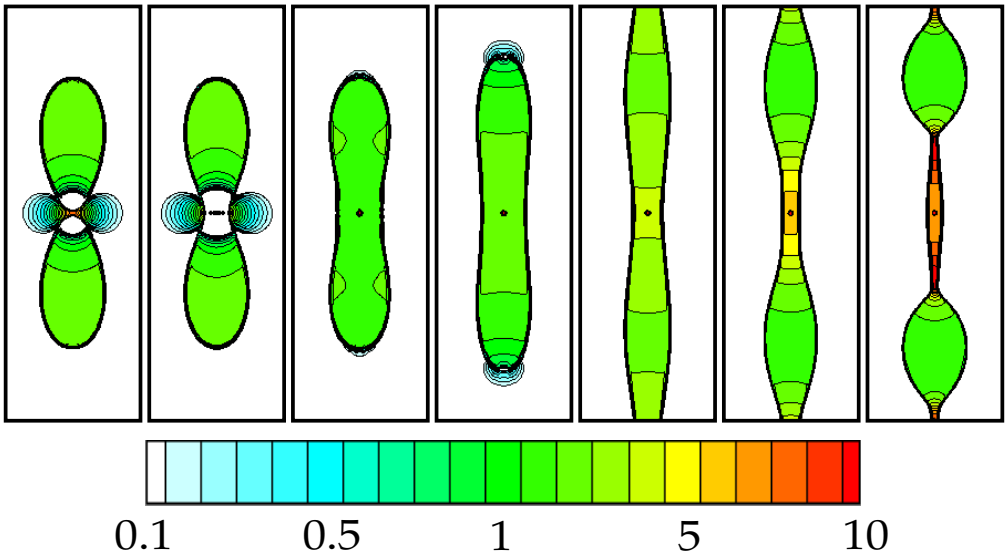

Figure 6.15: Time lapse images with overlaid pressure contours for Ca = 0.20, $\kappa = 15$, Oh = 1.0, $\Delta q = 0.05$, $S = 6$ and $Q = 20$, for t = 45, 45.5, 48.5, 55, 80, 95, 105.

increase in the cone angle past the critical value predicted by TCAM coincides with the pressure in the neck reducing to below the corresponding value in the lobes adjacent to it (frames 5-7). Now the fluid flows out of the neck, rather than into it, shrinking the neck and eventually resulting in pinch off. This demonstrates why the TCAM cannot be used to predict the incomplete coalescence cases studied in this Letter. As the cone angle *prior to contact* is lower than β_{cr} for all the cases studied, the TCAM always predicts coalescence. However, as seen here, electrokinetic forces after contact determine whether the transient cone angle exceeds the critical limit *during* the coalescence process. In cases where it does, partial coalescence or non-coalescence, rather than coalescence, occurs. This model is referred to as the transient electrokinetic-capillary model (TECM). The key insight of the TECM is that incomplete coalescence can be induced by a high electrophoretic separation force, resulting from the total charge separated in both drops, which is conducted to the ends of the conjoined drop post contact. The rest of this chapter will focus on characterising the TECM predictions.

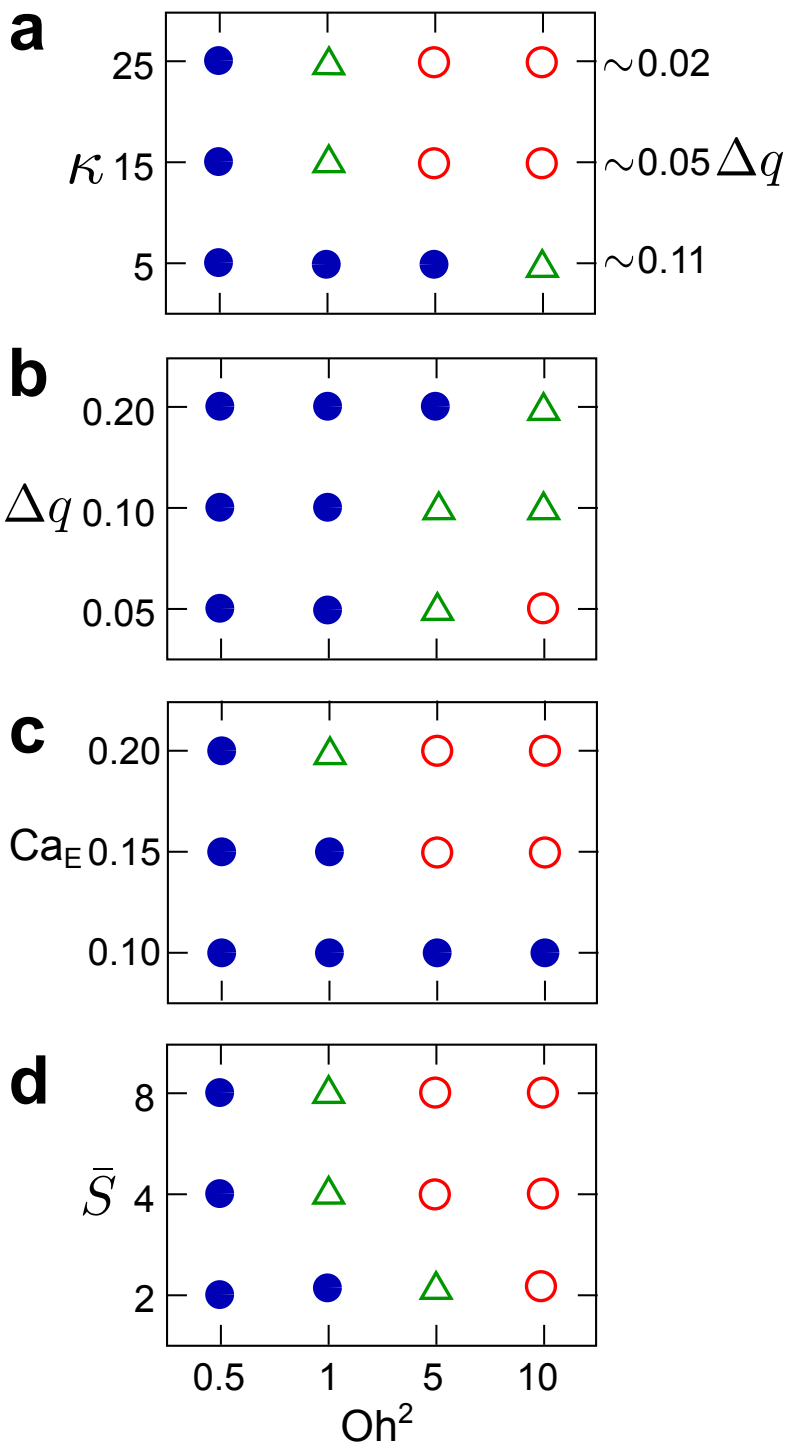

Figure 6.16: Phasemaps showing type of coalescence phenomena observed by varying Oh and (a) electric field (Ca), (b) drop ionic conductivity (κ), (c) absolute drop charge (Δq) and (d) separation distance (S). Complete coalescence is depicted by solid blue circles, partial coalescence by open green triangles and non-coalescence by open red circles.

6.4.3 Phase maps for coalescence transitions

A complete analytical description of the TECM is challenging as the electrokinetic flow behaviour is complex, but the qualitative impact of relevant parameters is illustrated in figure 6.16 with the aid of low-resolution phase maps. In each case, Oh, which represents importance of electrokinetic effects, is varied along with another parameter. Cases where complete coalescence is observed are depicted by solid circles, partial coalescence by open triangles and non-coalescence by open circles, respectively. Figure 6.16a shows that increasing the electric field increases the likelihood of transition from coalescence to non-coalescence (C-NC), for a fixed Oh, consistent with the TCAM (Ristenpart *et al.*, 2009; Bird *et al.*, 2009). Figure 6.16b shows that increasing drop ionic conductivity (for a fixed Oh) also aids the C-NC transition, which can be explained in the TECM by the increased charge separation that results from a higher initial ionic conductivity. This translates to an increased electrophoretic separation force post contact, as greater charge is conducted to the outer tips. Hamlin *et al.* (2012) found, while studying macroscale drops, a critical ionic conductivity separating regimes of partial coalescence and non-coalescence for a drop-interface system; the results shown here extend their work to microscale drop-drop systems.

Note that the dimensionless charge density Δq is varied with κ to keep the dimensional drop charge fixed ($\Delta q \propto \kappa^2$). The separation distance between electrodes is small relative to channel dimensions in some CCEP/ECD LoC devices (Drews *et al.*, 2013). Hence, the impact of initial separation distance (S) is studied in 6.16c, and it is seen that increasing S (for a fixed Oh) favours the C-NC transition. This is because, for a larger S, the charge separates for a longer time period in each drop prior to their contact, which predictably increases the strength of the electrophoretic separation force post contact. Finally, the impact of absolute drop charge (Δq) on the C-NC transition (6.16d) shows that it is, counter-intuitively, inversely correlated. The partial and non-coalescence cases, therefore, tend to occur at lower values of drop charge, for a fixed Oh. This is analogous to the observation of increased probability of complete coalescence for greater drop charge seen in the previous section. It results from the increased velocity of the drops when their charge is increased, making them accelerate towards each other, and start coalescing quicker, resulting in less charge separation at contact. It is also sensitive to the assumption made in this work that the the drops are charged by transfer of ions *out of the* drop and onto the electrode rather than vice-versa, which is reasonable given the

charging process is not well understood Im *et al.* (2011). This means the attractive force between the drops is strengthened by increasing Δq, but the electrophoretic separation force post-contact is weakened, making incomplete coalescence less likely in the TECM framework.

6.4.4 Conclusions

In summary, the transition from coalescence to non-coalescence of oppositely-charged microdrops was studied. The popular Taylor cone angle model (TCAM) was demonstrated to be inadequate for microdrops, because it precludes the possibility of electrical forces from playing a role once the drops have contacted. Instead, a complementary model which focuses on effects of charge transport post-contact was proposed, called the transient electrokinetic-capillary model (TECM). The TECM explained our predictions along with shedding light on previous experimental results obtained for intermediate electric fields for macrodrops (Mhatre *et al.*, 2015; Guo & He, 2014). A hitherto unknown intermediate partial coalescence regime was discovered, and the transitions between the three regimes was mapped using parameter phase-maps. The work detailed here prove instructive to designing microfluidic devices where the drops are charged directly by contact with electrodes, as oppositely-charged drops frequently interact in these devices.

7 Current and future work

> *I've never seen the Icarus story as a lesson about the limitations of humans. I see it as a lesson about the limitations of wax as an adhesive.*
>
> Randall Munroe

This chapter concludes this thesis and is divided into three parts. First, in addition to the conclusions detailed in each chapter, it is also possible to draw some general conclusions which are provided (§ 7.1). Second, a brief taste of problems not included in the results chapters are discussed (§ 7.2). These problem setups were studied during the course of research, but were not completed in time to make it into the preceding chapters of this thesis. Finally some possible future research is suggested, involving mathematical modelling, numerical methods, and investigation of physics (§ 7.3).

7.1 Concluding remarks

In this section, some concluding remarks for the thesis are presented. In chapter 1, the field of drop microfluidics was introduced, and the research gap was identified, namely a fundamental understanding of electrically-induced drop deformation, breakup, and coalescence, in the presence of mobile charge distribution. The literature review in chapter 2 traced the study of drop electrohydrodynamics back to its origins in understanding natural phenomena such as raindrops in thunderstorms. A description of the early experiments was provided, as well as the subsequent analytical theory development that focused on the three popular limits in the literature, namely the perfect dielectric, perfect conductor, and the leaky dielectric models. The numerical implementation of these models was reviewed as well, and the difference in electric force formulation for each model was discussed. These simplified formulations did not consider the motion of mobile ions within the drop, which influences the overall system behaviour at the microscale. The best current understanding of ion-induced phenomena comes from electrokinetic theory which was outlined. In chapter 3, governing equations for an electrokinetic model were listed, and the numerical implementation of the multiphase electrokinetic model

was detailed.

In chapter 4, this model was used to study the deformation and breakup of an isolated drop in an electric field. The goal was to provide information about drop stability for LoC applications where breakup was undesirable. A phase map was developed to characterise the breakup for different drop ion concentrations and external electric fields. The two different types of breakup seen in the literature - 'tip-streaming' and 'pinch-off' - were shown to result from the same charge-driven Rayleigh instability of the fluid columns that form behind drop tips. In chapter 5 the focus was on finding information about drop stability for LoC applications where drop breakup was desirable, such as drop formation. The goal was to discover quantitative information of the progeny droplets ejected at breakup. Using the time and length scales of capillary pinch-off phenomena, scaling relations were formulated to predict the charge and size of progeny droplets, across a wide range of parameters. A universal scaling law relating the progeny droplet size to its charge was also devised. In chapter 6 drop coalescence was studied, for simple systems involving either a drop and an interface or two drops. Numerous novel phenomena were detailed, including two types of partial coalescence, and non-coalescence. Some qualitative phase maps were developed to characterise the results observed. A scaling relation was also formulated for the drop-interface system.

7.2 Current work

This section briefly describes some of the ongoing work relevant to the thesis topic.

7.2.1 Electrical suppression of hydrodynamic partial coalescence

While the bulk of chapter 6 was focused on *electrohydrodynamic* partial coalescence, partial coalescence (and subsequent residual droplet formation) can also occur in a purely *hydrodynamic* system, such as raindrop splashing into a puddle. Charles & Mason (1960*b*) were the first to systematically study the coalescence of a liquid drop falling on its bulk liquid interface for different liquid combinations. In a subsequent paper they experimentally observed partial coalescence, where a residual droplet is ejected from during the coalescence of the parent drop with the bulk liquid interface (Charles & Mason, 1960*a*) . As discussed in § 6.3.2, the coalescence process can be understood as a competition between vertical and horizontal collapses, both driven by interfacial tension. The vertical collapse is inherently favoured, and complete coalescence is the more

likely outcome. For the horizontal collapse to prevail, and pinch off of the drop to occur, the vertical collapse must be sufficiently delayed by a suitable mechanism. Charles & Mason (1960*b*) hypothesized that the mechanism responsible for this phenomenon was the Rayleigh-Plateau pinch-off instability that caused an isolated deformed drop to breakup. Subsequent studies (Thoroddsen & Takehara, 2000; Mohamed-Kassim & Longmire, 2004; Aryafar & Kavehpour, 2006; Aryafar *et al.*, 2006) have focused on different aspects of the partial coalescence process, such as the velocity of film drainage time, size of the ejected residual droplets, and development of (self-similar) scaling regimes to describe the coalescence phenomena.

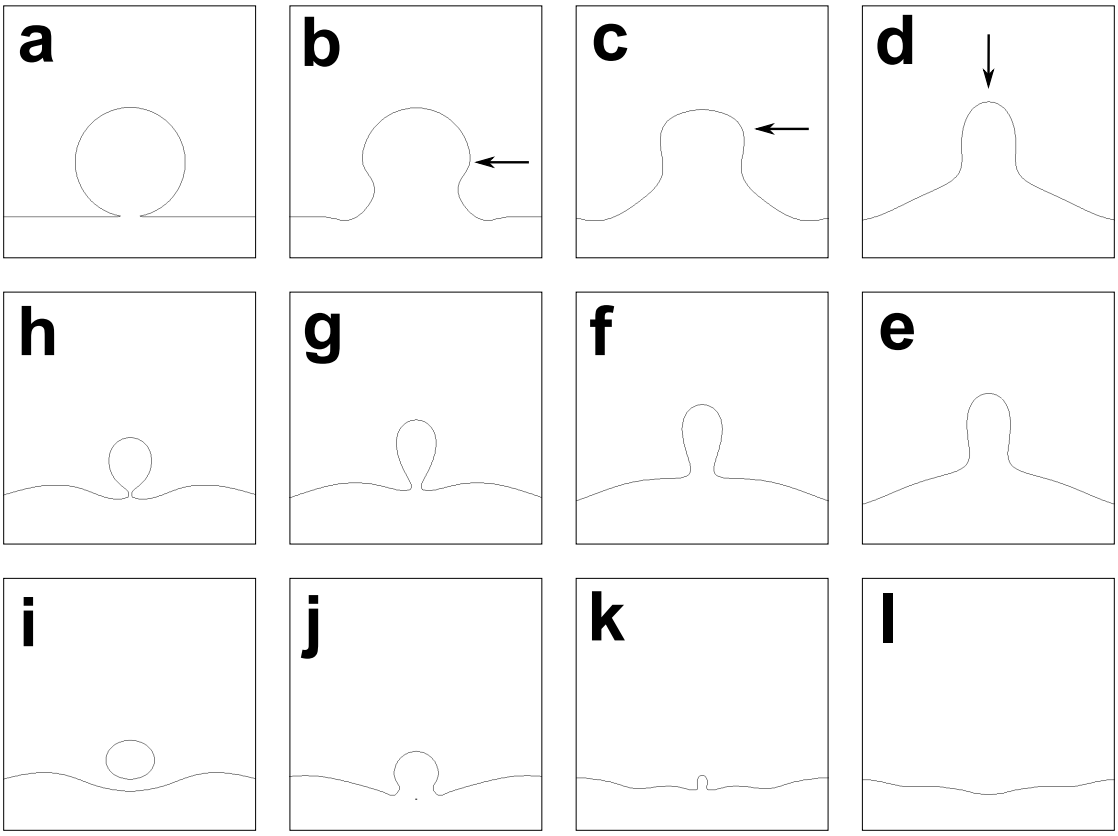

Figure 7.1: Time lapse images (clockwise, starting from top left) of a water drop ($\mathrm{Oh}^2 = 0.00053$, $\bar{\mu} = 0.53$, and $\bar{\rho} = 0.53$) undergoing complete coalescence, $t = 0, 40, 80, 120, 140, 160, 180, 200, 220, 260, 300, 320$.

Blanchette & Bigioni (2006) combined high-speed video imaging with numerical simulations to show that partial coalescence did not, in fact, result from the Rayleigh instability

as proposed by Charles & Mason (1960*a*). Instead, the coalescence phenomena resulted from an interfacial-tension-generated vertical stretching of the drop at its summit. A typical case is shown in Figure 7.1, for a drop having $\mathrm{Oh}^2 = 0.00053$, and a viscosity ratio of $\bar{\mu} = 0.53$ and unity density ratio. The drop is intialised in contact with the interface with a ruptured interfacial film (Figure 7.1a). Due to the low Oh, and consequently high interfacial tension, the widening of the drop neck occurs rapidly, and this results in the formation of capillary waves. These capillary waves travel upwards along the side of the drop surface, and can be visualised in frames b-d of Figure 7.1. When the capillary waves converge at the drop summit, they create a upward-acting force that acts to delay the vertical collapse, and horizontal collapse occurs first, pinching-off a residual droplet. This process can repeat 6-8 times for a liquid drop at a water/air interface (Thoroddsen & Takehara, 2000), but fewer occurrences (1-3) are observed at water/oil interfaces (Chen *et al.*, 2006). In Figure 7.1, complete coalescence is observed after a single partial coalescence event (frames i-l).

In a subsequent paper, Blanchette & Bigioni (2009) developed an approximate compound criterion to predict partial coalescence; assuming zero gravity, pinch-off was predicted if

$$\frac{\mathrm{Oh}(1 + 0.53/\bar{\mu}\,)}{\sqrt{1 + 2.22/\bar{\rho}}} < 0.026. \tag{7.1}$$

Thus the (hydrodynamic) partial coalescence is suppressed by viscous forces when Oh is below a critical value. This criterion (Equation 7.1) fails in case of outer phases with high viscosities (Gilet *et al.*, 2007), or for a non-zero Bond number (Ray *et al.*, 2010), but agreed well with the results for the parameter ranges studied in this work.

Now, an electric field is applied to the system studied in Figure 7.1. A $\mathrm{Ca_E} = 0.30$ and a permittivity ratio of $\bar{\epsilon} = 10$ is chosen for the simulation results shown in Figure 7.2. As the Oh for the case is below the critical limit ($\mathrm{Oh}^2 < 10^{-2}$), electrokinetic effects can be ignored as concluded in chapter 5, so $\kappa = 0$. As with Figure 7.1, partial coalescence is observed in Figure 7.2. However, the coalescence process is delayed significantly, as can be seen by comparing the times in the captions for Figure 7.1 and Figure 7.2. Also, the residual droplet appears more elongated prior to pinch-off (compare Figure 7.1g and Figure 7.2c), resulting in a prolate-spheroidal residual droplet (Figure 7.2e), rather than the oblate-spheroidal residual droplet seen in Figure 7.1i. When the permittivity ratio is increased to $\bar{\epsilon} = 20$ in figure Figure 7.3, the vertical stretching of the drop increases

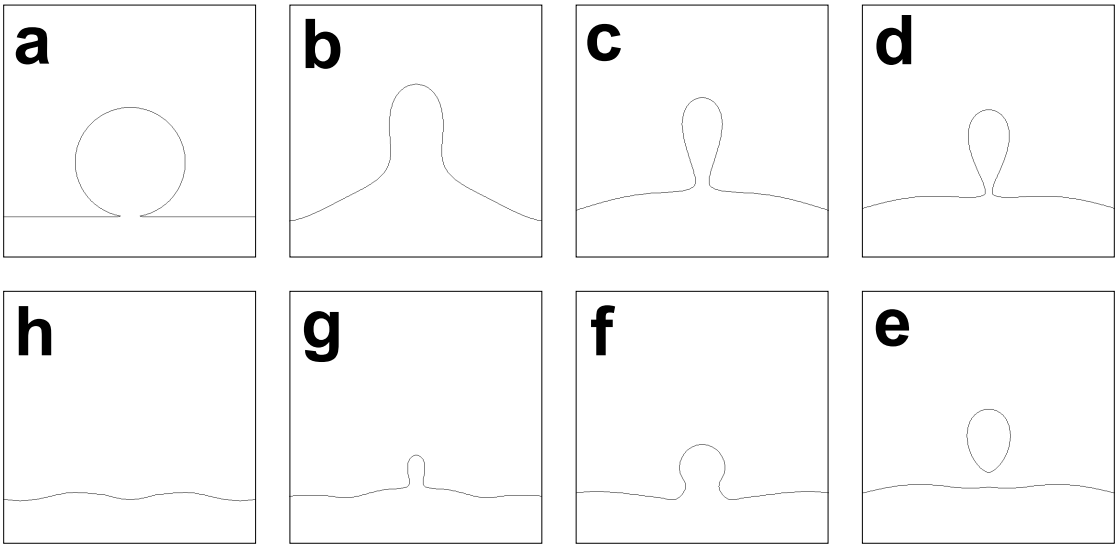

Figure 7.2: Time lapse images (clockwise, starting from top left) of a water drop ($\mathrm{Oh}^2 = 0.00053$, $\bar{\mu} = 0.53$, $\mathrm{Ca_E} = 0.30$, $\kappa = 0$, and $\bar{\epsilon} = 10$) undergoing complete coalescence, $t = 0, 120, 200, 220, 240, 340, 380, 420$.

further, and, crucially partial coalescence is not observed. Instead the drop coalesces in a single-stage, and the coalescence process takes longer compared to Figure 7.1 and Figure 7.2.

It is well known that electrostatic effects can be used to accelerate electric coalescence, as well as suppress partial coalescence (Charles & Mason, 1960*a*; Eow *et al.*, 2001*b*; Teigen *et al.*, 2006), but the underlying mechanism is not well-understood. Here we propose a simple mechanism based on the direction of the surface tension and (dielectric) electric forces. The surface tension force, once the neck has expanded to maximum length, acts radially inwards at every point on the drop surface. This force is represented in the Navier-Stokes equations as,

$$\boldsymbol{F}_{\mathrm{S}} = \frac{1}{\mathrm{We}}\kappa\delta(r)\boldsymbol{n}. \tag{7.2}$$

In the absence of electrokinetic forces, the permittivity force term can be written as

$$\boldsymbol{F}_{\mathrm{E}} = -\frac{1}{2}\boldsymbol{E}\,\boldsymbol{.}\,\boldsymbol{E}\nabla\epsilon. \tag{7.3}$$

In the case where the permittivity of the drop is greater than the surrounding fluid, as is the case for a water-oil system, this force will act radially outward at every point on the surface of the drop (Figure 7.4). Therefore, given that the permittivity force opposes the

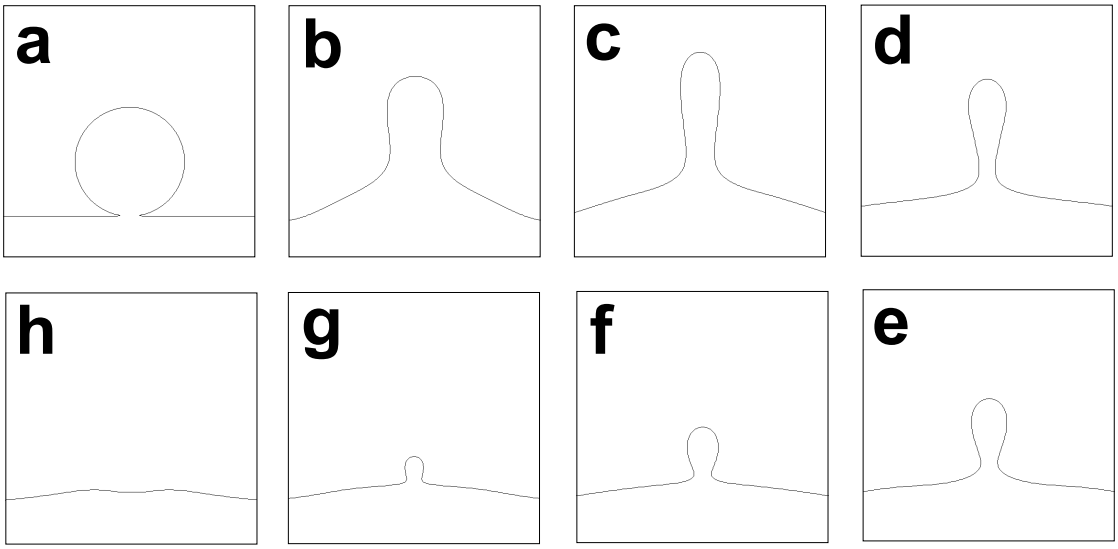

Figure 7.3: Time lapse images (clockwise, starting from top left) of a water drop ($\mathrm{Oh}^2 = 0.00053$, $\bar{\mu} = 0.53$, $\mathrm{Ca_E} = 0.30$, $\kappa = 0$, and $\bar{\epsilon} = 20$) undergoing complete coalescence, $t = 0, 120, 140, 180, 280, 340, 380, 420, 460$.

interfacial tension at the surface, an effective interfacial tension term can be defined as the difference between the two forces,

$$\boldsymbol{F}_{\mathrm{S_{eff}}} = \frac{1}{\mathrm{We}}\kappa\delta(r)\boldsymbol{n} + \frac{1}{2}\boldsymbol{E}\,\boldsymbol{.}\,\boldsymbol{E}\nabla\epsilon. \tag{7.4}$$

The dynamics of the coalescence process can be now understood in terms of this effective interfacial tension force ($\boldsymbol{F}_{\mathrm{S_{eff}}}$). The addition of an electric field in Figure 7.2 decreases the effective interfacial tension, resulting in a longer coalescence time when compared to Figure 7.1. The modified surface tension term in $\boldsymbol{F}_{\mathrm{S_{eff}}}$ can also be used to define an effective Oh ($\mathrm{Oh_{eff}}$), which provides insight into the electrical suppression of partial coalescence observed in Figure 7.3. As the electric force is increased, $\boldsymbol{F}_{\mathrm{S_{eff}}}$ decreases, and therefore $\mathrm{Oh_{eff}}$ increases. The input parameters for the case in Figure 7.3 satisfy the partial coalescence criterion in Equation 7.1, when calculated using the original Oh. However, if the the criterion were to be recalculated using $\mathrm{Oh_{eff}}$, the criterion would be no longer satisfied, as the higher effective interfacial tension results in complete coalescence of the drop. This mechanism agrees well with our numerical results. Future plans include developing a quantitative measure for $\boldsymbol{F}_{\mathrm{S_{eff}}}$, and scaling the residual droplet size using this parameter.

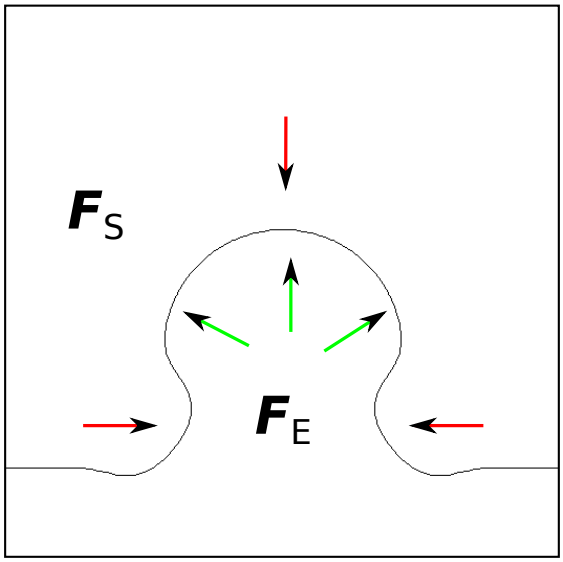

Figure 7.4: A schematic showing the direction of the interfacial ($\boldsymbol{F}_S$) and electric ($\boldsymbol{F}_E$) forces acting on the drop.

7.2.2 The influence of permittivity force on the coalescence of charged drops

Non-coalescence of charged drops at liquid interfaces

In chapter 6, the simulations for charged drop coalescence were conducted assuming a unity permittivity ratio between the phases, and consequently, zero permittivity force. *Passive* partial coalescence was observed for Oh ≤ 1, and *active* partial coalescence for Oh > 1. Here, the impact of increasing the permittivity ratio to $\bar{\epsilon} = 20$ on the active active partial coalescence process is studied in Figure 7.5. The coalescence phenomenon is unlike any observed in chapter 6. The drop deforms and forms a lobe at the inner end prior to contact (Figure 7.5d) similar to the unstable isolated drop cases studied in chapter 4 and chapter 5. Once the drop contacts the interface, charge transfer occurs, and the neck of the drop starts to shrink *immediately* (Figure 7.5e-f). Consequently the mass transfer of the drop contents into the bulk liquid is negligible, and the drop is summarily ejected (Figure 7.5g-h); the residual droplet measurements ($a/R = 0.969$) confirm this fact. This phenomenon is qualitatively similar to the bouncing of drops studied in § 6.4, and therefore can be accurately classified as a *non-coalescence* phenomena. Future work on this problem involves scaling the residual droplet size and charge, as well as developing phasemaps which delineate regions of complete coalescence, passive partial coalescence,

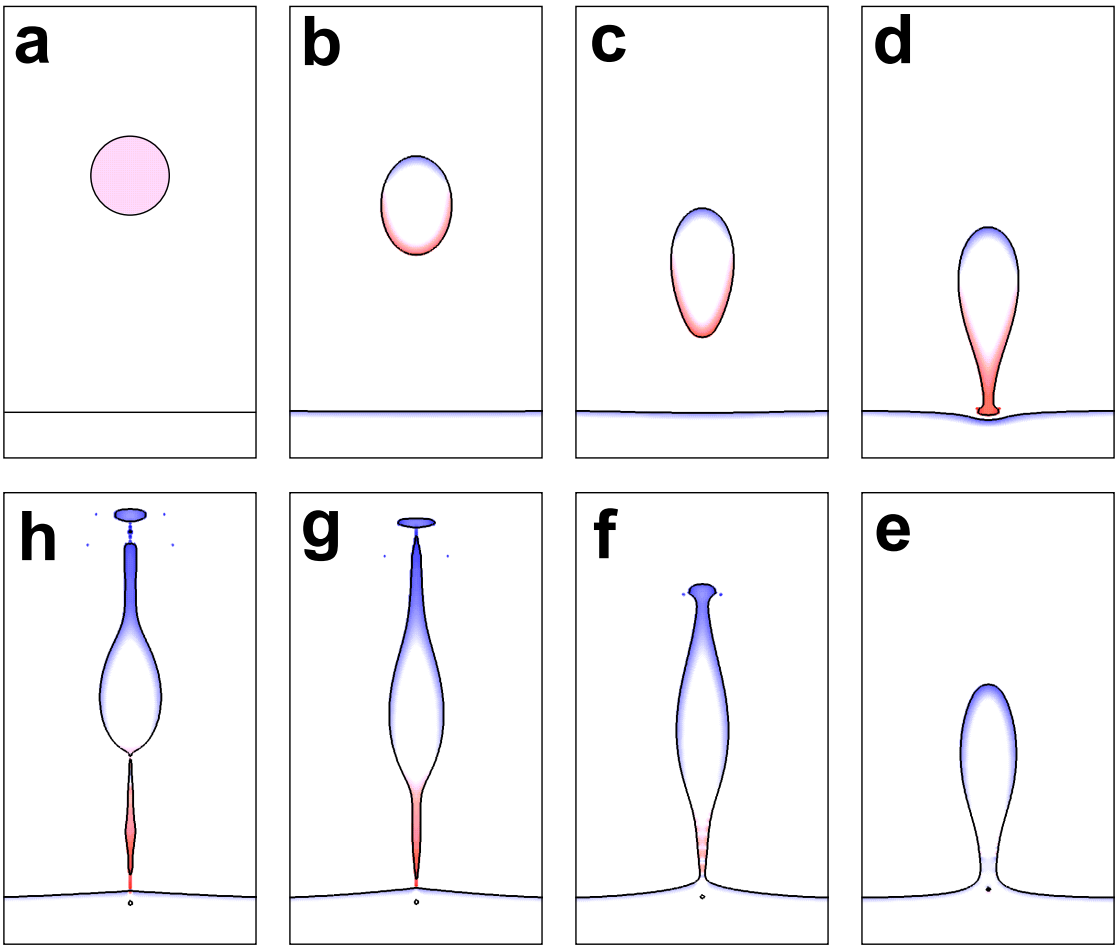

Figure 7.5: Time lapse images (clockwise, starting from top left) of a water drop ($\mathrm{Oh}^2 = 10$, $\bar{\mu} = 1$, $\mathrm{Ca_E} = 0.20$, $\kappa = 15$, $\bar{\epsilon} = 20$, $\bar{S} = 5$, and $\Delta q = 0.05$) undergoing non-coalescence ($a/R = 0.969$), $t = 0, 100, 300, 400, 500, 600, 700, 800$.

active partial coalescence, and non-coalescence.

Fission of charged drops at liquid interfaces

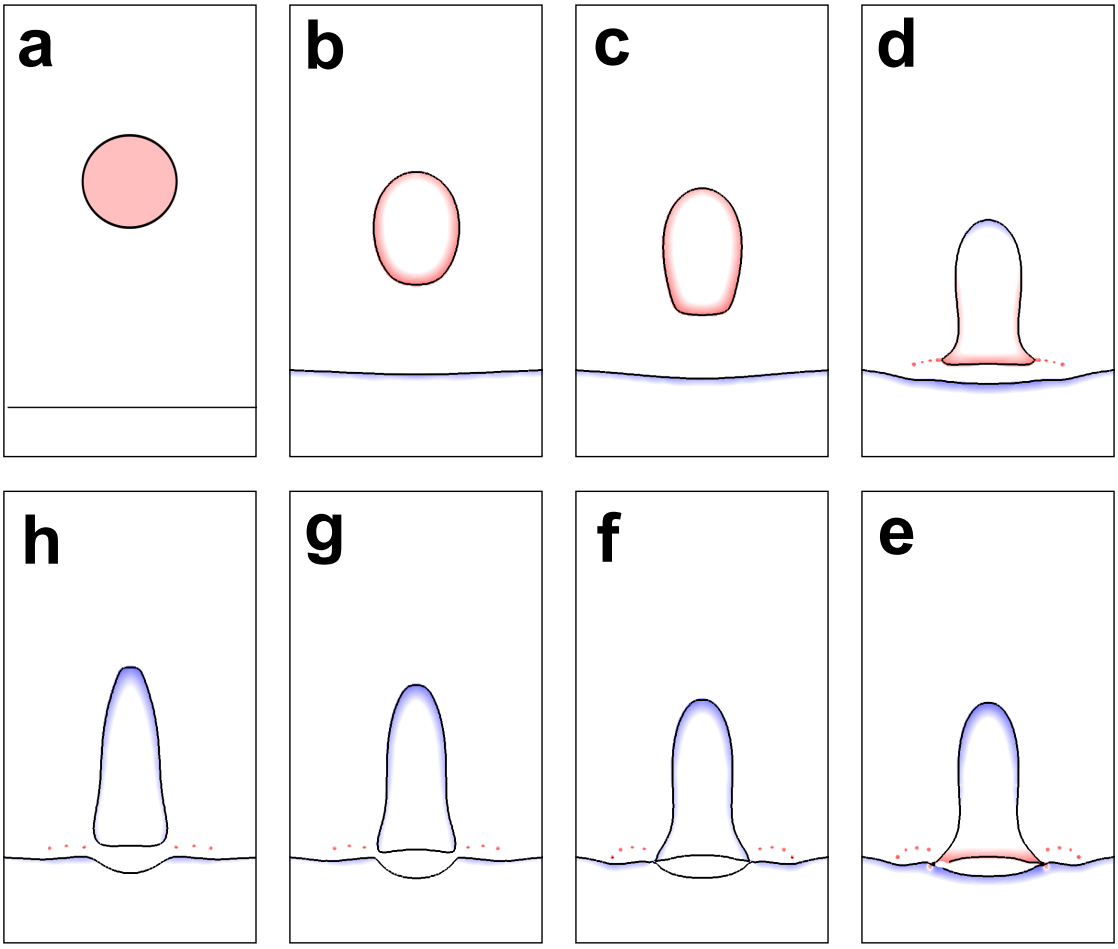

Figure 7.6: Time lapse images (clockwise, starting from top left) of a water drop ($\mathrm{Oh}^2 = 100$, $\bar{\mu} = 1$, $\mathrm{Ca_E} = 0.20$, $\kappa = 15$, $\bar{\epsilon} = 50$, $\bar{S} = 3$, and $\Delta q = 0.05$) undergoing fission, $t = 0, 200, 300, 600, 750, 800, 1000, 1200$.

In Figure 7.6, the coalescence of a charged drop with $\mathrm{Oh}^2 = 100$ and $\bar{\epsilon} = 50$ is studied. The increased Oh and $\bar{\epsilon}$ compared to Figure 7.5 mean that both charge and permittivity forces are higher here. These increased electric forces result in the occurrence of a qualitatively new phenomena; the drop appears to flatten and burst prior to contact. During the bursting process, a fine stream of droplets is ejected from the corners of the flattened end of the primary drop as it approaches the interface. This bursting of charged

drops was only observed at $\bar{\epsilon} > 40$ in the simulations conducted. A high drop permittivity and conductivity results in a small diffuse charge layer combined with a small value of electric field inside the drop. This approaches the description for the 'perfect conductor' limit for macroscale drops (§ 2.2.2). In fact Wang *et al.* (2014) observed a similar bursting phenomena for dilute HCl drops, and argued that it was probably a manifestation of the Coulombic fission for drops with high interfacial charge. Huo *et al.* (2015) showed that this phenomena was more likely to occur at high conductivity and permittivity, analogous to the numerical results shown here. However, as the charge is contained *inside* the drops rather than on the interface, it is not clear that the Coulombic fission mechanism is necessarily applicable to the results shown here; this problem requires further study. An example of the experimentally observed fission is shown in Figure 7.7. Note that for the experiment in Figure 7.7 the drops are setup as pendant drops on oppositely charged electrodes, which makes them fixed in space. Consequently, they cannot move away from each other after charge transfer, unlike the drop in our simulations (Figure 7.6).

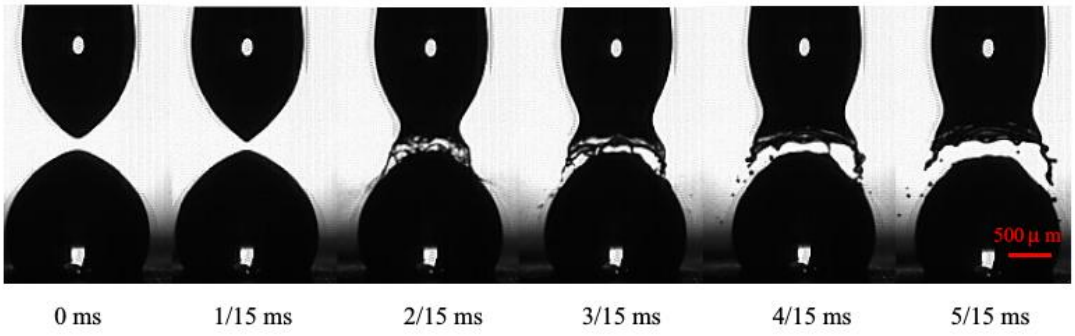

Figure 7.7: Time lapse images (starting from left) of a drop of hydrochloric acid solution undergoing fission at 1.5 kV. The time interval is 1/15 ms, and the solution conductivity is 820 $\mu s/cm$. Reproduced from Huo *et al.* (2015).

7.3 Future work

The suggestions for future work can be divided into three categories: Mathematical modelling, numerical methods, and investigation of physics.

7.3.1 Mathematical modelling

The model used in this thesis consisted of the full Navier-Stokes equations in each phase, with additional source terms to account for interfacial tension and electric forces. The transport of ions was considered using the Nernst-Planck equation, and was coupled to the electric field with the Poisson equation. The model can be extended in several ways, three of which are highlighted below:

Including accurate interfacial forces

The model has already been extended to allow for interfacial charge (Davidson *et al.*, 2014, 2016) which will be used in future work. It is common for microfluidic interfaces to contain surface-active agents or surfactants, which can arise naturally as impurities or can be intentionally added to modify the interfacial tension properties. The surfactant concentration on the interface plays an important role in drop electrohydrodynamics (Nganguia *et al.*, 2013), and can calculated by solving an additional surfactant transport equation (Teigen & Munkejord, 2010) which modifies the surface tension force locally. Another issue ignored in the model is the presence of short-range forces, such as the attractive van der Walls forces or the steric repulsion forces (Ho & Tai, 1998). Though some of these forces can be modelled along with interface-reconstruction algorithms[1], an accurate representation of the forces requires a separate numerical model at the lower length scale, such as a molecular dynamics approach (Nie *et al.*, 2004). The continuum and molecular models are then coupled together to form a multiscale model.

Including alternating electric fields

Electrohydrodynamic manipulation of drops using Alternating Current (AC) electric fields is gaining popularity in the literature, and has been used to study oscillations (Yan *et al.*, 2015), electrocoalescence (Mousavi *et al.*, 2014; Chen *et al.*, 2015), and microfluidic flow-focusing (Tan *et al.*, 2014*b*; Castro-Hernández *et al.*, 2015) of water drops. A time-dependent field means that the ion conduction is severely restricted because the polarity of the electric field varies multiple times each second. Hence dielectric and dielectrophoretic forces tend to determine the dynamics of the drops. A comparison of the results in this thesis with an AC model would be instructive to see which applications are suitable for DC vs AC electrohydrodynamics.

[1] A popular approach is using DLVO theory, which represents the electrostatic and van der Waals forces as a potential field (Eijkel & van den Berg, 2005)

Modelling non-Newtonian fluids

Non-Newtonian models have been used to numerically study problems as diverse as stretching of electrified jets (Feng, 2002, 2003), drop-interface coalescence (Yue *et al.*, 2006), dripping-to-jetting transitions (Ren *et al.*, 2015), and breakup of liquid filaments (Castrejón-Pita *et al.*, 2015). Microfluidic flows can involve non-Newtonian fluids such as physiological fluids (Srinivasan *et al.*, 2004) or polymer solutions (Ziemecka *et al.*, 2011). A multiphase version of the code used in this study has been, in the past, adapted to model viscoelastic (Harvie *et al.*, 2006*a*, 2008*a*) and shear-thinning (Harvie *et al.*, 2007) drops. This non-Newtonian model can be extended to include electrokinetics, and then used to study electrohydrodynamics of non-Newtonian drops.

7.3.2 Numerical methods

The governing equations are solved on a staggered, uniform mesh; fluid pressures, ion concentrations, and electric potentials are located at cell centers, while the velocity components are located at cell faces. The ion concentrations were advected along with the disperse phase volume fraction using the algorithm of Youngs (1982).

Transport of ions across the interface

The algorithm used in this model sets the flux of ions across the interface to be zero, as either of the two phases is assumed to be non-conducting. However, this algorithm can be extended to allow ion transport across the interface, based on local concentration or electric potential gradients. This extended algorithm can be used to study physically interesting phenomena, such as the extraction of cations from an ionic drop observed by Ahn *et al.* (2014). They showed that a positively charged drop of ionic liquid can sometimes 'leak' cations into the dielectric outer phase, to the extent that the net charge on the drop goes from positive to negative during its journey to the negative electrode. The drop therefore reverses direction midway and is conducted back to the positive electrode (Ahn *et al.*, 2014). An algorithm that allows for ions in both phases could also be used to model aqueous two-phase systems (ATPS) which, though rare, are gaining importance in droplet microfluidics (Hardt & Hahn, 2011). The low interfacial tension of ATPS allows for the creation of drops with unusual shapes, which has applications in reagent delivery to mammalian cells (Tavana *et al.*, 2009), for example.

Code parallelisation

The code used here employs serial processing, which means that each case is simulated on one processor at a time. This limits the complexity of the problem that can be solved, as systems involving more than a few drops would take a prohibitively long time to compute. For example, the longest simulations in this thesis took about three months to complete. This problem can be overcome by the use of parallel computing, where the simulation of each case is divided across multiple processors, with resultant performance gains of usually between 100x and 1000x depending on computational resources. The use of parallel computing requires compartmentalising the geometry into sub-domains, such that each sub-domain is allocated to a different processor (Evans *et al.*, 2000). Such parallelisation of the code, in conjunction with other improvements listed in this section, would allow for the simulation of larger scale, more realistic systems. An earlier (single phase) version of the code has been parallelised, which provides a viable platform for future development.

Dynamic grid refinement

In general, high resolution is needed to accurately capture topological changes that occur during breakup/coalescence of drops. As a uniform, structured grid is used here, some phenomena, such as the Taylor-cone driven bouncing of oppositely charged drops observed by Ristenpart *et al.* (2009) cannot be reproduced by our model. This is because the capillary bridge that transfers the charge between the drops is a few orders of magnitude smaller than the drop radius; it is therefore smaller than the mesh resolution in our simulations and cannot be resolved. It is feasible that this problem could be mitigated by the use of Adaptive Mesh Refinement (AMR) techniques. AMR techniques change the spacing between grid points at locations of interest dynamically over the course of the simulation, maintaining a higher resolution at the drop interface, for example. There exist AMR algorithms that have been shown to work well with VoF codes (Chen & Yang, 2014), and can be included in the model used in this thesis.

7.3.3 Investigation of physics

The contributions of this thesis have been entirely in the investigation of novel physical phenomena, and there exist many ways to build on the work done here. A few are highlighted below.

Coalescence of unequal-sized drops

Two limits are considered in this thesis for drop coalescence studies; the second drop is either the same size as the first drop (binary drop coalescence) or the second drop has far smaller curvature than the first drop (drop-interface coalescence). However, a lot of coalescence scenarios in LoC devices involve drops that are not identical, but not too dissimilar in size either (Mazutis & Griffiths, 2012). Novel coalescence phenomena have been observed for unequal-sized drops (Zhang *et al.*, 2009), and surface tension variations can enhance the mixing of the drops' contents (Blanchette, 2010). However, few numerical studies have looked at the electrohydrodynamics of unequal-sized drop coalescence, for both contacting and non-contacting (moving/charged) drop systems, for multiple ratios of drop radii.

Evolution of larger systems and new geometries

In this thesis, the breakup and coalescence scenarios were simulated for isolated systems involving one or two drops. However, practical LoC applications usually involve the manipulation of drops within the device dimensions. This could involve channels, contractions, and T-junctions among others (Gu *et al.*, 2011). It would be instructive to therefore simulate drop breakup/coalescence studies in confined environments typical of LoC devices, with additional geometric elements influencing to the drop dynamics. As the code has been used to study hydrodynamic drop deformation through a microfluidic contraction (Harvie & Davidson, 2005) and electroviscous flow of oil drops in an electrolyte (Davidson *et al.*, 2016). Therefore, the model can be readily extended to simulate multiphase electrokinetic flow in realistic geometries.

Electrohydrodynamics of drops resting on a solid surface

A prominent category of droplet microfluidics, digital microfluidics, involves manipulating arrays of drops are rested on a planar surface. These drops are actuated by electrowetting (Fair, 2007) (§ 1.5.1). While electrowetting has been investigated at macroscale (using a leaky dielectric model (Lin *et al.*, 2012)) and nanoscale (using molecular dynamics (Zhang *et al.*, 2016)), there exist no numerical studies for microscale drops (using an electrokinetic model) even though the vast number of LoC devices use microfluidic drops. Simulating three-phase systems involving solid/liquid interactions is subtly different from the liquid-liquid multiphase systems studied in this thesis. The respective interfacial tensions at the three-phase contact line and equilibrium contact angle need to be calculated as additional

outputs from the simulation. The model used here can be extended to study problems involving electrowetting of aqueous drops; it can then be applied to scenarios of interest, such as calculating the rate of spreading at different potentials (Chen *et al.*, 2013), and the influence of surface topography on the drop dynamics (Ramiasa *et al.*, 2014).

Bibliography

Abbi, S. S. & Chandra, R. 1956 On the equilibrium of a small conducting liquid drop in a uniform external electric field. *Proc. Natl. Inst. Sci. India, Part A* **1** (1), 363–368.

Adamiak, K. & Floryan, J. M. 2010 Dynamics of water droplet distortion and break-up in a uniform electric field. In *2010 IEEE Industry Applications Society Annual Meeting*, pp. 1–8. IEEE.

Agresti, J. J., Antipov, E., Abate, A. R., Ahn, K., Rowat, A. C., Baret, J., Marquez, M., Klibanov, A. M., Griffiths, A. D. & Weitz, D. A. 2010 Ultrahigh-throughput screening in drop-based microfluidics for directed evolution. *Proceedings of the National Academy of Sciences* **107** (14), 4004–4009.

Ahn, M. M., Im, D. J. & Kang, I. S. 2013 Geometric characterization of optimal electrode designs for improved droplet charging and actuation. *Analyst* **138** (24), 7362–7368.

Ahn, M. M., Im, D. J., Kim, J. G., Lee, D. W. & Kang, I. S. 2014 Extraction of cations from an ionic liquid droplet in a dielectric liquid under electric field. *Journal of Physical Chemistry Letters* **5** (17), 3021–3025.

Ahn, M. M., Im, D. J., Yoo, B. S. & Kang, I. S. 2015 Characterization of electrode alignment for optimal droplet charging and actuation in droplet-based microfluidic system. *Electrophoresis* **36** (17), 2086–2093.

Ajayi, O. O. 1978 A note on Taylor's electrohydrodynamic theory. *Proceedings of the Royal Society of London* **364** (1719), 499–507.

Allan, R. S. & Mason, S. G. 1962 Particle behaviour in shear and electric fields I. deformation and burst of fluid drops. *Proceedings of the Royal Society A: Mathematical, Physical and Engineering Sciences* **267** (1328), 45–61.

Ambravaneswaran, B., Subramani, H. J., Phillips, S. D. & Basaran, O. A. 2004 Dripping-jetting transitions in a dripping faucet. *Physical Review Letters* **93** (3), 034501–4.

Andersson, H. & van den Berg, A. 2003 Microfluidic devices for cellomics: A review. *Sensors and Actuators, B: Chemical* **92** (3), 315–325.

Anilkumar, A. V., Lee, C. P. & Wang, T. G. 1991 Surface-tension-induced mixing following coalescence of initially stationary drops. *Physics of Fluids A: Fluid Dynamics* **3** (11), 2587–2591.

Anna, S. L. & Mayer, H. C. 2006 Microscale tipstreaming in a microfluidic flow focusing device. *Physics of Fluids* **18** (12), 12151201–13.

Aryafar, H. & Kavehpour, H. P. 2006 Drop coalescence through planar surfaces. *Physics of Fluids* **18** (7), 0721051–6.

Aryafar, H. & Kavehpour, H. P. 2009 Electrocoalescence: effects of DC electric fields on coalescence of drops at planar interfaces. *Langmuir* **25** (21), 12460–5.

Aryafar, H., Lukyanets, A. S. & Kavehpour, H. P. 2006 Inertia-Dominated Coalescence of Drops. *Applied Mathematics Research eXpress* **2006**, 1–8.

Atten, P. 1993 Electrocoalescence of water droplets in an insulating liquid. *Journal of Electrostatics* **30**, 259–270.

Auroux, P. A., Iossifidis, D., Reyes, D. R. & Manz, A. 2002 Micro total analysis systems. 2. Analytical standard operations and applications. *Analytical Chemistry* **74** (12), 2637–2652.

Baroud, C. N., Gallaire, F. & Dangla, R. 2010 Dynamics of microfluidic droplets. *Lab on a Chip* **10** (16), 2032–45.

Basaran, O. A. 1992 Nonlinear oscillations of viscous liquid drops. *Journal of Fluid Mechanics* **241**, 169–198.

Basaran, O. A. 2002 Small-scale free surface flows with breakup: Drop formation and emerging applications. *AIChE Journal* **48** (9), 1842–1848.

Basaran, O. A. & Patzek, T. W. 1995 Nonlinear oscillations and breakup of conducting, inviscid drops in an externally applied electric field. *Industrial & Engineering Chemistry Research* **34** (10), 3454–3465.

Basaran, O. A. & Scriven, L. E. 1989 Axisymmetric shapes and stability of charged drops in an external electric field. *Physics of Fluids A* **1** (5), 795–798.

Batchelor, G. K. 1976 Geoffrey Ingram Taylor. 7 March 1886 – 27 June 1975. *Biographical Memoirs of Fellows of the Royal Society* **22** (1), 565–633.

Baygents, J. C. 1998 Electrohydrodynamic deformation and interaction of drop pairs. *Journal of Fluid Mechanics* **368**, 359–375.

Baygents, J. C. & Saville, D. A. 1990 The circulation produced in a drop by an electric field : A high field strength electrokinetic model. In *AIP Conference Proceedings*, pp. 7–17. AIP.

Bazant, M. Z. 2015 Electrokinetics meets electrohydrodynamics. *Journal of Fluid Mechanics* **782**, 1–4.

Becker, H. 2009*a* Chips, money, industry, education and the "killer application". *Lab on a Chip* **9** (12), 1659–1660.

Becker, H. 2009*b* Hype, hope and hubris: the quest for the killer application in microfluidics. *Lab on a Chip* **9** (15), 2119–2122.

Becker, H. 2009*c* IP or no IP: that is the question. *Lab on a Chip* **9** (23), 3327–3329.

Becker, H. 2009*d* It's the economy.... *Lab on a Chip* **9** (19), 2759–2762.

Becker, H. 2010*a* Collective wisdom. *Lab on a Chip* **10** (11), 1351–1354.

Becker, H. 2010*b* Mind the gap! *Lab on a Chip* **10** (3), 271–73.

Becker, H. 2010*c* One size fits all? *Lab on a Chip* **10** (15), 1894–1897.

Becker, H. 2010*d* Start me up.... *Lab on a Chip* **10** (23), 3197–3200.

Becker, H. 2011 All I want for Christmas. *Lab on a Chip* **11** (9), 1571–1573.

Beebe, D. J., Mensing, G. A. & Walker, G. M. 2002 Physics and applications of microfluidics in biology. *Annual Review of Biomedical Engineering* **4**, 261–286.

Bentenitis, N. & Krause, S. 2005 Droplet deformation in DC electric fields: The extended leaky dielectric model. *Langmuir* **21** (14), 6194–6209.

van den Berg, A. & Bergveld, P. 2006 Labs-on-a-Chip: origin, highlights and future perspectives. On the occasion of the 10th microTAS conference. *Lab on a Chip* **6** (10), 1266–1273.

Berry, J., Davidson, M. & Harvie, D. 2011*a* Electrokinetic development length of electroviscous flow through a contraction. *ANZIAM Journal* **52**, C837–C852.

Berry, J. D., Davidson, M. R., Bharti, R. P. & Harvie, D. J. E. 2011*b* Effect of wall permittivity on electroviscous flow through a contraction. *Biomicrofluidics* **5** (4), 0441021–17.

Berry, J. D., Davidson, M. R. & Harvie, D. J. E. 2013 A multiphase electrokinetic flow model for electrolytes with liquid/liquid interfaces. *Journal of Computational Physics* **251**, 209–222.

Berry, J. D., Davidson, M. R., & Harvie, D. J. E. 2012 Deformation of liquid drops containing ions in the presence of an electric field. In *9th International Conference on Heat Transfer, Fluid Mechanics and Thermodynamics, 2012*.

Bharti, R. P., Harvie, D. J. E. & Davidson, M. R. 2008 Steady flow of ionic liquid through a cylindrical microfluidic contraction-expansion pipe: Electroviscous effects and pressure drop. *Chemical Engineering Science* **63** (14), 3593–3604.

Bharti, R. P., Harvie, D. J. E. & Davidson, M. R. 2009 Electroviscous effects in steady fully developed flow of a power-law liquid through a cylindrical microchannel. *International Journal of Heat and Fluid Flow* **30** (4), 804–811.

Bird, J., Ristenpart, W., Belmonte, A. & Stone, H. 2009 Critical angle for electrically driven coalescence of two conical droplets. *Physical Review Letters* **103** (16), 1645021–4.

Bird, R. B., Stewart, W. E. & Lightfoot, A. N. 2002 *Transport Phenomena*. Wiley.

Biscombe, C. J. C., Davidson, M. R. & Harvie, D. J. E. 2012 Microfluidic circuit analysis II: Implications of ion conservation for microchannels connected in series. *Journal of Colloid and Interface Science* **365** (1), 16–27.

Bjørklund, E. 2009 The level-set method applied to droplet dynamics in the presence of an electric field. *Computers & Fluids* **38** (2), 358–369.

Blanchette, F. 2010 Simulation of mixing within drops due to surface tension variations. *Physical Review Letters* **105** (7), 0745011–4.

Blanchette, F. & Bigioni, T. P. 2006 Partial coalescence of drops at liquid interfaces. *Nature Physics* **2** (4), 254–257.

Blanchette, F. & Bigioni, T. P. 2009 Dynamics of drop coalescence at fluid interfaces. *Journal of Fluid Mechanics* **620**, 333–352.

Bonthuis, D. J., Gekle, S. & Netz, R. R. 2012 Profile of the static permittivity tensor of water at interfaces: Consequences for capacitance, hydration interaction and ion adsorption. *Langmuir* **28** (20), 7679–7694.

Boris, J. P. & Book, D. L. 1976 Flux-corrected transport. III. Minimal-error FCT algorithms. *Journal of Computational Physics* **20** (4), 397–431.

Brackbill, J., Kothe, D. & Zemach, C. 1992 A continuum method for modeling surface tension. *Journal of Computational Physics* **100** (2), 335–354.

Brazier-Smith, P. R. 1972 The stability of charged drops in uniform electric fields. *Quarterly Journal of the Royal Meteorological Society* **98** (416), 434–439.

Bringer, M. R., Gerdts, C. J., Song, H., Tice, J. D. & Ismagilov, R. F. 2004 Microfluidic systems for chemical kinetics that rely on chaotic mixing in droplets. *Philosophical Transactions of the Royal Society London A* **362** (1818), 1087–1104.

Brody, J. P., Yager, P., Goldstein, R. E. & Austin, R. H. 1996 Biotechnology at low Reynolds numbers. *Biophysical Journal* **71** (6), 3430–3441.

Bruus, H. 2007 *Theoretical Microfluidics*. Oxford University Press.

Burton, J. C., Rutledge, J. E. & Taborek, P. 2004 Fluid pinch-off dynamics at nanometer length scales. *Physical Review Letters* **92** (24), 2445051–4.

Burton, J. C. & Taborek, P. 2011 Simulations of coulombic fission of charged inviscid drops. *Physical Review Letters* **106** (14), 1–4.

Carnie, S. L. & Torrie, G. M. 1984 The statistical mechanics of the electrical double layer. *Advances in Chemical Physics* **546**, 141–253.

Carnie, S. L., Torrie, G. M. & Valleau, J. P. 1984 Ion-size effects in the primitive model double layer. *Molecular Physics* **53** (1), 253–256.

Castellanos, A. & González, A. 1998 Nonlinear electrohydrodynamics of free surfaces. *IEEE Transactions on Dielectrics and Electrical Insulation* **5** (3), 334–343.

Castrejón-Pita, J. R., Castrejón-Pita, A. A., Thete, S. S., Sambath, K., Hutchings, I. M., Hinch, J., Lister, J. R. & Basaran, O. A. 2015 Plethora of transitions during breakup of liquid filaments. *Proceedings of the National Academy of Sciences* **112** (15), 4582–4587.

Castro-Hernández, E., García-Sánchez, P., Tan, S. H., Gañán-Calvo, A. M., Baret, J.-C. & Ramos, A. 2015 Breakup length of AC electrified jets in a microfluidic flow-focusing junction. *Microfluidics and Nanofluidics* **19** (4), 787–794.

Chang, H.-C. & Yeo, L. Y. 2010 *Electrokinetically-Driven Microfluidics and Nanofluidics*. Cambridge University Press.

Charles, G. & Mason, S. 1960*a* The mechanism of partial coalescence of liquid drops at liquid/liquid interfaces. *Journal of Colloid Science* **15**, 105–122.

Charles, G. E. & Mason, S. G. 1960*b* The coalescence of liquid drops with flat liquid/liquid interfaces. *Journal of Colloid Science* **15**, 236–267.

Chen, A. U., Notz, P. K. & Basaran, O. A. 2002 Computational and experimental analysis of pinch-off and scaling. *Physical Review Letters* **88** (17), 174501–4.

Chen, C. H., Shah, R. K., Abate, A. R. & Weitz, D. A. 2009 Janus particles templated from double emulsion droplets generated using microfluidics. *Langmuir* **25** (8), 4320–4323.

Chen, L., Li, C., Van Der Vegt, N. F. A., Auernhammer, G. K. & Bonaccurso, E. 2013 Initial electrospreading of aqueous electrolyte drops. *Physical Review Letters* **110** (2), 1–5.

Chen, X., Mandre, S. & Feng, J. J. 2006 Partial coalescence between a drop and a liquid-liquid interface. *Physics of Fluids* **18** (5), 0517051–4.

Chen, X., Song, Y., Li, D. & Hu, G. 2015 Deformation and interaction of droplet pairs in a microchannel under AC electric fields. *Physical Review Applied* **4** (2), 0240051–17.

Chen, X. & Yang, V. 2014 Thickness-based adaptive mesh refinement methods for multi-phase flow simulations with thin regions. *Journal of Computational Physics* **269**, 22–39.

Cheow, L. F., Yobas, L. & Kwong, D. L. 2007 Digital microfluidics: Droplet based logic gates. *Applied Physics Letters* **90** (5), 2006–2008.

Choi, H.-J. & Montemagno, C. D. 2006 Biosynthesis within a bubble architecture. *Nanotechnology* **17** (9), 2198–2202.

Choi, J., Kim, Y. J., Lee, S., Son, S. U., Ko, H. S., Nguyen, V. D. & Byun, D. 2008 Drop-on-demand printing of conductive ink by electrostatic field induced inkjet head. *Applied Physics Letters* **93** (19), 3–5.

Choi, K., Ng, A. H. C., Fobel, R. & Wheeler, A. R. 2012 Digital microfluidics. *Annual Review of Analytical Chemistry* **5**, 413–40.

Chung, S. K., Rhee, K. & Cho, S. K. 2010 Bubble actuation by electrowetting-on-dielectric (EWOD) and its applications: A review. *International Journal of Precision Engineering and Manufacturing* **11** (6), 991–1006.

Clanet, C. & Lasheras, J. C. 1999 Transition from dripping to jetting. *Journal of Fluid Mechanics* **383**, 307–326.

Clausell-Tormos, J., Lieber, D., Baret, J. C., El-Harrak, A., Miller, O. J., Frenz, L., Blouwolff, J., Humphry, K. J., Köster, S., Duan, H., Holtze, C., Weitz, D. A., Griffiths, A. D. & Merten, C. A. 2008 Droplet-Based Microfluidic Platforms for the Encapsulation and Screening of Mammalian Cells and Multicellular Organisms. *Chemistry and Biology* **15** (5), 427–437.

Collins, R. T., Harris, M. T. & Basaran, O. A. 2007*a* Breakup of electrified jets. *Journal of Fluid Mechanics* **588**, 75–129.

Collins, R. T., Jones, J. J., Harris, M. T. & Basaran, O. A. 2007*b* Electrohydrodynamic tip streaming and emission of charged drops from liquid cones. *Nature Physics* **4** (2), 149–154.

Collins, R. T., Sambath, K., Harris, M. T. & Basaran, O. A. 2013 Universal scaling laws for the disintegration of electrified drops. *Proceedings of the National Academy of Sciences of the United States of America* **110** (13), 4905–10.

Corson, L. T., Tsakonas, C., Duffy, B. R., Mottram, N. J., Sage, I. C., Brown, C. V. & Wilson, S. K. 2014 Deformation of a nearly hemispherical conducting drop due to an electric field : Theory and experiment. *Physics of Fluids* **26** (12), 1–20.

Creux, P., Lachaise, J., Graciaa, A., Beattie, J. K. & Djerdjev, A. M. 2009 Strong Specific Hydroxide Ion Binding at the Pristine Oil / Water and Air / Water Interfaces. *Journal of Physical Chemistry B* **113** (43), 14146–14150.

Crowdy, D. 2008 Conducting drops subject to electric fields in 2D Stokes flows. *IMA Journal of Applied Mathematics* **73** (5), 740–758.

Davidson, M. R., Berry, J. D. & Harvie, D. J. E. 2014 Numerical simulation of the deformation of charged drops of electrolyte. *Advances in Fluid Mechanics X* **82**, 203–214.

Davidson, M. R., Berry, J. D., Pillai, R. & Harvie, D. J. E. 2016 Numerical simulation of two-fluid flow of electrolyte solution with charged deforming interfaces. *Applied Mathematical Modelling* **40** (3), 1989–2001.

Davidson, M. R., Bharti, R. P. & Harvie, D. J. E. 2010 Electroviscous effects in a Carreau liquid flowing through a cylindrical microfluidic contraction. *Chemical Engineering Science* **65** (23), 6259–6269.

Davidson, M. R., Bharti, R. P., Liovic, P. & Harvie, D. J. E. 2008 Electroviscous effects in low Reynolds number flow through a microfluidic contraction with rectangular cross-section. *World Academy of Science, Engineering and Technology* **30**, 256–260.

Davidson, M. R., Cooper-White, J. J. & Tirtaatmadja, V. 2004 Shear-thinning drop formation. *ANZIAM Journal* **45E**, C405–C418.

Davidson, M. R. & Harvie, D. J. E. 2007*a* Electroviscous effects in low Reynolds number liquid flow through a slit-like microfluidic contraction. *Chemical Engineering Science* **62** (16), 4229–4240.

Davidson, M. R. & Harvie, D. J. E. 2007*b* Predicting the effect of interfacial flow of insoluble surfactant on the deformation of drops rising in a liquid. *ANZIAM Journal* **48**, 661–676.

Davidson, M. R., Harvie, D. J. E. & Cooper-White, J. 2006 Simulations of pendant drop formation of a viscoelastic liquid. *Korea-Australia Rheology Journal* **18** (2), 41–49.

Davidson, M. R., Harvie, D. J. E. & Cooper-White, J. J. 2005 Flow focusing in microchannels. *ANZIAM Journal* **46E**, C47–C58.

Davidson, M. R. & Rudman, M. 2002 Volume-of-Fluid calculation of heat or mass transfer across deforming interfaces in two-fluid flow. *Numerical Heat Transfer, Part B: Fundamentals* **41** (3), 291–308.

Delgado, A. V., Gonzalez-Caballero, F., Hunter, R. J., Koopal, L. K. & Lyklema, J. 2007 Measurement and interpretation of electrokinetic phenomena. *Journal of Colloid and Interface Science* **309** (2), 194–224.

Delville, J.-P., Vincent, M. R. d. S., Schroll, R. D., Chraïbi, H., Issenmann, B., Wunenburger, R., Lasseux, D., Zhang, W. W. & Brasselet, E. 2009 Laser microfluidics: fluid actuation by light. *Journal of Optics A: Pure and Applied Optics* **11** (3), 1–15.

Ding, X., Li, P., Lin, S.-C. S., Stratton, Z. S., Nama, N., Guo, F., Slotcavage, D., Mao, X., Shi, J., Costanzo, F. & Huang, T. J. 2013 Surface acoustic wave microfluidics. *Lab on a Chip* **13** (18), 3626–3649.

Dittrich, P. S., Jahnz, M. & Schwille, P. 2005 A new embedded process for compartmentalized cell-free protein expression and on-line detection in microfluidic devices. *ChemBioChem* **6** (5), 811–814.

Drews, A. M., Cartier, C. A. & Bishop, K. J. M. 2015 Contact Charge Electrophoresis: Experiment and Theory. *Langmuir* **31**, 3808–3814.

Drews, A. M., Lee, H.-Y. & Bishop, K. J. M. 2013 Ratcheted electrophoresis for rapid particle transport. *Lab on a Chip* **13**, 4295–4298.

Dubash, N. 2007 Behaviour of a conducting drop in a viscous fluid subject to an electric field. Ph.d. thesis, Imperial University.

Dubash, N. & Mestel, a. J. 2007*a* Behavior near critical for a conducting drop in an electric field. *Physics of Fluids* **19** (7), 1–9.

Dubash, N. & Mestel, A. J. 2007*b* Behaviour of a conducting drop in a highly viscous fluid subject to an electric field. *Journal of Fluid Mechanics* **581**, 469–492.

Dubash, N. & Mestel, a. J. 2007*c* Breakup behavior of a conducting drop suspended in a viscous fluid subject to an electric field. *Physics of Fluids* **19** (7), 072101–13.

Eggers, J. 1993 Universal pinching of 3 D axisymmetric free-surface flow. *Physical Review Letters* **71** (21), 3458–60.

Eggers, J. 1997 Nonlinear dynamics and breakup of free-surface flows. *Reviews of Modern Physics* **69** (1833), 865–929.

Eggers, J. & Villermaux, E. 2008 Physics of liquid jets. *Reports on Progress in Physics* **71** (3), 1–79.

Eijkel, J. C. T. & van den Berg, A. 2005 Nanofluidics: What is it and what can we expect from it? *Microfluidics and Nanofluidics* **1** (3), 249–267.

Einstein, A. 1905 Über die von der molekularkinetischen Theorie der Wärme ge- forderte Bewegung von in ruhenden Flüssigkeiten suspendierten Teilchen. *Annalen der Physik* **322**, 549–560.

Eow, J. S. & Ghadiri, M. 2002 Electrocoalesce-separators for the separation of aqueous drops from a flowing dielectric viscous liquid. *Separation and Purification Technology* **29** (1), 63–77.

Eow, J. S. & Ghadiri, M. 2003 Motion, deformation and break-up of aqueous drops in oils under high electric field strengths. *Chemical Engineering and Processing: Process Intensification* **42** (4), 259–272.

Eow, J. S., Ghadiri, M. & Sharif, A. 2001*a* Deformation and break-up of aqueous drops in dielectric liquids in high electric fields. *Journal of Electrostatics* **52**, 463–469.

Eow, J. S., Ghadiri, M. & Sharif, A. 2003 Experimental studies of deformation and break-up of aqueous drops in high electric fields. *Colloids and Surfaces A: Physicochemical and Engineering Aspects* **225** (1), 193–210.

Eow, J. S., Ghadiri, M., Sharif, A. O. & Williams, T. J. 2001*b* Electrostatic enhancement of coalescence of water droplets in oil: a review of the current understanding. *Chemical Engineering Journal* **84** (3), 173–192.

Esmaeeli, A. & Behjatian, A. 2012 Electrohydrodynamics of a liquid drop in confined domains. *Physical Review E* **86** (3), 1–13.

Esmaeeli, A. & Sharifi, P. 2011*a* The transient dynamics of a liquid column in a uniform transverse electric field of small strength. *Journal of Electrostatics* **69** (6), 504–511.

Esmaeeli, A. & Sharifi, P. 2011*b* Transient electrohydrodynamics of a liquid drop. *Physical Review E* **84** (3), 1–11.

Evans, E. W., Johnson, S. P., Leggett, P. F. & Cross, M. 2000 Automatic and effective multi-dimensional parallelisation of structured mesh based codes. *Parallel Computing* **26** (6), 677–703.

Fair, R. B. 2007 Digital microfluidics: is a true lab-on-a-chip possible? *Microfluidics and Nanofluidics* **3** (3), 245–281.

Feng, J. J. 2002 The stretching of an electrified non-Newtonian jet: A model for electrospinning. *Physics of Fluids* **14** (11), 3912–3926.

Feng, J. J. 2003 Stretching of a straight electrically charged viscoelastic jet. *Journal of Non-Newtonian Fluid Mechanics* **116** (1), 55–70.

Feng, J. Q. 1999 Electrohydrodynamic behaviour of a drop subjected to a steady uniform electric field at finite electric Reynolds number. *Proceedings of the Royal Society A: Mathematical, Physical and Engineering Sciences* **455** (1986), 2245–2269.

Feng, J. Q. & Beard, K. V. 1991 Three-dimensional oscillation characteristics of electrostatically deformed drops. *Journal of Fluid Mechanics* **227**, 429–447.

Feng, J. Q. & Scott, T. C. 1996 A computational analysis of electrohydrodynamics of a leaky dielectric drop in an electric field. *Journal of Fluid Mechanics* **311**, 289–326.

Fernández de la Mora, J. 2007 The Fluid Dynamics of Taylor Cones. *Annual Review of Fluid Mechanics* **39** (1), 217–243.

Fidalgo, L. M., Whyte, G., Ruotolo, B. T., Benesch, J. L. P., Stengel, F., Abell, C., Robinson, C. V. & Huck, W. T. S. 2009 Coupling microdroplet microreactors with mass spectrometry: reading the contents of single droplets online. *Angewandte Chemie* **48** (20), 3665–8.

Figeys, D. & Pinto, D. 2000 Lab-on-a-Chip: A Revolution in Biological and Medical Sciences. *Analytical Chemistry* **72** (9), 330 A–335 A.

Friend, J. & Yeo, L. Y. 2011 Microscale acoustofluidics: Microfluidics driven via acoustics and ultrasonics. *Reviews of Modern Physics* **83** (2), 647–704.

Frumkin, A. 1946 New electrocapillary phenomena. *Journal of Colloid Science* **1** (3), 277–291.

Fu, T., Wu, Y., Ma, Y. & Li, H. Z. 2012 Droplet formation and breakup dynamics in microfluidic flow-focusing devices: From dripping to jetting. *Chemical Engineering Science* **84**, 207–217.

Funakoshi, K., Suzuki, H. & Takeuchi, S. 2006 Lipid Bilayer Formation by Contacting Monolayers in a Microfluidic Device for Membrane Protein Analysis. *Analytical Chemistry* **78** (24), 8169–8174.

Gambhire, P. & Thaokar, R. M. 2012 Role of conductivity in the electrohydrodynamic patterning of air-liquid interfaces. *Physical Review E* **86** (3), 1–11.

Gañán-Calvo, A. M., Dávila, J. & Barrero, A. 1997 Current and droplet size in the electrospraying of liquids. Scaling laws. *Journal of Aerosol Science* **28** (2), 249–275.

Gañán-Calvo, A. M., González-Prieto, R., Riesco-Chueca, P., Herrada, M. A. & Flores-Mosquera, M. 2007 Focusing capillary jets close to the continuum limit. *Nature Physics* **3** (10), 737–742.

Gañán-Calvo, A. M., López-Herrera, J. M., Rebollo-Muñoz, N. & Montanero, J. M. 2016 The onset of electrospray: the universal scaling laws of the first ejection. *Scientific Reports* **6**, 1–9.

García-Sánchez, P., Ramos, A. & González, A. 2009 Flow reversal in traveling-wave electrokinetics: an analysis of forces due to ionic concentration gradients. *Langmuir* **25** (9), 4988–97.

Garton, C. G. & Krasucki, Z. 1964 Bubbles in Insulating Liquids: Stability in an Electric Field. *Proceedings of the Royal Society A: Mathematical, Physical and Engineering Sciences* **280** (1381), 211–226.

Gerdts, C. J., Sharoyan, D. E. & Ismagilov, R. F. 2004 A synthetic reaction network: Chemical amplification using nonequilibrium autocatalytic reactions coupled in time. *Journal of the American Chemical Society* **126** (20), 6327–6331.

Ghazian, O., Adamiak, K. & Castle, G. S. P. 2013 Numerical simulation of electrically deformed droplets less conductive than ambient fluid. *Colloids and Surfaces A: Physicochemical and Engineering Aspects* **423**, 27–34.

Gilbert, W. 1600 *De Magnete*, 1958th edn. London: Peter Short.

Gilet, T., Mulleners, K., Lecomte, J., Vandewalle, N. & Dorbolo, S. 2007 Critical parameters for the partial coalescence of a droplet. *Physical Review E* **75** (3), 0363031–14.

Gong, H., Peng, Y., Yang, Z., Shang, H. & Zhang, X. 2015 Stable deformation of droplets surface subjected to a high-voltage electric field in oil. *Colloids and Surfaces A: Physicochemical and Engineering Aspects* **468**, 315–321.

Gouy, M. 1910 Sur la constitution de la charge électrique à la surface d'un électrolyte. *Journal de Physique Théorique et Appliquée* **9** (1), 457–468.

Gravesen, P., Branebjerg, J. & Jens, O. S. 1993 Microfluidics - a review. *Journal of Micromechanics and Microengineering* **3** (4), 168–182.

Grimm, R. L. & Beauchamp, J. L. 2005 Dynamics of field-induced droplet ionization: Time-resolved studies of distortion, jetting, and progeny formation from charged and neutral methanol droplets exposed. *The Journal of Physical Chemistry B* **109** (16), 8244–50.

Gu, H., Duits, M. H. G. & Mugele, F. 2011 Droplets formation and merging in two-phase flow microfluidics. *International Journal of Molecular Sciences* **12** (4), 2572–2597.

Gu, W., Heil, P. E., Choi, H. & Kim, K. 2007 Comprehensive model for fine Coulomb fission of liquid droplets charged to Rayleigh limit. *Applied Physics Letters* **91** (6), 214–216.

Günther, A. & Jensen, K. F. 2006 Multiphase microfluidics: from flow characteristics to chemical and materials synthesis. *Lab on a Chip* **6** (12), 1487–503.

Guo, C. & He, L. 2014 Coalescence behaviour of two large water-drops in viscous oil under a DC electric field. *Journal of Electrostatics* **72** (6), 470–476.

Guo, M. T., Rotem, A., Heyman, J. A. & Weitz, D. A. 2012 Droplet microfluidics for high-throughput biological assays. *Lab on a Chip* **12** (12), 2146–2155.

Guzowski, J., Korczyk, P. M., Jakiela, S. & Garstecki, P. 2011 Automated high-throughput generation of droplets. *Lab on a Chip* **11** (21), 3593–3595.

Ha, J.-W. & Yang, S.-M. 2000*a* Electrohydrodynamics and electrorotation of a drop with fluid less conductive than that of the ambient fluid. *Physics of Fluids* **12** (4), 764–772.

Ha, J.-W. J.-W. & Yang, S.-M. S.-M. 2000*b* Deformation and breakup of Newtonian and non-Newtonian conducting drops in an electric field. *Journal of Fluid Mechanics* **405** (1), 131–156.

Halim, A. & Esmaeeli, A. 2013 Computational studies on the transient electrohydrodynamics of a liquid drop. *Fluid Dynamics and Materials Processing* **9** (4), 435–460.

Hamlin, B. S., Creasey, J. C. & Ristenpart, W. D. 2012 Electrically tunable partial coalescence of oppositely charged drops. *Physical Review Letters* **109** (9), 1–5.

Hansen, J. S., Dyre, J. C., Daivis, P., Todd, B. D. & Bruus, H. 2015 Continuum nanofluidics. *Langmuir* **31** (49), 13275–13289.

Hardt, S. & Hahn, T. 2011 Microfluidics with aqueous two-phase systems. *Lab on a Chip* **12**, 434–442.

Harvie, D. J. E., Cooperwhite, J. J. & Davidson, M. R. 2008*a* Deformation of a viscoelastic droplet passing through a microfluidic contraction. *Journal of Non-Newtonian Fluid Mechanics* **155** (1), 67–79.

Harvie, D. J. E. & Davidson, M. R. 2005 A parametric study of droplet deformation through a microfluidic contraction. *ANZIAM Journal* **46E**, C150–C166.

Harvie, D. J. E., Davidson, M. R. & Cooper-White, J. J. 2006*a* Simulations of viscoelastic droplet deformation through a microfluidic contraction. *WIT Transactions on Engineering Sciences* **52**, 69–78.

Harvie, D. J. E., Davidson, M. R., Cooper-White, J. J. & Rudman, M. 2006*b* A parametric study of droplet deformation through a microfluidic contraction: Low viscosity Newtonian droplets. *Chemical Engineering Science* **61** (15), 5149–5158.

Harvie, D. J. E., Davidson, M. R., Cooper-White, J. J. & Rudman, M. 2007 A parametric study of droplet deformation through a microfluidic contraction: Shear thinning liquids. *International Journal of Multiphase Flow* **33** (5), 545–556.

Harvie, D. J. E., Davidson, M. R. & Rudman, M. 2006*c* An analysis of parasitic current generation in Volume of Fluid simulations. *Applied Mathematical Modelling* **30** (10), 1056–1066.

Harvie, D. J. E., Rudman, M. & Davidson, M. R. 2008*b* Parasitic current generation in Combined Level Set and Volume of Fluid immiscible fluid simulations. *ANZIAM Journal* **48**, C868–C884.

Hashimoto, M., Garstecki, P., Stone, H. a. & Whitesides, G. M. 2008 Interfacial instabilities in a microfluidic Hele-Shaw cell. *Soft Matter* **4** (7), 1403–1413.

Haywood, R. J., Renksizbulut, M. & Raithby, G. D. 1991 Transient deformation of freely-suspended liquid droplets in electrostatic fields. *AIChE Journal* **37** (9), 1305–1317.

Helmensdorfer, S. & Topping, P. 2013 Bouncing of charged droplets: An explanation using mean curvature flow. *Europhysics Letters* **104** (3), 34001.

Higuera, F. 2008 Breakup of a supported drop of a viscous conducting liquid in a uniform electric field. *Physical Review E* **78** (1), 1–11.

Hirt, C. W. & Nichols, B. D. 1981 Volume of fluid (VOF) method for the dynamics of free boundaries. *Journal of Computational Physics* **39** (1), 201–225.

Ho, C.-M. & Tai, Y.-C. 1998 Micro-Electro-Mechanical- Systems (MEMS) and Fluid flows. *Annual Review of Fluid Mechanics* **30**, 579–612.

Hua, J., Lim, L. K. & Wang, C.-H. 2008 Numerical simulation of deformation/motion of a drop suspended in viscous liquids under influence of steady electric fields. *Physics of Fluids* **20** (11), 113302–16.

Huebner, A., Sharma, S., Srisa-Art, M., Hollfelder, F., Edel, J. B. & DeMello, A. J. 2008 Microdroplets: A sea of applications? *Lab on a Chip* **8** (8), 1244–1254.

Hunter, H. C. & Ray, A. K. 2009 On progeny droplets emitted during Coulombic fission of charged microdrops. *Physical Chemistry Chemical Physics* **11** (29), 6156–6165.

Hunter, R. J. 1981 *Zeta Potential in Colloid Science: Principles and Applications*. Academic Press.

Huo, Y., Wang, J., Qiu, H., Zuo, Z. & Fan, Y. 2015 Noncontact rebound and fission of oppositely charged droplets. *Experiments in Fluids* **56** (3), 56–65.

Im, D. J., Kang, I. S., Korea, S. & Korea, S. 2015 Electrophoretic Manipulation of a Charged Droplet. In *Encyclopedia of Microfluidics and Nanofluidics*, pp. 935–945.

Im, D. J., Noh, J., Moon, D. & Kang, I. S. 2011 Electrophoresis of a charged droplet in a dielectric liquid for droplet actuation. *Analytical Chemistry* **83** (13), 5168–5174.

Im, D. J., Yoo, B. S., Ahn, M. M., Moon, D. & Kang, I. S. 2013 Digital electrophoresis of charged droplets. *Analytical Chemistry* **85** (8), 4038–4044.

Joensson, H. N. & Andersson, H. A. 2012 Droplet microfluidics-A tool for single-cell analysis. *Angewandte Chemie* **51** (49), 12176–12192.

Jung, Y. M. & Kang, I. S. 2009 A novel actuation method of transporting droplets by using electrical charging of droplet in a dielectric fluid. *Biomicrofluidics* **3** (2), 0224021–11.

Jung, Y. M., Oh, H. C. & Kang, I. S. 2008 Electrical charging of a conducting water droplet in a dielectric fluid on the electrode surface. *Journal of Colloid and Interface Science* **322** (2), 617–623.

Kamholz, A. 2004 Proliferation of microfluidics in literature and intellectual property. *Lab on a Chip* **4** (2), 16N–20N.

Karniadakis, G., Beskok, A. & Aluru, N. 2008 *Microflows and Nonoflows*. Springer.

Karyappa, R. B., Deshmukh, S. D. & Thaokar, R. M. 2014 Breakup of a conducting drop in a uniform electric field. *Journal of Fluid Mechanics* **754**, 550–589.

Katsikis, G., Cybulski, J. S. & Prakash, M. 2015 Synchronous universal droplet logic and control. *Nature Physics* **11** (7), 588–597.

Kelly, B. T., Baret, J. C., Taly, V. & Griffiths, A. D. 2007 Miniaturizing chemistry and biology in microdroplets. *Chemical Communications* (18), 1773–1788.

Khademhosseini, A., Langer, R., Borenstein, J. & Vacanti, J. P. 2006 Microscale technologies for tissue engineering. *Proceedings of the National Academy of Sciences of the United States of America* **103** (8), 2480–2487.

Kirby, B. J. 2010 *Micro- and Nanoscale Fluid Mechanics*. Cambridge University Press.

Knight, J. 2002 Microfluidics: Honey, I shrunk the lab. *Nature* **418** (6897), 474–475.

Lac, E. & Homsy, G. M. 2007 Axisymmetric deformation and stability of a viscous drop in a steady electric field. *Journal of Fluid Mechanics* **590**, 239–264.

Lanauze, J. A., Walker, L. M. & Khair, A. S. 2013 The influence of inertia and charge relaxation on electrohydrodynamic drop deformation. *Physics of Fluids* **25** (11), 112101–19.

Laser, D. J. & Santiago, J. G. 2004 A review of micropumps. *Journal of Micromechanics and Microengineering* **14** (6), R35–R64.

Le, H. P. 1998 Progress and trends in ink-jet printing technology. *Journal of Imaging Science and Technology* **42** (1), 49–62.

Lecault, V., Vaninsberghe, M., Sekulovic, S., Knapp, D. J. H. F., Wohrer, S., Bowden, W., Viel, F., McLaughlin, T., Jarandehei, A., Miller, M., Falconnet, D., White, A. K., Kent, D. G., Copley, M. R., Taghipour, F., Eaves, C. J., Humphries, R. K., Piret, J. M. & Hansen, C. L. 2011 High-throughput analysis of single hematopoietic stem cell proliferation in microfluidic cell culture arrays. *Nature Methods* **8** (7), 581–586.

Lee, J. S. H. & Li, D. 2006 Electroosmotic flow at a liquid-air interface. *Microfluidics and Nanofluidics* **2** (4), 361–365.

Lee, J. W., Nilson, R. H., Templeton, J. A., Gri, S. K., Kung, A. & Wong, B. M. 2012 Comparison of Molecular Dynamics with Classical Density Functional and Poisson-Boltzmann Theories of the Electric Double Layer in Nanochannels. *Journal of Chemical Theory and Computation* **8** (6), 2012–2022.

Lee, M. W., Kim, N. Y. & Yoon, S. S. 2013 On pinchoff behavior of electrified droplets. *Journal of Aerosol Science* **57**, 114–124.

Li, D. 2004 *Electrokinetics in Microfluidics*. Academic Press.

Li, F., Ozen, O., Aubry, N., Papageorgiou, D. T. & Petropoulos, P. G. 2007 Linear stability of a two-fluid interface for electrohydrodynamic mixing in a channel. *Journal of Fluid Mechanics* **583**, 347–377.

Lim, L. K., Hua, J., Wang, C.-H. & Smith, K. A. 2010 Numerical simulation of cone-jet formation in electrohydrodynamic atomization. *AIChE Journal* **57** (1), 57–78.

Lin, Y., Skjetne, P. & Carlson, A. 2012 A phase field model for multiphase electro-hydrodynamic flow. *International Journal of Multiphase Flow* **45**, 1–11.

Link, D., Anna, S., Weitz, D. & Stone, H. A. 2004 Geometrically Mediated Breakup of Drops in Microfluidic Devices. *Physical Review Letters* **92** (5), 0545031–4.

Link, D. R., Grasland-Mongrain, E., Duri, A., Sarrazin, F., Cheng, Z., Cristobal, G., Marquez, M. & Weitz, D. A. 2006 Electric control of droplets in microfluidic devices. *Angewandte Chemie* **45** (16), 2556–60.

Lippmann, G. 1875 Relation entre les phénomènes électriques et capillaires. *Annales de Chimie et de Physique* **5**, 494–549.

Lister, J. R. & Stone, H. A. 1998 Capillary breakup of a viscous thread surrounded by another viscous fluid. *Physics of Fluids* **10** (11), 2758–2763.

Livak-Dahl, E., Sinn, I. & Burns, M. 2011 Microfluidic chemical analysis systems. *Annual Review of Chemical and Biomolecular Engineering* **2**, 325–53.

López-Herrera, J. M., Gañán-Calvo, A. M., Popinet, S. & Herrada, M. A. 2015 Electrokinetic effects in the breakup of electrified jets: A Volume-Of-Fluid numerical study. *International Journal of Multiphase Flow* **71**, 14–22.

López-Herrera, J. M., Popinet, S. & Herrada, M. 2011 A charge-conservative approach for simulating electrohydrodynamic two-phase flows using volume-of-fluid. *Journal of Computational Physics* **230** (5), 1939–1955.

López-Herrera, J. M., Riesco-Chueca, P. & Gañán-Calvo, A. M. 2005 Linear stability analysis of axisymmetric perturbations in imperfectly conducting liquid jets. *Physics of Fluids* **17** (3), 1–22.

Lyklema, J. 2003 Electrokinetics after Smoluchowski. *Colloids and Surfaces A: Physicochemical and Engineering Aspects* **222** (1), 5–14.

Lyklema, J., Rovillard, S. & De Coninck, J. 1998 Electrokinetics: The properties of the stagnant layer unraveled. *Langmuir* **14** (20), 5659–5663.

Macky, W. A. 1931 Some Investigations on the Deformation and Breaking of Water Drops in Strong Electric Fields. *Proceedings of the Royal Society A: Mathematical, Physical and Engineering Sciences* **133** (822), 565–587.

Mandal, S., Chaudhury, K. & Chakraborty, S. 2014 Transient dynamics of confined liquid drops in a uniform electric field. *Physical Review E* **89** (5), 1–17.

Mani, A., Zangle, T. A. & Santiago, J. G. 2009 On the propagation of concentration polarization from microchannel-nanochannel interfaces. Part I: Analytical model and characteristic analysis. *Langmuir* **25** (6), 3898–908.

Manz, A., Day, P. & Zhang, Y. 2012 *Microdroplet Technology: Principles and Emerging Applications in Biology and Chemistry*. Springer.

Manz, A., Harrison, D. J., Verpoorte, E. M. J., Fettinger, J. C., Paulus, A., Ludi, H. & Widmer, H. M. 1992 Planar chips technology for miniaturization and integration of separation techniques into monitoring systems: capillary electrophoresis on a chip. *Journal of Chromatography* **593** (1), 253–258.

Manz, A., Widmers, H. M. & Graber, N. 1990 Miniaturized total chemical analysis systems: A novel concept for chemical sensing. *Sensors and Actuators B: Chemical* **1** (1), 244–248.

Marston, P. L. 1980 Shape Oscillation and Static Deformation of Drops and Bubbles Driven by Modulated Radiation Stresses – Theory. *Journal of Acoustical Society of America* **67**, 16–26.

Masliyah, J. H. 2006 *Electrokinetic and Colloid Transport Phenomena*. Wiley Press.

Mazutis, L. & Griffiths, A. D. 2012 Selective droplet coalescence using microfluidic systems. *Lab on a Chip* **12** (10), 1800–6.

Mcdonald, J. C., Anderson, J. R. & Chiu, D. T. 2000 Fabrication of microfluidic systems in poly(dimethylsiloxane). *Electrophoresis* **21** (1), 27–40.

McKinley, G. H. & Renardy, M. 2011 Wolfgang von Ohnesorge. *Physics of Fluids* **23** (12), 127101–6.

Melcher, J. R. & Taylor, G. I. G. 1969 Electrohydrodynamics: a review of the role of interfacial shear stresses. *Annual Review of Fluid Mechanics* **1**, 111–146.

Mhatre, S., Deshmukh, S. & Thaokar, R. M. 2015 Electrocoalescence of a drop pair. *Physics of Fluids* **27**, 0921061–24.

Miller, O. J., Bernath, K., Agresti, J. J., Amitai, G., Kelly, B. T., Mastrobattista, E., Taly, V., Magdassi, S., Tawfik, D. S. & Griffiths, A. D. 2006 Directed evolution by in vitro compartmentalization. *Nature Methods* **3** (7), 561–570.

Minardi, C. S., Taghioskoui, M., Jang, S. J. & Jorabchi, K. 2013 Reagent delivery by partial coalescence and noncoalescence of aqueous microdroplets in oil. *Analytical Chemistry* **85** (13), 6491–6.

Mohamed-Kassim, Z. & Longmire, E. K. 2004 Drop coalescence through a liquid/liquid interface. *Physics of Fluids* **16** (7), 2170–2180.

Monaghan, J. J. 1992 Smoothed Particle Hydrodynamics. *Annual Review of Astronomy and Astrophyics* **30**, 543–74.

Moore, G. E. 1965 Cramming more components onto integrated circuits. *Electronics* **38** (8), 114–117.

Morton, D., Rudman, M. & Liow, J.-L. 2000 An investigation of the flow regimes resulting from splashing drops. *Physics of Fluids* **12** (4), 747–763.

Mousavi, S., Ghadiri, M. & Buckley, M. 2014 Electro-coalescence of water drops in oils under pulsatile electric fields. *Chemical Engineering Science* **120**, 130–142.

Mousavichoubeh, M., Ghadiri, M. & Shariaty-Niassar, M. 2011*a* Electro-coalescence of an aqueous droplet at an oil-water interface. *Chemical Engineering and Processing: Process Intensification* **50** (3), 338–344.

Mousavichoubeh, M., Shariaty-Niassar, M. & Ghadiri, M. 2011*b* The effect of interfacial tension on secondary drop formation in electro-coalescence of water droplets in oil. *Chemical Engineering Science* **66** (21), 5330–5337.

Mugele, F. 2009 Fluid dynamics: To merge or not to merge ... *Nature* **461**, 356.

Mugele, F. & Baret, J.-C. 2005 Electrowetting: from basics to applications. *Journal of Physics: Condensed Matter* **17** (28), R705–R774.

Nelson, W. C. & Kim, C.-J. 2012 Droplet actuation by electrowetting-on-dielectric (EWOD): a review. *Journal of Adhesion Science and Technology* **26** (12-17), 1747–1771.

Nganguia, H., Young, Y.-N., Layton, A. T., Lai, M.-C. & Hu, W.-F. 2016 Electrohydrodynamics of a viscous drop with inertia. *Physical Review E* **93** (5), 1–9.

Nganguia, H., Young, Y. N., Vlahovska, P. M., Bławzdziewcz, J., Zhang, J. & Lin, H. 2013 Equilibrium electro-deformation of a surfactant-laden viscous drop. *Physics of Fluids* **25** (9), 0921061–19.

Nguyen, N. T. 2012 Micro-magnetofluidics: Interactions between magnetism and fluid flow on the microscale. *Microfluidics and Nanofluidics* **12** (1), 1–16.

Nguyen, N.-T. & Wu, Z. 2005 Micromixers-a review. *Journal of Micromechanics and Microengineering* **15** (2), R1–R16.

Nie, X. B., Chen, S. Y., E, W. N. & Robbins, M. O. 2004 A continuum and molecular dynamics hybrid method for micro- and nano-fluid flow. *Journal of Fluid Mechanics* **500**, 55–64.

Noh, W. F. & Woodward, P. 1976 SLIC (simple line interface calculation). In *Lecture Notes in Physics*, pp. 330–340. New York: Springer.

Nolan, J. J. 1926 The breaking of water drops by electric fields. *Proceedings of the Royal Irish Academy. Section A: Mathematical and Physical Sciences* **37**, 28–39.

Norman, R. & Haas, I. 1960 Solid-state micrologic elements. In *Solid-State Circuits Conference. Digest of Technical Papers. 1960 IEEE International Volume: III*, pp. 82–83.

Oh, K. W. & Ahn, C. H. 2006 A review of microvalves. *Journal of Micromechanics and Microengineering* **16** (5), R13–R39.

O'Konski, C. T. & Harris, F. E. 1957 Electric free energy and the deformation of droplets in electrically conducting systems. *The Journal of Physical Chemistry* **61** (9), 1172–1174.

O'Konski, C. T. & Thatcher Jr, H. C. 1953 The distortion of aerosol droplets by an electric field. *The Journal of Physical Chemistry* **5** (11), 9–12.

Ozen, O., Aubry, N., Papageorgiou, D. T. & Petropoulos, P. G. 2006 Electrohydrodynamic linear stability of two immiscible fluids in channel flow. *Electrochimica Acta* **51** (25), 5316–5323.

Pagonabarraga, I., Rotenberg, B. & Frenkel, D. 2010 Recent advances in the modelling and simulation of electrokinetic effects: bridging the gap between atomistic and macroscopic descriptions. *Physical Chemistry Chemical Physics* **12** (33), 9566–9580.

Paknemat, H., Pishevar, A. R. & Pournaderi, P. 2012 Numerical simulation of drop deformations and breakup modes caused by direct current electric fields. *Physics of Fluids* **24** (10), 102101–26.

Park, J.-U., Hardy, M., Kang, S. J., Barton, K., Adair, K., Mukhopadhyay, D. K., Lee, C. Y., Strano, M. S., Alleyne, A. G., Georgiadis, J. G., Ferreira, P. M. & Rogers, J. A. 2007 High-resolution electrohydrodynamic jet printing. *Nature Materials* **6** (10), 782–9.

Pascall, A. J. & Squires, T. M. 2011 Electrokinetics at liquid/liquid interfaces. *Journal of Fluid Mechanics* **684**, 163–191.

Persat, A., Suss, M. E. & Santiago, J. G. 2009*a* Basic principles of electrolyte chemistry for microfluidic electrokinetics. Part I: Coupling between ion mobility, electrolysis, and acid-base equilibria. *Lab on a Chip* **9** (17), 2437–2552.

Persat, A., Suss, M. E. & Santiago, J. G. 2009*b* Basic principles of electrolyte chemistry for microfluidic electrokinetics. Part II: Coupling between ion mobility, electrolysis, and acid-base equilibria. *Lab on a Chip* **9** (17), 2454–2469.

Peters, J. M. H. 1982 Einstein's relation. *European Journal of Physics* **3**, 19–21.

Peterson, M. A. 2001 Galileo's Discovery of Scaling Laws. *American Journal of Physics* **70** (6), 575–580.

Pethig, R. 2010 Review article-dielectrophoresis: status of the theory, technology, and applications. *Biomicrofluidics* **4** (2), 1–35.

Pillai, R., Berry, J. D., Harvie, D. J. E. & Davidson, M. R. 2014 Effect of interfacial tension and electric field on charge separation dynamics inside stable and unstable microdrops. In *19th Australasian Fluid Mechanics Conference*, pp. 8–11.

Pillai, R., Berry, J. D., Harvie, D. J. E. & Davidson, M. R. 2015*a* Electrolytic drops in an electric field: A numerical study of drop deformation and breakup. *Physical Review E* **92** (1), 0130071–15.

Pillai, R., Berry, J. D., Harvie, D. J. E. & Davidson, M. R. 2015*b* Electrophoretic Effects on Satellite Droplet Formation During Electrocoalescence of Microdrops. In *11th International Conference on CFD in the Minerals and Process Industries*.

Pillai, R., Berry, J. D., Harvie, D. J. E. & Davidson, M. R. 2016*a* Electrohydrodynamic deformation and interaction of microscale drop pairs. *International Journal of Computational Methods and Experimental Measurements* **4** (1), 33–41.

Pillai, R., Berry, J. D., Harvie, D. J. E. & Davidson, M. R. 2016*b* Electrokinetics of isolated electrified drops. *Soft Matter* **12** (14), 3310–3325.

Pillai, R., Berry, J. D., Harvie, D. J. E. & Davidson, M. R. 2016*c* Electrophoretically mediated partial coalescence of a charged microdrop. *Chemical Engineering Science* (To appear).

Pohl, H. A. 1951 The motion and precipitation of suspensoids in divergent electric fields. *Journal of Applied Physics* **22** (7), 869–871.

Pompano, R. R., Liu, W., Du, W. & Ismagilov, R. F. 2011 Microfluidics using spatially defined arrays of droplets in one, two, and three dimensions. *Annual Review of Analytical Chemistry* **4**, 59–81.

Prosperetti, A. 1980 Free oscillations of drops and bubbles: the initial-value problem. *Journal of Fluid Mechanics* **100** (02), 333–347.

Qian, S. & Bau, H. H. 2009 Magneto-hydrodynamics based microfluidics. *Mechanics Research Communications* **36** (1), 10–21.

Quincke, G. H. 1861 Ueber die Fortführung materieller Theilchen durch strömende Elektricität. *Annalen der Physik und Chemie* **189**, 513–598.

Ramiasa, M., Ralston, J., Fetzer, R. & Sedev, R. 2014 The influence of topography on dynamic wetting. *Advances in Colloid and Interface Science* **206**, 275–293.

Ramos, A. & Castellanos, A. 1994 Conical points in liquid-liquid interfaces subjected to electric fields. *Physics Letters A* **184** (3), 268–272.

Ray, B., Biswas, G. & Sharma, A. 2010 Generation of secondary droplets in coalescence of a drop at a liquid-liquid interface. *Journal of Fluid Mechanics* **655**, 72–104.

Rayleigh, L. 1879 On the capillary phenomena of jets. *Proceedings of the Royal Society of London* **29**, 71–97.

Rayleigh, L. 1882 XX. On the equilibrium of liquid conducting masses charged with electricity. *The London, Edinburgh, and Dublin Philosophical Society* **14** (87), 184–186.

Ren, Y., Liu, Z. & Shum, H. C. 2015 Breakup dynamics and dripping-to-jetting transition in a Newtonian/shear-thinning multiphase microsystem. *Lab on a Chip* **15** (1), 121–134.

Reuss, F. F. 1809 Sur un nouvel effet de l'électricité galvanique. *Mem. Soc. Imp. Natur. Moscou* **2**, 327–337.

Reyes, D. R., Iossifidis, D., Auroux, P.-A. & Manz, A. 2002 Micro total analysis systems. 1. Introduction, theory, and technology. *Analytical Chemistry* **74** (12), 2623–2636.

Rhodes, D. & Yariv, E. 2010 The elongated shape of a dielectric drop deformed by a strong electric field. *Journal of Fluid Mechanics* **664**, 286–296.

Ristenpart, W. D., Bird, J. C., Belmonte, A., Dollar, F. & Stone, H. A. 2009 Non-coalescence of oppositely charged drops. *Nature* **461** (7262), 377–80.

Rosenkilde, C. E. 1969 A Dielectric Fluid Drop an Electric Field. *Proceedings of the Royal Society of London A.* **312** (1511), 473–494.

Rudman, M. 1997 Volume-Tracking Methods for Interfacial Flow Calculations. *International Journal for Numerical Methods in Fluids* **24** (7), 671–691.

Rudman, M. 1998 A volume-tracking method for incompressible multifluid flows with large density variations. *International Journal for Numerical Methods in Fluids* **28** (2), 357–378.

Sadri, B., Tabatabaee-Hosseini, P., Hokmabad, B. V., Charan, M. R. & Esmaeilzadeh, E. 2013 Experimental study on the regimes of W/O interface in the presence of vertical electric field. *Journal of Colloid and Interface Science* **400**, 104–15.

Salipante, P. F. & Vlahovska, P. M. 2010 Electrohydrodynamics of drops in strong uniform DC electric fields. *Physics of Fluids* **22** (11).

Saran, C. 2009 Apollo 11: The computers that put man on the moon.

Saville, D. A. 1974 Electrohydrodynamic oscillation and stability of a charged drop. *Physics of Fluids* **17** (1), 54–60.

Saville, D. A. 1997 Electrohydrodynamics: the Taylor-Melcher leaky dielectric model. *Annual Review of Fluid Mechanics* **29**, 27–64.

Schnitzer, O. & Yariv, E. 2015 The Taylor - Melcher leaky dielectric model as a macroscale electrokinetic description. *Journal of Fluid Mechanics* **773**, 1–33.

Scott, T. C., Basaran, O. A. & Byers, C. H. 1990 Characteristics of electric-field-induced oscillations of translating liquid droplets. *Industrial & Engineering Chemistry Research* **29** (5), 901–909.

Seemann, R., Brinkmann, M., Pfohl, T. & Herminghaus, S. 2012 Droplet based microfluidics. *Reports on Progress in Physics* **75** (75), 16601–41.

Shah, R. K., Shum, H. C., Rowat, A. C., Lee, D., Agresti, J. J., Utada, A. S., Chu, L. Y., Kim, J. W., Fernandez-Nieves, A., Martinez, C. J. & Weitz, D. A. 2008 Designer emulsions using microfluidics. *Materials Today* **11** (4), 18–27.

Sherwood, J. D. 1988 Breakup of fluid droplets in electric and magnetic fields. *Journal of Fluid Mechanics* **188**, 133–146.

Sherwood, J. D. 1999 The deformation of a fluid drop in an electric field: a slender-body analysis. *Journal of Physics A: Mathematical and General* **24**, 4047–4053.

Shoji, S., Esashi, M. & Matsuo, T. 1988 Prototype miniature blood gas analyser fabricated on a silicon wafer. *Sensors and Actuators* **14** (2), 101–107.

Shui, L., Eijkel, J. C. T. & van den Berg, A. 2007 Multiphase flow in microfluidic systems - Control and applications of droplets and interfaces. *Advances in Colloid and Interface Science* **133** (1), 35–49.

Song, H., Chen, D. L. & Ismagilov, R. F. 2006 Reactions in droplets in microfluidic channels. *Angewandte Chemie* **45** (44), 7336–56.

Song, H., Tice, J. D. & Ismagilov, R. F. 2003 A Microfluidic System for Controlling Reaction Networks in Time. *Angewandte Chemie* **115** (7), 792–796.

Sozou, C. 1973 Electrohydrodynamics of a liquid drop: the development of the flow field. *Proceedings of the Royal Society A: Mathematical, Physical and Engineering Sciences* **334** (1598), 343–356.

Squires, T. M. & Quake, S. R. 2005 Microfluidics: Fluid physics at the nanoliter scale. *Reviews of Modern Physics* **77** (3), 977–1026.

Srinivasan, V., Pamula, V. K. & Fair, R. B. 2004 An integrated digital microfluidic lab-on-a-chip for clinical diagnostics on human physiological fluids. *Lab on a Chip* **4** (4), 310–315.

Stern, O. 1924 Zur theorie der elektrolytischen doppelschicht. *Zeitschrift fur Elektrochemie* **30**, 508–516.

Stone, H. A., Lister, J. R. & Brenner, M. P. 1999 Drops with conical ends in electric and magnetic fields. *Proceedings of the Royal Society A: Mathematical, Physical and Engineering Sciences* **455** (1981), 329–347.

Stone, H. A., Stroock, A. D. & Ajdari, A. 2004 Engineering flows in small devices. *Annual Review of Fluid Mechanics* **36** (1), 381–411.

Stratton, J. A. 1941 *Electromagnetic Theory*. Hoboken, New Jersey: John Wiley and Sons.

Subramani, H. J., Yeoh, H. K., Suryo, R., Xu, Q., Ambravaneswaran, B. & Basaran, O. A. 2006 Simplicity and complexity in a dripping faucet. *Physics of Fluids* **18** (3), 0321061–13.

Subramanyam, S. V. 1969 A note on the damping and oscillations of a fluid drop moving in another fluid. *Journal of Fluid Mechanics* **37** (4), 715–725.

Supeene, G., Koch, C. R. & Bhattacharjee, S. 2008 Deformation of a droplet in an electric field: Nonlinear transient response in perfect and leaky dielectric media. *Journal of Colloid and Interface Science* **318** (2), 463–476.

Sweet, R. G. 1965 High frequency recording with electrostatically deflected ink jets. *Review of Scientific Instruments* **36** (2), 131–136.

Tan, S. H., Maes, F., Semin, B., Vrignon, J. & Baret, J. C. 2014*a* The microfluidic jukebox. *Scientific Reports* **4** (4787), 1–8.

Tan, S. H., Semin, B. & Baret, J. C. 2014*b* Microfluidic flow-focusing in ac electric fields. *Lab on a Chip* **14** (6), 1099–106.

Tavana, H., Jovic, A., Mosadegh, B., Lee, Q. Y., Liu, X., Luker, K. E., Luker, G. D., Weiss, S. J. & Takayama, S. 2009 Nanolitre liquid patterning in aqueous environments for spatially defined reagent delivery to mammalian cells. *Nature Materials* **8** (9), 736–41.

Taylor, G. I. 1964 Disintegration of water drops in an electric field. *Proceedings of the Royal Society A: Mathematical, Physical and Engineering Sciences* **280** (1382), 383–397.

Taylor, G. I. 1966 Studies in electrohydrodynamics. I. the circulation produced in a drop by electrical field. *Proceedings of the Royal Society A: Mathematical, Physical and Engineering Sciences* **291** (1425), 159–166.

Teh, S.-Y., Lin, R., Hung, L.-H. & Lee, A. P. 2008 Droplet microfluidics. *Lab on a Chip* **8** (2), 198–220.

Teigen, K. E. & Munkejord, S. T. 2010 Influence of surfactant on drop deformation in an electric field. *Physics of Fluids* **22** (11), 1121041–9.

Teigen, K. E., Munkejord, S. T. & Bjørklund, E. 2006 A computational study of the coalescence process between a drop and an interface in an electric field. In *6th International Conference on CFD in the Oil, Gas, Metallurgical and Process Industries*.

Terry, S. C., Jerman, J. H. & Angell, J. B. 1979 A gas chromatographic air analyzer fabricated on a silicon wafer. *IEEE Transactions on Electron Devices* **26** (12), 1880–1886.

Theberge, A. B., Courtois, F., Schaerli, Y., Fischlechner, M., Abell, C., Hollfelder, F. & Huck, W. T. S. 2010 Microdroplets in microfluidics: an evolving platform for discoveries in chemistry and biology. *Angewandte Chemie* **49** (34), 5846–68.

Thiam, A. R., Bremond, N. & Bibette, J. 2009 Breaking of an emulsion under an ac electric field. *Physical Review Letters* **102** (18), 1–4.

Thomson, J. J. 1894 On the electricity of drops. *Philosophical Magazine* **37** (227), 1–2.

Thoroddsen, S. T. & Takehara, K. 2000 The coalescence cascade of a drop. *Physics of Fluids* **12** (6), 1265–1267.

Thorsen, T. 2002 Microfluidic Large-Scale Integration. *Science* **298** (5593), 580–584.

Tomar, G., Gerlach, D., Biswas, G., Alleborn, N., Sharma, a., Durst, F., Welch, S. & Delgado, a. 2007 Two-phase electrohydrodynamic simulations using a volume-of-fluid approach. *Journal of Computational Physics* **227** (2), 1267–1285.

Tomotika, S. 1935 On the Instability of a Cylindrical Thread of a Viscous Liquid Surrounded by Another Viscous Fluid. *Proceedings of the Royal Society A: Mathematical, Physical and Engineering Sciences* **150** (870), 322–337.

Torza, S., Cox, R. G. & Mason, S. G. 1971 Electrohydrodynamic deformation and burst of liquid drops. *Philosophical Transactions of the Royal Society A: Mathematical, Physical and Engineering Sciences* **269** (1198), 295–319.

Tsukada, T., Katayama, T., Ito, Y. & Hozawa, M. 1993 Theoretical and experimental studies of circulations inside and outside a deformed drop under a uniform field. *Journal of Chemical Engineering of Japan* **26** (6), 698–703.

Utada, A. S., Fernandez-Nieves, A., Stone, H. A. & Weitz, D. A. 2007 Dripping to jetting transitions in coflowing liquid streams. *Physical Review Letters* **99** (9), 1–4.

Utada, A. S., Lorenceau, E., Link, D. R., Kaplan, P. D., Stone, H. A. & Weitz, D. A. 2005 Monodisperse double emulsions generated from a microcapillary device. *Science* **308** (5721), 537–541.

Verpoorte, E. & De Rooij, N. F. 2003 Microfluidics meets MEMS. *Proceedings of the IEEE* **91** (6), 930–953.

Versteeg, H. K. & Malalasekera, W. 2011 *An Introduction to Computational Fluid Dynamics: The Finite Volume Method*. Pearson Education Limited.

Vizika, O. & Saville, D. a. 1991 The electrohydrodynamic deformation of drops suspended in liquids in steady and oscillatory electric fields. *Journal of Fluid Mechanics* **239**, 1–21.

Wang, B.-B., Wang, X.-D., Yan, W.-M. & Wang, T.-H. 2015 Molecular dynamics simulations on coalescence and non-coalescence of conducting droplets. *Langmuir* **31** (27), 7457–7462.

Wang, J., Wang, B. & Qiu, H. 2014 Coalescence and breakup of oppositely charged droplets. *Scientific Reports* **4** (7123), 1–6.

Wang, J. T., Wang, J. & Han, J. J. 2011 Fabrication of advanced particles and particle-based materials assisted by droplet-based microfluidics. *Small* **7** (13), 1728–1754.

Wang, Q. 2012 Breakup of a poorly conducting liquid thread subject to a radial electric field at zero Reynolds number. *Physics of Fluids* **24** (10), 1–22.

Wang, Q., Suo, Z. & Zhao, X. 2012 Bursting drops in solid dielectrics caused by high voltages. *Nature communications* **3**, 1–7.

Weibel, D. B. & Whitesides, G. M. 2006 Applications of microfluidics in chemical biology. *Current Opinion in Chemical Biology* **10** (6), 584–591.

Weigl, B. H., Bardell, R. L. & Cabrera, C. R. 2003 Lab-on-a-chip for drug development. *Advanced Drug Delivery Reviews* **55** (3), 349–377.

Wesseling, P. 1991 *An introduction to multigrid methods*. R.T. Edwards Inc.

Whitaker, D. L., Kim, C., Vicente, C. L., Weilert, M. a., Maris, H. J. & Seidel, G. M. 1998 Shape oscillations in levitated He II drops. *Journal of Low Temperature Physics* **113** (3), 491–499.

Whitesides, G. M. 2006 The origins and the future of microfluidics. *Nature* **442** (7101), 368–73.

Whitesides, G. M., Ostuni, E., Jiang, X. & Ingber, D. E. 2001 Soft Lithography in Biology and Biochemistry. *Annual Review of Biomedical Engineering* **3**, 335–73.

Wikipedia 2016 iPhone 7 p. https://en.wikipedia.org/wiki/IPhone_7.

Williams, R., Peisajovich, S. G., Miller, O. J., Magdassi, S., Tawfik, D. S. & Griffiths, A. D. 2006 Amplification of complex gene libraries by emulsion PCR. *Nature Methods* **3** (7), 545–550.

Wilson, C. T. R. 1911 On a method of making visible the paths of ionising particles through a gas. *Proceedings of the Royal Society A: Mathematical, Physical and Engineering Sciences* **85** (578), 285–289.

Wilson, C. T. R. 1912 On an expansion apparatus for making visible the tracks of ionising particles in gases and some results obtained by its use. *Proceedings of the Royal Society A: Mathematical, Physical and Engineering Sciences* **87** (595), 277–292.

Wilson, C. T. R. & Taylor, G. I. 1925 The bursting of soap-bubbles in a uniform electric field. *Mathematical Proceedings of the Cambridge Philosophical Society* **22** (5), 728–730.

Wörner, M. 2012 Numerical modeling of multiphase flows in microfluidics and micro process engineering: A review of methods and applications. *Microfluidics and Nanofluidics* **12** (6), 841–886.

Worthington, A. M. 1882 On Impact with a Liquid Surface. *Proceedings of the Royal Society of London* **34** (220), 217–230.

Wu, N. & Russel, W. B. 2009 Micro- and nano-patterns created via electrohydrodynamic instabilities. *Nano Today* **4** (2), 180–192.

Xia, Y. & Whitesides, G. M. 1998 Soft Lithography. *Annual Review of Material Science* **28**, 153–184.

Xu, S., Nie, Z., Seo, M., Lewis, P., Kumacheva, E., Stone, H. A., Garstecki, P., Weibel, D. B., Gitlin, I. & Whitesides, G. M. 2005 Generation of monodisperse particles by using microfluidics: Control over size, shape, and composition. *Angewandte Chemie* **44** (5), 724–728.

Yan, H., He, L., Luo, X., Wang, J., Huang, X., Lü, Y. & Yang, D. 2015 Investigation on Transient Oscillation of Droplet Deformation before Conical Breakup under Alternating Current Electric Field. *Langmuir* **31** (30), 8275–8283.

Yang, R.-J., Hou, H.-H., Wang, Y.-N. & Fu, L.-M. 2016 Micro-magnetofluidics in microfluidic systems : A review. *Sensors & Actuators: B. Chemical* **224**, 1–15.

Yao, Y., Beussman, K. M. & Wang, Y. 2015 Computational studies of droplet dynamics in a steady electric field. In *ASME Proceedings Fluids and Heat Transfer*, pp. 1–5.

Yariv, E. & Rhodes, D. 2013 Electrohydrodynamic Drop Deformation by Strong Electric Fields: Slender-Body Analysis. *SIAM Journal on Applied Mathematics* **73** (6), 2143–2161.

Yeo, L. Y., Chang, H.-C., Chan, P. P. Y. & Friend, J. R. 2011 Microfluidic devices for bioapplications. *Small* **7** (1), 12–48.

Yeo, L. Y. & Friend, J. R. 2014 Surface Acoustic Wave Microfluidics. *Annual Review of Fluid Mechanics* **46**, 379–406.

Youngs, D. L. 1982 Time-dependent multi-material flow with large fluid distortion. In *Numerical Methods for Fluid Dynamics*, pp. 273–285. New York: Academic Press.

Yue, P., Zhou, C. & Feng, J. J. 2006 A computational study of the coalescence between a drop and an interface in Newtonian and viscoelastic fluids. *Physics of Fluids* **18** (10), 1021021–13.

Zagnoni, M., Le Lain, G. & Cooper, J. M. 2010 Electrocoalescence mechanisms of microdroplets using localized electric fields in microfluidic channels. *Langmuir* **26** (18), 14443–9.

Zalesak, S. T. 1979 Fully multidimensional flux-corrected transport algorithms for fluids. *Journal of Computational Physics* **31** (3), 335–362.

Zangle, T. a., Mani, A. & Santiago, J. G. 2009 On the propagation of concentration polarization from microchannel-nanochannel interfaces. Part II: Numerical and experimental study. *Langmuir* **25** (6), 3909–16.

Zeleny, J. 1914 The Electrical Discharge from Liquid Points, and a Hydrostatic Method of Measuring the Electric Intensity at Their Surfaces. *Physical Review* **3** (2), 69–91.

Zeleny, J. 1917 Instability of electrified liquid surfaces. *Physical Review* **10** (1), 1–6.

Zhang, F., Li, E. & Thoroddsen, S. 2009 Satellite Formation during Coalescence of Unequal Size Drops. *Physical Review Letters* **102** (10), 1045021–4.

Zhang, H., Hassanali, A. A., Shin, Y. K., Knight, C. & Singer, S. J. 2011 The water-amorphous silica interface: Analysis of the Stern layer and surface conduction. *Journal of Chemical Physics* **134** (2), 0247051–13.

Zhang, H., Tumarkin, E., Peerani, R., Nie, Z., Sullan, R. M. A., Walker, G. C. & Kumacheva, E. 2006 Microfluidic production of biopolymer microcapsules with controlled morphology. *Journal of the American Chemical Society* **128** (37), 12205–12210.

Zhang, J., Borg, M. K., Ritos, K. & Reese, J. M. 2016 Electrowetting Controls the Deposit Patterns of Evaporated Salt Water Nanodroplets. *Langmuir* **32** (6), 1542–1549.

Zhang, J., Zahn, J. D. & Lin, H. 2013*a* Transient solution for droplet deformation under electric fields. *Physical Review E* **87** (4), 1–9.

Zhang, T., Chakrabarty, K. & Fair, R. B. 2004 Behavioral Modeling and Performance Evaluation of Microelectrofluidics-Based PCR Systems Using SystemC. *IEEE Transactions on Computer-Aided Design of Integrated Circuits and Systems* **23** (6), 843–858.

Zhang, X. & Basaran, O. A. 1995 An experimental study of dynamics of drop formation. *Physics of Fluids* **7** (6), 1184.

Zhang, Y., Liu, Y., Wang, X., Shen, Y., Ji, R. & Cai, B. 2013*b* Investigation of the charging characteristics of micron sized droplets based on parallel plate capacitor model. *Langmuir* **29** (5), 1676–1682.

Zhao, C. & Yang, C. 2012 Advances in electrokinetics and their applications in micro/nano fluidics. *Microfluidics and Nanofluidics* **13** (2), 179–203.

Zhao, C.-X. & Middelberg, A. P. 2011 Two-phase microfluidic flows. *Chemical Engineering Science* **66** (7), 1394–1411.

Zholkovskij, E. K., Masliyah, J. H. & Czarnecki, J. 2002 An electrokinetic model of drop deformation in an electric field. *Journal of Fluid Mechanics* **472**, 1–27.

Zhu, Y. & Fang, Q. 2013 Analytical detection techniques for droplet microfluidics-A review. *Analytica Chimica Acta* **787**, 24–35.

Ziemecka, I., van Steijn, V., Koper, G. J. M., Kreutzer, M. T. & van Esch, J. H. 2011 All-aqueous core-shell droplets produced in a microfluidic device. *Soft Matter* **7** (21), 9878–9880.

Zubarev, N. M. 2005 Formation of singularities on the surface of a liquid metal in a strong electric field. *Journal of Experimental and Theoretical Physics Letters* **73** (10), 613–617.